INVESTIGATING LIGHT SOLVENT AIDED PROCESS IN COLD LAKE OIL-SAND RESERVOIR USING EXPERIMENTAL AND NUMERICAL APPROACHES

by

Sara Eghbali

A THESIS SUBMITTED IN PARTIAL FULFILLMENT OF
THE REQUIREMENTS FOR THE DEGREE OF
DOCTOR OF PHILOSOPHY

in

Petroleum Engineering

Department of Civil and Environmental Engineering

UNIVERSITY OF ALBERTA

Abstract

Steam assisted- gravity drainage (SAGD) is the main in-situ bitumen recovery process in which saturated steam is injected into the bitumen zone. However, it has some drawbacks, which include high-energy consumption and significant environmental concerns. Solvent Aided Process (SAP) is a method proposed to improve SAGD's efficiency and to reduce its associated emissions by reducing Cumulative Steam Oil Ratio (CSOR). Previous studies showed that co-injecting steam with a wide range of solvents including normal alkanes from C_4 to C_8 and diluents improved oil production rates and reduced CSORs. Although co-injecting solvents with steam has improved bitumen recovery, understanding the effect of key parameters controlling SAP's performance and designing an optimum co-injection remain challenging. Also, the effects of solvents lighter than C_5 such as CO_2, C_3 and C_4 on the efficiency of SAP are not well understood. Understanding and modelling fluid-fluid interactions in solvent-bitumen systems including the phase behavior and viscosity of solvent-bitumen systems is essential for developing an optimum SAP for bitumen recovery.

In this research, experimental and numerical simulation studies are undertaken to optimize SAP's performance by co-injecting steam with CO_2, C_3 and C_4 solvents. The experimental study investigates the phase behavior of CO_2-, C_3- and C_4-bitumen systems. An Equation of State (EOS) is calibrated against the measured Pressure-Volume-Temperature (PVT) data to predict phase behaviour of the solvent-bitumen systems. A robust algorithm is developed for reliable prediction of multi-phase equilibrium. Also, viscosities of these systems are measured and used to modify a viscosity model. The developed algorithm and the calibrated EOS are used to predict

phase-equilibrium regions in the compositional space for the solvent-bitumen at elevated temperatures. The calibrated EOS and viscosity model are applied in a simulation model to understand the phase behavior of steam-solvent-bitumen at steam-bitumen interface and to optimize SAP in Clearwater Formation. The simulation study optimizes SAP in terms of solvent type, solvent concentration and co-injection strategy.

The advantage of the developed algorithm for multiphase equilibria calculations is robust and efficient prediction of complex phase behavior. This complex phase behavior is possible during SAP where a vapor phase and three liquid phases can coexist (i.e., L_1: rich in bitumen component, L_2: rich in solvent and W: aqueous phase).

Multiphase equilibria and viscosity calculations show that existence of additional solvent above a defined threshold of solvent concentration has limited effect on reducing bitumen viscosity. C_4 leads to higher viscosity reduction compared to C_3 and CO_2. In contrast with CO_2 and C_3, C_4 has the potential of extracting hydrocarbon components in a solvent-rich liquid phase (i.e., L_2 phase).

Numerical simulations of solvent-steam co-injection show that bitumen rate increases as a result of bitumen dilution. However, bitumen rate decreases after a while to a stabilized value. This happens as condensed water accumulates below the chamber over time. Therefore, condensed solvent accumulates at the top of the accumulated water within a limited region due to the gravity segregation. This causes reduction of the effective contact area between the condensed solvent and bitumen. Consequently, oil production rate stabilizes as more steam-solvent are co-injected. Therefore, an optimum co-injection scenario should be designed to maximize bitumen recovery and efficiency of this process.

Abstract

Bitumen viscosity near the chamber edge is higher for C_3-steam co-injection respect to C_4-steam co-injection. This is because C_3 has less solubility than C_4 in the oil phase and chamber temperature is lower in C_3-steam co-injection. This leads to more efficicent oil displacement near the edge in C_4-steam co-injection compared to C_3-steam co-injection. In constrast with C_3-steam co-injection, scenarios of C_4-steam co-injection with variable solvent concentration and descending trend of solvent concnetration has less ultimate recovery and Net Present Value compared with the constant concentration strategy with optimum concentration.

Results show that C_3- and C_4-steam co-injections lead to increase in bitumen recovery factor and reduction in CSOR over corresponding SAGD scenarios. On the other hand, CO_2-steam co-injection causes about 10% reduction in bitumen recovery factor compared to SAGD. Wettability of the reservoir rock has significant effect on performance of SAP using light solvents. Increasing oil wetness of the reservoir increases bitumen recovery. This is because there is less water blockage and more effective contact area between the condensed solvent and the heated bitumen in a more oil wet reservoir.

Preface

All or parts of Chapters 3 to 5 have been published as journal or conference papers. I was responsible for conducting experiments, model development, computer programming, writing and editing these papers. My co-authors were responsible for providing relevant data from their respective companies, providing useful comments and discussions on field practices, reviewing the manuscript drafts and securing company approvals for these publications.

Chapter 3 is published as Eghbali, S., and Okuno, R. 2015. Successive Substitution Augmented for Global Minimization of the Gibbs Free Energy. SPE Annual Technical Conference and Exhibition. SPE 175060-MS.

Chapter 4 is published as Eghbali, S., and Dehghanpour, H. 2018. An Experimental and Modelling Study of Solvent-Bitumen Phase Behavior at Elevated Temperatures using Cold Lake Bitumen. SPE Journal.

Chapter 4 is submitted as Eghbali, S., and Dehghanpour, H. 2018. An Experimental and Modeling Study on Interactions of Cold Lake Bitumen with CO_2, C_3, and C_4 at High Temperatures. Energy and Fuels Journal.

Chapter 5 is published as Eghbali, S., Dehghanpour, H., Dragani, J., and Zhang, X., 2018. Phase Behavior and Viscosity of Bitumen-CO_2/Light Hydrocarbon Mixtures at Elevated Temperatures: A Cold Lake Case Study. SPE Canada Heavy Oil Technical Conference. Society of Petroleum Engineers.

Chapter 6 is submitted as Eghbali, S. and Dehghanpour, H., 2018. Simulation Study on Solvent-Aided Process using Light Hydrocarbon Solvents in Clearwater Oil-Sand Formation. Journal of Petroleum Science and Engineering.

Dedicated with sincere gratitude to

to my beloved parents and my lovely husband, Maziar, who have been a constant source of support and encouragement during the challenges of this journey. I am truly thankful for having you in my life.

Acknowledgement

I would like to take this opportunity to express my gratitude and sincere thanks to my supervisor, Dr. Hassan Dehghanpour for his guidance and insightful ideas during my research and study at the University of Alberta. I also thank Dr. Ryosuke Okuno for his supervision in Chapter 3 of this thesis. I am thankful to Dr. Selma Guigard, Dr. Kamy Sepehrnoori, Dr. Alireza Nouri, Dr. Nicholas Beier and Dr. Hooman Askari Nasab, my examining committee members for their brilliant comments and suggestions.

I gratefully acknowledge the financial support from National Sciences and Engineering Council of Canada (NSERC) and I acknowledge Imperial Oil and Cenovus Energy for supporting this research and providing bitumen samples. I thank Mr. Jarrett Dragani and Mr. Xin Zhang from Cenovus Energy and Dr. Saber Mohammadi, Dr. Obinna Ezulike and Mr. Yousef Abbasi for their helpful technical comments. Also, I thank Todd Kinnee for his assistance in conducting PVT experiments.

I would like to appreciate my colleagues (Khan Athar, Ali Habibi, Mahmood Yassin, Mansour Molazem, Lin Yuan, Yingkun Fu, Yanmin Xu, Mingxiang, Xu, Son Tran, Mohammad Yousefi, Maryam Eghbalvala, Tamer Moussa, Taregh Soleiman Asl, Hamidreza Yarveicy, Mohammad Hossein Doranehgard, Sabbir Hossain and Serge Pegov) for their insightful contributions and fruitful discussions. Also, I appreciate the help of some administrative staff members of the civil and environmental engineering department (Anne Jones, Arlene Figley, Jomana Haymour and Trina Cattral). They were willing to listen and help at all times.

I would like to thank my parents and sister for their love, support and encouragement throughout my life that enlightened my path and gave me the strength to pace towards my achievements and for all of the sacrifices that they've made on my behalf. My deepest gratitude goes to my husband and love of my life, Maziar, for his unconditional love, patience and continual support that enabled me to complete this thesis.

Table of Contents

List of Tables

List of Figures

Chapter 1: General Introduction

First, this chapter introduces Canadian bitumen resources and their properties. Second, it describes Steam Assisted Gravity Drainage process (SAGD) and Solvent Aided Process (SAP) as an alternative to SAGD. Third, it considers the challenges associated with optimization of SAP. At the end, it presents research motivations, research objectives and structure of the thesis.

1.1 CANADIAN BITUMEN RESOURCES

The three major Canadian bitumen deposits are predominantly in the province of Alberta. They are Athabasca, Cold Lake and Peace River as shown in Figure 1-1 (Nasr and Ayodele, 2005). The average depth of the deposits are 300 m, 400 m and 500 m, respectively. The Alberta Energy and Utilities Board (AEUB) estimate the total initial volume-in-place of bitumen to be 259.1 billion m^3 (AEUB, 2002). This estimate could ultimately reach 400 billion m^3 by the time all exploratory developments are completed. Out of the total volume, 24 billion m^3 are available for surface mining techniques. The Athabasca deposit is the only deposit with surface mineable reserves. About 376 billion m^3 lie too deep to be surface-mined and are exploitable by in-situ technologies (Nasr and Ayodele, 2005). The Cold Lake deposit comprises four separate reservoirs that lie in McMurray, Clearwater, Lower Grand Rapids and Upper Grand Rapids and covers an area of approximately 21000 km^2 (Nasr and Ayodele, 2005). We investigate co-injection of solvent with steam in Clearwater Formation.

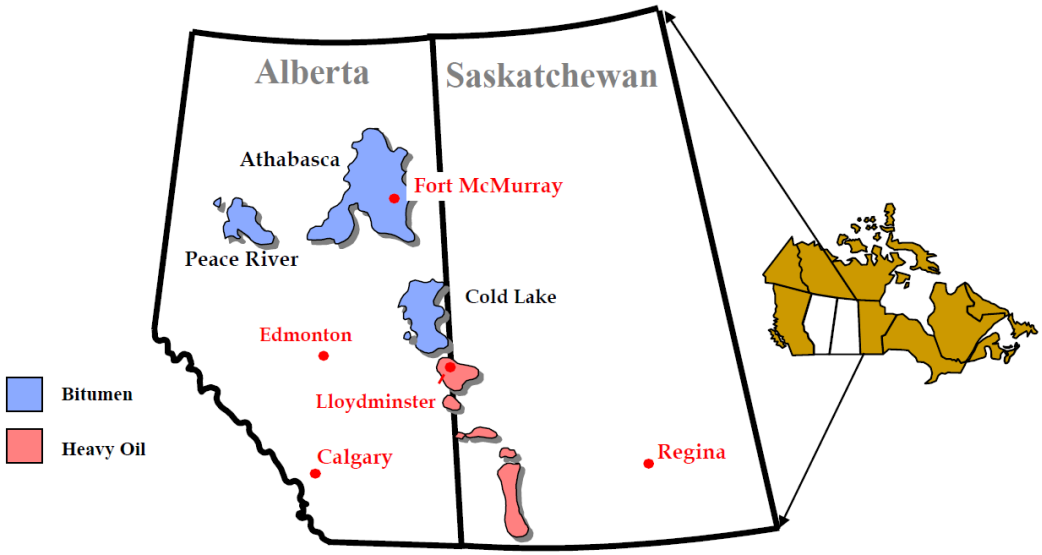

Figure 1-1: Major oil-sand deposits of Canada (Nasr and Ayodele, 2005)

1.2 CANADIAN OIL-SAND AND BITUMEN PROPERTIES

The oil-sands of Alberta are generally unconsolidated where the rock grains are loosely arranged. Their solid matrix comprises 90% quartz and 10% silt and clay. The bitumen saturation of the reservoirs is a function of porosity and permeability. A typical composition of rich oil sands is approximately 83% sand, 14% bitumen and 3% water by weight. The average composition of Alberta bitumen is 84% carbon, 10% hydrogen, 0.9% oxygen, 0.4% nitrogen and 4.7% sulphur (Speight, 1978).

The density and viscosity of bitumen varies by location and the API (American Petroleum Institute) gravity ranges between 8 and 12. Table 1-1 shows the API classifications (Tedeschi, 1991). Bitumen is oil having API gravity below 10 and viscosity above 10000 cP. Until recently, the low API and high viscosity of bitumen caused great difficulty in extraction of bitumen. SAGD is the dominant technology employed in recovery of heavy oil and oil-sands. The fortunate characteristic of the oil-sands is that the bitumen is not in direct contact with the sand grains and the grains are dominantly water wet, therefore, steam-based methods such as SAGD can be successful (Takamura, 1982). SAGD and its challenges are explained in the next section.

Table 1-1: API classifications (Tedeschi, 1991)

Classification	API	In-situ viscosity (cP)
Light	>31.1	-
Medium	22.3-31.1	-
Heavy	10-22.3	-
Extra Heavy	<10	<10000
Bitumen	<10	<10000

1.3 STEAM ASSISTED GRAVITY DRAINAGE (SAGD)

The economic potential of Alberta oil-sands is immense because its bitumen reserves exceed 255 billion m^3 (Ranger and Gingras, 2003). Alberta's oil-in-place is roughly seven times the size of Saudi Arabia's proven reserves (BP, 2011). Steam-assisted gravity drainage (SAGD) is currently the most widely used in-situ thermal technique for the recovery of bitumen (Butler, 1997). In the SAGD process, steam is continuously injected, with pressures typically ranging from 1000 to 7000 kPa, into an oil-bearing zone through a horizontal injection well placed 4 m to 4.5 m above a horizontal production well as shown in Figure 1-4 (Nasr et al., 2003). The injected steam propagates into the reservoir forming a steam chamber. The steam condenses at the chamber edge. This steam condensation is accompanied by the transfer of both its sensible and latent heat to the surroundings. Generally, the chamber edge is a zone where the coexistence of oleic, vapor and aqueous phases transitions to that of only oleic and aqueous phases (Keshavarz et al., 2014). In SAGD process, vapor phase contains vaporized water and probably very light components of in-situ bitumen if any, while oleic phase contains in-situ bitumen and aqueous phase contains condensed water. A fraction of the thermal energy released by steam is absorbed by bitumen situated beyond the chamber edge. This results in the reduction of bitumen viscosity and mobilization of the bitumen. The mobilized bitumen and condensed steam (i.e., water) drain under the influence of gravity into the production well, resulting in the expansion of the steam chamber. Many ongoing research initiatives are directed at improving the energy efficiency and emission intensity of the SAGD process (Nasr et al., 2003).

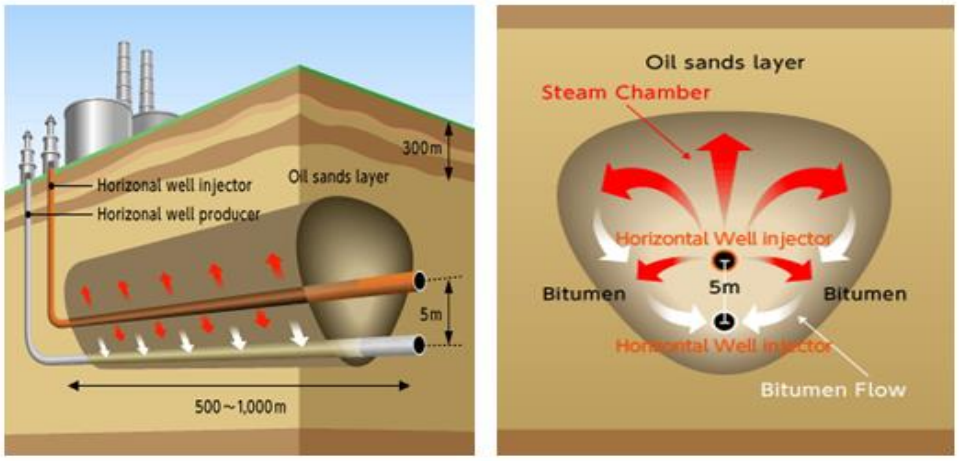

Figure 1-2: Schematic of the wells and steam chamber in SAGD process (Ahmedzhanov et al., 2013)

A common parameter used to quantify the performance of SAGD process is cumulative steam-oil-ratio (CSOR). This parameter is defined as the ratio of the cumulative steam injected (cold water equivalent) to the cumulative bitumen produced.

There are some drawbacks associated with SAGD process. They include high energy consumption and significant environmental concerns, including use of large volumes of fresh water and extensive greenhouse gas emissions. Significant emissions of greenhouse gases, large consumption of fresh water for steam generation, high costs of produced water treatment for reuse and environmental concerns regarding the waste water disposal make this process costly and environmentally unfriendly. Lowering CSOR could offer a profitable path to reduce emissions and water demand by reducing the amount of generated steam. This increases the efficiency of SAGD process.

1.4 SOLVENT AIDED PROCESS (SAP)

Solvent Aided Process is an alternative method to improve SAGD's efficiency and to reduce its associated emissions by reducing CSOR (Gupta et al., 2001). Compared to SAGD process, co-injecting solvent with steam (e.g., 1 to 20 wt.% solvent with the injection stream) enable more viscosity reduction by a combination of heat and mass-transfer effects and reduce steam requirements. The net result is an improvement in oil production rates and CSORs and a reduction in energy and water requirements compared to the SAGD process (Nasr et al., 2003; Gates, 2007). Existing studies using laboratory experiments and numerical simulation observed higher oil-production rates in SAP compared to SAGD. These studies considered a wide range of solvents including pure hydrocarbons (C_5 to C_8) and diluents (i.e., mixture of C_7 to

C_{12}) (Nasr et al., 2003; Gates, 2007; Ivory et al., 2008; Li and Mamora, 2010; Li et al., 2011; Yazdani et al., 2011).

Injecting CO_2, C_3 and C_4 into oil-sand reservoirs might be efficient for reducing heavy oil viscosity and improving heavy-oil recovery (Gupta et al., 2001; Saner and Patton 1986; Butler and Mokrys, 1993; Mohammed-Singh and Singhal 2005; Sahin et al. 2008; Kariznovi 2013; Badamchi-Zadeh et al., 2009; Eghbali and Dehghanpour, 2018). CO_2 has a higher solubility in oil compared with N_2 and C_1 at the same temperature and pressure (Haddadnia et al., 2017). Moreover, CO_2 is nontoxic and non-flammable (Kariznovi, 2013). C_4 has high solubility in heavy oil and bitumen, which might lead to a significant reduction in the oil viscosity (Kariznovi, 2013). Studies on the injection of C_3, C_4, or mixtures of C_3 and C_4 at low temperatures reported high oil production (Butler and Mokrys, 1993; Das and Butler 1995; Talbi and Maini 2003). Experimental results of injecting C_3 showed higher oil production (up to 50% oil recovery factor (Talbi and Maini, 2003) compared with hot water-solvent injection (Butler and Mokrys, 1993).

1.5 OPTIMIZATION OF SAP

Due to the solvent cost, it is required to find the most economical and efficient process with the lowest solvent concentration. When the high costs of solvents is taken into account, a proper design seems to be crucial to conduct an economically feasible co-injection process. This leads to an optimum design of the process for proper solvent selection as well as a co-injection strategy (i.e., amount and type of solvent versus time) that can maximize the potential advantages of steam-solvent co-injection.

Simulations, experimental studies (i.e., laboratory scale) and pilot scale studies showed improved oil production rates and lower CSOR in SAP (Nasr et al., 2003; Ivory et al., 2008; Gates, 2007; Gupta et al., 2005; Gupta and Gittins, 2006; Li et al., 2011b; Yazdani et al., 2011; Li and Mamora, 2010; Ardali et al., 2012; Mohammadzadeh et al., 2012). However, several studies showed that co-injection of some solvents with steam has no improvement or even a declined performance compared to steam-only injection (Jiang et al., 1998; Canbolat et al., 2002; Li and Mamora, 2011; Shu and Hartman 1988).

There are several feasible combinations of steam and solvents for SAP. However, evaluating these combinations using field scale pilots is difficult and costly.

Therefore, it is required to perform simulation. Simulation and experimental studies have been performed to investigate different factors controlling oil recovery in SAP. These factors include solvent type, solvent concentration and injection strategy. Govind et al. (2008) examined co-injection of steam with C_4, C_5, a mixture of C_6-C_8 and C_7 at 4000 kPa. They concluded that co-injection of C_4 leads to the highest recovery. Ardali et al. (2012) showed that co-injection of C_6 with steam leads to 20% increase in bitumen ultimate recovery factor. Li et al. (2011) found that heavy solvents such as C_7 and C_{12} are suitable solvents at optimal concentrations of 5-7% mol according to the production performance.

Several simulation studies for SAP optimization show conflicting results. This is due to the complexity of heat and mass transfer coupled with simulation input uncertainties such as solvent-bitumen phase behavior. Moreover, the effect of steam-light solvents (i.e., C_3 and C_4)-bitumen phase behavior on bitumen viscosity at the steam-bitumen interface is not well understood.

Previous studies have been performed to optimize injection strategy in solvent assisted SAGD process. They suggested moving from heavier solvents to lighter solvents during solvent-steam co-injection. Therefore, heavier solvents which are more expensive than lighter ones can be recovered later by co-injecting lighter solvents (Gates and Gutek, 2008; Gupta and Gittins, 2007b; Edmunds et al., 2010). However, optimizing the injection strategy has not been performed for light solvents by considering economic evaluations in SAP.

1.6 RESEARCH MOTIVATION AND OBJECTIVES

In the previous sections, the potential advantages of SAP over SAGD were briefly described. SAP is gaining worldwide attention due to its encouraging results in some applications. Compared to steam-only injection in SAGD, successful applications of SAP in field and laboratory studies show improved oil production rates, increased ultimate recovery factors and reduced steam oil ratio (Nasr et al. 2003; Ivory et al. 2008; Gupta et al. 2005; Gupta and Gittins 2006; Leaute, 2002; Leaute and Carey, 2005; Redford and McKay 1980; Li and Mamora 2010; Ardali et al., 2012; Mohammadzadeh et al., 2012). However, there is also evidence that co-injection of some solvents with steam resulted in no improvement or even worse performance compared to steam-only injection (Jiang et al., 1998; Canbolat et el., 2002; Li and Mamora, 2011; Shu and Hartman, 1988).

Although some of the experimental and simulation studies showed improvements in bitumen recovery by co-injecting solvents with steam, understanding the phase behavior of steam-solvent-bitumen at steam-bitumen interface and designing an optimum process remain challenging. Also, the effects of solvents lighter than C_5 such as CO_2, C_3 and C_4 on the efficiency and economics of SAP are not well understood. A proper design of co-injection process seems to be crucial for the practicality of these processes due to the high cost of solvents. This leads to necessity of optimizing the process for proper solvent type selection, solvent concentration as well as a co-injection strategy.

Complex multiphase behavior can occur during steam-solvent co-injection processes. Reliable phase behavior prediction and investigating fluid-fluid interactions are necessary in developing optimum SAP. As it will be explained in Chapter 3, there are two approaches available in literature for multiphase equilibrium calculations. These approaches include Conventional flash-stability and Simultaneous calculations. Conventional algorithms has been successfully applied for various compositional flow problems in the literature (e.g., Mehra et al., 1983; Nghiem and Li, 1984; Perschke, 1988; Han and Rangaiah, 1998). However, it is a series of local solutions for assumed numbers of phases, which requires obtaining and correcting false solutions for multiphase problems. The conventional algorithm is susceptible to failure especially in complex phase behaviour systems. The reason is that correcting the false solutions in phase-stability analysis is highly sensitive to the initial guess. The simultaneous phase stability-flash algorithm presented by Gupta et al. (1991) has numerical issues associated with degenerate equations near phase boundaries (Abdel-Ghani 1995; Alsaifi and Englezos, 2011).

The objective of this study is to investigate the effects of CO_2, C_3 and C_4 on performance of SAP and optimize these processes in terms of solvent type, solvent concentration and co-injection strategy. To achieve this goal, we consider the following sub-goals:

1. Develop a robust algorithm to predict multiphase equilibrium in solvent-bitumen systems over a wide range of temperatures
2. Measure phase behavior of solvent-bitumen systems at elevated temperatures to calibrate an Equation of State against the measured data

3. Predict phase behavior of the solvent-bitumen systems using the calibrated Equation of State (EOS) and the developed algorithm in composition space at elevated temperatures
4. Measure viscosity of solvent-bitumen systems at elevated temperatures and calibrate a viscosity model, applicable for reservoir flow simulation, against the measured data
5. Obtain a threshold solvent concentration in solvent-bitumen systems using several multiphase equilibria and viscosity calculations at elevated temperatures and operating pressure of SAP
6. Create a synthetic simulation model and integrate the calibrated phase behavior and viscosity models to investigate the key parameters controlling efficiency of CO_2-, C_3- and C_4-steam co-injections
7. Investigate the effects of C_3 and C_4 on phase behavior of steam-solvent-bitumen near the steam-bitumen interface during SAP
8. Design co-injection scenarios with constant concentration and variable-concentration strategies for the synthetic simulation model. Optimize SAP's performance in terms of solvent type, solvent concentration and co-injection strategy by considering economic analyses

1.7 ORGANIZATION OF THESIS

This is a paper-based thesis. After a short introduction section (Chapter 1) that includes a general overview, problem statement and research objectives, Chapters 2 through 6 are presented. Chapter 2 includes the background and literature review. Each of the Chapters of 3 to 6 has its own literature review, results and discussions and summary.

In Chapter 3, a modelling study is performed to develop a robust algorithm for multi-phase equilibrium calculations. Performance of the new algorithm is compared with the conventional algorithm.

In Chapter 4, a detailed experimental and modelling phase behavior study is conducted on CO_2-, C_3-, and C_4-bitumen systems. A bitumen sample from Cold Lake region is characterized and used for Constant Composition Expansion (CCE) test experiments. Peng-Robinson EOS is calibrated against the measured CCE test data to

obtain a predictive EOS model in a wide range of temperature. Using the EOS model and multiphase equilibria calculations, phase behavior and equilibrium regions of CO_2-, C_3-, and C_4-bitumen systems are compared. Also, the effect of solvent dissolution on asphaltene precipitation is investigated at elevated temperatures.

In Chapter 5, an experimental and modelling study is conducted to measure and model viscosity of CO_2-, C_3-, and C_4-bitumen systems at elevated temperatures. The calibrated EOS from Chapter 4 along with the calibrated viscosity model are applied in several phase equilibria and viscosity calculations to obtain a threshold solvent concentration for each solvent in solvent-bitumen systems at elevated temperatures.

In Chapter 6, a synthetic simulation model is created to simulate SAGD and SAP in Clearwater oil-sand Formation. A sensitivity analysis on grid size is performed to obtain an optimum grid size for fine-scale simulations. Using the numerical simulation model, the effects of key parameters controlling SAP's efficiency are investigated. These parameters include reservoir wettability, solvent type, solvent concentration and co-injection strategy. To understand the effect of solvent type, we investigate the phase behavior of steam-solvent-bitumen at the steam-bitumen interface. The effects of light solvents on the performance of this process are compared and optimum scenarios are designed for C_3-, and C_4-steam co-injections to maximize bitumen recovery and Net Present Value.

The final Chapter (Chapter 7) summarizes the main contributions of this work and provides recommendations for future work.

Chapter 2: Background

Measuring and modelling phase behavior of solvent-bitumen mixtures at elevated temperatures is required to design an optimum scenario for bitumen recovery using solvent aided process. To predict phase behavior of the solvent-bitumen-water system in a solvent aided process, phase equilibrium calculations is necessary. In this Chapter, first, we present the fundamentals of phase equilibrium and stability calculations. Second, we present phase behavior studies on CO2-, C3- and C4-bitumen/heavy oil systems from literature.

2.1 MINIMIZATION OF GIBBS FREE ENERGY

Conservation of energy is the first law of thermodynamics (Sandler, 2017):

$$dU = dq + dw \tag{2-1}$$

Where U is internal energy, q is heat, and w is work. The second law of thermodynamics states that the total entropy for an isolated system S_{total} cannot decrease for a spontaneous process, therefore:

$$dS_{total} = dS + dS' \geq 0 \tag{2-2}$$

Where S and S' are entropies of the system and surroundings, respectively, within an isolated system. Substituting $dS' \equiv dq'/T' = -dq/T$ when system and surroundings have the same temperature (i.e., T= T') leads to:

$$dS \geq dq/T \tag{2-3}$$

Combining Eqs. 2-1 and 2-2 where there is no non-expansion work leads to:

$$TdS - dU - PdV \geq 0 \tag{2-4}$$

where P is pressure and V is volume. From the definition of the Gibbs Free Energy

$G \equiv U + PV - TS$, therefore:

$$dG = dU + PdV + VdP - TdS - SdT \tag{2-5}$$

Substituting Eq. 2-5 into Eq. 2-4 lead to $dG - VdP + SdT \leq 0$.

Above equation at a fixed temperature and pressure is simplified to:

$$dG \leq 0 \tag{2-6}$$

Eq. 2-6 states that for a spontaneous process Gibbs Free Energy is minimized. Also, the solution of phase equilibrium calculations at a fixed temperature and pressure is the minimum of the Gibbs Free Energy (Sandler, 2017).

2.1.1 Flash Calculations

Formulation of phase equilibrium calculations for a multiphase, multicomponent, closed system at a fixed temperature and pressure is presented in this section. The total differential of the Gibbs Free Energy for a system including N_P-phases and N_C components is:

$$dG = \left(\frac{\partial G}{\partial T}\right)_{p,n} dT + \left(\frac{\partial G}{\partial P}\right)_{T,n} dP + \sum_{j=1}^{Np}\sum_{i=1}^{Nc} \overline{G}_{ij} dn_{ij} \tag{2-7}$$

Where $\overline{G}_{ij}$ is the partial molar Gibbs Free Energy of component i in phase j. n_{ij} is the moles of component i in phase j. At a fixed temperature and pressure, Eq. 2-7 is simplified as below:

$$dG = \sum_{j=1}^{Np}\sum_{i=1}^{Nc} \overline{G}_{ij} dn_{ij} \tag{2-8}$$

The necessary condition for minimization of Gibbs Free Energy is that the first order derivatives of the Gibbs Free Energy with respect to independent mole numbers are zero. For a closed system, we have:

$$n_{iNp} = 1 - \sum_{j=1}^{Np-1} n_{ij} \tag{2-9}$$

Therefore,

$$\frac{\partial n_{ij}}{\partial n_{ik}} = 1 \text{ for } j = k \tag{2-10}$$

$$\frac{\partial n_{ij}}{\partial n_{ik}} = 0 \text{ for } j \neq k \text{ and } j \neq N_P \tag{2-11}$$

$$\frac{\partial n_{ij}}{\partial n_{ik}} = -1 \text{ for } j = N_P \tag{2-12}$$

Using Eqs. 2-8 to 2-12:

$$\frac{\partial G}{\partial n_{mn}} = \sum_{j=1}^{Np}\sum_{i=1}^{Nc} n_{ij} \frac{\partial \overline{G}_{ij}}{\partial n_{mn}} + \overline{G}_{mn} - \overline{G}_{mNp} = \overline{G}_{mn} - \overline{G}_{mNp} \tag{2-13}$$

Where m = 1,…, N_C and n = 1,…,($N_P - 1$). In Eq. 2-13, the first term is zero according to the Gibbs-Duhem equation. Therefore, the first-order necessary condition for minimizing Gibbs Free Energy is:

$$\overline{G}_{ij} - \overline{G}_{iNp} = 0 \text{ where } i=1,\ldots, Nc, j=1,\ldots,N_{p-1} \quad (2\text{-}14)$$

In terms of fugacity, Eq. 2-14 becomes fugacity equations:

$$\ln f_{ij} - \ln f_{iNp} = 0 \text{ where } i=1,\ldots, Nc, j=1,\ldots,N_{p-1} \quad (2\text{-}15)$$

Where f_{ij} is the fugacity of component i in phase j. Phase N_P is the reference phase. A conventional formulation for flash calculations is solution of fugacity equations 2-15 subject to material balance equations (Okuno, 2009):

$$z_i = \sum_{j=1}^{N_P} \beta_j x_{ij} \quad (2\text{-}16)$$

$$\sum_{j=1}^{N_P} \beta_j = 1.0 \quad (2\text{-}17)$$

$$\sum_{i=1}^{N_C} x_{ij} = 1.0, \quad (2\text{-}18)$$

Where $\beta_j \geq 0$ and $x_{ij} \geq 0$ for i = 1, 2, …, N_C and j =1, 2, …, N_P. z_i is the overall mole fraction of component i, x_{ij} is the mole fraction of component i in phase j, β_j is the mole fraction of phase j. Since fugacity equations are the first-order necessary condition for minimizing Gibbs Free Energy, solving these equations provides a stationary point of the Gibbs Free Energy. The stationary point can be a minimum, saddle, or maximum point. Robustness of flash calculations depends on the formulation and the applied algorithm (Okuno, 2009). Stability analysis is required as a sufficient condition to ensure that the obtained stationary point from flash calculation is the global minimum of Gibbs Free Energy.

2.1.1.1. Solution of Fugacity Equations

Successive substitution (SS) is the traditional and common algorithm for flash calculation based on fugacity equations. In this algorithm independent variables are K-values, which are defined as follows:

$$K_{ij} = \frac{x_{ij}}{x_{iNp}} \quad \text{for 1,..., Nc and 1,..., } N_{p-1} \quad (2\text{-}19)$$

Where phase N_p is the reference phase and K-values represent the partitioning tendency of components among phases. SS solves Eqs. 2-15 for K_{ij} (i = 1,…,N_C and j = 1,…,N_{P-1}) subject to the material balance equations (2-16 to 2-18). Using definition

of fugacity coefficients ($\varphi_{ij} = \frac{f_{ij}}{Px_{ij}}$) and substituting Eqs. 2-19 in Eqs. 2-15 and rearrangement of Eqs. 2-15 yields the following iteration scheme:

$$\ln K_{ij}^{k+1} = \ln \varphi_{iNp}^{k} - \ln \varphi_{ij}^{k} \text{ for i=1,..,Nc and j=1,.., } N_{p-1} \quad (2\text{-}20)$$

Where the superscripts (k) are the iteration steps. In this procedure, phase compositions are calculated at each iteration to calculate fugacity coefficients and K-values. This procedure is a constant-K flash calculation proposed by Rachford and Rice (1952). The objective of a constant-K flash calculation is to calculate the phase mole fractions and phase compositions for a fixed overall composition and set of K-values. Substitution of Eqs. 2-17 and 2-18 into Eq. 2-16 results in:

$$x_{iNp} = \frac{z_i}{t_i} \text{ where } t_i = 1 - \sum_{j=1}^{Np-1}(1 - K_{ij})\beta_j \quad \text{for i=1,..,Nc} \quad (2\text{-}21)$$

Using Eqs. 2-18 and 2-19:

$$\sum_{i=1}^{Nc}(1 - K_{ij})x_{iNp} = 0 \text{ for j=1,..,} N_{p-1} \quad (2\text{-}22)$$

Substitution of Eqs. 2-21 into Eqs. 2-22 results in

$$f_j(\beta) = \sum_{i=1}^{Nc}\left(1 - K_{ij}\right)\frac{z_i}{t_i} = 0 \quad \text{for j=1,..,} N_{p-1} \quad (2\text{-}23)$$

Where β is a vector of β_j ($j = 1,\ldots,N_{P-1}$).

Eqs. 2-23 are solved in a constant-K flash calculation in the inner iteration loop to calculate phase compositions and phase mole fractions at each iteration. K-values are updated in the outer iteration loop using Eqs. 2-20.Wilson's correlation (1969) is commonly used to provide initial estimates for the K-values for two phases (Heidemann, 1983). The Wilson's correlation is given as:

$$K_i = P_{Ri}\exp[5.373(1 + \omega_i)(1 - T_{Ri})] \quad (2\text{-}24)$$

Where $P_{Ri} = \frac{P}{P_{ci}}$ and $T_{Ri} = \frac{T}{T_{ci}}$, ω_i is the acentric factor of component i, and P_{ci} and T_{ci} are the critical pressure and temperature of component i, respectively. Steps of the SS algorithm are as follows (Okuno, 2009):

1. Provide initial estimates for ($N_P - 1$) sets of K-values.

2. Calculate phase mole fractions and compositions using Eqs. 2-23

3. Calculate fugacity coefficients for N_P phases using a cubic EOS.

4. Check for convergence if the residuals of the fugacity equations 2-15 is less than a tolerance. Stop if the fugacity equations are converged. Otherwise, continue to step 5.

5. Update the (N_{P-1}) sets of K-values using Eqs. 2-20.

6. Go to step 2.

2.1.2 Stability Analysis

Fundamental formulations of stability analysis are presented in this section. Stability analysis can detect stability of a phase mixture at a given temperature, pressure, and composition. If that phase is unstable, a flash calculation is performed. When the number of equilibrium phases is smaller than that assumed by stability analysis, the subsequent flash calculation solves an unnecessarily large system of equations. In case of convergence, solving these equations provides the correct solution . If the number of equilibrium phases is greater than the assumed number, the correct solution cannot be obtained and depending on the initial estimate, the converged solution from flash calculation will be false solution (Okuno, 2009).

Baker et al. (1982) demonstrated that the tangent plane to the Gibbs Free Energy surface at a stable equilibrium state at a given temperature and pressure cannot lie above the Gibbs Free Energy surface at any composition. Michelsen (1982a) developed a computational procedure for stability analysis based on the analysis of Baker et al. (1982). Michelsen (1982a) defined the tangent plane distance (TPD) function. The TPD function is the difference between the Gibbs Free Energy and the tangent plane to the Gibbs Free Energy at a specified phase composition of. If the TPD function is non-negative, the phase is stable. The TPD function can be derived using the first-order Taylor series expansion of the Gibbs Free Energy around a specified phase composition (i.e., z) (Okuno, 2009):

$$T(x) = G(z) + \sum_{i=1}^{Nc}(x_i - z_i)\frac{\partial G}{\partial x_i}|_{x=z} = G(z) + \sum_{i=1}^{Nc}(x_i - z_i)\left(\overline{G}_i(z) - \overline{G}_{Nc}(z) + \sum_{i=1}^{Nc} x_j \frac{\partial \overline{G}_j}{\partial x_i}\right) = G(z) + \sum_{i=1}^{Nc} x_i \overline{G}_i(z) - \sum_{i=1}^{Nc} z_i \overline{G}_i(z) = \sum_{i=1}^{Nc} x_i \overline{G}_i(z) \quad (2\text{-}25)$$

The Gibbs-Duhem equation eliminated the summation term in the brackets. Therefore, the TPD function D(x) is:

$$D(x) = G(x) - T(x) = \sum_{i=1}^{Nc} x_i(\overline{G}_i(x) - \overline{G}_i(z)) \quad (2\text{-}26)$$

Dimensionless form of Eq. 2-26 is:

$$D_R(x) = \frac{D}{RT} = \sum_{i=1}^{Nc} x_i(\ln x_i\varphi_i(x) - \ln z_i\varphi_i(z)) \quad (2\text{-}27)$$

Stability analysis based on formulation of TPD function searches for a composition where the TPD function is negative. If a composition with a negative TPD is found, the current phase (i.e., z) is unstable. Otherwise, the current phase is stable. According to stationary point method of Michelsen (1982a), if TPD function defined at a phase composition (i.e., z) is non-negative at TPD stationary points, the phase is stable. At stationary points, the first-order derivatives of D(x) are zero:

$$\frac{\partial D(x)}{\partial x_i} = \frac{\partial}{\partial x_i}\left(\sum_{i=1}^{Nc} x_i\overline{(G_i}(x) - \overline{G}_i(z))\right) = \overline{(G_i}(x) - \overline{G}_i(z)) - (\overline{G}_{Nc}(x) - \overline{G}_{Nc}(z)) = 0 \quad (2\text{-}28)$$

Therefore,

$$\overline{G}_i(x) - \overline{G}_i(z) = \overline{G}_{Nc}(x) - \overline{G}_{Nc}(z) \quad \text{for i=1,..,Nc-1} \quad (2\text{-}29)$$

Substitution of Eqs. 2-29 into Eq. 2-26 leads to:

$$D(x) = \sum_{i=1}^{Nc} x_i\overline{(G_{Nc}}(x) - \overline{G}_{Nc}(z)) = \overline{G}_i(x) - \overline{G}_i(z) \text{ for } i=1,..,Nc \quad (2\text{-}30)$$

Rearranging Eqs. 2-30 results in:

$$\ln X_i\varphi(x) - \ln z_i\varphi(z) = 0 \quad \text{where } X_i = x_i \exp(-\frac{D}{RT}) \text{ for } i=1,..,Nc \quad (2\text{-}31)$$

Eqs. 2-31 are the stationarity equations. The stationary point method locates stationary points using equations $\sum_{j=1}^{Nc} x_i = 1$, $x_i \geq 0$ for i=1,…,Nc and Eqs. 2-30. This method checks if $\sum_{i=1}^{Nc} X_i > 1.0$. If a stationary point with $\sum_{i=1}^{Nc} X_i > 1.0$ is found, then the current phase (i.e., z) is unstable. Otherwise, the current phase is stable. Stability analysis is performed for a single-phase mixture or individual phases of a multiphase mixture (Okuno, 2009).

The conventional algorithms developed after Michelsen (1982a, 1982b) are based on the sequential application of phase-stability and flash calculations. That is, a phase-stability calculation is performed for the current phase composition where the tangent plane to the Gibbs Free Energy surface is defined. If it detects phase instability, a flash calculation is performed under the assumption that one more equilibrium phase is present.

2.2 PHASE BEHAVIOR OF CO_2-BITUMEN

Carbon Dioxide (CO_2) is the main product of the fossil fuel combustion CO_2 is one of the most common greenhouse gases produced from industry operations (Orr 2004; Metz et al. 2005). Therefore, the development of techniques that reduce the amount of CO_2 in the atmosphere has received high attention. These techniques include CO_2 sequestration, CO_2 injection into depleted oil and gas reservoirs and using CO_2 injection for enhanced oil recovery methods (Kariznovi, 2013).

CO_2 is non-toxic, non-flammable and readily available. These factors make CO_2 a good solvent for oil recovery processes. CO_2 has higher solubility than C_1 and N_2 in bitumen (Haddadnia et al., 2017). In addition to the oil recovery processes, CO_2 has applications in bitumen upgrading and can be considered as a potential candidate for supercritical extraction of the valuable component from bitumen (La and Guigard, 2015). CO_2 has potential to be used as a carrier gas for solvent-based process or as an additive to steam-based processes (Kariznovi, 2013).

Robinson et al. (1980) and Robinson and Sim (1981) conducted phase behaviour experiments on Athabasca bitumen saturated with CO_2 at high temperatures (up to 150^{o}C) and Cold Lake bitumen saturated with CO_2, respectively. Mehrotra and Svrcek (1984) measured the solubility of CO_2 in Marguerite Lake bitumen for the temperature range from 12 to 103^{o}C and pressures 1 to 6700 kPa. They also reported the saturated liquid density and viscosity. Mehrotra and Svrcek (1985b) measured the solubility, density, and viscosity of gas saturated Peace River bitumen with N_2, CO, C_1, CO_2 and C_2 gases for a temperature range of 16-107^{o}C and pressures up to 10000 kPa. Jha (1986) conducted a phase behaviour study for mixtures of CO_2-Saskatchewan heavy oil at temperature of 28°C. He measured viscosity, density, saturation pressure, gas-oil ratio, and swelling factor for each experiment. Mehrotra and Svrcek (1988a) measured the solubility, density, and viscosity of saturated Cold Lake bitumen with CO_2 for the temperatures of 16^{o}C to 103^{o}C and pressures up to 10000 kPa. Solubility of CO_2 in Cold Lake bitumen varies from 1.7 wt.% up to 13.4 wt.% in this temperature and pressure range. It is also found that CO_2 solubility increases with increasing pressure and decreases by increasing temperature.

Badamchi-Zadeh et al. (2009b) measured the saturation pressure, solubility and corresponding liquid phase densities and viscosities of mixtures of CO_2 and C_3 in Athabasca bitumen in temperature range of 10 to 50°C. Huang and Radoz (1990)

measured solubility of CO_2 in five bitumen fractions. The results demonstrated reduction in the solubility of CO_2 as the average molecular weight of the fractions increases. Sayegh et al. (1990) measured the phase behaviour and physical properties of the mixtures of Lindbergh heavy oil-CO_2. They measured the composition, density, and viscosity of the saturated crude oil with CO_2. Han et al. (1992) experimentally investigated the vapour-liquid equilibrium of a CO_2-Peace River bitumen system at temperatures of 45°C and 55°C.

Frauenfeld et al. (2002) measured the solubility CO_2 in Lloydminster Aberfeldy oil at temperatures of less than 20ºC. Kariznovi (2013) measured solubility of CO_2 in Surmount bitumen in temperature range of 50-188 ºC and pressure range of 1100 to 6100 kPa. Solubility of CO_2 varies between 1.59-8 wt.% from this study.

2.3 PHASE BEHAVIOR OF C_3-BITUMEN

Propane (C_3) has a critical temperature of 96.7 ºC and a critical pressure of 4247.7 kPa. C_3 has high solubility in heavy oil and bitumen compared to C_2, CO_2, C_1 and N_2 (Nourozieh, 2013). Han et al. (1998) studied the phase behaviour of Fengcheng bitumen with supercritical C_3 at temperatures (108, 115, and 125) °C and at the pressures (4400 to 8600) kPa.

Frauenfeld et al. (2002) conducted phase behavior experiments to measure the solubilities of C_2 and C_3 in Cold Lake blend oil and the solubility of C_3 in Lloydminster Aberfeldy oil at temperatures less than 20°C. Freitag et al. (2005) measured the solubility, density and viscosity of a Winter (Lloydminster) oil-C_3 system at 15 ºC and 28°C, and at the pressures lower than vapour pressure of C_3. Luo et al. (2007a) measured the solubility of C_3 in three Lloydminster heavy oil samples with different asphaltene contents at the temperature of 23°C and at the pressures less than 800 kPa (less than vapor pressure of C_3). The results showed that C_3 has the highest solubility in the oil sample with the lowest asphaltene content. Badamchi-Zadeh et al. (2009a) measured the solubility, density and viscosity of saturated oil phase in Athabasca bitumen-C_3 system for the temperatures (10 to 50) °C. Nourozieh (2013) measured solubility of C_3 in Surmount bitumen in temperature range of 50-190 ºC and pressure range of 1000-8000 kPa. Solubility of C_3 varied in the range of 1.4-24 wt.% from this study.

2.4 PHASE BEHAVIOR OF C_4-BITUMEN

Butane is a hydrocarbon compound, which is an alkane. This alkane has two structural isomers, n-butane and iso-butane. Throughout this thesis, n-butane (nC_4) is referred to as butane (C_4). C_4 has a critical temperature of 151.97 ^oC and a critical pressure of 3796 kPa (Yaws, 1999). C_4 is primarily found in natural gas and can be considered as a solvent for heavy oil and bitumen recovery. C_4 has a relatively high solubility in heavy oil and bitumen. This leads to a significant viscosity reduction of the oil saturated with C_4 (Kariznovi, 2013).

Kariznovi (2013) measured solubility of C_4 in Surmount bitumen. The results showed that the solubility of C_4 in Surmont bitumen varies from 1.83 to 19.5 wt.% for $100^oC<T<190^oC$ and 841 kPa<P<5066 kPa. C_4 has been used as a solvent in the Vapor Extraction (VAPEX) process in laboratory experiments (Das and Butler, 1995; Yazdani and Maini, 2009). Phase behaviour study of C_4-heavy oil systems in the literature is limited to a few studies. Luo (2009) measured the solubility of butane in Lloydminter heavy oil at five different equilibrium pressures (<6000 kPa) at a constant temperature of 23.9°C. Yazdani and Maini (2010) measured the solubility, density and viscosity of a the saturated oil phase in C_4-Frog Lake (Lloydminster) heavy oil system at room temperature for pressures lower than the vapour pressure of C_4.

SUMMARY

The conventional algorithm is a series of local solutions for assumed numbers of phases, which requires obtaining and correcting false solutions for multiphase problems. Correction of false solutions in phase-stability analysis is highly sensitive to the initial guess used for the search for potential equilibrium phases.

Therefore, a robust algorithm is developed for minimizing Gibbs Free Energy using isothermal isobaric flash. The main novelty lies in the unified usage of tangent-plane distance function for multiphase flash and stability analysis.

Optimizing a solvent-aided process (SAP) requires accurate measurement of phase behavior and a representative model for predicting multiphase behavior at reservoir conditions. However, detailed phase behavior of bitumen-solvent mixtures at operating conditions of SAP has not been thoroughly investigated. Apart from limited studies on phase behaviour measurement of CO_2-, C_3- and C_4-bitumen systems at SAP conditions (Kariznovi, 2013; Nourouzieh et al., 2014; Gao et al., 2016), the

effects of solvent type and concentration on SAP are not well understood. In addition, there are limited experimental studies on liquid-liquid-phase separation at elevated temperatures. Also, the visualization of bitumen-solvent phase behavior at elevated pressures and temperatures has not been reported previously.

Chapter 3: Robust Algorithm for Multiphase Equilibria Calculations

3.1 INTRODUCTION

In this section, first, we introduce the importance of reliable prediction of phase behaviour and the challenges of this prediction. Second, we introduce two approaches of calculating multiphase equilibria.

3.1.1 Phase behaviour prediction

Reliable and efficient phase behavior prediction is of great importance in chemical and petroleum engineering applications particularly for multiphase systems. The reason is that failure to predict phase equilibria correctly in reservoir simulation causes incorrect reservoir fluid properties estimation affecting simulation results significantly.

Multiphase isothermal-isobaric flash calculations are required in chemical and petroleum industries. A multiphase equilibrium calculation requires global minimization of the Gibbs Free Energy subject to material balance. The desired solution of these computations including equilibrium compositions and phase quantities lies only at the global minimum of Gibbs Free Energy.

The main challenge of equilibrium calculations is unknown number of equilibrium phases. To overcome this issue, stability criterion is utilized to test stability of the solution (Baker et al., 1982; Michelsen, 1982). By determining the number of phases at equilibrium, possibility of convergence to the correct equilibrium conditions increases. Hence, two distinct steps are required in phase equilibrium calculation methods: determination of the number of phases by some technique, and selection and solution of the proper governing equations (Han and Rangaiah, 1998). The two steps can be handled in a simultaneous procedure (Gupta et al., 1990; 1991) or a sequential procedure by adding a phase in the computation and testing the stability of the mixture (Gautam and Seider, 1979; Michelsen, 1982; Nghiem and Li, 1984).

3.1.2 Algorithms of Multiphase Equilibria Calculations

The conventional algorithms developed after Michelsen (1982a, 1982b) are based on the sequential application of phase-stability and flash calculations. That is, a phase-stability calculation is performed for a composition, at which the tangent plane to the Gibbs Free Energy surface is defined. If it detects phase instability, a flash calculation is performed under the assumption that one more equilibrium phase is present.

This conventional algorithm has been successfully applied for various compositional flow problems in the literature (e.g., Mehra et al., 1983; Nghiem and Li, 1984; Perschke, 1988; Han and Rangaiah, 1998). However, it is a series of local solutions for assumed numbers of phases, which requires obtaining and correcting false solutions for multiphase problems. Correction of false solutions in phase-stability analysis is highly sensitive to the initial guess used for the search for potential equilibrium phases. Also, it is not always possible to obtain reasonable initial guess (i.e., K values) for stability analysis of multiphase reservoir fluids.

For example, three different types of two equilibrium phases (L_1 + V, L_1 + L_2, and L_2 + V) exist in composition space that contains three equilibrium phases (L_1 + L_2 + V). L and V represent liquid and gaseous phases, respectively. L_1 and L_2 stand for the oleic and liquid solvent-rich phases, respectively. When L_1 + L_2 or L_2 + V is of the global minimum in the Gibbs Free Energy at the specified flash conditions, the conventional algorithms initiated with Wilson's correlation often fail to converge to the correct solution or tend to be attracted by local minima through negative flash (Whitson and Michelsen, 1989) before reaching the correct solution.

One way to improve the robustness of multiphase flash is to use multiple initial guesses in phase-stability analysis as given in Michelsen (1982b), Perschke (1988), and Li and Firoozabadi (2012). Often, many stability calculations with different initial guesses still give a false solution in multiphase flash. Therefore, it still requires obtaining and correcting false solutions. These false solutions are near local minima of the Gibbs Free Energy subject to material balance.

Gupta et al. (1991) presented a novel methodology to perform phase-stability and flash calculations simultaneously. However, a few researchers (Abdel-Ghani 1995; Alsaifi and Englezos, 2011) reported numerical issues associated with

degenerate equations near phase boundaries based on the formulation of Gupta et al. (1991) formulation. Also, they introduced an additional set of equations called "stability equations" in their paper. We will clearly show that the complete formulation does not require Gupta et al.'s (1991) stability equations. It has been found that the initialization scheme proposed by Gupta (1990) and Gupta et al. (1991) often fails for multiphase problems. Even when it starts the iteration, the original algorithm of Gupta et al. (1991) is not robust since it does not check the feasibility of each Rachford-Rice (RR) solution.

This chapter presents a set of equations and constraints that can be easily solved for minimization of the Gibbs Free Energy for isothermal isobaric flash. The main novelty lies in the unified usage of the tangent-plane distance function (Baker et al. 1982; Michelsen 1982a) for multiphase flash integrated with stability analysis for an arbitrary number of iterative compositions. A new algorithm is developed for minimization of the Gibbs Free Energy on the basis of successive substitution augmented with some important steps for robustness. Case studies are given to demonstrate the robustness of the developed algorithm.

3.2 METHODOLOGY

3.2.1 Algorithm

This section presents a new algorithm for global minimization of the Gibbs Free Energy as formulated below. A step-wise description is presented along with key equations.

The correct phase equilibrium for a given P, T, and z_i ($i = 1, 2, \ldots, N_C$) is defined by x_{ij} ($i = 1, 2, \ldots, N_C$ and $j = 1, 2, \ldots, N_P$) that gives the global minimum of

$$\underline{G}_R = \sum_{j=1}^{N_P} \sum_{i=1}^{N_C} \beta_j x_{ij} \ln(x_{ij}\varphi_{ij}), \tag{3-1}$$

where P is pressure, T is temperature, z_i is the overall mole fraction of component i, x_{ij} is the mole fraction of component i in phase j, β_j is the mole fraction of phase j, N_C is the number of components, and N_P is the number of equilibrium phases. The following constraints are to be satisfied:

$$z_i = \sum_{j=1}^{N_P} \beta_j x_{ij} \tag{3-2}$$

$$\sum_{j=1}^{N_P} \beta_j = 1.0 \tag{3-3}$$

$$\sum_{i=1}^{N_C} x_{ij} = 1.0, \tag{3-4}$$

where $\beta_j \geq 0$ and $x_{ij} \geq 0$ for i = 1, 2, …, N_C and j =1, 2, …, N_P.

The tangent plane to the Gibbs Free Energy surface at a stable equilibrium state cannot lie above the Gibbs Free Energy surface at any composition (Baker et al., 1982; Michelsen, 1982a). Therefore,

$$D_j = \sum_{i=1}^{N_C} x_{ij}\left(\ln x_{ij}\varphi_{ij} - \ln x_{iRef}\varphi_{iRef}\right) \geq 0 \tag{3-5}$$

for j = 1, 2, …, N_S at a specified T and P. N_S is the number of stationary points of the dimensionless tangent plane distance function, D, defined with a reference equilibrium-phase composition (x_{iRef}, where i = 1, 2,…, N_C). Note that $N_S = N_P + N_U$, where $N_U \geq 0$ and is the number of unstable stationary points of D. Eq. 3-5 can be also written as

$$D_j = \ln x_{ij}\varphi_{ij} - \ln x_{iRef}\varphi_{iRef} \geq 0 \tag{3-6}$$

because the gradients of D in composition space are zero at a stationary point.

The unified formulation for phase-stability and flash calculations in the current paper is to find a set of x_{ij} (i = 1, 2, …, N_C, and j =1, 2, …, N_S) such that $D_j = 0$ subject to equations 3-2, 3-3, and 3-4 for equilibrium phases j = 1, 2, …, N_P, and $D_j > 0$ subject to equation 3-4 for unstable stationary points j = (N_{P+1}), (N_{P+2})…, N_S. The algorithm presented in the current paper uses the tangent plane distance function, D, with adaptive selection of the reference composition for an arbitrary number of iterative compositions, which converge to stationary points with tangent plane distances D_j.

The developed algorithm uses the tangent plane distance equations to update all iterative compositions x_{ij} (i = 1, 2, …, N_C and j = 1, 2, …, N_S) through K values on the basis of successive substitution. The tangent plane distance equations are as follows.

$$f_{ij} = \ln x_{ij}\varphi_{ij} - \ln x_{ir}\varphi_{ir} - \theta_j = 0 \tag{3-7}$$

N_C is the number of components, and N_S is the number of sampling compositions at which phase stability is measured during the iteration. θ_j is stability variable of phase j. f_{ij} is residual of the tangent plane equations. The fugacity coefficient of component i at sampling composition j is denoted as φ_{ij}. A reference composition is expressed as x_{ir} (i = 1, 2, …, N_C). K values are defined as

$$K_{ij} = x_{ij}/\left(e^{\theta_j} x_{ir}\right) \tag{3-8}$$

for i = 1, 2, …, N_C, and j = 1, 2, …, N_S except for r.

At an equilibrium state upon convergence, Eq. 3-7 becomes Eq. 3-6; i.e., $\theta_j = D_j$ and the reference composition corresponds to one of equilibrium phases, which is denoted as x_{iRef}in Eq. 2-6. N_P equilibrium phases satisfy $D_j = 0$ along with Eqs. 3-2, 3-3, and 3-4 for j = 1, 2, …, N_P. N_U unstable stationary points satisfy $D_j > 0$ and Eq. 3-4 for j = (N_P + 1), (N_P + 2), …, N_S, where $N_S = N_P + N_U$.

During the iterations, N_S sampling compositions belong to either the equilibrium set P or the unstable set U. In set P, $\theta_j = 0$ and $\beta_j > 0$ for j = 1, 2, …, N_P. In set U, $\theta_j > 0$ and $\beta_j = 0$ for j = (N_P + 1), (N_P + 2), …, N_S. Successive substitution is performed to solve Eq. 3-7 together with Eqs. 3-2, 3-3, and 3-4 for K values. The reference composition is selected from set P adaptively, as described later.

For set P, Eq. 3-8 becomes $K_{ij} = x_{ij}/x_{ir}$. The conventional RR equations give the relationship between K values and mole fractions of apparent phases (β_j's) as follows:

$$g_j = \sum_{i=1}^{N_C} \left(x_{ir} - x_{ij}\right) = \sum_{i=1}^{N_C} \left(1 - K_{ij}\right) z_i/t_i = 0 \tag{3-9}$$

for sampling point j ≠ r within set P, where g_j is RR equation of phase j, $t_i = 1 - \sum_{k=1,k\neq r}^{Np} (1 - K_{ik})\beta_k$ for i = 1, 2, …, N_C. Compositions are given as $x_{ir} = z_i/t_i$ and $x_{ij} = K_{ij}x_{ir}$ for sampling point j ≠ r.

For set U, the summation constraint $\Sigma_i x_{ij} = 1.0$ gives

$$\theta_j = -\ln\left[\sum_{i=1}^{N_C} K_{ij} x_{ir}\right] \tag{3-10}$$

for sampling composition j within set U. Compositions for set U are given as $x_{ij} = e^{\theta_j} K_{ij} x_{ir}$ for i = 1, 2, …, N_C.

The fundamental structure of the current algorithm broadly follows the traditional successive substitution algorithms for flash and stability analysis (Michelsen, 1982; Nghiem and Li, 1984). That is, each iteration first solves Eqs. 3-9 for compositions for set P for a given set of K values and overall composition. Then, Eq. 3-10 is used to obtain compositions for set U for a given set of K values and reference composition. After that, K values are updated for sets P and U by use of Eq. 3-7, $\ln K_{ij} = \ln\varphi_{ir} - \ln\varphi_{ij}$.

The main difference from the conventional flash and stability analysis lies in the unified usage of the tangent plane distance equations (Eq. 3-7) for an arbitrary number of sampling compositions. This gives the flexibility in terms of robustness and efficiency that the algorithm offers; e.g., use of more sampling compositions increases the level of robustness at the expense of the increased number of equations, at least for the initial stage of iteration.

With the well-known convergence behavior of successive substitution (Mehra et al. 1983; Ammar and Renon 1987; Kaul 1992), sampling compositions converge to stationary points on the tangent plane distance function at an equilibrium state. As will be discussed later, sampling compositions naturally merge for a case in which N_S is greater than the number of stationary points present upon convergence.

N_S sampling compositions can be initialized by a biased or unbiased distribution in composition space. Biased initialization methods include use of a correlation suitable for the fluid of interest, such as Wilson's correlation, Li and Firoozabadi (2012), and Zhu and Okuno (2014b), and use of certain information from the previous time-step in flow simulation. Unbiased initialization methods include a random distribution and a distribution near vertices in composition space. The unbiased methods are useful when no reliable information is available for equilibrium phases of the fluid of interest.

A reference composition is also initialized to define Eq. 3-7. First, function D (Eq. 3-5) is used for N_S sampling compositions with the overall composition as the reference. Then, the initial reference composition is defined at which D is the minimum among the N_S sampling compositions.

Other important steps for robustness include the feasibility check for each RR solution by use of the method of Okuno et al. (2010). Also, the constraints regarding β_j and θ_j described previously are used for classification of sampling compositions for sets P and U.

The Peng-Robinson (PR) EOS (Peng and Robinson 1976a, 1976b) with the van der Waals mixing rules as presented in Appendix A is used to calculate thermodynamic properties in this research. A stepwise description of the algorithm is given below. The corresponding flow chart is given in Figure 3-1.

Step 1. Set N_S sampling compositions $\vec{x}_j^{(k)}$ for j = 1, 2, …, N_S by a certain initialization scheme as described previously. The number in the bracket represents the iteration-step number; k = 1 for the initial iteration.

Step 2. Calculate D_j for j = 1, 2,…, N_S with $\vec{z}$ as the reference composition from Eq. 3-5. Select the sampling composition with the minimum D value as the reference composition, $\vec{x}_r^{(1)}$. Initialize K values, $\vec{K}_j^{(1)}$, by use of $\ln K_{ij} = \ln\varphi_{ir} - \ln\varphi_{ij}$ for j = 1, 2, …, N_S except for r. Recalculate D_j with $\vec{x}_r^{(1)}$ and set N_U as the number of sampling compositions with positive D values. $N_P = N_S - N_U$. If $N_P = 1$, go to step 6. Otherwise, continue to step 3.

Step 3. Check the feasibility of the RR solution for set P. If feasible, go to step 5. Otherwise, continue to step 4.

Step 4. Exclude from set P as many sampling compositions as required until the feasibility is satisfied for the given RR problem. Update N_P. $N_U = N_S - N_P$. If $N_P = 1$, go to step 6. Otherwise, continue to step 5. The exclusion of sampling compositions from set P is performed on the basis of their D_j values from Eq. 3-5. That is, the sampling composition with the largest D_j value among set P is first excluded. The subsequent exclusions, if necessary, are in the order of decreasing D_j. If step 4 is taken in the first iteration (k = 1), the D_j values calculated in step 2 are directly used.

Step 5. Perform the convex minimization to obtain $\vec{x}_j^{(k)}$ and $\beta_j^{(k)}$ for set P that satisfy Eq. 3-9, as presented in Okuno et al. (2010). The convergence criterion is that $\|g_j\|_\infty < \varepsilon_g$ (e.g., $\varepsilon_g = 10^{-10}$).

Step 6. Obtain $\vec{x}_j^{(k)}$ and $\theta_j^{(k)}$ for set U by use of Eq. 3-10.

Step 7. Check to see if there is any $\theta_j^{(k)}$ that is negative in set U. If so, update $\vec{x}_r$ and N_U. $N_P = N_S - N_U$. Go to step 10. Otherwise, continue to step 8. The sampling composition with the minimum θ_j value is selected for updating $\vec{x}_r$. In step 8, a sampling composition with $0 < \beta_j < 1$ is selected for updating $\vec{x}_r$.

Step 8. Check to see if there is any $\beta_j^{(k)}$ that is negative in set P. If so, perform necessary updates for $\vec{x}_r$ and N_U. $N_P = N_S - N_U$. Go to step 10. Otherwise, continue to step 9.

Step 9. Check for convergence. Stop if $\|f_{ij}\|_\infty < \varepsilon_f$ (e.g., $\varepsilon_f = 10^{-12}$). Otherwise, continue to step 10.

Step 10. Check to see if there are any compositions to be merged on the basis of the criterion that the max norm for two compositions is less than ε_x (e.g., $\varepsilon_x = 10^{-3}$). If so, perform necessary updates for N_S and N_U. $N_P = N_S - N_U$.

Step 11. Update K values by use of Eqs. 3-7 and 3-8; i.e., $\ln K_{ij}^{(k+1)} = \ln\varphi_{ir}^{(k)} - \ln\varphi_{ij}^{(k)}$ for i = 1, 2, …, N_C and $j \neq r$. Increase the iteration-step index by one; k = k + 1. Go to step 6 if $N_P = 1$. Otherwise, go to step 3.

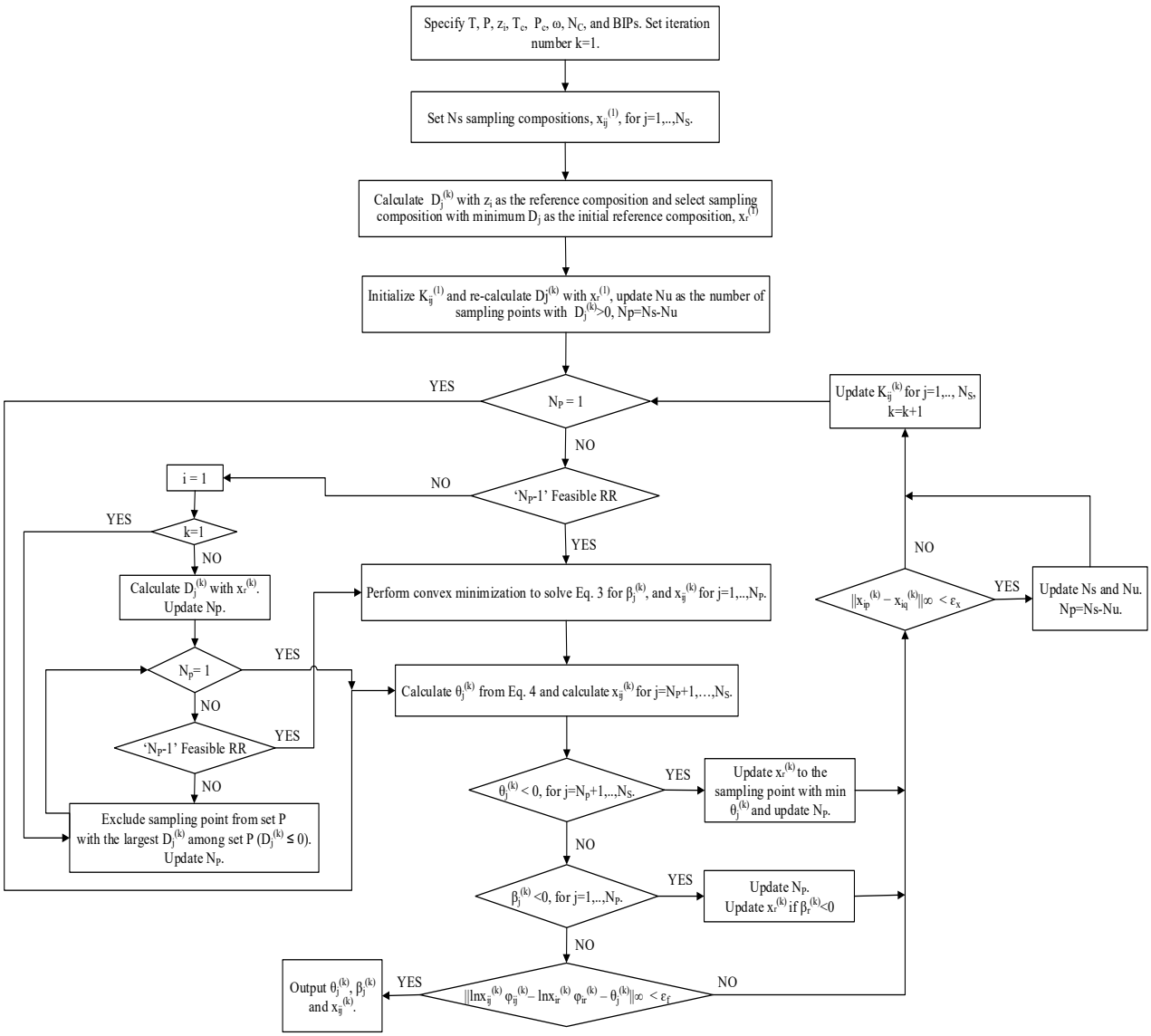

Figure 3-1: Flow chart of the new algorithm developed for multiphase equilibria calculations

3.2.2 Comparison of the new algorithm with Gupta et al.'s (1991)

The algorithm presented in Section 3.2.1 is substantially different from that of Gupta et al. (1991). An important difference comes from the difference in formulation. They introduced an additional set of equations, $\beta_j\theta_j = 0$, which were called "stability equations" in their papers. A similar set of equations, $\beta_j\theta_j/(\beta_j + \theta_j) = 0$, were then solved simultaneously with the RR equations in their algorithm. However, section 3.2.1 clearly shows that the complete formulation does not require Gupta et al.'s (1991) stability equations. The correct set of equations in the current paper does not have the degeneracy issues that Gupta et al.'s (1991) algorithm exhibits near phase boundaries due to their stability equations, as reported by Alsaifi and Englezos (2011).

The robustness of the current algorithm also comes from the careful initialization and adaptive selection of the reference composition. The initialization scheme of Gupta (1990) eliminates the sampling compositions that have positive D values from Eq. 3-5 with $\vec{z}$ as the reference composition. However, this often leads to a complete failure of the calculation. The improvements over Gupta et al. (1991) were developed by following the fundamental theory behind the formulation (see section 3.2.1) that the lowest Gibbs Free Energy should be searched for in composition space.

The simplicity of the formulation has led to the straightforward iteration steps, which are essentially the widely-used successive substitution. Unlike in other publications following Gupta et al. (1991), such as Abdel-Ghani (1995), Chaikunchuensakun et al. (2002), and Alsaifi and Englezos (2011), the robust solution of multiphase RR equations (Okuno et al., 2010) further enhances the robustness of the current algorithm.

3.3 RESULTS AND DISCUSSION

In this section, case studies are given to demonstrate the robustness and simplicity of the algorithm developed in this research, in comparison with the sequential method (Michelsen, 1982) and the method of Gupta et al. (1991). The new algorithm can make multiphase flash problems straightforward by not having to solve for and correct false solutions.

In the sequential method used for this section, single-phase stability analysis is performed with two initial guesses, searching for a V-like phase first and a L-like phase next, on the basis of Wilson's K values (Michelsen 1982a). For stability analysis for

one of multiple phases, initial guesses recommended by Firoozabadi (1999) are used in addition to the V-like (i.e., $x_i=z_iK_i$) and L-like (i.e., $x_i=z_i/K_i$) guesses, in the following order: a V-like phase, a L-like phase, compositions near vertices in composition space, the midpoint of phase compositions, and $\varphi_i x_i$ for i = 1, 2, …, N_C. Stability analysis in this section uses only successive substitution for the fair comparison between the new algorithm and conventional ones in terms of robustness. The convergence criterion for stability analysis is that the max norm of stationarity equations is less than 10^{-8}.

For flash calculations in the sequential method used for this section, two numerical schemes have been tested: use of only successive substitution, and the combination of successive substitution and Newton's minimization of the Gibbs Free Energy. The convergence criterion used is that the max norm of fugacity equations is less than 10^{-12}. The switching criterion from successive substitution to the minimization algorithm is that the max norm of fugacity equations is less than 10^{-3}. However, the two sets of numerical schemes have given the same solutions for the sequential method in the cases tested in this section.

For the new algorithm, initial sampling compositions are distributed near vertices of composition space for cases 1 and 4, but also randomly distributed for Cases 2 and 3 using a random-number generator. This flexibility in initialization is one of the advantages over the conventional algorithms, as discussed in the previous section.

One advantage of our formulation and algorithm in this research is the ability is to provide correct solution for the multiphase flash without going through several false solutions. The advantage of our algorithm over the conventional sequential methods is pronounced when the correct solution in a multiphase calculation does not include either the L_1 or V phase. This can frequently occur in many gas and steam injection processes with multiple partially miscible phases.

3.3.1 Case 1

This case uses ternary mixtures of H_2O, C_3, and n-C_{16} to show a few important features of the new algorithm. The properties used for the components are given in Table 3-1. Figure 3-2 shows the two- and three-phase regions in composition space at 430 K and 35 bars. In the figure, L, V, and W represent the oleic, gaseous, and aqueous phases, respectively.

Application of the algorithm along the mixing line between (0.0, 0.9, 0.1) and (0.9, 0.0, 0.1) results in the behavior of β_j and θ_j shown in Figure 3-3. One unstable stationary point (in set U) is observed in the two-phase regions (L + V and L + W) along the mixing line. As mentioned in the algorithm section, the converged θ values correspond to the dimensionless tangent plane distances at stationary points (see Eq. 3-6). The converged θ (or D) values qualitatively indicate the level of instability at the corresponding compositions. Hence, the new algorithm provides more global information about the Gibbs Free Energy than the conventional flash algorithms, when it converges with unstable stationary points. Unlike the current algorithm, the negative flash approach (Whitson and Michelsen, 1989) may indicate phase instability by negative β values, when obtaining a false solution.

Table 3-1: Properties of the components for case 1

Component	P_C (bar)	T_C (K)	ω
H_2O	220.89	647.3	0.344
C_3	42.46	369.8	0.152
n-C_{16}	14.19	717.0	0.742
Binary Interaction Parameters			
	H_2O	C_3	n-C_{16}
H_2O	0.0000	0.6841	0.3583
C_3	0.6841	0.0000	0.0000
n-C_{16}	0.3583	0.0000	0.0000

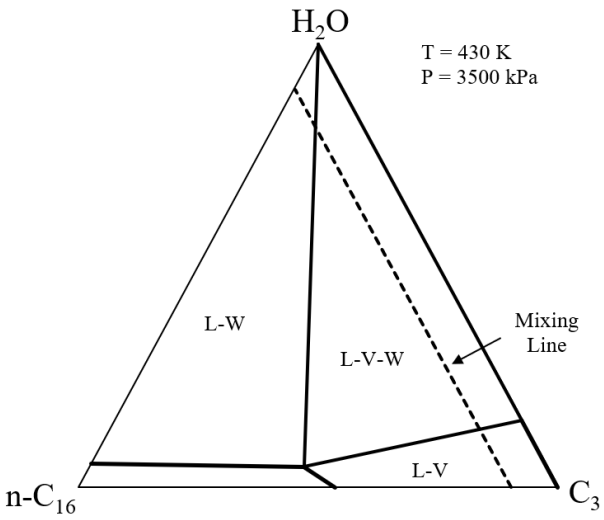

Figure 3-2: Phase boundaries for the ternary system of H_2O, C_3, and n-C_{16} at 430 K and 3500 kPa. L, V, and W represent oleic, gaseous, and aqueous phases, respectively. Properties of the components are given in Table 3-1.

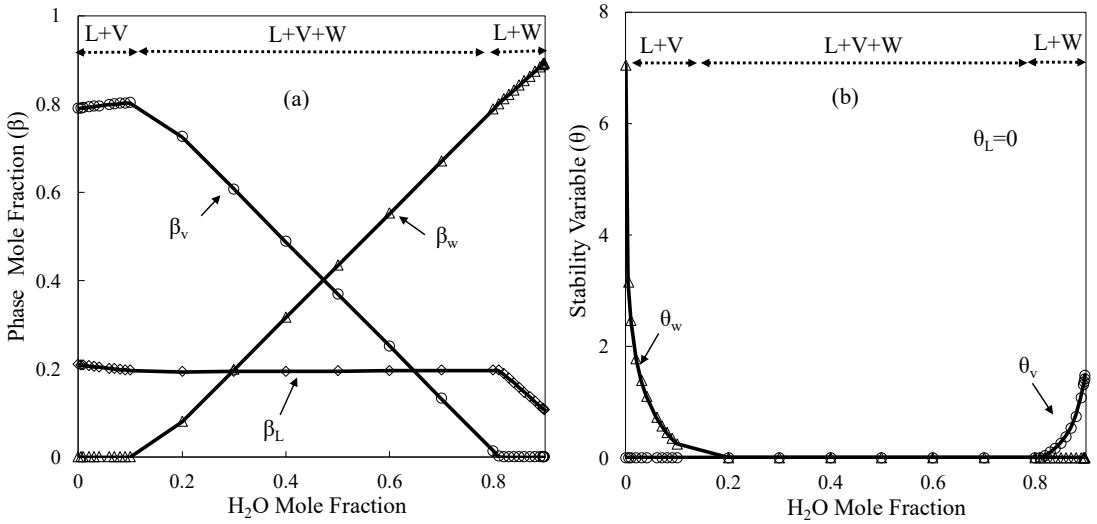

Figure 3-3: Variation of parameters with the new algorithm applied along the mixing line given in Figure 3-2 (a) Phase mole fraction (b) Stability variable.

Figure 3-4 shows the Gibbs Free Energy and converged tangent planes for three overall compositions with the H_2O concentrations of 0.10, 0.75, and 0.84 along the mixing line. The algorithm has successfully converged to the lowest Gibbs Free Energy subject to material balance for each overall composition. The D values at unstable stationary points in Figure 3-4 can be confirmed with Figure 3-3.

Figures 3-2, 3-3, and 3-4 clearly show that different sets of equilibrium phases can be easily calculated as thermodynamically stable stationary points using the unified algorithm that directly converges to the correct solution. It was observed that distributed sampling compositions (e.g., six compositions) naturally merge to three stationary points corresponding to the L, V, and W phases on the Gibbs Free Energy surface given in Figure 3-4. The convergence behavior is determined by the traditional successive substitution as described in the previous section. An illustrative figure for such a case is available upon request along with input data.

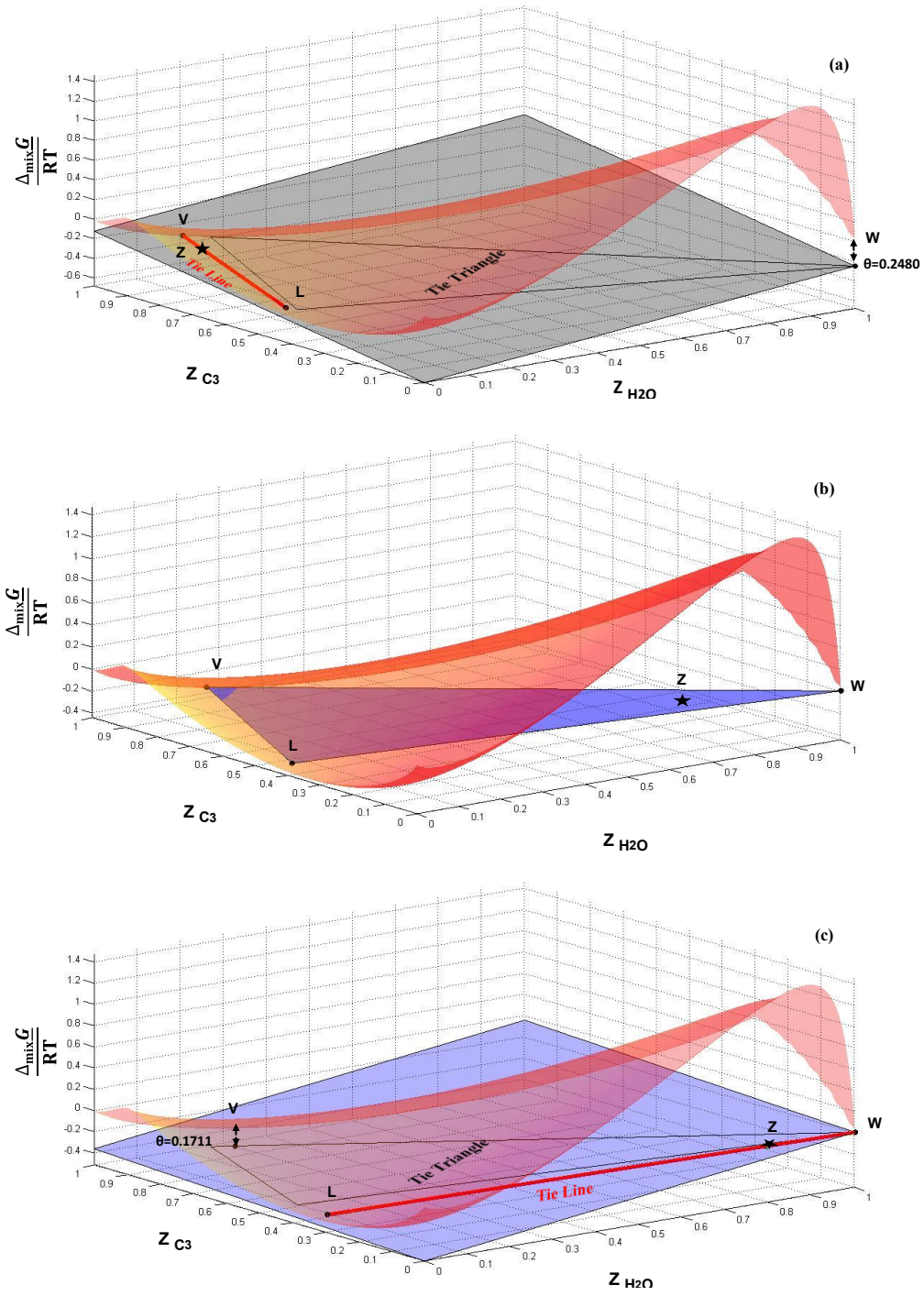

Figure 3-4: Gibbs Free Energy surface and converged tangent plane along the mixing line given in Figure 3-2. (a) $zH_2O = 0.1$. (b) $zH_2O = 0.75$. (c) $zH_2O = 0.84$.

3.3.2 Case 2

This case uses the binary mixture of C_1 and H_2S at 190 K and 40.53 bars to show several issues of the sequential methods and the robustness of the new algorithm. Table 3-2 gives the properties of the components. The Gibbs Free Energy surface in composition space exhibits three lobes corresponding to the L_1, L_2, and V phases in the order of increasing C_1 concentration (z_{C1}) (Figure 3-5). The new algorithm is initialized with three sampling compositions; two of them are distributed near vertices of composition space and the other is a random point within the composition space. The sequential method fails to find the correct solutions with L_2 + V for z_{C1} from 0.968 to 0.982.

For $0.968 \leq z_{C1} < 0.980$, the sequential algorithm only finds an L phase in the single-phase stability analysis, and the subsequent two-phase flash results in a local minimum with L_1 + V. Then, the stability analysis for one of the two phases finds an L_2 phase. However, three-phase flash is not feasible for a binary mixture, due to the degree of freedom of one. Hence, the final result from the sequential algorithm is the L_1 + V phases that have been obtained. Table 3-3 shows the correct solution from the new algorithm and the incorrect solution from the sequential method at z_{C1} of 0.970. The new algorithm does not need to perform three-phase flash to reach the correct two-phase solution (L_2 + V). The Gibbs Free Energy after convergence of the solution from the new algorithm is -0.539476213. This is less than the corresponding value from the sequential method (i.e., -0.537697750).

For $0.980 \leq z_{C1} \leq 0.982$, the sequential algorithm fails to find phase instability in single-phase stability analysis. The sequential algorithm convergence to a single-phase solution. However, the new algorithm properly converges to the L_2 and V phases. Table 3-4 shows the solution for z_{C1} of 0.980. The Gibbs Free Energy of the converged solution from the new algorithm is -0.492028012. This is less than the single-phase Gibbs Free Energy from the sequential algorithm (i.e., -0.491838307).

Even if the degree of freedom is more than one for the sequential method, it has been observed that the sequential method initiated with Wilson's K values tends to fail to find the correct solution that does not involve the L_1 or V phase. An example is the ternary mixture of 60 mol% CO_2, 12 mol% C_1, and 28 mol% n-C_{20} at 250 K and 38 bars. Three phases (i.e., L_1, L_2, and V) are present in composition space, and the overall composition in the L_1-L_2 region is located in the vicinity of the tie triangle. The

sequential method cannot find phase instability in the two-sided stability analysis with the V and L estimates from Wilson's correlation.

Table 3-2: Properties of the components for case 2

Component	P_C (bar)	T_C (K)	ω	BIP
C_1	46.0016	190.6	0.008	0.00
H_2S	89.3686	373.2	0.1000	0.08

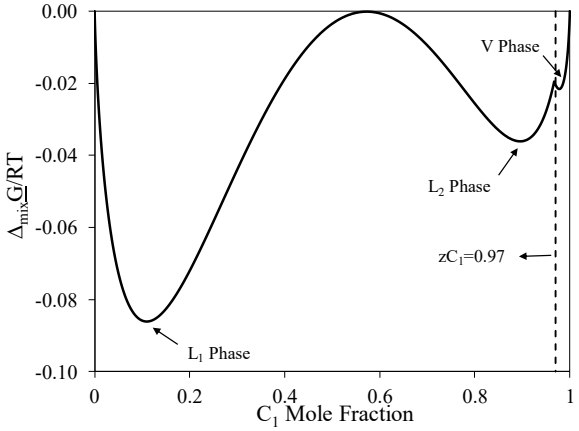

Figure 3-5: Gibbs Free Energy surface in composition space for the binary system of C_1 and H_2S. Properties of the components are given in Table 3-2. The temperature and pressure are 190 K and 40.53 bar, respectively. The three lobes indicated correspond to the L_1, L_2, and V phases in the order of increasing C_1 mole fraction in composition space.

Table 3-3: Results for case 2 with the new and the conventional algorithm. Properties of the components are given in Table 3-2. The overall composition is 97% C_1 and 3% H_2S. The specified temperature and pressure are 190 K and 40.53 bar.

	New Algorithm			Conventional Algorithm	
Component	L_1	V	L_2	L_1	V
C_1	0.18634266482	0.98268738632	0.93604368336	0.12587785433	0.97953528887
H_2S	0.81365733518	0.01731261368	0.06395631664	0.87412214567	0.02046471113
β	0	0.7280	0.2720	0.0112	0.9888
θ	0.1323	0	0	-	-
$\underline{G}_R/RT$	-0.53947621262			-0.5376977504	

Table 3-4: Solution for case 2 with the new algorithm. Properties of the components are given in Table 3-2. The overall composition is 98% C_1 and 2% H_2S. The specified temperature and pressure are 190 K and 40.53 bar. The correct set of three phase compositions is identical to the one presented in Table 3-3. The conventional algorithm fails to find phase instability in single-phase stability analysis for this flash calculation.

Component	L_1	V	L_2
β	0	0.9424	0.0576
θ	0.1323	0	0
$\underline{G}_R/RT$	-0.492028012		

3.3.3 Case 3

This case presents the complex phase behavior calculated for a mixture of H_2O, n-C_4, and bitumen at 417 K and 35 bars. The components' properties are given in Table

3-5. Two different types of three-phase equilibria are present in composition space; one is $L_1 + L_2 + V$ and the other is $W + L_1 + V$. Each of the two-phase edges of the tie triangles forms a two-phase region. Therefore, a flash calculation within this composition space may experience several local minima before reaching the correct solution. The difficulty depends on the quality of the initial estimates used for phase compositions, or K values. However, no established correlations are available for K values involving the L_2 phase (Zhu and Okuno, 2015a).

The overall composition of 2 mol% H_2O, 95 mol% n-C_4, and 3 mol% bitumen at 417 K and 3500 kPa, yields $L_1 + L_2 + V$ phases in equilibrium. The new algorithm was initiated with randomly-selected three sampling compositions and three compositions near the vertices of composition space. It converged to the correct solution (Table 3-6) after 136 iterations. The converged tangent plane gives four stationary points, out of which one unstable composition near 100% H_2O has the θ (or D) value of 0.6272.

The sequential method results in the same solution through a false solution in two-phase flash. The two-sided stability analysis for the overall composition takes 304 iterations. Then, two-phase flash requires 123 iterations with successive substitution alone, or 28 iterations with the combination of successive substitution and Newton's minimization. After that, one of the two phases is tested for phase stability. Phase instability is detected with the initial guess of $\varphi_i x_i$. The two-phase stability calculations with five different initial guesses take 446 iterations in total. Finally, three-phase flash requires 120 iterations with successive substitution alone, or 19 iterations with the combination of successive substitution and Newton's minimization. As shown in this case, the simplicity of the new algorithm is advantageous for complex phase behavior.

Table 3-5: Properties of the components for case 3.

Component	P_C (bar)	T_C (K)	ω
H_2O	277.15	672.48	0.2699
n-C_4	36.01	421.56	0.2127
Bitumen	10.64	847.17	1.0406
Binary Interaction Parameters			
	H_2O	**n-C_4**	**Bitumen**
H_2O	0.000	0.560	0.110
n-C_4	0.560	0.000	0.075
Bitumen	0.110	0.075	0.000

Table 3-6: Solution for case 3 with the new algorithm. Properties of the components are given in Table 3-5. The overall composition is 2% H_2O, 95% n-C_4, and 3% bitumen. The specified temperature and pressure are 417 K and 35 bar. The conventional algorithm converges to the same solution at the expense of a large number of iterations in sequential stability and flash calculations.

Component	W	L_1	L_2	V
H_2O	9.99E-01	0.02757144227	0.01722624506	0.03886906998
n-C_4	2.21E-11	0.77654778633	0.96351359109	0.96099473155
Bitumen	0	0.19588077141	0.01926016386	0.00013619847
β	0	0.0710	0.8348	0.0942
θ	0.6272	0	0	0
$\underline{G}_R$/RT		-0.95634664		

3.3.4 Case 4

This case is to show the importance of the initialization scheme and checking the feasibility in multiphase RR solution. Mixtures of H_2O, C_3, and n-C_{16} are used, for which Table 3-1 shows the components' properties.

First, the mixture of 80 mol% H_2O, 19 mol% C_3, and 1 mol% n-C_{16} is considered at 566 K and 130 bars, near a critical endpoint. The algorithm of Gupta et al. (1991) results in non-convergence for this case because the RR solution during the iteration diverges with the following K values: (6.48974×10^{-1}, 3.01954×10^{3}, 4.08377×10^{10}) for V + W, and (4.85708×10^{-1}, 2.64248×10^{3}, 2.27912×10^{11}) for L + W. Such divergence occurs when the RR equations are nearly degenerate near a critical endpoint (Zhu and Okuno, 2015b). It is crucial to control Newton's step size to keep the feasibility in RR solution, as in Okuno et al. (2010). The new algorithm converges to the correct solution shown in Table 3-7 in 8 iterations with no difficulty.

A second example is the mixture of 87 mol% H_2O, 3 mol% C_3, and 10 mol% n-C_{16} at 574.5 K and 125 bars. The new algorithm converges to the correct solution given in Table 3-8 in 6 iterations. However, it requires the proper initialization of RR solution (see Okuno et al., 2010) when K values are as follows: (1.21887, 9.31203×10^{-4}, 3.40328×10^{-10}) for V + W, and (6.31210×10^{-1}, 1.45442, 1.16067×10^{1}) for L + W. If the simplistic selection is made for initial β values, 1/3, for the three phases, the RR solution results in divergence. However, Gupta et al. (1991) did not discuss how to initialize a RR solution.

A third example is the mixture of 75 mol% H_2O, 15 mol% C_3, and 10 mol% n-C_{16} at 560 K and 65 bars. For this mixture, the initialization scheme proposed by Gupta (1990) results in a RR problem with an open feasible domain, resulting in the failure in initialization. The new algorithm initialized with sampling compositions distributed

near the vertices of composition space converges to the solution given in Table 3-9 in 32 iterations. Two of the three sampling compositions that are initially present merge into the V phase at the 12th iteration. Unlike in Gupta et al. (1991), the RR routine embedded in the new flash algorithm is guaranteed to converge to the correct solution. It is important to confirm the existence of the unique solution for a given multiphase RR problem prior to the iteration as shown in Okuno et al. (2010).

Table 3-7: Solution for the first mixture of case 4 with the new algorithm. Properties of the components are given in Table 3-1. The overall composition is 80% H_2O, 19% C_3, and 1% n-C_{16}. The specified temperature and pressure are 566 K and 130 bar. The algorithm of Gupta et al. (1991) results in non-convergence because the Rachford-Rice solution during the iteration diverges.

Component	V	W
H_2O	0.667919405	0.999888865
C_3	0.315472893	0.000111135
n-C_{16}	0.016607701	0
β	0.6021	0.3979
θ	0	0
$\underline{G}_R$/RT	-0.823421643	

Table 3-8: Solution for the second mixture of case 4 with the new algorithm. Properties of the components are given in Table 3-1. The overall composition is 87% H_2O, 3% C_3, and 10% n-C_{16}. The specified temperature and pressure are 574.5 K and 125 bar.

Component	L_1	W
H_2O	0.501407818	0.999929554
C_3	0.114906006	7.04E-05
n-C_{16}	0.383686176	1.11E-11
β	0.2606	0.7394
θ	0	0
$\underline{G}_R$/RT	-0.550358484	

Table 3-9: Solution for the third mixture of case 4 with the new algorithm. Properties of the components are given in Table 3-1. The overall composition is 75% H_2O, 15% C_3, and 10% n-C_{16}. The specified temperature and pressure are 560 K and 65 bar. The algorithm of Gupta et al. (1991) fails for this case due to an open feasible domain in the initial RR problem based on their initialization scheme.

Component	L_1	V
H_2O	0.324593359	0.795746207
C_3	0.095516095	0.15585894
n-C_{16}	0.579890546	0.048394853
β	0.0971	0.9029
θ	0	0
$\underline{G}_R$/RT	-0.967879426	

3.4 SUMMARY

This chapter presented a new algorithm for global minimization of the Gibbs Free Energy for isothermal, isobaric flash. The correct set of equations is solved with

successive substitution for stationary points of the tangent plane distance defined at a reference composition. Conclusions are as follows:

1. The number of equilibrium phases is part of the solution in the new algorithm, in contrast to the sequential stability/flash approach. Therefore, false solutions are not necessary for multiphase flash with the new algorithm. The advantage of the new algorithm in terms of robustness and efficiency is more pronounced for more complex phase behavior, in which multiple local minima of the Gibbs Free Energy are present.

2. The new algorithm can be initialized with either a biased or unbiased scheme because it can handle an arbitrary number of sampling compositions. This also yields the flexibility that the algorithm offers in terms of robustness and efficiency. For example, one can initialize the algorithm with more sampling compositions for enhanced robustness by capturing more information regarding the Gibbs Free Energy during the iteration. If reasonable estimates are available for equilibrium phases, one can use the biased initialization to reduce the number of equations to be solved.

3. The new algorithm does not use the stability equations of Gupta et al. (1991) because they are not necessary with the correct formulation presented in this research.

3.5 NOMENCLATURE

Roman Symbols

D	=	Tangent plane distance
f_{ij}	=	Residual of the tangent plane equations defined in Eq. 3-7
g_j	=	Residuals of the material balance equations
$\underline{G}$	=	Molar Gibbs Free Energy
K_{ij}	=	K value for component i in phase j
$\vec{K}$	=	Vector consisting of N_C K values (equilibrium constants)
L_1	=	Oleic phase
L_2	=	Solvent-rich liquid phase
N_C	=	Number of components
N_P	=	Number of phases
N_S	=	Number of sampling compositions
N_U	=	Number of sampling compositions in set U
P	=	Equilibrium set or pressure, bar
P_C	=	Critical pressure, bar
r	=	Reference composition
T	=	Temperature, K
T_C	=	Critical temperature, K
U	=	Unstable set
V	=	Vapor or gaseous phase
W	=	Aqueous phase
$\vec{x}_j$	=	Vector consisting of N_C concentrations
x_{ij}	=	Mole fraction of component i in phase j
z_i	=	Overall mole fraction of component i

Greek Symbols

β_j = Mole fraction of phase j
ε = Small number used for convergence test (e.g., 10^{-12})
φ_{ij} = Fugacity coefficient of component i in phase j
ω = Acentric factor
θ = Stability variable

Subscripts
C = Critical property
i = Component index
j = Phase index
L = Oleic phase
mix = Mixing
P = Phase
r = Reference composition
R = Reduced property
Ref = Reference phase
S = Sampling composition
U = Unstable
V = Vapor phase
W = Aqueous phase
k = Index for iteration steps

Abbreviations
BIP = Binary interaction parameter
EOS = Equation of state
PR = Peng-Robinson
RR = Rachford-Rice

Chapter 4: Phase Behavior of Solvent-Bitumen Systems

4.1 INTRODUCTION

In this section, we present a brief literature review on phase behavior of CO_2-, C_3-, and C_4-bitumen systems.

4.1.1 Phase Behavior of CO_2-Bitumen Systems

Mehrotra and Svrcek (1984, 1985a, b, c) measured the effect of temperature and pressure on CO_2 solubility in bitumen samples from Athabasca, Cold Lake, Wabasca, Peace River, and Marguerite Lake reservoirs. Deo et al. (1991) measured solubility of CO_2 in Athabasca bitumen at 358.2 K and 393.2 K and pressures up to 6200 kPa. Han et al. (1992) experimentally investigated the vapor-liquid equilibrium of a CO_2-Peace River bitumen system at two temperatures of 318.2 K and 328.2 K. Badamchi-Zadeh et al. (2009) measured the solubility of CO_2 in Athabasca bitumen for the Vapor-Extraction (VAPEX) process. Most of the existing studies are limited to temperatures up to 393.2 K.

4.1.2 Phase Behavior of C_3-Bitumen Systems

C_3 has high solubility in heavy oil and bitumen and leads to significant viscosity reduction (Nourozieh, 2013). The solubility of C_3 in different heavy oil and bitumen samples has been previously measured at T<301.1 K (Frauenfeld et al., 2002, Freitag et al., 2005, Luo et al., 2007a,b). Badamchi-Zadeh et al. (2009) measured C_3 solubility in Athabasca bitumen at 283.2 K<T<323.2 K. Han et al. (1998) studied the phase behavior of Fengcheng bitumen with supercritical C_3 at 381.2 K, 388.2 K, and 398.2 K and pressures of 4400 to 8600 kPa. Nourozieh (2013) measured solubility of C_3 in Surmont bitumen for T>323.2 K. There are limited studies that have measured the phase behavior of C_3-bitumen systems at high temperatures and pressures.

4.1.3 Phase Behavior of C_4-Bitumen Systems

C_4 has been used as a solvent in several VAPEX laboratory experiments (Das and Butler 1995; Yazdani and Maini 2010). However, phase behavior of C_4-bitumen might be completely different at high temperatures. There are limited experimental

studies on the phase behavior of C_4-bitumen at Solvent Aided Process (SAP) conditions (Nourozieh et al. 2014; Gao et al. 2016). Nourozieh et al. (2014) reported phase transitions for vapor-liquid and liquid-liquid equilibrium of C_4-bitumen mixtures at temperatures up to 463.2 K. Gao et al. (2016) presented multiphase boundaries of C_4-Athabasca-bitumen and C_4-Athabasca-bitumen-water mixtures. C_4 might accumulate near the steam-chamber edge in the SAP. C_4 accumulation leads to the appearance of a second liquid phase rich in C_4 (i.e., L_2) at elevated temperatures near the steam-chamber edge (Gao et al., 2016). Therefore, it is required to understand liquid-liquid separation and multiphase behavior of a C_4-bitumen system at high temperatures. There are limited experimental studies on liquid-liquid-phase separation and the distribution of bitumen components between the phases at elevated temperatures.

4.1.4 Modelling Phase Behavior of Solvent-Bitumen Systems

Literature on EOS modelling for heavy-oil/bitumen-solvent mixtures is relatively scarce (Diaz et al. 2011). Diaz et al. (2011) predicted the saturation pressures and liquid-liquid boundaries for pseudo-ternary mixtures of C_3-CO_2-Athabasca bitumen. Li and Yang (2013) modelled the phase behavior of C_4-C_3-heavy-oil mixtures for temperatures up to 396.2 K. Saber and Shaw (2011) used the Peng Robinson-EOS (PR-EOS) to model the phase behavior of Athabasca bitumen and n-C_{10}. Kumar and Okuno (2016) presented a new algorithm for characterization of multiphase behavior for solvent-injection simulation. Predicting the performance of solvent-based and solvent-assisted processes is challenging because the introduction of a solvent into an oil-sand reservoir can lead to a complex phase behavior. For any given heavy oil-solvent mixture, liquid-liquid, vapor-liquid, or vapor-liquid-liquid regions might occur. The performance of these processes is highly dependent on the solvent type, solvent concentration and operational conditions (Li et al., 2011). It has been suggested that higher solvent concentrations results in higher oil production rate (Govind et al., 2008). However, solvent cost, solvent retention, and solvent losses make it critical to find an optimal solvent concentration for SAP. Therefore, optimizing SAP requires accurate measurement of phase behavior and a representative model for predicting multiphase behavior at reservoir conditions. However, detailed phase behavior of bitumen-solvent mixtures at reservoir conditions in SAP has not been thoroughly investigated. Although some related studies have been published during the last decade

(Kariznovi, 2013; Nourouzieh et al., 2014; Gao et al., 2016), the effects of change in the main operational conditions (e.g., solvent type and concentration) during the SAP are not well-understood. In addition, the visual monitoring of bitumen-solvent phase behavior at elevated pressures and temperatures has not been reported previously.

4.1.5 Asphaltene Precipitation

One potential side effect of utilizing solvent-based processes is asphaltene precipitation, which may cause problems for flow behavior in the reservoir and oil processing. The effect of temperature, pressure, and oil composition on asphaltene precipitation has been investigated in literature (Edmonds et al., 1999, Akbarzadeh et al., 2007, Kokal et al., 2003, Gonzales and Galeana, 2004). Most of these studies were performed on light oil samples and at high operating pressures (P>7000 kPag), which have limited applications to SAP in oil-sands reservoirs. Other studies investigated the effect of different solvents on asphaltene precipitation in oil-sands reservoirs. However, there have been limited studies on the effect of CO_2, C_3 and C_4 on asphaltene precipitation under SAP conditions. Nielsen et al. (1994) observed a decrease in asphaltene precipitation by increasing temperature and pressure in the presence of C_5. There are also some studies which investigated the effect of n-alkane carbon number on asphaltene precipitation (Haghighat and Maini, 2008, Wang and Buckley, 2003; Wiehe et al., 2005). However, these studies were conducted at VAPEX conditions. Moreno and Babadagli (2013) investigated the effect of solvents (i.e., C_3 to C_6 and C_{10}) on asphaltene precipitation at temperatures up to 120°C.

In this chapter, we compare phase behavior of CO_2-, C_3-, and C_4-Clearwater bitumen systems using experimental and modelling approaches. First, multiphase behavior of these systems at different solvent concentrations is studied using a visual PVT cell. Then, an EOS model is calibrated against the measured data. Liquid-vapor, liquid-liquid, liquid-liquid-vapor regions have been visualized, and phase boundaries between these regions have been fully studied. Also, we experimentally investigate the effect of solvent in bitumen dissolution on asphaltene precipitation at elevated temperatures.

4.2 METHODOLOGY

4.2.1 Bitumen Characterization

The bitumen sample is collected from the Cenovus Osprey Pilot, producing oil from the Clearwater Formation (see Figure 4-1). Bitumen molecular weight (MW) and specific gravity (SG) are measured to be 475 g/mol and 1.024 g/cm^3, respectively. Compositional analysis of the bitumen sample is obtained by the D2887-84 method (Nadkarni, 2007) up to C_{99} (see Figure 4-2 and Table 4-1). Total bitumen MW is measured by the freezing-point-depression method, using a cryoscope. Properties of the Clearwater bitumen sample are presented in Table 4-2. Saturate/aromatic/resin/asphaltene (SARA) analysis is also conducted to obtain the weight fractions of saturates, aromatics, resins, and asphaltenes in the bitumen using the liquid/solid chromatography method (Table 4-3). CO_2, C_3 and nC_4 with purities of 99.9%, 99.5% and 99.5%, respectively, are used as solvents in the experiments.

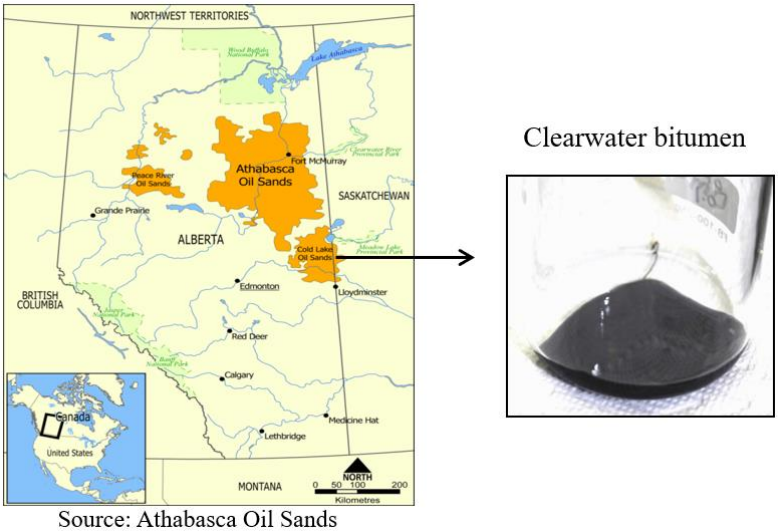

Source: Athabasca Oil Sands

Figure 4-1: Clearwater bitumen from Cold Lake region

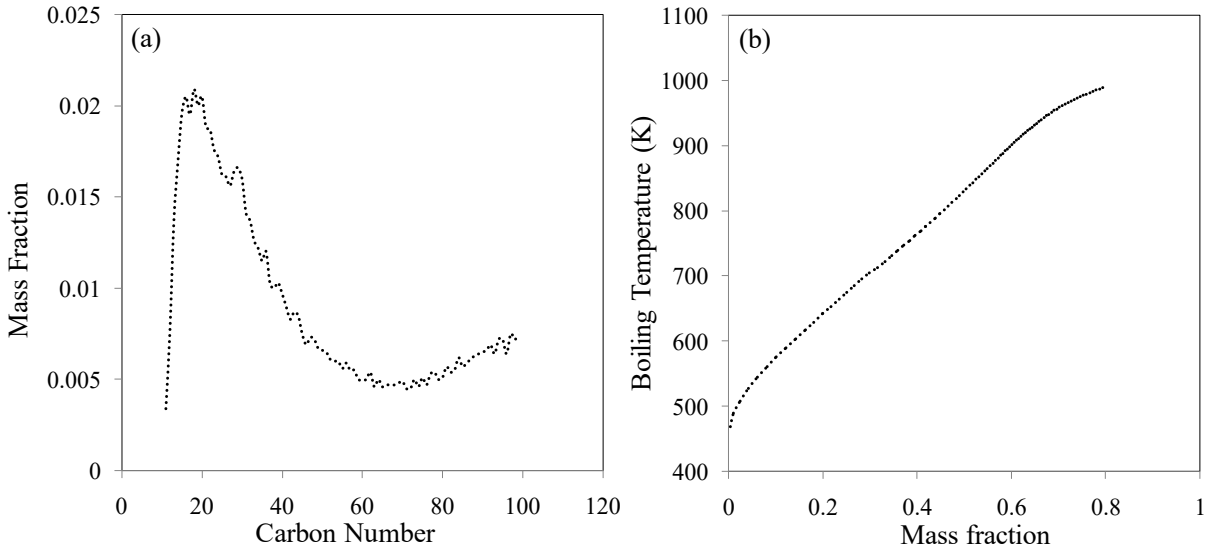

Figure 4-2: Simulated distillation results for Clearwater bitumen a) Compositional analysis b) True boiling point distribution

Table 4-1: Compositional analysis of Clearwater bitumen from Simulated Distillation method

Carbon Number	Tb (K)	Weight Fraction	Carbon Number	Tb (K)	Weight Fraction
11	469.15	0.0034	56	873.15	0.0059
12	489.15	0.0076	57	877.15	0.0055
13	508.15	0.0137	58	881.15	0.0055
14	527.15	0.0169	59	885.15	0.005
15	544.15	0.0196	60	888.15	0.005
16	560.15	0.0205	61	892.15	0.005
17	575.15	0.0195	62	895.15	0.0054
18	589.15	0.0209	63	898.15	0.0046
19	603.15	0.0200	64	902.15	0.005
20	617.15	0.0205	65	905.15	0.0046
21	629.15	0.0188	66	908.15	0.0047
22	642.15	0.0187	67	911.15	0.0047
23	653.15	0.0176	68	914.15	0.0047
24	664.15	0.0172	69	917.15	0.0048
25	674.15	0.0162	70	920.15	0.0049
26	685.15	0.0161	71	923.15	0.0045
27	695.15	0.0156	72	926.15	0.0045
28	704.15	0.0164	73	928.15	0.005
29	713.15	0.0166	74	931.15	0.0046
30	722.15	0.0160	75	934.15	0.0051
31	731.15	0.0141	76	937.15	0.0047
32	739.15	0.0137	77	940.15	0.0053
33	747.15	0.0126	78	943.15	0.0054
34	754.15	0.0122	79	946.15	0.005
35	762.15	0.0115	80	948.15	0.0051
36	769.15	0.0120	81	951.15	0.0057
37	776.15	0.0102	82	954.15	0.0054

38	782.15	0.0100	83	956.15	0.0055
39	789.15	0.0103	84	959.15	0.0062
40	795.15	0.0097	85	961.15	0.0057
41	801.15	0.0090	86	964.15	0.0059
42	807.15	0.0083	87	966.15	0.0061
43	813.15	0.0087	88	968.15	0.0063
44	818.15	0.0085	89	970.15	0.0064
45	823.15	0.0075	90	973.15	0.0065
46	829.15	0.0069	91	975.15	0.0066
47	834.15	0.0073	92	977.15	0.0069
48	839.15	0.0072	93	979.15	0.0064
49	843.15	0.0067	94	981.15	0.0072
50	848.15	0.0066	95	983.15	0.0072
51	852.15	0.0065	96	985.15	0.0064
52	857.15	0.0061	97	987.15	0.0075
53	861.15	0.0060	98	989.15	0.0072
54	865.15	0.0060	99	991.15	0.0074
55	869.15	0.0056	100+	…	0.198

Table 4-2: Clearwater bitumen properties

property	value
Mw	475
SG	1.024
Viscosity at 293.2 K (cP)	$5.9 \times 10^4 \pm 500$

Table 4-3: SARA analysis of Clearwater bitumen

Component	Weight fraction
Saturate	0.43
Aromatic	0.19
Resin	0.21
Asphaltene	0.17

4.2.2 Constant Composition Expansion (CCE) Tests

CCE experiments are conducted on CO_2-, C_3-, and C_4-bitumen systems at temperatures ranging from 343.2 to 433.2 K using a PVT cell apparatus. Feed composition of the solvent-bitumen systems in CCE tests are designed as follows:

- 5.9 wt.% CO_2 in CO_2-Clearwater bitumen system
- 28.4 wt.% C_4 in C_4-Clearwater bitumen system (feed 1)
- 84.6 wt.% C_4 in C_4-Clearwater bitumen system (feed 2)
- 28.4 wt.% C_3 in C_3-Clearwater bitumen system (feed 1)
- 78.3 wt.% C_3 in C_3-Clearwater bitumen system (feed 2)

The pressure and temperature of the PVT cell are limited to 103392 kPag and 472.2 K, respectively. The total capacity of the cell is 112 cm^3. A floating piston isolates the fluid sample from hydraulic oil. A high-pressure positive-displacement pump controls the pressure of the hydraulic oil. An air bath with an accuracy of ±0.1°C controls the temperature of the cell. The PVT cell is equipped with a cathetometer to measure the height of the piston. Accuracy of the volume measurement is ±0.016 cm^3. The uncertainty of the Heise pressure gauge is ±0.07% of full-scale, 103392 kPag. In addition, a high-pressure precision gauge with accuracy of ±0.01% of full-scale 68929 kPag is also connected to the PVT cell for more-accurate pressure measurement. The dead volume of this PVT cell is 1.754 cm^3. A CCE test provides information regarding the saturation pressure as a function of temperature and the relative volumetric amounts of equilibrated phases. For each CCE test, temperature is maintained at a prespecified value using an air bath. Figure 4-3 shows the PVT set up and a schematic of the apparatus. Specified amounts of solvent and bitumen are injected into the cell, and pressure is increased with a hydraulic pump and a floating piston to maintain single-phase fluid in the cell. The experiment is started at a pressure higher than the saturation point (i.e., bubble point pressure) where the initial mixture volume is recorded. The mixture volume is increased stepwise, and the cell pressure is recorded at each step. The saturation point is recorded as the pressure at which an additional phase begins to form. The fluid mass in the cell divided by the total volume of the cell at the saturation point is used as the saturation density. CCE tests are conducted for dead oil (i.e., 0 wt.% solvent) in temperatures ranging from 303.2 to 433.2 K to correlate bitumen density with temperature and pressure. Because the initial mass injected into the PVT cell is conserved, bitumen density at specified temperature and pressure is calculated using the measured bitumen volume and density at reference conditions:

$$\rho_2 = \frac{\rho_{ref} V_{ref}}{V_2} \tag{4-1}$$

V_2 and ρ_2 are sample volume and density in the PVT cell, respectively, at a given temperature and pressure. V_{ref} and ρ_{ref} are the sample volume and density in the PVT cell, respectively, at atmospheric pressure and a specified temperature. The bitumen density at atmospheric pressure is measured using the Attension Sigma 700 instrument in temperatures ranging from 303.2 to 453.2 K.

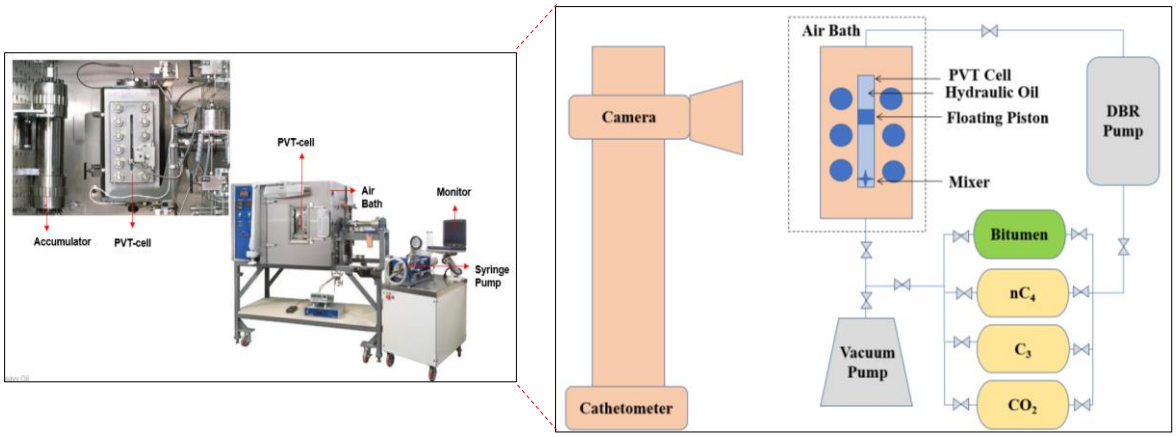

Figure 4-3: Schematic of the PVT set up used for conducting CCE experiments

4.2.3 Asphaltene Filtration Test

Filtration tests were conducted at high temperatures after the CCE tests to quantify precipitated asphaltenes as a result of solvent-bitumen interactions. Equilibrated mixtures of solvent-bitumen in the PVT cell were filtered through a customized HPHT-cell containing Whatman filter papers (grade 42, 2.5 µm) as shown in Figure 4-4. After the filtration, the asphaltene content of the precipitate was measured. The precipitate includes both asphaltenes and maltenes; hence the paper was rinsed with n-heptane in a Soxhlet distillation system to remove the maltenes. The remaining precipitate (asphaltenes) was rinsed with toluene and dried under a fume hood for several days until the total mass reached a constant value. After filtration, PVT lines and the PVT cell were washed with toluene to collect any precipitates through the system. The mixture of toluene and precipitates was dried and filtered through filter paper using n-heptane. The remaining asphaltene was extracted using the same procedure used for the precipitate from the filtration cell. Mass of this asphaltene was included in calculating the total precipitated asphaltenes. The following solvent-bitumen systems which have been used for CCE tests were tested for the precipitated asphaltene content. To investigate the effect of solvent concentration on asphaltene precipitation, filtration tests were conducted on two C_3-Clearwater bitumen systems with two concentrations of C_3 in the system.

- 5.9 wt.% CO_2 in CO_2-Clearwater bitumen system
- 28.4 wt.% C_4 in C_4-Clearwater bitumen system
- 28.4 wt.% C_3 in C_3-Clearwater bitumen system
- 78.3 wt.% C_3 in C_3-Clearwater bitumen system

Figure 4-4: HPHT filtration cell used for asphaltene filtration tests

4.2.4 Modelling Phase Behavior of Solvent-Bitumen Systems

4.2.4.1. Bitumen Characterization:

According to the oil compositional analysis, the weight percentage of the heavy fraction (C_{100+}) is significant (approximately 19.8 wt.%). Because heavier components can significantly affect the phase behavior of heavy oil, it is critical to split the "plus" fraction into pseudo-components (PCs) (Pedersen et al. 2007). The plus fraction is split using the methodology proposed by Pedersen et al. (1985). The MW of each component can be estimated by (Pedersen et al. 2007):

$$\mathrm{Mw_i} = 14\mathrm{CN_i} - 4 \tag{4-2}$$

MW_i and CN_i are the MW and carbon number of component i. An average MW of 2200 g/mol was assigned to the C_{100+} fraction of the bitumen according to the study by Diaz et al. (2011). Assumed or estimated MWs are corrected by a factor (m) to match the total MW of the bitumen (i.e., 475 g/mol).

4.2.4.2. Estimation of Critical Properties:

Empirical correlations have been proposed to estimate critical properties as a function of boiling temperature ($T_{b,i}$) and SG (Lee and Kesler 1975; Twu 1983). The SG of each carbon number fraction is estimated using the correlations presented in Appendix A. Initial SG values are obtained from Riazi (2005). The SG of the plus fraction is obtained from the correlation developed by Alboudwarej et al. (2006). The initial SG value of each fraction is corrected by a factor (m') to match the bitumen SG. The $T_{b,i}$ of the heavier fractions (heavier than C_{99}) is not available from compositional analysis but is estimated from Riazi (2005). The $T_{b,i}$ of the plus fraction is estimated from the Pedersen et al. (1985) correlation. The physical properties of the components, including the plus fraction, are estimated from the Lee and Kesler (1975) correlations

as a function of $T_{b,i}$ and SGi. In addition, the critical volumes are estimated by the correlation proposed by Twu (1983).

4.2.4.3. Lumping:

The bitumen mixture consisting of several components are lumped into four pseudo-components (PCs) by the methodology proposed by Pedersen et al. (1985). According to this method, the PCs have equal mass (i.e., $\sum_{i=n}^{i=m} z_i Mw_i$). Hence, PC_1 includes C_{11} through C_{25} components, PC_2 includes C_{26} through C_{47} components, PC_3 includes C_{48} through C_{92} components, and PC_4 includes C_{93+}. Critical properties of each PC are estimated using the Pedersen et al. (1985) grouping scheme (see Eqs. A-12 through A-14).

4.2.4.4. Regression of EOS:

To address several deficiencies for estimating critical properties, the EOS model should be calibrated against experimental data. Calibrating an EOS model for a fluid system involves finding a set of optimized physical properties (e.g., Tc, Pc, and ω) and binary-interaction parameters (BIPs) for a reasonable number of components for the system (Danesh 1998). These uncertain parameters are adjusted to minimize the absolute average relative deviation (AARD):

$$\mathrm{AARD} = \frac{1}{N_{data}} \sum_{j=1}^{N_{data}} \frac{|\psi_j^{Cal} - \psi_j^{exp}|}{\psi_j^{exp}} \tag{4-3}$$

Where ψ_j^{Cal} and ψ_j^{exp} are the calculated and measured values and N_{data} is the number of data points. Initial guesses for BIPs between CO_2-, C_3 and C_4-bitumen are estimated using Kumar (2016) and those between water-hydrocarbon components are estimated using Venkatramani and Okuno (2014). PR-EOS with van der Waals mixing rules (Peng and Robinson, 1978) is used for calibration and phase-behavior calculations as presented in Appendix A. PVTsim Nova (2015) is used for the regression process.

4.2.4.5. Phase Equilibrium Calculations and Ternary Diagrams:

Multiphase equilibrium calculations are performed using the calibrated PR-EOS and the developed algorithm presented in Chapter 3. Using the algorithm, the number and amount of the equilibrated phases and their compositions are calculated. For the purpose of visualizing multiphase regions in composition space, pseudo-ternary diagrams of the CO_2-, C_3- and C_4-bitumen systems are plotted at 4000 kPa and in the

temperature range of 120 ºC to 180 ºC. To generate pseudo-ternary diagrams, bitumen components are lumped into two pseudo components (PC_1' and PC_2') and the EOS model is re-calibrated. CCE test data from the CO_2-, C_3-and C_4-bitumen systems are used to optimize T_c, P_c and ω of two pseudo components and the BIP values between solvents and the two bitumen pseudo components. Pseudo-ternary diagrams are generated using the re-calibrated EOS and the algorithm developed in Chapter 3.

Tables A-1 and Table A-2 summarize the physical properties of the two pseudo components and the optimized BIP values for the re-calibrated EOS. Re-calibrated EOS can predict measured saturation pressure of CO_2-bitumen system, C_4-bitumen (feed 1), C_4-bitumen (feed 2), C_3-bitumen (feed 1) and C_3-bitumen (feed 2) with AARD of 4.9%, 8.4%, 20%, 12.5% and 43.5%, respectively. The re-calibrated EOS is only used for the purpose of generating pseudo-ternary diagrams to visualize the phase regions in compositional space. For multiphase equilibria calculations, we use the EOS model where bitumen components are lumped to four pseudo components. The reason is that the EOS model with more bitumen pseudo-components can provide more accurate results respect to the re-calibrated EOS.

4.3 RESULTS AND DISCUSSION

4.3.1 Bitumen Density

Bitumen density is measured in the temperature range of 305.2 to 433.2 K and atmospheric pressure (Figure 4-5). The correlation shown in Eq. 4-4 is fitted to the data points with an AARD of 0.4%,

$$\rho_0 = 1760.0854 - 3.5004T + 3.3821e^{-3}T^2 \quad (4\text{-}4)$$

Where ρ_0 is in kg/m^3 and T is in K.

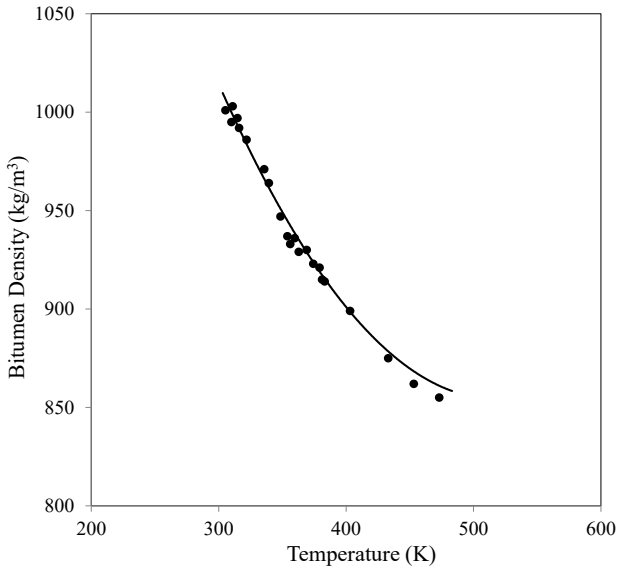

Figure 4-5: Clearwater bitumen density versus temperature at atmospheric pressure

As explained in the CCE Tests subsection, a CCE test is used to calculate bitumen density vs. pressure and temperature, as presented in Table 4-4. The Tait equation (Dymond and Malhotra, 1988) is used for correlating density data (with AARD of 0.36%) as follows,

$$\rho = \frac{\rho_0(T, P_0)}{1 - \beta \ln\left(\frac{B + P}{B + 100}\right)} \tag{4-5}$$

$$\rho_0 = 1760.0854 - 3.5004T + 3.3821e^{-3}T^2 \tag{4-6}$$

$$\beta = -0.0254 + 9.2696e^{-5}T \tag{4-7}$$

$$B = 49.7044 - \frac{4.1231e^4}{T} + \frac{8.5350e^6}{T^2} \tag{4-8}$$

In this equation T, P and density are in K, kPa, and kg/m^3, respectively. Pressure-volume (P-V) data from the CCE tests on the bitumen at 411.7 and 431 K are shown in Figure 4-6. The fluid-saturation pressure is estimated when there is a change in slope of the equilibrium P-V data. The saturation pressures of dead oil are interpreted to be 331.2 kPa at 411.7 K and 486.5 kPa at 431 K using the slope changes in the P-V data (see Figure 4-6). This point corresponds to the boundary between the L_1- and L_1/V-phase regions at each temperature. The resulting saturation pressures are close to the saturation pressure of water at the corresponding temperatures. Because the bitumen sample contained 0.14 wt.% water, the measured saturation pressures were likely the

result of water flashing within the PVT cell at the test conditions. This is also verified by compositional analysis of the vapor phase, which is almost pure water.

Table 4-4: Experimental data for fitting density correlation

T (K)	P (kPa)	Density (Kg/m^3)	T (K)	P (kPa)	Density (Kg/m^3)
305.4	101.3	1001.00	298.2	4660.9	1018.76
310.0	101.3	995.00	298.2	5267.6	1018.96
311.0	101.3	1003.00	298.2	8253.0	1019.96
314.7	101.3	997.00	298.2	10328.3	1021.16
316.0	101.3	992.00	333.2	1358.2	972.57
321.9	101.3	986.00	333.2	2392.5	973.50
335.7	101.3	971.00	333.2	3833.5	974.06
339.5	101.3	964.00	333.2	5364.1	975.17
348.5	101.3	947.00	333.2	6881.0	976.48
353.9	101.3	937.00	333.2	8618.5	977.79
356.2	101.3	933.00	333.2	10355.9	979.30
359.7	101.3	936.00	411.7	1158.3	958.63
362.9	101.3	929.00	411.7	2061.5	960.71
369.2	101.3	930.00	411.7	3433.6	962.97
374.2	101.3	923.00	411.7	5171.1	964.89
379.2	101.3	921.00	411.7	6577.6	966.12
381.3	101.3	915.00	411.7	8280.6	967.52
383.2	101.3	914.00	411.7	10355.9	969.29
403.2	101.3	899.00	430.7	1213.5	933.08
433.2	101.3	875.00	430.7	2744.1	936.75
453.2	101.3	862.00	430.7	4957.3	939.27
473.2	101.3	855.00	430.7	7584.2	941.97
298.2	986.0	1016.77	430.7	8983.9	942.99
298.2	1909.9	1017.37	430.7	10369.8	944.01
298.2	3406.0	1018.16	….	.....	….

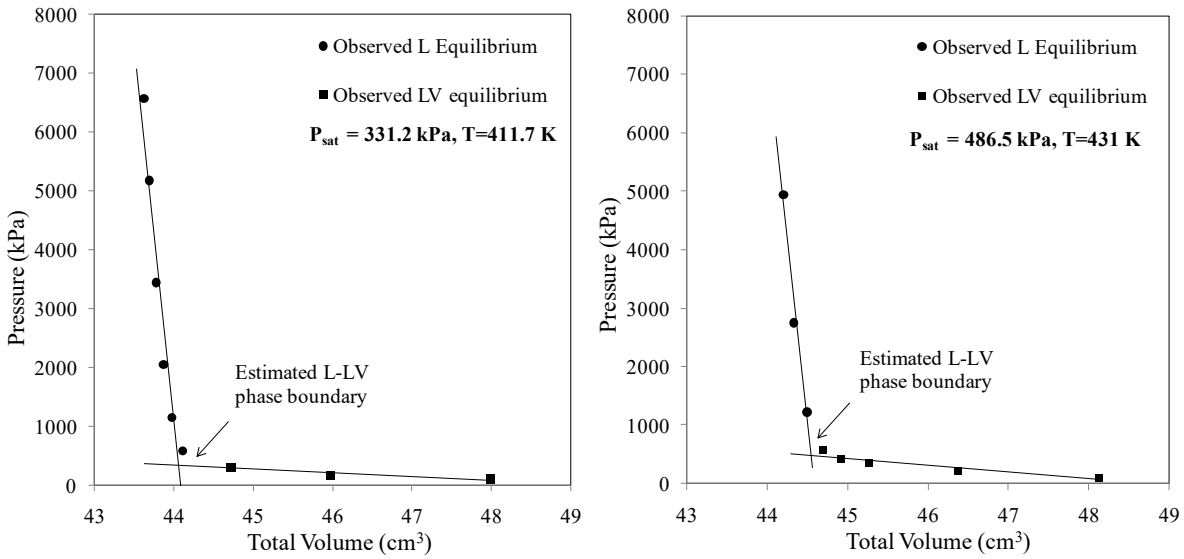

Figure 4-6: P-V data from the CCE experiments on the bitumen at 411.7 K and 431 K

4.3.2 Bitumen Viscosity:

Measured bitumen-viscosity data are correlated with temperature using the following model for viscosity of solvent-free bitumen at atmospheric pressure (Mehrotra and Svrcek, 1986):

$$\mu_{\text{Bitumen}}(\text{cp}) = \exp(\exp(\text{A} \times \ln(\text{T(K)}) + \text{B})) \quad (4\text{-}9)$$

The viscosity data are presented in Table 4-5. The best curve fit for the data in the range of 302.2 to 437.2 K results in coefficients of A=3.19 and B=20.54 where T is in K and μ_{Bitumen} is in cp (Figure 4-7). The coefficient of determination (R^2) for the correlation is 0.96, and the AARD is 7.8%. Bitumen viscosity changes from 27,630 ± 500 cp at 302.2 K to 25.5 ± 0.5 cp at 437.2 K.

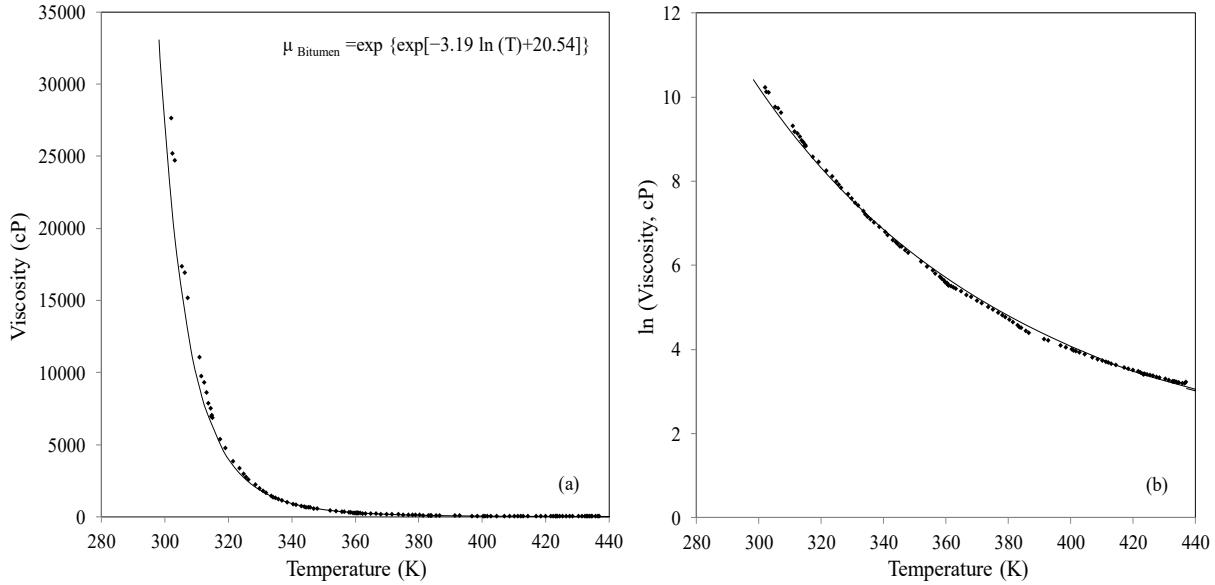

Figure 4-7: Measured bitumen viscosity (cp) vs. temperature (K) in (a) a Cartesian plot and (b) a semi-log plot and the best-fit curve with R^2 of 0.96

Table 4-5: Measured viscosity data for Clearwater bitumen sample at atmospheric pressure

T (K)	μ (cp)	T (°C)	μ (cp)	T (°C)	μ (cp)	T (°C)	μ (cp)
302.0	27630	335.8	1205	366.7	201.3	412.2	40
302.5	25210	337.0	1129	368.1	190.1	413.0	39.07
303.1	24700	338.6	1005	370.0	175.2	414.5	37.93
305.3	17350	340.5	891.1	371.6	163.7	417.2	35.66
306.3	16930	341.4	834.1	373.6	151.1	418.6	34.52
307.2	15160	343.1	742.6	375.2	141	420.1	33.49
311.0	11070	343.9	703.8	376.8	131	421.7	32.45
311.5	9767	344.5	669.7	378.1	123.2	422.5	31.63
312.5	9302	345.3	637.2	379.1	117.6	423.2	30.9
313.2	8620	345.8	637.2	380.4	110.9	423.5	30.2
313.8	7880	346.9	578.3	381.5	105.4	423.8	30.7
314.4	7521	348.0	547.3	383.1	97.67	424.6	30.19

314.7	6963	352.1	442.5	383.7	93.64	425.5	29.85
314.9	7056	354.0	394.8	384.1	91.47	426.5	29.26
315.1	6857	355.8	356.6	386.6	81.55	427.6	28.67
317.4	5369	356.7	333.8	385.6	85.27	428.6	28.16
319.2	4744	358.1	308	391.5	69.76	430.4	27.14
321.6	3848	358.7	293.9	392.9	67.9	431.6	26.47
323.5	3366	359.4	280.9	396.8	60.69	432.6	25.71
324.9	2958	359.9	270.7	398.6	57.67	433.1	25.54
325.6	2741	360.3	265.1	400.4	54.7	433.4	25.45
326.4	2567	360.5	259.7	401.0	53.39	434.0	25.18
328.6	2208	360.7	255.4	401.7	52.4	434.5	24.98
329.8	1981	360.8	253.6	402.9	51.01	434.8	24.78
331.0	1798	361.0	251.7	404.6	48.83	435.9	24.68
331.9	1674	361.7	245.5	407.1	45.58	436.6	24.37
333.6	1460	362.4	238.1	408.8	43.59	437.0	25.43
334.2	1363	363.3	230.7	410.3	42.12	....	....
334.9	1293	364.9	217.7	411.3	41.04	....	....

4.3.3 CO_2-Cold Lake Bitumen

The advantage of CO_2 over C_1 and N_2 is its higher solubility in bitumen (Haddadnia et al., 2017). The solubility of CO_2 in bitumen is of the same order as that of C_2. Previous experiments indicate high CO_2 solubility in bitumen, especially at low temperatures. Mehrotra and Svrcek (1988) measured CO_2 solubility in Cold Lake bitumen for the temperature range of 288.2 to 371.2 K and pressure range of 1998 to 11028 kPa. From this study, CO_2 solubility in Cold Lake bitumen varied from 1.65 to 13.4 wt.%. It is also noted that CO_2 solubility increases by increasing pressure and decreases by increasing temperature. We conducted CCE tests at five temperatures on a CO_2-Clearwater bitumen system with 5.9 wt.% CO_2 (i.e., 39 g bitumen and 2.5 g CO_2). The overall solvent concentrations in this study are selected in a way to be higher than the measured solubilities of that solvents in bitumen from literature at the test temperature and pressure range. P-V data obtained from the CCE tests are presented in Figure 4-8. The saturation point is estimated depending on the point where the slope changes in the P-V data. It is observed that saturation pressure increases from 5812.7 kPa at 339.8 K to 10,517.8 kPa at 435 K. Moreover, at lower temperatures, there is sharper slope change between the single oleic-phase region and the two-phase region. This indicates that the isothermal compressibility of the saturated bitumen increases with temperature. CCE tests indicate that 5.9 wt.% CO_2 can be dissolved totally in bitumen at pressures much higher than reservoir pressure (i.e., 9141.3 kPa at 414 K).

In other words, CO_2 solubility at reservoir pressure and elevated temperatures should be lower than 5.9 wt.%. The swelling factor (SF) of the bitumen-CO_2 mixture is calculated using

$$SF = \frac{(V_m)_{T,P_{sat}}}{(V_b)_{T,P_0}} \times \frac{1}{1 - x_s} \tag{4-10}$$

Where V_m is the molar volume of the solvent-bitumen mixture at saturation pressure and test temperature, V_b is the molar volume of the bitumen at atmospheric pressure and test temperature, and x_s is the mole fraction of the solvent in the mixture. The SF of the CO_2-bitumen mixture is nearly unity at all temperatures. The isothermal compressibility factor (C_T) of the single oleic phase at each temperature is calculated at pressures higher than the corresponding saturation pressures. The arithmetic average of the calculated compressibility factors is calculated at each temperature. As presented in Table 4-6, C_T changes from 2.5×10^{-7} kPa^{-1} at 339.8 K to 6.5×10^{-6} kPa^{-1} at 435 K.

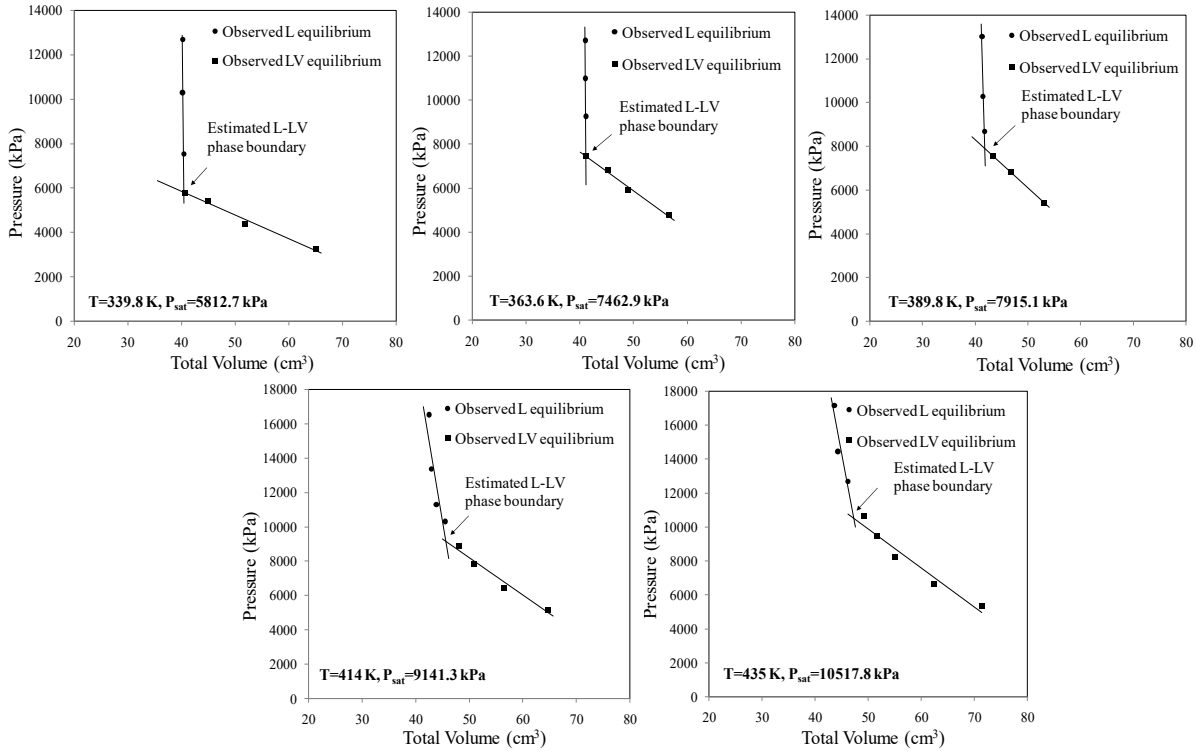

Figure 4-8: P-V data from the CCE experiments on Clearwater bitumen-CO_2 system with 5.9 wt.% CO_2 in temperature range of 339.8 K to 435 K

Table 4-6: Isothermal compressibility and swelling factor of CO_2-bitumen system at different temperatures

Temperature (K)	C_T (kPa^{-1})	SF
339.8	2.5×10^{-7}	1.00
363.6	7.8×10^{-7}	1.00
389.8	9.1×10^{-7}	1.01
414	4.4×10^{-6}	1.04

435	6.5×10^{-6}	1.06

4.3.4 C_3-Cold Lake Bitumen

4.3.4.1. C_3-Bitumen CCE Test, Feed 1 (28.4 wt.% C_3)

CCE tests were conducted at three temperatures on a C_3-Clearwater bitumen system with 28.4 wt.% C_3 (20.21g bitumen and 8g C_3). P-V curves obtained from the CCE tests are presented in Figure 4-9. A sharp reduction in the slope of the P-V curve is observed at each temperature as the volume of the PVT cell increases. The pressure at which the slope change occurs represents the saturation point (P_{sat}) of the C_3-bitumen mixture, below which a free vapor phase forms in the cell. Saturation pressure increases from 3168.6 kPa at 348.2 K to 9585.2 kPa at 431.8 K. The slope change in the P-V curves becomes gentler at higher temperatures because the saturated bitumen curve ($P>P_{sat}$) exhibits a milder slope and the vapor curve ($P<P_{sat}$) exhibits a steeper slope. The reduction in slope for the saturated bitumen curve ($P>P_{sat}$) is due to the increase in isothermal compressibility of saturated bitumen at higher temperatures. The observed reduction in vapor isothermal compressibility ($P<P_{sat}$) at higher temperatures is because the temperature of the cell exceeds the supercritical temperature of C_3 (369.9 K) in the latter two conditions (i.e., 412.1 K and 431.8 K). Supercritical C_3 exhibits a lower compressibility than vapor C_3 (Mattar et al., 1975). SF values at different test conditions are calculated as listed in Table 4-7.

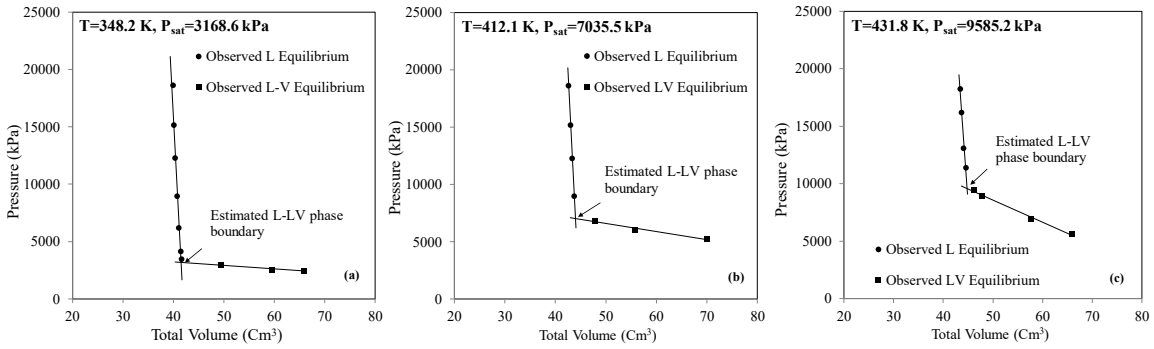

Figure 4-9: P-V data from the CCE experiments on C_3-bitumen system with 28.4 wt.% C_3 at a) 348.2 K b) 412.2 K and c) 431.8 K

Table 4-7: Swelling factor and average Isothermal compressibility of C_3-bitumen system (Feed 1) in L phase region at different temperatures

Temperature (K)	C_T (kPa^{-1})	SF
348.15	1.2E-06	1.93
412.05	2.2E-06	1.94
431.75	2.3E-06	1.95

4.3.4.2. C_3-Bitumen CCE Test, Feed 2 (78.3 wt.% C_3)

Three sets of CCE test were conducted on a system of C_3-Clearwater bitumen with 78.3 wt.% C_3 (i.e., 4.9 gr bitumen and 17.8 gr C_3). P-V curves were obtained from the CCE tests at 357.2 K, 366.5 K, and 411.2 K and are presented in Figure 4-10. The saturation pressure increases from 3831.7 kPa at 357.2 K to 10618.6 kPa at 411.2 K.

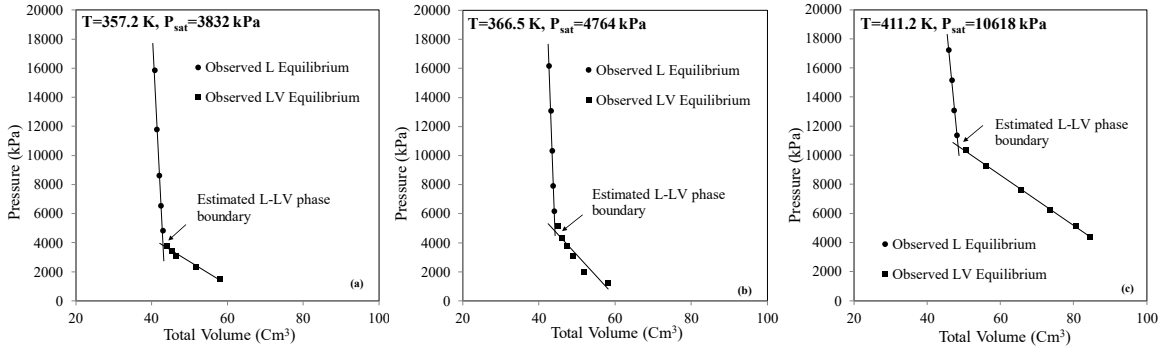

Figure 4-10: P-V data from CCE tests of feed 2 (i.e., 78.3 wt.% C_3) in C_3-bitumen system at a) 357.2 K b) 366.5 K and c) 411.2 K

4.3.5 C_4-Cold Lake Bitumen

C_4 is inherently more soluble in bitumen than CO_2 because of its lower vapor pressure (Hildebrand, 1936). Measurements indicate that the solubility of C_4 in Surmont bitumen varies from 1.83 to 19.5 wt.% for 373.2 K<T<463.2 K and 841 kPa<P<5066 kPa (Kariznovi, 2013). The following subsections report the results of CCE tests on two feeds of C_4-Clearwater bitumen. Feed 1 contains 28.4 wt.% C_4 and Feed 2 contains 84.6 wt.% C_4. A higher solvent concentration was examined with Feed 2 (84.6 wt.% C_4) to observe the effect of high solvent concentration on phase behavior at the edge of the steam chamber. This high solvent concentration occurs near the chamber edge due to the accumulation of solvent in the oil phase during solvent-aided process.

4.3.5.1. C_4-Bitumen CCE Test, Feed 1 (28.4 wt.% C_4):

We conducted CCE tests on a system of C_4-Clearwater bitumen with 28.4 wt.% C_4 (i.e., 20.2 g bitumen and 8 g C_4). Figure 4-11 shows the P-V results from the CCE tests performed on a system of C_4-Clearwater bitumen with 28.4 wt.% C_4. The saturation pressure increases from 1014.6 kPa at 347.8 K to 3330.6 kPa at 432.3 K. A milder slope of the data in the two-phase region is observed for the C_4-bitumen system compared with that for the CO_2-bitumen system. This is attributed to the fact that the two-phase region for most of the CO_2-bitumen CCE tests (four out of five) were at T > $Tc_{,CO2}$ (i.e., 304.1 K) and P > $Pc_{,CO2}$ (i.e., 7377.3 kPa), causing vaporized CO_2 to

exist in its supercritical state. Vaporized C_4 in all C_4-bitumen CCE tests is in the gas state, which has higher compressibility than supercritical CO_2.

The SF and the C_T of the C_4-bitumen system (Feed 1) are also calculated and presented in Table 4-8. C_T increases from 1.3×10^{-6} kPa^{-1} at 347.8 K to 4.2×10^{-6} kPa^{-1} at 432.3 K, and the SF increases from 1.84 at 347.8 K to 1.87 at 432.3 K. To compare swelling effect of different solvents on bitumen, SF is estimated using the calibrated EOS which will be presented further. The estimated SF values by dissolution of 28.4 wt.% C_3 (81% mol) in bitumen is 1.9 at 140°C. For the purpose of comparison, the SF values by dissolution of 81% mol CO_2 and 81% mol C_4 in bitumen is 1.46 and 2 at 140°C, respectively.

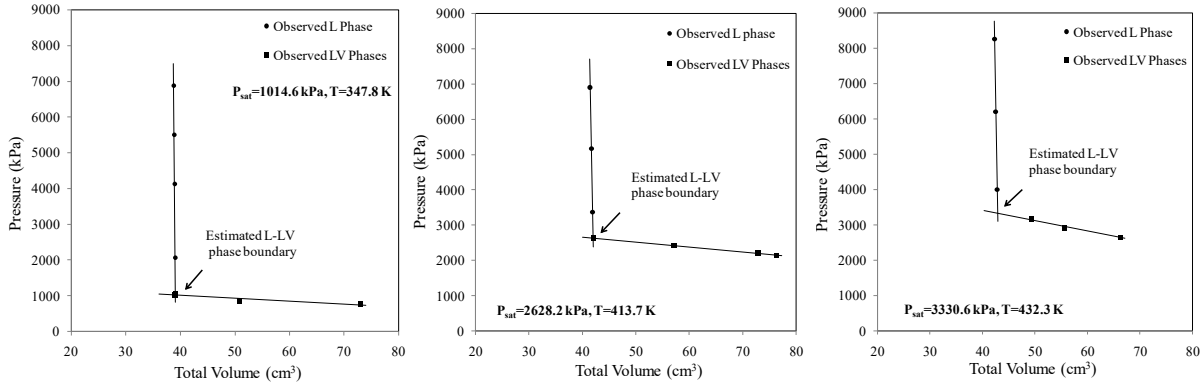

Figure 4-11: Results of CCE test for Clearwater bitumen-C_4 system with 28.4 wt. % C_4 (Feed 1) for temperature range of 347.8 K to 432.3 K

Table 4-8: Isothermal compressibility and swelling factor of C_4-bitumen system, feed 1 at different temperatures

Temperature (K)	C_T (kPa^{-1})	SF
347.8	1.3×10^{-6}	1.84
413.7	2.2×10^{-6}	1.85
432.3	4.2×10^{-6}	1.87

4.3.5.2. C_4-Bitumen CCE Test, Feed 2 (84.6 wt.% C_4):

We also conducted CCE tests on the C_4-Clearwater bitumen system with 84.6 wt.% C_4 (i.e., 4.5 g bitumen and 24.9 g C_4). A high C_4 concentration is selected to investigate the possibility of forming three phases at equilibrium conditions near the edge of the steam chamber. Figure 4-12a shows the equilibrated phases at 382 K and three pressures of 5376.1, 1750.8, and 1378.6 kPa. A single L_2 phase, two L_1/L_2 phases, and three $L_1/L_2/V$ phases exist at 5376.1, 1750.8, and 1378.6 kPa, respectively. Figure 4-12b shows the P-V data at 382 K. The first separation of the L_1 phase from L_2 is observed at 2205.7 kPa, which is confirmed by a slight slope change in the P-V curve close to this pressure. As Figure 4-12a shows, the L_2 phase is less dense than L_1

and has a reddish color. This phase is rich in C_4, which will be shown by the results of multiphase-equilibrium calculations. Because pure C_4 is colorless, the reddish color of L_2 can be explained by light-end hydrocarbon components from the bitumen being extracted into the L_2 phase. A vapor phase is also observed under equilibrium conditions at lower pressures. This phase is nearly pure C_4, which will be confirmed by the results of flash calculations. Phase-boundary pressure between the L_2 and L_1/L_2 regions and also between the L_1/L_2 and $L_1/L_2/V$ regions can be estimated using the two distinct slope changes in the P-V data. As Figure 4-12b shows, these phase-boundary pressures are estimated to be at 2076.1 and 1557.1 kPa, respectively. We conduct a similar CCE test on Feed 2 (i.e., C_4 concentration of 84.6 wt.%) at 411.7 K. Figure 4-13a shows the equilibrated phases at four pressures of 13785.6, 6823.9, 5652.1, and 2757.1 kPa. The single L_2 phase exists at 13785.6 kPa. By decreasing pressure to 5652.1 kPa, the L_2 phase turns red and an oleic phase (L_1) begins to appear that is heavier than the light (C_4-rich) oleic phase (L_2). This shows the distribution of light- and heavy-hydrocarbon components into the L_2 and L_1 phases, respectively. When the pressure is decreased from 6823.9 kPa to 5652.1 kPa, the L_2 phase turns lighter in color. This indicates extraction of lighter components by the L_2 phase at lower pressures. By the appearance of the vapor phase, three phases of L_1, L_2, and V come into equilibrium at 2757.1 kPa. Saturation pressures for the L_2- and L_1/L_2-phase boundaries and L_1/L_2- and $L_1/L_2/V$-phase boundaries are estimated from two slope changes in the P-V data (Figure 4-13b). By increasing temperature from 382 to 411.7 K, saturation pressures for the L_2- and L_1/L_2-phase boundaries and the L_1/L_2- and $L_1/L_2/V$-phase boundaries increase from 2076.1 to 6903.2 kPa and from 1557.1 to 3649.8 kPa, respectively.

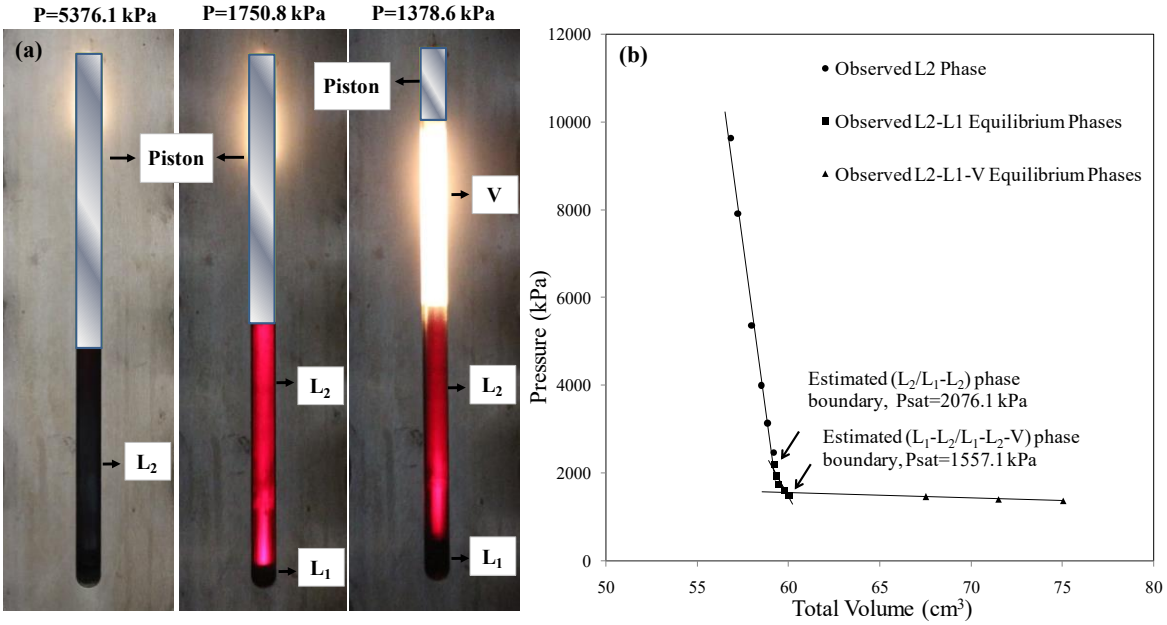

Figure 4-12: Results of CCE test for Clearwater bitumen-C_4 system with 84.6 wt.% C_4 (Feed 2) at 382 K:a) Equilibrium phases in PVT cell at three pressure stages of 5376.1 kPa, 1750.8 kPa and 1378.6 kPa :, L_1: heavy oleic phase, L_2 : light (C_4-rich) oleic phase, V:gaseous phase, b) P-V data from CCE test showing L_2/L_1-L_2 and L_1-L_2/L_1-L_2-V phase boundaries

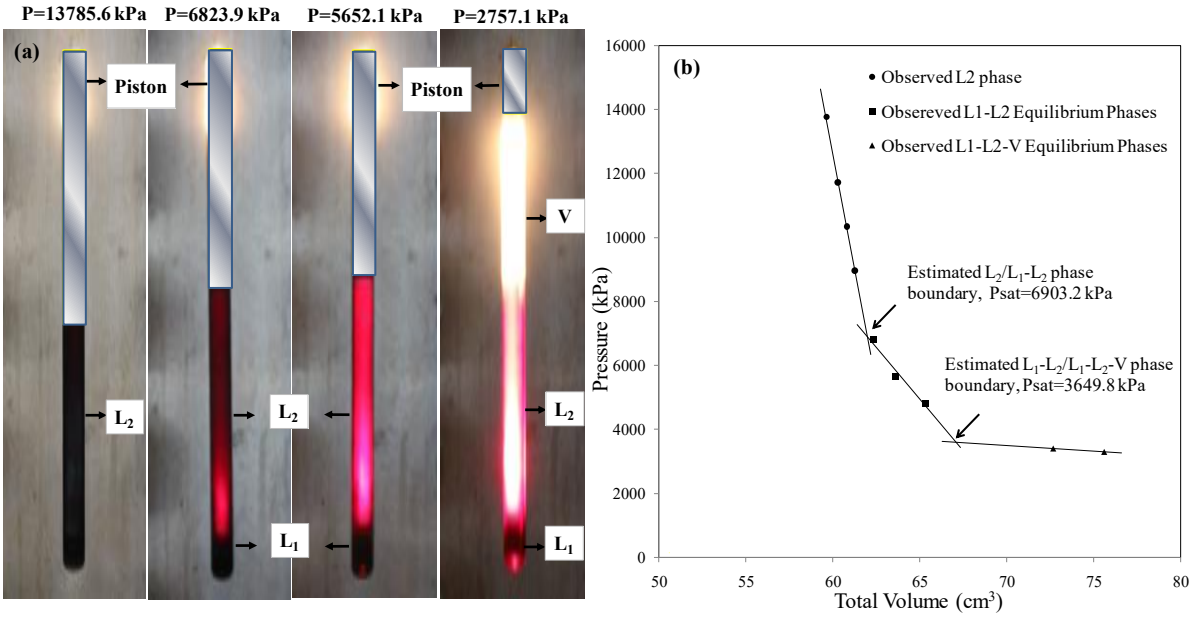

Figure 4-13: Results of CCE test for Clearwater bitumen-C_4 system with 84.6 wt.% C_4 (Feed 2) at 138.5°C: a) Equilibrium phases in PVT cell at four pressure stages of 13785.6 kPa, 6823.9 kPa, 5652.1 kPa and 2757.1 kPa (I: heavy oleic phase, L_1, II: L_2:light (C_4-rich) oleic phase, V: gaseous phase, b) P-V data from CCE test showing L_2/L_1-L_2 and L_1-L_2/L_1-L_2-V phase boundaries.

4.3.6 Sampling

Samples from the L_1 and L_2 phases were collected from the equilibrated C_4-bitumen mixture (Feed 2, 84.6 wt.% C_4) at 411.7 K and 2963.9 kPa after being flashed under atmospheric-pressure and room-temperature conditions (i.e., dead L_1 and dead L_2 samples). Figure 4-14 shows samples from the two phases and the original bitumen.

The dead L_2 sample has a brown color and the dead L_1 sample is semi-solid and has a dark-black color, as shown in Figure 4-14. As presented in Figure 4-15, the dead L_2 sample is much less viscous than the original bitumen. Compositional analysis of the dead L_1 and dead L_2 samples are conducted by simulated distillation method (D2887-84). Mass distribution of the pseudo-components up to C_{99} is presented in Figure 4-16 and compared with the compositional analysis of bitumen. The rest of the components are considered as residue (heavy fraction: C_{100+}), with boiling temperatures higher than 993 K. It can be observed that the dead L_2 sample has the most PCs with low carbon numbers ($<C_{30}$). However, the dead L_1 sample has the fewest PCs with low carbon numbers. The mass percentages of the heavy fraction (C_{100+}) for dead L_2 and dead L_1 samples are measured to be 5.07 and 46.27 wt.%, respectively. The mass percentage of the heavy fraction in the dead L_1 sample is much higher than that in the original bitumen (19.8 wt.%).

CCE tests showed that when bitumen is in equilibrium with a high concentration of C_4 (i.e., 84.6 wt.%), there is a possibility for the existence of two oleic phases (i.e., L_1 and L_2). Our multiphase-equilibrium calculations indicate that the L_2 phase is rich in C_4. Because pure liquid C_4 is colorless, the red color of the L_2 phase implies that it can extract a significant amount of intermediate components from the bitumen. The asphaltene content of the samples and also the original bitumen are measured by the IP-143 method (Institute of Petroleum, 1988) with n-heptane as the precipitant. The asphaltene content of the original bitumen is 11 wt.%. It is found that the dead L_1 sample contains 30 wt.% asphaltene, whereas the dead L_2 sample has negligible asphaltene content (0.59 wt.%). The existence of C_4 in the system causes distribution of asphaltene components from bitumen in a heavy phase (i.e., L_1). Moreover, asphaltenes are insoluble in the L_2 phase, which is rich in C_4. Hence, the L_1 phase contains higher asphaltene content than both the L_2 phase and the original bitumen, suggesting partial upgrading of the bitumen. Asphaltene precipitation was not explicitly observed during the test because the equipment setup does not contain a solid-phase-detection unit.

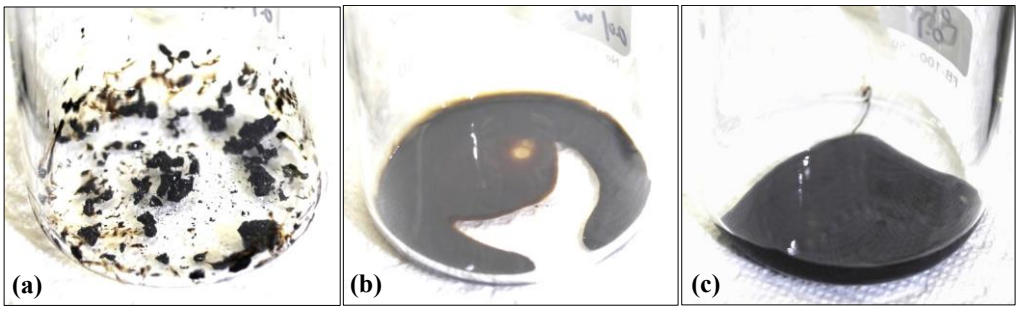

Figure 4-14: Pictures of the samples from a) dead L_1 phase b) dead L_2 phase and c) Clearwater bitumen

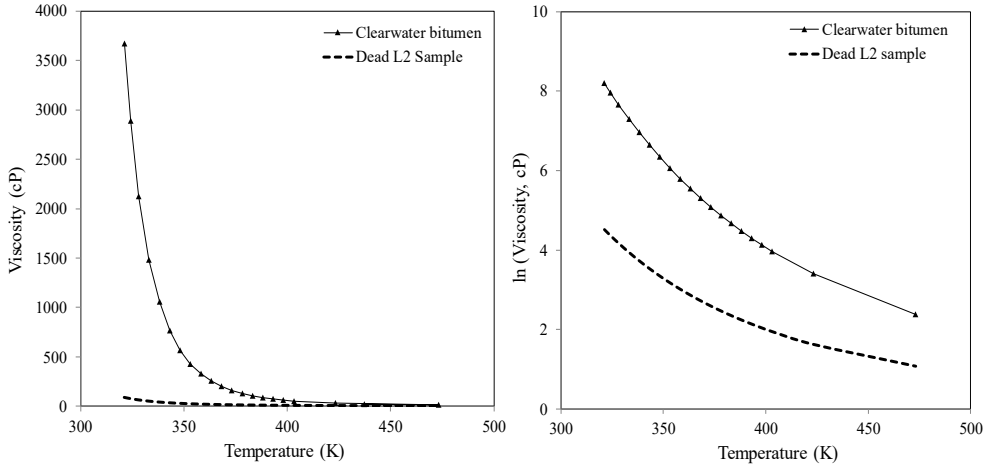

Figure 4-15: Comparing the measured viscosity of the dead L_2 sample and the original bitumen vs. temperature

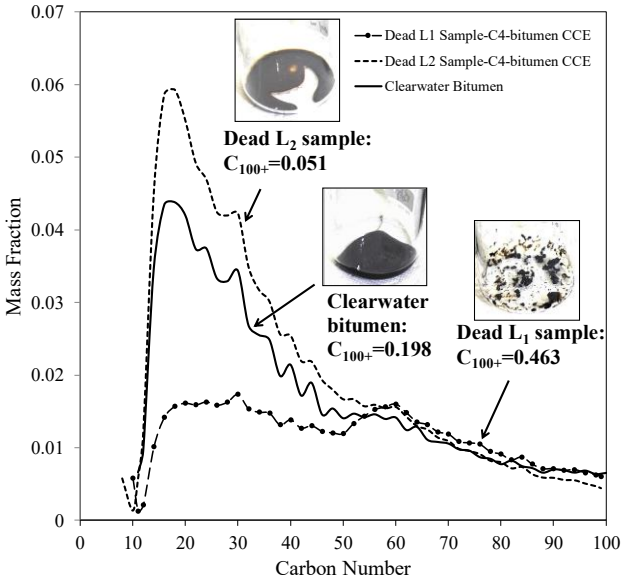

Figure 4-16: Fractional mass distribution of the carbon cuts for two oleic samples flashed at atmospheric pressure (i.e., L_1: heavy oleic phase and L_2: light (C_4-rich) oleic phase) from Clearwater bitumen-C_4 system with 84.6 wt.% C_4 (Feed 2)

A sample was taken from the liquid phase equilibrated with vapor phase at 138.5°C and 2964 kPa from the C_3-bitumen system with 78.3 wt.% C_3 for oil composition analysis. Figure 4-17 shows the simulated distillation results of the liquid phase from the C_3-bitumen system (dead C_3 L_1 phase) alongside the characterized Clearwater bitumen (baseline) and dead L_1 and dead L_2 liquid phases from the 84.6

wt.% C_4-bitumen system (dead C_4 L_1 phase and dead C_4 L_2 phase). The results show that more heavy components exist in the C_3 L_1 phase compared with the original bitumen. Although not shown in Figure 4-17, the C_{100+} fraction in the C_3 L_1 sample (28.1 wt.%) is higher than that in the original bitumen (19.8 wt.%). The asphaltene content of original bitumen, C_4 L_2, C_4 L_1, and C_3 L_1 samples were measured by IP-143 method and estimated to be 11 wt.%, 0.59 wt.%, 30 wt.% and 15.5 wt.%, respectively. Comparing the distribution curves and plus fraction values shows existence of heavier hydrocarbon components in the L_1 sample of the C_4-bitumen system than the C_3-bitumen system. As a result of extracting-condensing mechanism, C_4 can extract lighter components into a second liquid phase (L_2), resulting in a heavier liquid phase (L_1) forming at the bottom of the cell. Another mechanism which may affect composition of the L_1 phase is asphaltene precipitation as a result of C_3/C_4 dissolution. This will be investigated in the next section.

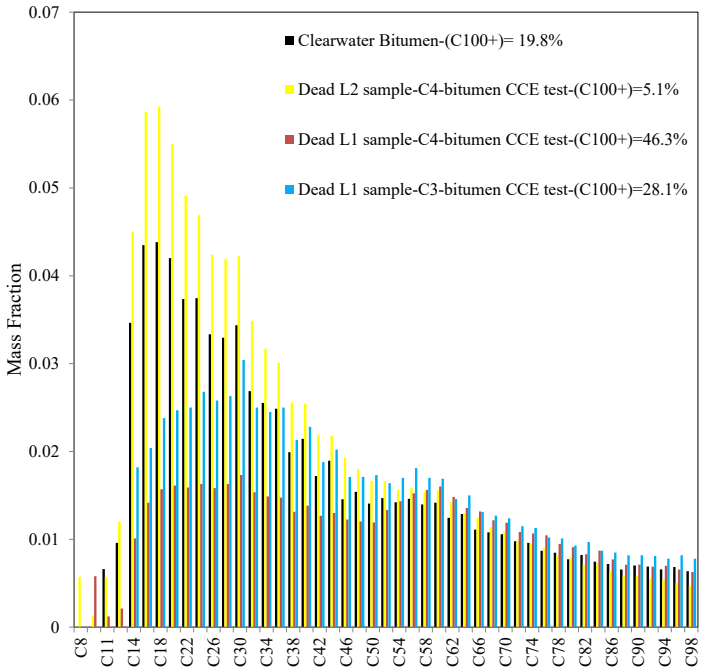

Figure 4-17: Fractional mass distribution measured by simulated distillation conducted on Clearwater bitumen and on samples flashed at atmospheric pressure (dead L_1: heavy liquid phase and dead L_2: light (C_4-rich) liquid phase from C_4-bitumen system with 84.6 wt.% C_4 (Feed 2) and dead L_1: liquid phase from C_3-bitumen system with 78.3 wt.% C_3)

4.3.7 Asphaltene Filtration Tests

Filtration tests were conducted to investigate the effect of solvent type and concentration on asphaltene precipitation at SAP conditions. An asphaltene filtration test was performed using the filtration cell on a CO_2-Clearwater bitumen system with 5.9 wt.% CO_2 after reaching equilibrium state in the PVT cell at 140°C and 2068 kPa.

The amount of asphaltene precipitated from the PVT flow lines and filter paper were 0.15g and 0.25g, out of 39g bitumen, respectively. The total mass of precipitated asphaltene (0.4g) equates to 1 wt.% precipitated asphaltene per unit mass of bitumen. This amount of asphaltene is precipitated by dissolution of 1.1 wt.% CO_2 in bitumen. To investigate the effect of hydrocarbon solvents on asphaltene precipitation, additional tests were performed on C_3 and C_4 systems, as summarized in Table 4-9.

Table 4-9: Results of Asphaltene filtration test on solvent-bitumen systems

Solvent	Solvent Concentration (wt.%)	PVT cell Condition	Solvent Solubility (wt.%)	Precipitated Asphaltene ($\%w_{asph}/w_{bitumen}$)
CO_2	5.9	2068 kPa, 140°C	1.1	1
C_4	28.4	2068 kPa, 140°C	14.9	2.9
C_3	28.4	2068 kPa, 140°C	4.2	3
C_3	78.3	8961 kPa , 140°C	27.5	10.3

From Table 4-9, the amount of asphaltene precipitation by C_3 is almost the same as that by C_4 at the same PVT cell conditions, despite C_3 having 3.5 times lower solubility. However, increasing cell pressure to 8961 kPa increases C_3 solubility by 6.5 times and asphaltene precipitation by 3.4 times. C_4 causes less asphaltene precipitation than C_3 due to its higher molecular weight and higher asphaltene dissolving power (Kokal et al., 1992).

In summary, at the same PVT cell conditions, C_3 and C_4 cause more asphaltene precipitation than CO_2. One reason can be an increase in the ratio of saturate to asphaltene of solvent-bitumen system by introducing C_3 and C_4 compared with CO_2. Another reason can be higher solubility of C_3 and C_4 than CO_2 in bitumen. Furthermore, the results show that increasing C_3 solubility increases asphaltene precipitation. Although C_3 causes more asphaltene precipitation than C_4, extracting-condensing mechanism in the C_4-bitumen system results in forming a heavier L_1 phase than the C_3-bitumen system as it was explained in the previous section.

4.3.8 Screening Criteria for Asphaltene Precipitation Potential

We used three screening methods to investigate the stability of bitumen and CO_2-, C_3-, and C_4-bitumen systems in terms of asphaltene precipitation. One of the most commonly used methods to classify the possibility of asphaltene-precipitation problems is the de Boer et al. (1995) plot. A de Boer et al. (1995) plot shows the relationship between the difference of initial pressure and saturation pressure ($P–P_b$) and the density of live oil at initial pressure conditions. Another method is the

colloidal-instability index (CII), which considers the crude oil as a colloidal solution made up of saturates, aromatics, resins, and asphaltenes. CII is defined as the mass ratio of the sum of asphaltenes and its flocculants (saturates) to the sum of its peptizers (resins and aromatics) in a crude oil:

$$\text{CII} = \frac{\text{Saturates+Asphaltenes}}{\text{Aromatic+Resins}} \tag{4-11}$$

The asphaltene/resin ratio (ARR) is the ratio of asphaltenes to resins. For a given oil, the higher the ratio, the more unstable the oil is. According to laboratory data, 0.35 is set as the cut-off point for the ARR, below which an oil is considered stable (Asomaning 2003). The CII and ARR use the weight percentages obtained from SARA analysis. CII has been used to predict the stability of asphaltenes in oil (Gaestel et al. 1971) and the stability of asphaltenes in crude-oil/solvent mixtures (Asomaning and Watkinson 2000). Asphaltenes of the oil are unstable for CII>0.9, although they are stable for CII<0.7. The stability of the asphaltenes falls in the uncertain region for 0.7<CII<0.9.

Required properties of Clearwater bitumen and CO_2-, C_3-, and C_4-Clearwater bitumen for using the de Boer et al. (1995) plot are presented in Table 4-10. Properties including oil-phase density and bubble point pressure (P_b) are obtained from the CCE experiments presented in Sections 4-3-4 to 4-3-6. Two indices of L and H represent the sample properties at the lowest and the highest temperature of the CCE tests, respectively. Reservoir pressure and initial reservoir temperature are assumed to be 4000 kPa and 288.2 K, respectively. P_b in the system of C_4-bitumen (84.6 wt.%) is assumed to be the measured P_b corresponding to the boundary between the L_1/L_2- and the L_1/L_2/V-phase regions. For the cases where P_b>P, the absolute value of their difference is used. For the samples where oil density is out of the de Boer et al. (1995) plot density range (i.e., D_H with density of 475 kg/m^3), the potential of asphaltene precipitation can be found by the extrapolation of the boundaries.

Figure 4-18 presents the de Boer et al. (1995) plot with the location of the systems studied in this Chapter. According to this plot, bitumen and systems of CO_2-bitumen, C_3-bitumen with 28.4 wt.% C_3 and C_4-bitumen with 28.4 wt.% C_4 will not have asphaltene-precipitation problems under reservoir and SAP conditions. However, C_3-bitumen with 78.3 wt.% C_3 and C_4-bitumen with 84.6 wt.% C_4 may result in asphaltene-related issues. Results of CII and ARR estimation show the potential of

asphaltene precipitation for all samples (i.e., CII>0.9 and ARR>0.35), which is in disagreement with de Boer et al. (1995) criteria. Because the de Boer et al. (1995) method uses the live-oil/reservoir properties, this method is a more-valid approach than CII and ARR for investigation of hydrocarbon fluids regarding the potential of asphaltene precipitation (Mohammadi 2016). Figure 4-18 shows higher potential of asphaltene precipitation for C_3-bitumen and C_4-bitumen systems at high solvent concentrations respect to the systems at low solvent concentration. This is also verified by filtration tests on systems of CO_2-bitumen (5.9 wt.%), C_3-, and C_4-bitumen (28.4 wt.% solvent) which indicated insignificant amount of asphaltene precipitation compared with the one in C_3-bitumen (78.3 wt.% solvent) system. Thus, application of C_3 and C_4 with high concentrations may cause asphaltene precipitation in solvent-based or solvent-aided thermal methods. For an accurate assessment of precipitation risks, it is recommended to include asphaltene precipitation in the fluid model using experimental onset data, which was not considered in this study. Because of the limitations of the experimental setup, asphaltene-onset data were not measured here.

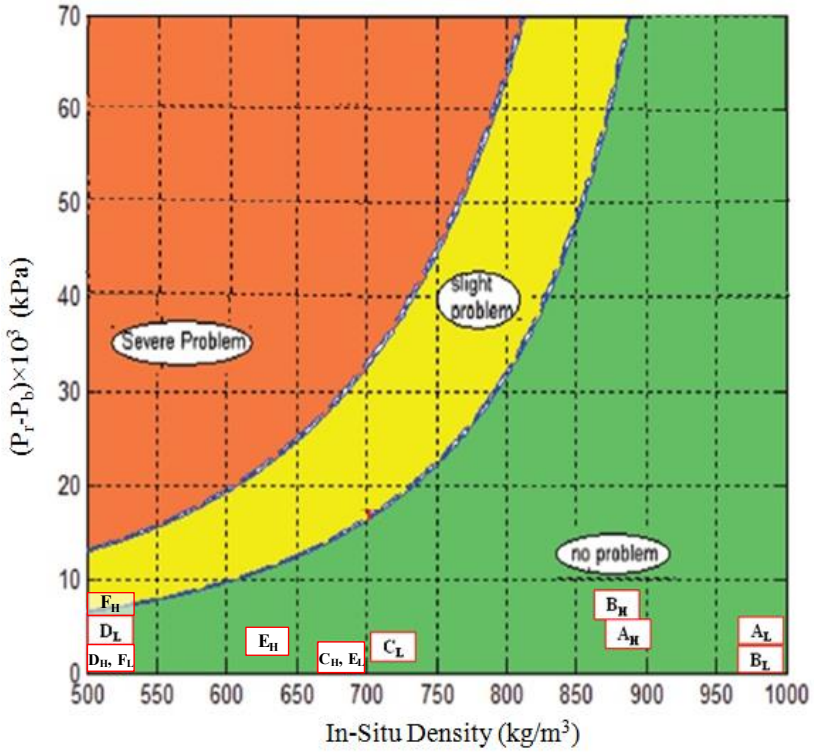

Figure 4-18: Results of investigating asphaltene precipitation potential in bitumen-solvent mixtures at reservoir condition using de-Boer plot (de Boer, 1995)

Table 4-10: Properties of samples and results of screening by three methods

sample	A	B	C	D	E	F
	Clearwater bitumen	Clearwater bitumen+5.96 wt.% CO_2	Clearwater bitumen+28.4 wt.% C_4	Clearwater bitumen+84.6 wt.% C_4	Clearwater bitumen+28.4 wt.% C_3	Clearwater bitumen+78.3 wt.% C_3

	L (288 K)	H (431 K)	L (340 K)	H (435 K)	L (348K)	H (432 K)	L (382 K)	H (412 K)	L (348 K)	H (432 K)	L (357 K)	H (411 K)
P_b (kPa)	0	483	5811	10512	1013	3329	1558	3653	3168.6	9585.2	3831.7	10618.4
$\|P-P_b\|$ (kPa)	3998	3515	1813	6514	2433	117	2440	345	829.4	5587.2	166.3	6620.4
Density (kg/m^3)	1032	907	1027	878	722	658	495	475	679.2	630.3	530.8	469.7
Screening results												
de Boer	stable	stable	stable	stable	stable	stable	semi-stable	stable	stable	stable	stable	unstable
CII	1.48	1.48	1.65	1.65	2.5	2.5	15.20	15.20	2.5	2.5	10.5	10.5
ARR	0.8	0.8	0.8	0.8	0.8	0.8	0.8	0.8	0.8	0.8	0.8	0.8

4.3.9 Modelling Phase Behavior of Solvent-Bitumen Systems

The measured saturation-pressure and density data from the CCE tests were used to calibrate PR-EOS to predict solvent-bitumen phase behavior. Regression variables include the critical properties of PCs (Tc, Pc, and ω) and BIPs between the water or solvent and PCs. The two measured saturation pressures observed for the dead-oil system (with 0.14 wt.% water content; see the subsection 'Bitumen Density') are applied for optimizing BIPs between water and PCs. According to the literature (Kato et al., 1981; Venkatramani and Okuno, 2014), the BIPs for water-CO_2, water-C_3 and water-C_4 systems are assumed to be 0.1900, 0.6567 and 0.6096, respectively. Table 4-11 presents the related regression parameters for the components after EOS calibration. Table 4-12 presents the optimized BIP values between solvent-PCs and water-PCs. The EOS matches the experimental data of CO_2-bitumen system with an AARD of 6.0%, C_3-bitumen system with an AARD of 13% (11.5% for Feed 1, 15% for Feed 2) and those of the two C_4-bitumen systems with AARD of 13.3% (10.3% for Feed 1 and 17.8% for Feed 2, respectively).

Table 4-11: Properties of the pseudo components used in the calibrated EOS

Component	z_i	Mw_i	T_c (°C)	P_c (kPa)	ω	V_c ($cm^3/gmol$)
CO_2	0.00	44.01	30.98	7375.98	0.23	94.27
C_3	0.00	44.10	96.65	4245.52	0.15	201.02
n-C_4	0.00	58.12	151.98	3796.03	0.20	254.71
Water	0.04	18.01	373.9	22063.97	0.34	63.05
PC_1	0.50	228.21	478.02	2073.03	0.72	812.19
PC_2	0.27	434.46	613.53	1307.99	1.08	1314.73
PC_3	0.13	870.00	738.70	823.01	1.42	1923.41
PC_4	0.06	1809.76	947.01	459.00	1.79	2803.64

Table 4-12: Optimized BIP values after EOS calibration

	CO_2	C_3	C_4	Water	PC_1	PC_2	PC_3	PC_4
CO_2	0.0000	0.1350	0.1300	0.1900	0.0449	0.0814	0.0896	0.0910
C_3	0.1350	0.0000	0.00087	0.6567	0.011	0.014	0.016	0.018
C_4	0.1300	0.00087	0.0000	0.6096	0.0344	0.0385	0.0409	0.0420

Water	0.1900	0.6567	0.6096	0.0000	0.3420	0.3420	0.3420	0.3420
PC_1	0.0449	0.011	0.0344	0.3420	0.0000	0.0000	0.0000	0.0000
PC_2	0.0814	0.014	0.0385	0.3420	0.0000	0.0000	0.0000	0.0000
PC_3	0.0896	0.016	0.0409	0.3420	0.0000	0.0000	0.0000	0.0000
PC_4	0.0910	0.018	0.0420	0.3420	0.0000	0.0000	0.0000	0.0000

The phase diagrams for bitumen-CO_2 and bitumen-C_4 systems with 28.4 wt.% C_4 (Feed 1) from the calibrated EOS model are shown in Figure 4-19. A comparison of the measured saturation pressure and densities with EOS predictions for the two systems is presented in Tables 4-13 and 4-14. The predicted phase boundary between the L_1- and L_1/V-phase regions matches the measured data points for the CO_2-bitumen and C_4-bitumen systems with reasonable AARD values of 6.0 and 10.3%, respectively.

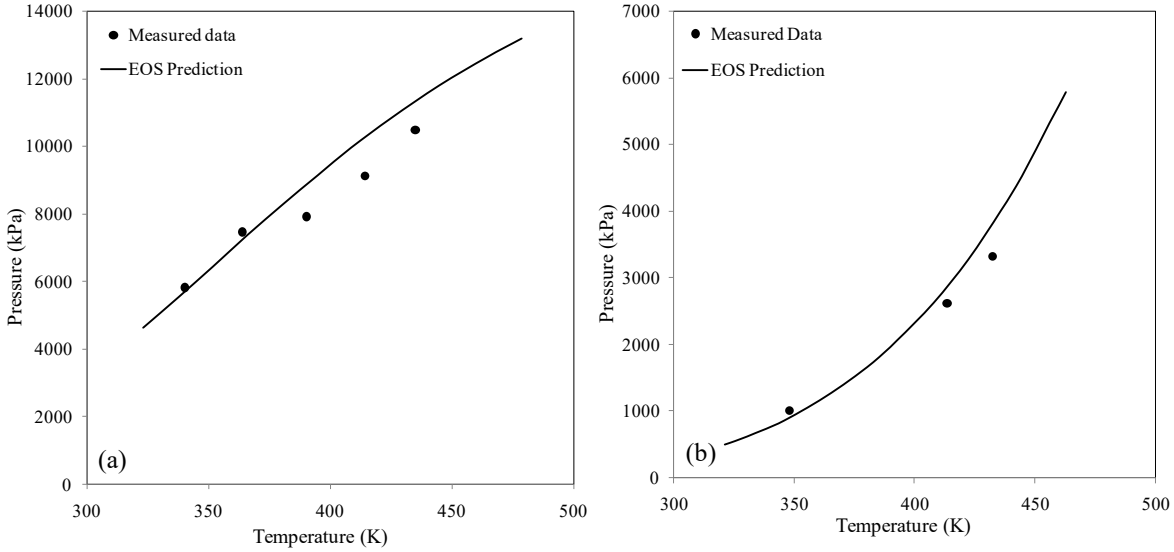

Figure 4-19: Measured and predicted phase boundary: a) Clearwater bitumen-CO_2 system with 5.9 wt.% CO_2 b) Clearwater bitumen-C_4 system with 28.4 wt.% C_4 (Feed 1)

Table 4-13: Comparison of the measured data and EOS predictions for system of CO_2-bitumen

T (K)	Experimental		Predictions from EOS model	
	P^{sat} (kPa)	ρ^{sat} (kg/m^3)	P^{sat} (kPa)	ρ^{sat} (kg/m^3)
339.8	5812.7	1027.3	5685.2	997.4
363.6	7462.9	1010.9	7218.2	990.7
389.8	7915.1	994.0	8858.7	983.1
414	9141.3	909.4	10255.9	975.7
435	10517.8	878.7	11342.9	962.8
AARD (%)			7.49	4.58

Table 4-14: Comparison of the measured data and EOS predictions for systems of C_4-bitumen (Feed 1 and 2)

Feed	Experimental			Predictions from EOS model	
	T (K)	P^{sat} (kPa)	ρ^{sat} (kg/m^3)	P^{sat} (kPa)	ρ^{sat} (kg/m^3)
1	432.3	3330.6	657.9	3789.7	717.5
	413.7	2628.2	671.4	2859.8	733.4
	347.8	1014.6	722.5	889.9	786.3
AARD (%)				11.6	9

Feed	Experimental			Predictions from EOS model	
	T (K)	P^{sat} (L_2/L_1L_2) (kPa)	P^{sat} (L_1L_2/L_1L_2V) (kPa)	P^{sat} (L_2/L_1L_2) (kPa)	P^{sat} (L_1L_2/L_1L_2V) (kPa)
2	382	2076.1	1557.1	1876.9	1781.8

411.7	6903.2	3649.8	4740.2	3070.1
	AARD (%)		17.8	

The phase diagram for the C_4-bitumen system with 84.6 wt.% C_4 (Feed 2) obtained from the calibrated EOS model is shown in Figure 4-20. Predicted boundaries between the L_2- and L_1/L_2-phase regions and also between the L_1/L_2- and $L_1/L_2/V$-phase regions match the measured data with AARD of 17.8% (Table 4-14). As Figure 4-20 shows, the upper pressure boundary of the $L_1/L_2/V$ three-phase region is close to the n-C_4 vapor-pressure curve.

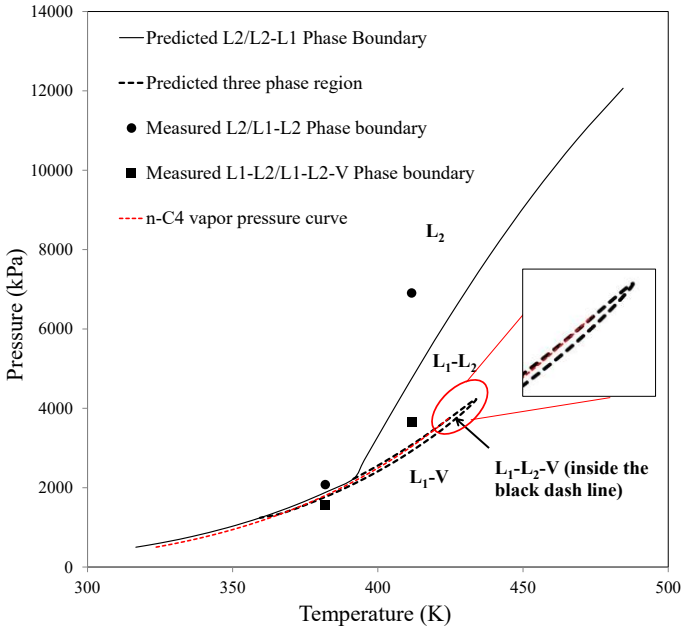

Figure 4-20: Measured and predicted phase boundaries for Clearwater bitumen-C_4 system with 84.6 wt.% C_4 (Feed 2)

The EOS matches the experimental data of C_3-bitumen system with an AARD of 13% (11.5% for Feed 1, 15% for Feed 2). Figure 4-21a and 4-21b show the predicted phase diagrams for the C_3-bitumen systems with 28.4 wt.% C_3 (Feed 1) and 78.3 wt.% C_3 (Feed 2) using the calibrated EOS model. Table 4-15 compares the measured saturation pressure and densities with those predicted by EOS for the two systems. The predicted phase boundary between L_1 and L_1-V phase regions matches the measured data points with reasonable AARDs of 11.5 % for Feed 1 and 15% for Feed 2.

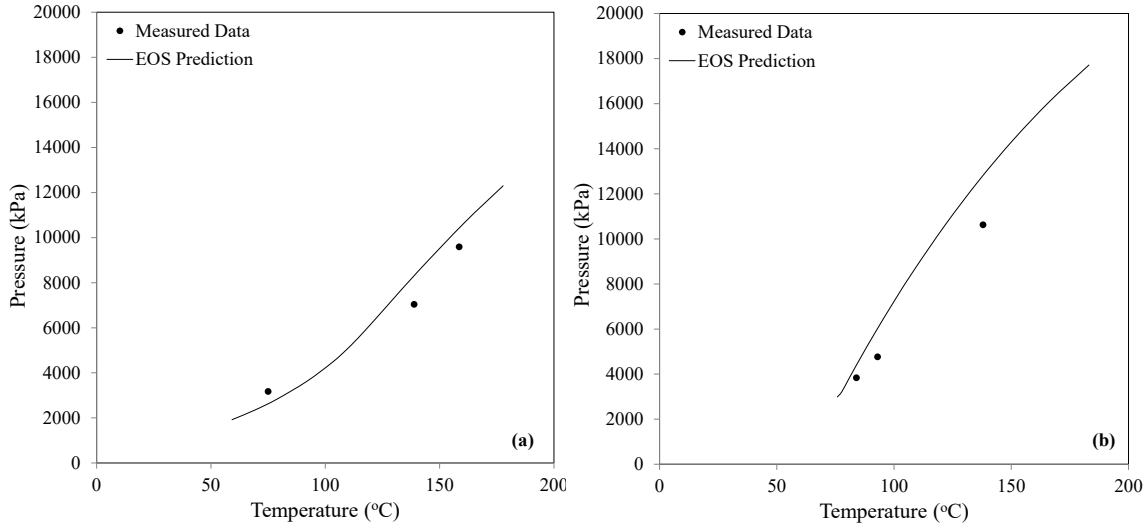

Figure 4-21: Measured and predicted phase boundary for C_3-bitumen system a) Feed 1 b) Feed 2

Table 4-15: Comparison of the measured data and EOS predictions for the C_3-bitumen system (Feed 1 and Feed 2)

Feed	T (°C)	Experimental		Predictions from EOS model	
		P^{sat} (kPa)	ρ^{sat} (kg/m^3)	P^{sat} (kPa)	ρ^{sat} (kg/m^3)
1	75	3168.6	679.2	2631.0	742.2
	138.9	7035.5	641.9	8316.2	692.7
	158.6	9585.2	630.3	10430.3	678.7
AARD (%)				14	8.2
2	84	3831.7	530.8	4406.6	453.1
	93	4763.7	514.5	6029.9	446.4
	138	10618.4	469.7	12820.7	412.9
AARD (%)				17	13

4.3.8.1. Multiphase-Equilibrium Calculations using the Calibrated EOS:

To investigate the equilibrium phases generated by interaction of bitumen with 84.6 wt.% C_4 (Feed 2), multiphase-equilibrium calculations were performed in the three-phase and two-phase regions. Multiphase-equilibrium calculations were performed using the EOS model at 411.7 K and three pressures of 4000, 2998.4, and 2901.9 kPa. Tables 4-16 through 4-18 indicate that the C_4-bitumen system (i.e., Feed 2) lies in the L_1/L_2-, $L_1/L_2/V$-, and L_1/V-phase regions at 4000, 2998.4, and 2901.9 kPa, respectively. Two phases of L_2 and L_1 coexist at 4000 kPa, which is near operating pressure during the SAP operation. The L_2 phase is rich in C_4 and has a higher mol fraction of C_4 than has L_1. The L_1 phase contains more hydrocarbon PCs than L_2. The vapor phase, which is nearly pure C_4, appears in the three-phase region (Table 4-17). It is also observed that by decreasing pressure from 4000 to 2998.4 kPa, the mol fractions of PC_1 and PC_2 increase in the L_2 phase. In contrast, the mole fractions of PC_3 and PC_4 decrease in the L_2 phase. This indicates the extraction of heavier

components at higher pressures by C_4, which is consistent with the darker color of the L_2 phase at higher pressures compared with that at lower pressures (Figure 4-13a). The lower boundary of the three-phase region could not be measured because the volume of the PVT cell is limited. The EOS model predicts this boundary to be at 2910.2 kPa at 411.7 K and 1759.7 kPa at 382 K. The results of phase-equilibrium calculations at 411.7 K and 2901.9 kPa show that at the lower boundary of the three-phase region, the L_1 and L_2 phases merge together in the presence of the vapor phase (Table 4-18).

Table 4-16: Composition and mole fraction of equilibrium phases at 411.7 K and 4000 kPa for Clearwater bitumen-C_4 system with 84.6 wt.% C_4 (Feed 2)

Feed-2	Predictions from EOS model (T=411.7 K, P=4000 kPa)		
	zi	L_2	L_1
H_2O	0.0052	0.0052	0.0074
C_4	0.9733	0.9746	0.8243
PC_1	0.0112	0.0110	0.0307
PC_2	0.0059	0.0057	0.0373
PC_3	0.0029	0.0026	0.0438
PC_4	0.0014	0.0010	0.0565
Phase mole fraction		0.9917	0.0083

Table 4-17: Composition and mole faction of equilibrium phases at 411.7 K and 2998.4 kPa (three-phase region) for Clearwater bitumen-C_4 system with 84.6 wt.% C_4 (Feed 2)

Feed-2	Predictions from EOS model (T=411.7 K, P=2998.4 kPa)			
	zi	V	L_2	L_1
H_2O	0.0052	0.0094	0.0025	0.0032
C_4	0.9733	0.9903	0.9710	0.8373
PC_1	0.0112	0.0003	0.0162	0.0457
PC_2	0.0059	0.0000	0.0072	0.0472
PC_3	0.0029	0.0000	0.0025	0.0393
PC_4	0.0014	0.0000	0.00062	0.0273
Phase mole fraction		0.3830	0.5790	0.0379

Table 4-18: Composition and mole fraction of equilibrium phases at 411.7 K and 2901.9 kPa (lower boundary of three-phase region) for C_4-bitumen system with 84.6 wt.% C4 (Feed 2),

Feed-2	Predictions from EOS model (T=411.7 K, P=2901.9 kPa)		
	zi	V	L_1
H_2O	0.0052	0.0060	0.0017
C_4	0.9733	0.9937	0.8814
PC_1	0.0112	0.0004	0.0603
PC_2	0.0059	0.0000	0.0328
PC_3	0.0029	0.0000	0.0161
PC_4	0.0014	0.0000	0.0077
Phase mole fraction		0.8189	0.1811

4.3.8.2. Effect of Solvent Concentration on Phase Behavior of Solvent-Bitumen Systems:

The pseudo-ternary diagram of the CO_2-bitumen system at 413.2 K and 4000 kPa is presented in Figure 4-22a. Ternary diagrams are scaled based on mol% of components. It is observed that for CO_2 concentrations less than a certain value (i.e., 2.2 wt.% at 413.2 K and 4000 kPa) along the mixing line, a single L_1 phase exists. In this region, increasing the solvent concentration leads to more solvent dissolution in the L_1 phase. For greater CO_2 concentrations (w_{CO2}), the L_1 and V phases come into equilibrium. In this region, CO_2 solubility in the L_1 phase is not affected significantly by CO_2 concentration. Similar equilibrium regions exist for this system at higher temperature (i.e., 433.2 K). Cross-plots of CO_2 solubility and L_1-phase mol fraction are plotted as functions of solvent concentration in Figure 4-22b. For w_{CO2}> 2.2 wt.% in the CO_2-bitumen system, the V phase comes into equilibrium with the L_1 phase. In this two-phase region, additional solvent is vaporized into the V phase and the L_1-phase mol fraction reduces. Multiphase equilibria calculations indicate that as the temperature decreases from 453.2 K to 393.2 K at 4000 kPa, CO_2 solubility does not exceed 2.5 wt.%.

Figure 4-22a presents the pseudo-ternary diagram of C_3-bitumen system at 413.2 K and 4000 kPa. According to the CCE test results, maximum of two phases including a liquid (L_1) and vapor phase (V) co-exist in equilibrium in C_3-bitumen system. A similar behavior is also observed at higher temperatures. In the L_1 phase region, C_3 solubility increases with respect to C_3 concentration (w_{C3}). Figure 4-23 shows that at 413.2 K and 4000 kPa, increasing C_3 concentration beyond 10.3 wt.% has a negligible effect on C_3 solubility. For w_{C3}>10.3 wt.% in the C_3-bitumen system, the vapor phase comes into equilibrium with the L_1 phase, additional solvent remains in the vapor phase and the L_1 phase mol fraction decreases. EOS predictions indicate that as the temperature decreases from 453.2 K to 393.2 K at 4000 kPa, C_3 solubility does not exceed 14.9 wt.%. CO_2 solubility is much less than C_3 solubility at each temperature.

The pseudo-ternary diagram of the C_4-bitumen system at 4000 kPa and 413.2 K is presented in Figure 4-24a. For C_4 concentrations (w_{C4}) higher than a certain value along the mixing line, a second oleic phase rich in C_4 appears (L_2) and the system becomes two phase (i.e., L_1/L_2) at 413.2 K. In contrary to the CO_2- and C_3-bitumen systems, no V phase forms at this temperature. However, at 433.2 K, the L_2 phase

disappears and turns into the V phase. The difference between the two-phase region at 433.2 and 413.2 K is the concentration of the heavy PC (PC_2') in the second phase (i.e., L_2 or V). By increasing the temperature from 413.2 to 433.2 K, the concentration of heavy-hydrocarbon components (PC_2') in the second phase approaches zero. This indicates changing the second phase from the L_2 to the V phase. Another indicator is a decrease in the second-phase density by increasing the temperature from 413.2 to 433.2 K (i.e., 500 to 300 kg/m^3). As w_{C4} increases along the mixing line, the L_1 and V phases come into equilibrium at 433.2 K and 4000 kPa. The two-phase region slightly expands at 433.2 K compared with that at 413.2 K. This indicates that for the same concentrations, the solubility of C_4 decreases in the L_1 phase as temperature increases from 413.2 to 433.2 K. The results of multiphase-equilibrium calculations for the C_4-bitumen system at 4000 kPa and 413.2 K are presented in Figure 4-24b. A single L_1 phase exists for a wide range of w_{C4} (0 to 59.6 wt.%), where increasing w_{C4} increases the C_4 solubility. When the C_4 concentration reaches 59.6 wt.%, the L_2 phase begins to form. At w_{C4}>59.6 wt.%, C_4 solubility decreases in the L_1 phase because of the distribution of C_4 between the two oleic phases. By increasing w_{C4} to more than 59.6 wt.%, C_4 condenses into the L_2 phase and the L_1-phase mol fraction decreases (Figure 4-24b). By increasing w_{C4} to more than 59.6 wt.%, bitumen upgrading occurs and the less-viscous L_2 phase can also be produced.

The results of multiphase-equilibrium calculations for C_4-bitumen at 433.2 K and 4000 kPa are presented in Figure 4-25. At this condition, the V phase appears for C_4 concentrations greater than 38 wt.%. In addition, C_4 solubility is not affected significantly by increasing w_{C4} in this two-phase region (i.e., L_1/V). Figure 4-25 shows that in the two-phase region, increasing C_4 concentration leads to more C_4 vaporization into the vapor phase and reduction in the L_1-phase mol fraction. Comparing Figure 4-24b with Figure 4-25 indicates that when the L_2 phase coexists in equilibrium with the L_1 phase, increasing w_{C4} leads to significant C_4 condensation in the L_2 phase and a sharp reduction in both the L_1-phase mole fraction and C_4 solubility. However, when a vapor phase exists in equilibrium with the L_1 phase, increasing w_{C4} leads to a smoother reduction in the L_1-phase mole fraction and insignificant effect on C_4 solubility. Therefore, additional C_4, which leads to the formation of the L_1/L_2 or L_1/V two-phase regions, might have more affinity to exist in the L_2 phase than in the V phase.

The C_4-bitumen system exhibits liquid-liquid (L_1-L_2) phase equilibrium for T<421.2 K, which is not observed for the C_3 and CO_2 systems when 393.2 K<T<453.2 K. This shows C_4 potential for dissolution of intermediate hydrocarbon components into a solvent-rich liquid phase which does not occur for the other two solvents. Multiphase equilibrium calculations for 393.2 K<T<453.2 K indicates that C_4 solubility in bitumen reaches up to 60 wt.%, which is much higher than the maximum solubility of CO_2 (i.e, 2.5 wt.%) and C_3 (i.e., 14.9 wt.%) in the same temperature range.

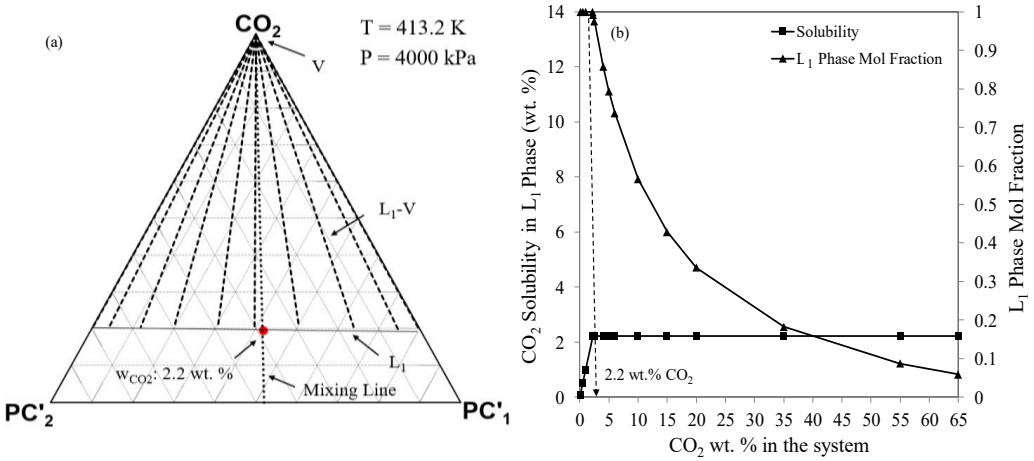

Figure 4-22: a) Pseudo-ternary diagram for CO_2-bitumen system at 4000 kPa and 413.2 K and effect of CO_2 concentration on b) solubility and liquid phase mole fraction at 413.2 K and 4000 kPa from EOS predictions

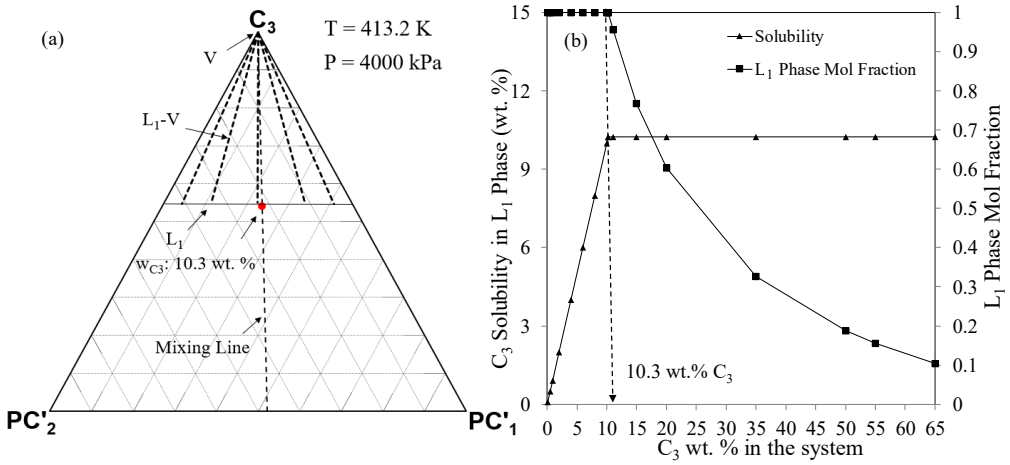

Figure 4-23: a) Pseudo-ternary diagram for C_3-bitumen system at 4000 kPa and 413.2 K and effect of C_3 concentration on b) solubility and liquid phase mole fraction at 413.2 K and 4000 kPa from EOS predictions

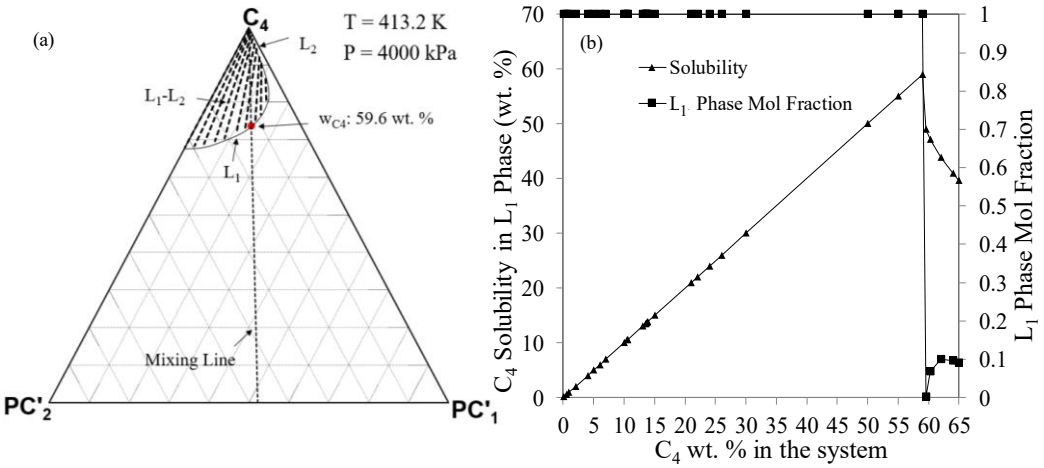

Figure 4-24: a) Pseudo-ternary diagram for C_4-bitumen system at 4000 kPa and 413.2 K and effect of C_4 concentration on b) solubility and liquid phase mole fraction at 413.2 K and 4000 kPa from EOS predictions

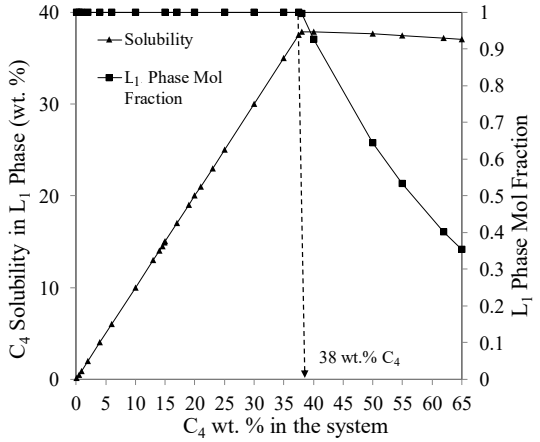

Figure 4-25: Effect of C_4 concentration on solubility and liquid phase mole fraction at 433.2 K and 4000 kPa from EOS predictions

4.4 SUMMARY

We characterized the multiphase behavior of CO_2-, C_3-, and C_4-bitumen systems by conducting CCE tests on Clearwater bitumen from the Cenovus Osprey Pilot. A PR-EOS model was regressed to data from the CCE tests to predict solvent solubility at reservoir pressure and different temperatures.

1. Experimental data of CO_2-bitumen, C_3-bitumen and C_4-bitumen systems and multiphase-equilibrium calculations indicate that C_4 has much higher solubility in bitumen than C_3 and CO_2 at reservoir pressure and elevated temperatures.

2. The C_4-bitumen CCE tests show the development of a secondary oleic phase (L_2) at 84.6 wt.% C_4. Three phases exist in equilibrium: a C_4-lean oleic phase (L_1) containing the highest amount of heavy-hydrocarbon components, a light (C_4-rich) oleic phase (L_2), and a vapor (V) phase that is almost pure C_4.

3. CCE test observations indicate the extraction of heavier components by the L_2 phase at higher pressures. The L_2 phase becomes darker by extracting heavier hydrocarbon components from the L_1 phase.

4. Compositional analysis and asphaltene-content measurement of the samples from the L_1 and L_2 phases indicate that C_4 can upgrade bitumen by extracting light-hydrocarbon components into the L_2 phase. This potential of C_4 for dissolving hydrocarbon components into a lighter C_4-rich liquid phase was not observed in the cases of C_3 and CO_2.

5. According to the experimental results, the C_4-bitumen system exhibits liquid/liquid separation at T<148 ºC. The EOS model indicates two types of two-phase regions for the C_4-bitumen system (L_1/L_2 in 120 ºC<T<148 ºC and L_1/V in 148 ºC<T<180 ºC). C_4 solubility increases significantly by increasing the concentration up to the value where the V/L_2 phase forms. However, by the appearance of the L_2 phase, a reduction in C_4 solubility occurs. Also, when the vapor phase forms, C_4 solubility cannot be increased further.

6. EOS predictions show that mixing the same molar percentage of CO_2, C_3 and C_4 with bitumen at constant temperature results in more bitumen swelling by C_4 and C_3 than CO_2. Bitumen swelling by dissolution of a specific amount of C_3 in bitumen is similar to that by C_4. Since C_4 solubility is much higher than C_3 solubility at a specific SAP condition, C_4 will result in higher swelling than C_3.

7. Multiphase equilibrium calculations at 120°C<T<180°C and 4000 kPa indicate that maximum C_4 solubility in bitumen (i.e., 60 wt.%) is higher than the maximum solubility of CO_2 (2.5 wt.%) and C_3 (14.9 wt.%) in bitumen.

8. CCE results and EOS predictions show that only liquid-vapor (L_1-V) equilibrium forms for CO_2-bitumen C_3-bitumen system. Simulated distillation results show that the L_1 phase from the C_4-bitumen CCE test is heavier than the L_1 phase from the C_3-bitumen CCE test and both are heavier than the original bitumen. Although C_3 may cause formation of asphaltene in the L_1 phase, C_4 can extract lighter hydrocarbon components into a C_4-rich liquid phase (L_2), resulting in a heavier liquid phase (L_1). The extracting-condensing mechanism and asphaltene precipitation result in a lighter L_1 phase in C_3-bitumen system than that in C_4-bitumen system.

9. C_3 and C_4 cause more asphaltene precipitation than CO_2. One reason can be an increase in the ratio of saturate to asphaltene of solvent-bitumen system by introducing C_3 and C_4 compared with CO_2. Another reason can be the higher solubility of C_3 and C_4 than CO_2 in bitumen. Mixing a high amount of C_3 with bitumen (i.e., 78.3 wt.% C_3) causes significant asphaltene precipitation in the L_1 phase. C_3 has more potential for asphaltene precipitation than C_4, and asphaltene precipitation by C_3 increases significantly by increasing C_3 dissolution. Application of C_3 and C_4 at high concentrations may cause asphaltene precipitation in solvent-based and solvent-aided thermal methods.

4.5 NOMENCLATURE

AARD	Average absolute relative deviation
ARR	Asphaltene-Resin Ratio
BIP	Binary interaction parameter
CII	Colloidal Instability Index
CN	Carbon number
EOS	Equation of State
MW	Molecular weight
PC	Pseudo component
PR-EOS	Peng-Robinson equation of state
P-V	Pressure-volume
R	Gas constant (J/kgmol.K)
SG	Specific gravity
SF	Swelling factor
TSC	Threshold solvent concentration (weight fraction)
V	Vapor phase

Greek symbols

ω	Acentric factor
Φ	Volume fraction
ν	Kinematic viscosity (m^2/s)
μ	Dynamic viscosity (cP)
ρ	Density (kg/m^3)

Roman symbols

C_T	Isothermal compressibility factor (kPa^{-1})
K_w	Watson characterization factor ($K^{1/3}$)
L_1	Oleic phase rich in bitumen
L_2	Oleic phase rich in solvent
P_{sat}	Saturation pressure (kPa)
P_r	Reservoir Pressure (kPa)
Pc	Critical pressure (kPa)
T_b	Boiling point temperature (K)
Tc	Critical temperature (K)
Vc	Critical volume ($cm^3/gmol$)
Vm	Molar volume ($m^3/kgmol$)
w	Weight fraction
x	Mole fraction
z	Overall mole fraction

Chapter 5: Viscosity of Solvent-Bitumen Systems

5.1 INTRODUCTION

Light solvents such as CO_2, C_3, and C_4 may also be efficient for reducing heavy oil viscosity and improving oil recovery (Gupta et al., 2001; Saner and Patton 1986; Butler and Mokrys, 1993; Mohammed-Singh and Singhal 2005; Sahin et al. 2008; Kariznovi 2013; Badamchi-Zadeh et al., 2009; Eghbali and Dehghanpour, 2018). An experimental pore scale study showed bitumen dilution and production by hot C_3 and C_4 in a condensing front (Xu et al., 2018). The dilution of bitumen with solvent drastically reduces bitumen viscosity (Miadonye et al., 2001). Therefore, it is necessary to measure viscosity of the diluted bitumen and obtain a viscosity model based on experimental data at high temperatures. In this section we present experimental and modelling studies on viscosity of solvents-bitumen mixtures from literature.

5.1.1 Liquid-Phase Viscosity Measurements

Viscosity of bitumen diluted with light hydrocarbon solvents has been measured and reported in literature. Table 5-1 summarizes the viscosity experiments for mixtures of light solvents and heavy oil/bitumen available in the literature. Similarly, the pressure and temperature effects on bitumen viscosity saturated with N_2, CO, CO_2, C_1, C_2, C_3, and C_4 have been previously studied (Mehrotra, and Svrcek, 1982; 1988; Kariznovi et al., 2014; Frauenfeld et al., 2002; Bazyleva, 2013).

Badamchi-Zadeh et al. (2009) measured the viscosity of Athabasca bitumen saturated with C_3 between T=10°C and T=50°C. Freitag et al. (2005) measured the viscosity of a C_3-Lloydminster oil system at T<30°C and $P<P_{sat,C3}$. Yazdani and Maini (2010) measured the viscosity of a C_4-Frog Lake (Lloydminster) heavy oil system at room temperature and $P<P_{sat,C4}$. Mehrotra and Svrcek (1982) measured viscosity for C_1-Athabasca mixtures for temperatures up to 100°C. Mehrotra and Svrcek (1988) also reported the saturated phase viscosity for C_1-Cold Lake bitumen mixtures in the temperature range of 15 to 103°C. Behzadfar (2014) measured the rheological

response of the bitumen–CO_2 mixture using the method of the reduced variables to study the effects of temperature, pressure, dissolved CO_2 and shear rate on saturated bitumen viscosity.

Viscosity of Athabasca bitumen saturated with CO_2 and C_4 was measured at T<190°C (Nourozieh et al., 2014; 2016). Kariznovi (2013) and Nourozieh (2013) measured viscosity of C_1- and C_3-Surmont bitumen systems for T<190°C, respectively.

Table 5-1: Summary of the viscosity measurements available in literature for mixtures of light solvents and heavy oil/bitumen

Solvent	Heavy oil/Bitumen	Temperature range (°C)	Reference
N_2, CO_2, C_1	Athabasca mixtures	25<T<100	(Mehrotra and Svrcek, 1982)
CO_2	Marguerite lake	12<T<103	(Mehrotra and Svrcek, 1984)
N_2, CO, CO_2, C_1, C_2	Peace river	16<T<107	Mehrotra and Svrcek, 1985; 1985b; 1985c)
N_2, CO_2, C_1, C_2, CO_2-C_1 mixture and CO_2-C_2 mixture	Cold lake	15<T<103	(Mehrotra and Svrcek, 1988)
C_2, C_3	Cold Lake/Lloydminster oil	15	(Frauenfeld et al., 2002)
C_1	Alasca heavy oil	T<60	(Bazyleva et al., 2013)
C_3	Athabasca bitumen	10<T<50	(Badamchi-Zadeh, et al. 2009)
C_3	Lloydminster oil	T=15 C and T=28 C	(Freitag et al., 2005)
C_4	Frog Lake	T=22	(Yazdani and Maini, 2010)
C_1, C_3, C_4	Surmont bitumen	T<190	(Kariznovi, 2013; Nourozieh, 2013)
CO_2, C_1, C_4	Athabasca bitumen	T<190	Nourozieh et al., 2014; 2016).

5.1.2 Viscosity Correlations and Mixing Rules

In addition to the experimental measurements, various correlations for the viscosity of diluted bitumen have been developed (see Table 5-2). Mehrotra (1992) developed a mixing rule for predicting the viscosity of bitumen saturated with pure gases of N_2, CO, CO_2, C_1 and C_2. Miadonye et al. (1995) developed a viscosity correlation to predict the viscosity-temperature relationship for bitumen samples mixed with diluents. These diluents include Great Canadian Oil-sand Company (GCOS) synthetic crude, Mobil solvent, and naphtha. Motahhari et al. (2011) correlated viscosity of bitumen-condensate mixtures using an expanded fluid viscosity model where viscosity is related to fluid density at any pressure and temperature.

The existing mixing rules in literature for estimating viscosity of liquid mixtures use the viscosity of individual components in the mixture. In these rules, the mixture viscosity is estimated by combining the viscosities of pure components using mol, weight or volume fraction of components. The most common mixing rule is logarithmic (Arrhenius) mixing rule. This mixing rule obtains viscosity of a liquid

mixture by averaging the logarithm of the viscosity of each component (Arrhenius, 1887). Viscosity predictions by logarithmic mixing rule is known to be unreliable for mixtures of heavy oil and bitumen with solution gas (such as C_1) and solvents (Ardali et al., 2010). Other viscosity models use the inverse (Bingham, 1918) or cube root (Kendall and Monroe, 1917 of the viscosity of each component. These mixing rules are reliable for low oil to solvent viscosity ratios (i.e., 1 to 100) which is way lower than the viscosity ratio of heavy oil-solvent systems (i.e., more than 1000) (Shu, 1984; Yazdani and Maini, 2010). Guan (2013) regressed Power-Law (Kendall and Monroe, 1917) and Lederer (1933) correlations against measured viscosity of toluene-, and xylene-Athabasca bitumen for temperatures of less than 345 K. Due to the observed deviations between literature models and experimental data, more complex mixing rules were proposed (Shu, 1984; Mehrotra et al., 1989a; Lobe, 1973; Cragoe, 1933). Most of these models use correlations tuned against a dataset of diluted crude oils which require density of the solvent-oil mixture.

Compositional viscosity models such as the corresponding states model (Pedersen and Fredenslund, 1987) and the LBC model (Lohrenz et al., 1964) have been commonly implemented in reservoir simulators. However, these models cannot be used to predict the viscosity of heavy oil and heavy oil-solvent mixtures since they were developed for light/moderate oils (Yazdani and Maini, 2010; Motahhari et al., 2013). To perform heavy oil reservoir simulation, it is required to measure the viscosity of heavy oil-solvent systems and fit a correlation to the data. For numerical simulation studies, logarithmic mixing rules have been used. Viscosities of pure solvents in liquid state have been fitted to pseudo-viscosities to match the viscosity data of solvent-oil mixture using the logarithmic mixing rule and the pure solvent viscosities (Ardali et al., 2010; Deng et al., 2010; Ashrafi et al., 2011). The considerable difference between pseudo-viscosity and actual viscosity of solvents in gas or liquid state can lead to uncertain simulation results. For example, fitting C_3liquid viscosity to honor live oil (C_3-diluted oil) viscosity data may not properly represent liquid C_3 properties.

Successful implementation of SAP requires accurate measurement and modelling of phase behavior and viscosity data at reservoir conditions. To the best of our knowledge there are limited studies that report the measured viscosity of CO_2-, C_3-, and C_4-Cold Lake bitumen systems under SAP operating conditions. Although

related laboratory studies have been published during the last decade (Kariznovi, 2013; Freitag et al., 2005; Nourozieh et al., 2014) the effects of light solvents on solvent-bitumen viscosity at various solvent concentrations during SAP is not well understood.

This study investigates the effects of dissolving CO_2-, C_3- and C_4 solvents in bitumen on viscosity of solvent-bitumen system at varying concentrations and high temperatures. This is achieved by measuring and modelling the system's viscosity. Also, we estimate a threshold concentration for each solvent above which additional solvent above which has insignificant effect on reducing viscosity of solvent-bitumen system.

Table 5-2: Viscosity correlations and mixing rules for predicting viscosity of liquid mixtures

Viscosity Correlations and Mixing Rules	Reference
Correlations	
$[(\mu-\mu^*)\zeta+10^{-4}]^{1/4}=0.1023+0.023364\rho_r+0.058533\,\rho_r^2-0.40758\rho_r^3+0.0093324\,\rho_r^4, \zeta=\frac{(\sum_{i=1}^{n}x_iT_{c,i})^{\frac{1}{6}}}{(\sum_{i=1}^{n}x_iM_i)^{\frac{1}{2}}(\sum_{i=1}^{n}x_iP_{c,i})^{\frac{2}{3}}}, \mu^*=\frac{\sum_{i=1}^{n}x_i\mu_i^{pure}\sqrt{M_i}}{x_i\sqrt{M_i}}, \mu_i^{pure}\zeta_i=34\,(10^{-5})T_{ri}^{0.94}$ for $T_{ri}<1.5$ and $\mu_i^{pure}\zeta_i=17.78\,(10^{-5})(4.58T_{ri}-1.67)^{\frac{5}{8}}$ for $T_{ri}>1.5, T_{ri}=\frac{T}{T_{ci}}, \zeta_i=\frac{T_{c,i}^{\frac{1}{6}}}{M_i^{\frac{1}{2}}p_c^{\frac{2}{3}}}, \rho_r=\frac{\rho}{\rho_c}, \rho_c=\frac{1}{\sum_{i=1}^{n}x_iV_{c,i}}$, T [K], P [atm]	(Lohrenz et al., 1964)
$\log\log(\mu)=a_1+a_2T+a_3P+\frac{a_4P}{T}$	(Mehrotra and Svrcek, 1982)
$\frac{\mu_{mix}(T,P)}{\mu_{ref}(T_{ref},P_{ref})}=(\frac{T_{C,mix}}{T_{C,ref}})^{-1/6}(\frac{P_{C,mix}}{P_{C,ref}})^{2/3}(\frac{M_{w,mix}}{M_{w,ref}})^{1/2}(\frac{\lambda_{mix}}{\lambda_{ref}})^{1/2}, M_{w,mix}=b_1(M_{w,w}^{b_2}-M_{w,n}^{b_2})+M_{w,n}, \lambda=1+b_3\rho_r^{b_4}M_w^{b_5}$, ref: methane,	(Pedersen and Fredenslund, 1987)
$\log(\mu+0.8)=\sum_{i=1}^{n}\upsilon_i\log(\mu_i+0.8)+\sum_{i=1}^{n}\sum_{j=1}^{n}\upsilon_i\upsilon_jB_{ij}, \upsilon_i=x_i(\frac{M_{w,i}}{\sum_{i=1}^{n}x_iM_{w,i}})^{0.5}$	(Mehrotra, 1992)
$\log\mu(pa.s)=\frac{b}{1+(\frac{T(°C)-30}{303.15})^S}+C, S=0.0066940\,b+3.5364, C=-3.002, b=\log\mu(\text{at }30\,°C\text{ and }1\text{ atm})-C$	(Miadonye et al., 1995)
$\mu-\mu_{G,mix}=0.165(\exp(c_{2,mix}\beta)-1), \beta=\frac{1}{\exp((\frac{\rho_{s,mix}^*}{\rho_{mix}})^{0.65}-1)}, \rho_{s,mix}^*=\frac{\rho_{s,mix}^o}{\exp(-c_{3,mix}P)}, \rho_{s,mix}^o=\left(\sum_{i=1}^{n}\frac{w_i}{\rho_{s,i}^o}\right)^{-1}, \frac{c_{2,mix}}{\rho_{s,mix}^o}=\sum_{i=1}^{n}w_i\frac{c_{2,i}}{\rho_{s,i}^o}, c_{3,mix}=\left(\sum_{i=1}^{n}\frac{w_i}{c_{3,i}}\right)^{-1}, \mu_{G,mix}=\sum_{i=1}^{n}\frac{x_i\mu_{i,G}^{pure}}{\sum_{j=1}^{n}x_j\varphi_{ij}}, \varphi_{ij}=\frac{[1+(\frac{\mu_{i,G}^{pure}}{\mu_{j,G}^{pure}})^{0.5}(\frac{M_{w,i}}{M_{w,j}})^{0.25}]^2}{\left[8\left(1+\frac{M_{w,i}}{M_{w,j}}\right)\right]^{0.5}}$, T[K], P[kPa], $\rho[\frac{kg}{m3}]$	(Motahhari et al., 2011)
Mixing rules	
$\log\mu=V_s\log\mu_s+V_o\log\mu_o$	(Arrhenius, 1887)
$\mu^{\frac{1}{3}}=w_A\mu_A^{\frac{1}{3}}+w_B\mu_B^{\frac{1}{3}}$	(Kendall and Monroe, 1917)
$\mu=(w_s\mu_s^n+w_o\mu_o^n)^{\frac{1}{n}}$	(Kendall and Monroe, 1917)
$\frac{1}{\mu}=\frac{V_s}{\mu_s}+\frac{V_o}{\mu_o}$	(Bingham, 1918)
$\ln\mu=\frac{\alpha V_s}{\alpha V_s+V_o}n\,\mu_s+(1-X_o)\ln\mu_o$	(Lederer, 1933)
$\mu=5\times10^{-4}\exp\left(\frac{1000\ln 20}{L}\right), L=w_s\mu_s+w_o\mu_o$	(Cragoe, 1933)
$\vartheta=V_s\vartheta_se^{V_o\alpha_o}+V_o\vartheta_oe^{V_s\alpha_s}, \alpha_s=-1.7\frac{\ln\vartheta_s}{\vartheta_s}, \alpha_o=0.27\ln\frac{\vartheta_o}{\vartheta_s}+\left(1.3\ln\frac{\vartheta_o}{\vartheta_s}\right)^{\frac{1}{2}}$	(Lobe, 1973)
$\ln\mu=\frac{\alpha V_s}{\alpha V_s+V_o}\ln\mu_s+(1-X_o)\ln\mu_o, \alpha=17.04\Delta\rho^{0.5237}\rho_s^{3.2745}\rho_o^{1.63167}$	(Shu, 1984)

$\ln \mu = (1 - X_s) \ln \mu_o + \frac{V_s}{\alpha V_o + V_s} \ln \mu_s \quad , \alpha = 0.255\gamma^{-4.16} T_r^{1.85} \left[\frac{e^{7.36} - e^{7.36(1-P_r)}}{e^{7.36}-1}\right], T_r = \frac{T[°R]}{547.57}, P_r = \frac{P[psia]}{1071}$ (Chung et al., 1988)

5.2 METHODOLOGY

Systematic laboratory and modelling approaches were utilized to investigate the effects of light solvents on bitumen viscosity at elevated temperatures. This approach comprises four key steps. First, we predict solubility (i.e., solvent mol fraction in the oil phase) of the solvents in bitumen using the EOS model calibrated against measured experimental data from Chapter 4. Second, we measure the viscosity of CO_2-, C_3-, and C_4-bitumen mixtures at various temperatures and solvent solubilities. Third, we calibrate the existing modified logarithmic mixing rule (Monnery, 1995; CMG, 2013) against the measured viscosities. This calibration is performed by tuning two parameters in the modified viscosity model. Also, we measure the viscosity of C_1-bitumen system. Then we extend application of the viscosity model for systems including bitumen and light hydrocarbons from C_1 to C_4. For this purpose, we perform a linear regression for the tuned parameters of the viscosity model versus carbon number of the hydrocarbon solvents. Then we interpolate the model parameters for C_2-bitumen mixtures. Fourth, we apply the calibrated EOS and the viscosity model to estimate threshold concentration for each solvent in solvent-bitumen systems at SAP conditions.

5.2.1 Viscosity Measurements of Solvent-Bitumen Mixtures

Here, we measure the viscosity of CO_2-, C_3-, and C_4-Clearwater bitumen mixtures over a wide range of solvent solubilities and temperatures using the set-up illustrated in Figure 5-1. The set-up includes a high-pressure and high-temperature (HPHT) reactor. The reactor has a thermal jacket to maintain a constant temperature. Therefore, the reactor can be used to establish an equilibrium condition at constant pressure and temperature for a specific solvent-bitumen mixing ratio. The reactor is equipped with a mixer to accelerate equilibration. A controller provides readouts of the cell pressure and temperature. The internal volume of the reactor cell is 600 cc. The reactor is also equipped with a liquid sampler. A HPHT electromagnetic-based viscometer (ViscoPro 2000) is installed at the outlet of the liquid sampler. The viscometer is a flow-through sensor and capable of measuring viscosity in the range of 0.25–20,000 mPa.s and at pressures up to 14 MPa. The HPHT electromagnetic-based viscometer uses two magnetic coils within a 316 stainless steel sensor and a

magnetic piston inside the measurement chamber. The magnetic piston is surrounded by the fluid sample in the chamber. Two coils inside the sensor body are used to magnetically force the piston back and forth within a predetermined distance (about 0.2 inches/5.08 mm). By alternatively powering the coils with a constant force, the piston's round trip travel time is measured. This travel time is converted to the test fluid's viscosity with 1% accuracy of the piston full scale. The viscometer's temperature is maintained using a silicon oil bath. A backpressure regulator (BPR) at the viscometer's outlet is connected to a N_2 tank to apply backpressure during viscosity measurement.

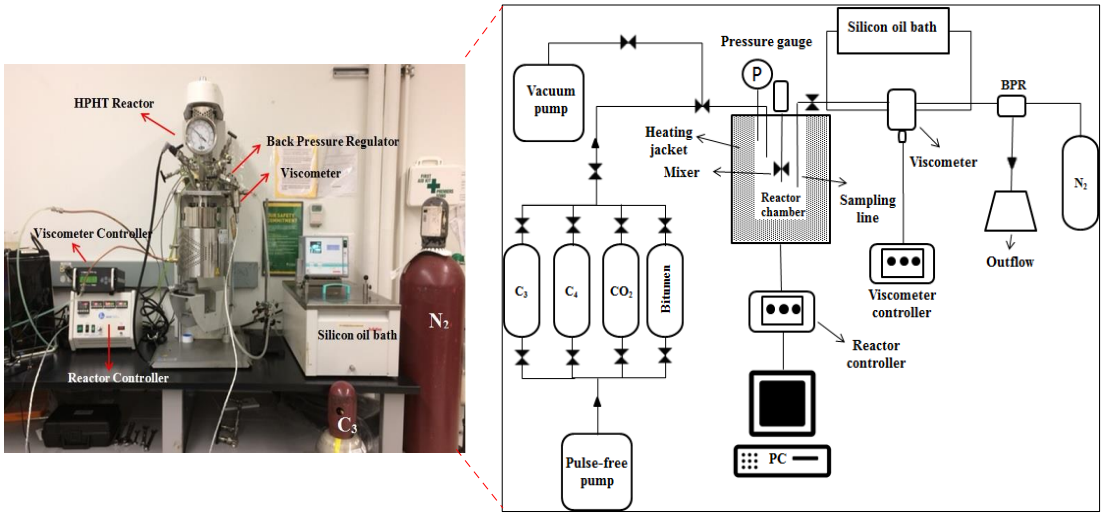

Figure 5-1: Schematic of the HPHT equipment for liquid phase viscosity measurement of solvent-bitumen systems

The cell was vacummed before the experiment. A specific amount of bitumen was injected into the cell. The cell temperature was held constant and a specific amount of solvent vapor was injected into the cell at the cell temperature and pressure below the saturation pressure of the solvent at that temperature ($P<P_{sat,solvent}$). The amount of injected vapor solvent was calculated based on the cell pressure right after injection, cell temperature, available cell volume for the vapor solvent and real gas equation of state. The solvent-bitumen mass ratio was designed to maintain vapor-liquid equilibrium in the reactor based on the Constant Composition Expansion (CCE) test results. The mixer was used to accelerate solvent dissolution and was turned off after 5 hours to allow the pressure to stabilize (i.e., equilibrium condition) prior to viscosity measurment. The regulator was set to a pressure less than the cell pressure to allow the liquid to flow through the sampler and viscometer. Immediately after observing flow through the regulator line, the sampler valve was closed and the pressure of the

regulator was set at the reactor pressure to ensure that the viscosity measurement was performed at the equilibrium conditions. Viscosity of the sample was recoreded by the data aquisition system and the mean of each 20 measurments was computed. Once the standard deviation of the readings with respect to the mean of previous 20 readings was less than 1%, the mean value was recorded. The temperatures of the reactor and viscometer were increased gradually up to 165°C and the viscosity of the equilibrated liquid phase was measured at almost constant pressure and several temperatures. At high temperatures, the viscometer piston was replaced with another caliberated piston for lower viscosities. Before changing the piston, the fluid inside the viscometer was drained, the viscometer was cleaned and a new sample was taken out of the cell, resulting in a reduction in the cell pressure. The amount of dissolved solvent in bitumen for each viscosity measurement was estimated by using the regressed EOS model at the cell pressure and the temperature.

5.2.2 Modelling Viscosity of Solvent-Bitumen Systems

In the conventional logarithmic mixing rule, mol fractions (x_i) act as weighting factors:

$$\ln \mu_L = \sum_{i=1}^{n} x_i \ln \mu_{iL} \tag{5-1}$$

The logarithmic mixing rule was modified by replacing the weighting factors with $N_k x_k$ for the binary systems of solvent and bitumen (Monnery, 1995; CMG, 2013):

$$\ln \mu_L = \sum_{i=k \text{ and } nk} N_i x_i \ln \mu_{iL} \tag{5-2}$$

Here, this model will be referred to as modified logarithmic mixing rule, where the components are partitioned into two groups of key and non-key components. Weighting factors are replaced with $N_k x_k$ for the key components and with $N_{nk} x_k$ for the non-key components; where N_k is a function of composition and N_{nk}s are equal. Similar to the logarithmic mixing rule, the summation of the modified weighting factors equals one (i.e. $\sum_{i=k \text{ and } nk} N_i x_i = 1$), and thus,

$$N_{nk} = \frac{1 - N_k x_k}{\sum_{i=nk} x_i} \tag{5-3}$$

The deviations (Venkatramani and Okuno, 2017) from the logarithmic mixing rule can be determined by:

$$N_k = 1 + \alpha_1[\frac{(1 - x_k) \times (1 - (1 - x_k)^{\alpha_2})}{x_k}] \quad (5\text{-}4)$$

Eq. 5-4 reduces to 1 when $\alpha_1 = 0$ and Eq. 5-2 reduces to the conventional logarithmic mixing rule (compare Eq. 5-1 and Eq. 5-2). Here, we optimized two tuning parameters for each solvent against the measured viscosity of solvent-bitumen mixture. In this optimization, we considered bitumen as the key component, and calculated the solvent's modified weighting factor from $\sum_{i=k \text{ and } nk} N_i x_i = 1$. μ_{iL} is the pure component's viscosity in the liquid state. Viscosity of the solvent in liquid state is required to calculate viscosity of the liquid phase. We obtained solvent viscosity in liquid state from the database of National Institute of Standards and Technology (NIST) (Linstrom and Mallard, 2017). For temperatures higher than solvent critical temperature, the solvent does not exist in liquid state and the corresponding liquid viscosity is hypothetical. Therefore, we estimated solvent liquid viscosity by extrapolation of the saturated liquid viscosities. We predicted bitumen viscosity using the correlation obtained in Chapter 4. The average error of the measurements is estimated from the following equation for each solvent-bitumen dataset.

$$\text{Error} = \frac{1}{N_{data}} \sum_{i=1}^{N_{data}} \frac{\text{Measurement Error } (=\frac{1}{100} * \text{full scale})_i}{\mu_i^{measured}} \quad (5\text{-}5)$$

Where full scale is the maximum measurable viscosity value by the magnetic piston which was used for the experiment.

5.2.2.1. Key Component in the Modified Viscosity Model

As we will show in Chapter 6, we use the modified viscosity model for predicting viscosity of the liquid phase of C_1-solvent-bitumen in reservoir flow simulation where the solvent is CO_2, C_3 or C_4. The modified model is verified against solvent-bitumen viscosity data. Therefore, we should ensure that the modifications on the logarithmic viscosity model will be applied only when solvent exists in the liquid phase. On the other hand, liquid phase viscosity of SAGD process should be calculated from logarithmic viscosity model. However, by adding solvent to the system, the modified viscosity model should be applied. As mentioned above, we considered bitumen as the key component for caliberation of the modified logarithmic viscosity model and we optimized α_1 and α_2 parameters against the measured data for each binary system of

solvent-bitumen. To apply this viscosity model in a commercial thermal simulator such as CMG, weighting factor of the key component (i.e., bitumen in this case) is generated as a function of the mol fraction of the key component in the oil phase (CMG, 2013). Weighting factors for the non-key components (i.e., C_1 and solvent) are assumed to be equal and are generated according to $\sum_{i=1}^{Nc} x_i N_i = 1$ constraint.

In the following we show that when the oil phase include C_1 in addition to the solvent and bitumen is the key component, C_1 weighting factor is always affected by bitumen weighting factor even if the solvent concentration is zero in the oil phase.

For SAGD with modified logarithmic viscosity model and bitumen as the key component, N_{C1} is calculated by simplifying $\sum_{i=1}^{Nc} x_i N_i = 1$ such that:

$$N_{C1} = \frac{1-x_b N_b}{1-x_b} \tag{5-6}$$

In Eq. 5-6, $N_b \neq 1$ for different values of x_b such that $N_{C1} \neq 1$. Therefore, the modified viscosity model cannot be converted to logarithmic model for the SAGD process when bitumen is the key component (and where $x_s = 0$). However, if the key component is the solvent (i.e., CO_2, C_3 or C_4) in the modified viscosity model, N_{C1} and N_b as the weighting factors of the non-key components are calculated as:

$$N_b = N_{C1} = \frac{1-x_s N_s}{1-x_s} \tag{5-7}$$

This equation is simplified to $N_b = N_{C1} = 1$ when $x_s = 0$. Therefore, modified logarithmic viscosity model converts to logarithmic model for the SAGD process. To avoid this inconsistency, we select solvent as the key component in the the modified logarithmic viscosity model and use the regressed the modified logarithmic viscosity model with solvent as the key component in the simulation.

5.2.3 Phase Behavior and Viscosity Calculations

As explained in Chapter 4, we performed multiphase equilibrium calculations using the calibrated PR-EOS and the developed algorithm presented in Chapter 3. Oil phase viscosity was calculated using Eq. 5-1 to Eq. 5-4 and the oil phase composition from the calibrated EOS predictions. Viscosity of the pure solvents in the liquid state at each temperature was obtained from the database of NIST (Linstrom and Mallard, 2017).

For temperatures above the solvent's critical temperature (where the corresponding liquid viscosity is hypothetical), solvent viscosity was estimated by extrapolating the saturated liquid viscosities at subcritical conditions.

5.2.3.1. Threshold Solvent Concentration

We define Threshold Solvent Concentration (TSC) as the concentration above which there is less than 0.3% normalized viscosity reduction per mol percent of solvent:

$$\frac{\mu_{x1,T}-\mu_{x2,T}}{\mu_{x=0,T}\times(x_2-x_1)} < 0.3 \quad (5\text{-}8)$$

Where x_1 and x_2 are solvent mol fractions in the solvent-bitumen system.

We estimate the TSC value for each solvent using the EOS and a modified viscosity model which will be presented in Section 5.3.2. The TSC values were evaluated at different temperatures based on the cross-plots of solvent solubility and bitumen viscosity versus solvent concentration. Then, the minimum TSC was selected among all TSC values in the temperature range of 120ºC<T<180ºC for each solvent. To achieve this, we use the multiphase equilibrium calculations which were performed along a mixing line at 4000 kPa and 120°C<T<180°C in Chapter 4. Then, the effect of solvent concentration on solvent solubility and L_1 phase viscosity in CO_2-, C_3- and C_4-bitumen systems was investigated using the multiphase equilibrium calculations and the modified viscosity model to estimate TSC value at each temperature for each system. Subsequently, the minimum TSC was selected among all TSC values in the temperature range of 120ºC<T<180ºC for each solvent.

5.3 RESULTS AND DISCUSSION

5.3.1 Viscosity Measurement of Solvent-Bitumen Systems

We measured viscosity of CO_2-, C_1-, C_3-, and C_4-Clearwater bitumen systems in the temperature range of 50°C to 165°C at different solvent concentrations (Figures 5-2a to 5-2d). The measured data are presented in Tables 5-3 to 5-6. The average error of the measurements estimated from Eq. 5-5 is less than 4% for each solvent-bitumen dataset.

Figures 5-2a to 5-2d show that at the same solubility, C_3 and C_4 dissolution results in greater viscosity reduction than C_1 and CO_2 dissolution. Bitumen viscosity can be reduced by 26%, 33% and 38% through the dissolution of 10% mol CO_2, C_3

and C_4 , respectively in bitumen at 140°C. As Figures 5-2a to 5-2d show, the profiles of ln μ versus solvent solubility have higher slopes for C_4- and C_3-bitumen mixtures compared to those for CO_2- and C_1-bitumen mixtures at low temperatures (i.e. T=50°C and 80°C). Therefore, the differences between the effects of solvents on viscosity reduction is more pronounced at lower temperatures. For our solvent-bitumen systems, the reduction in viscosity relative to dead oil is more pronounced at lower temperatures. At low temperatures, the solubility of solvent plays a significant role in viscosity reduction in addition to the temperature effect. At high temperatures, the effect of solvent dissolution is masked by the significant effect of increasing temperature on reducing the dead oil viscosity. Bitumen viscosity can be reduced by 45% and 38% by dissolution of 10% mol C_4 in bitumen at 80°C and 140°C, respectively.

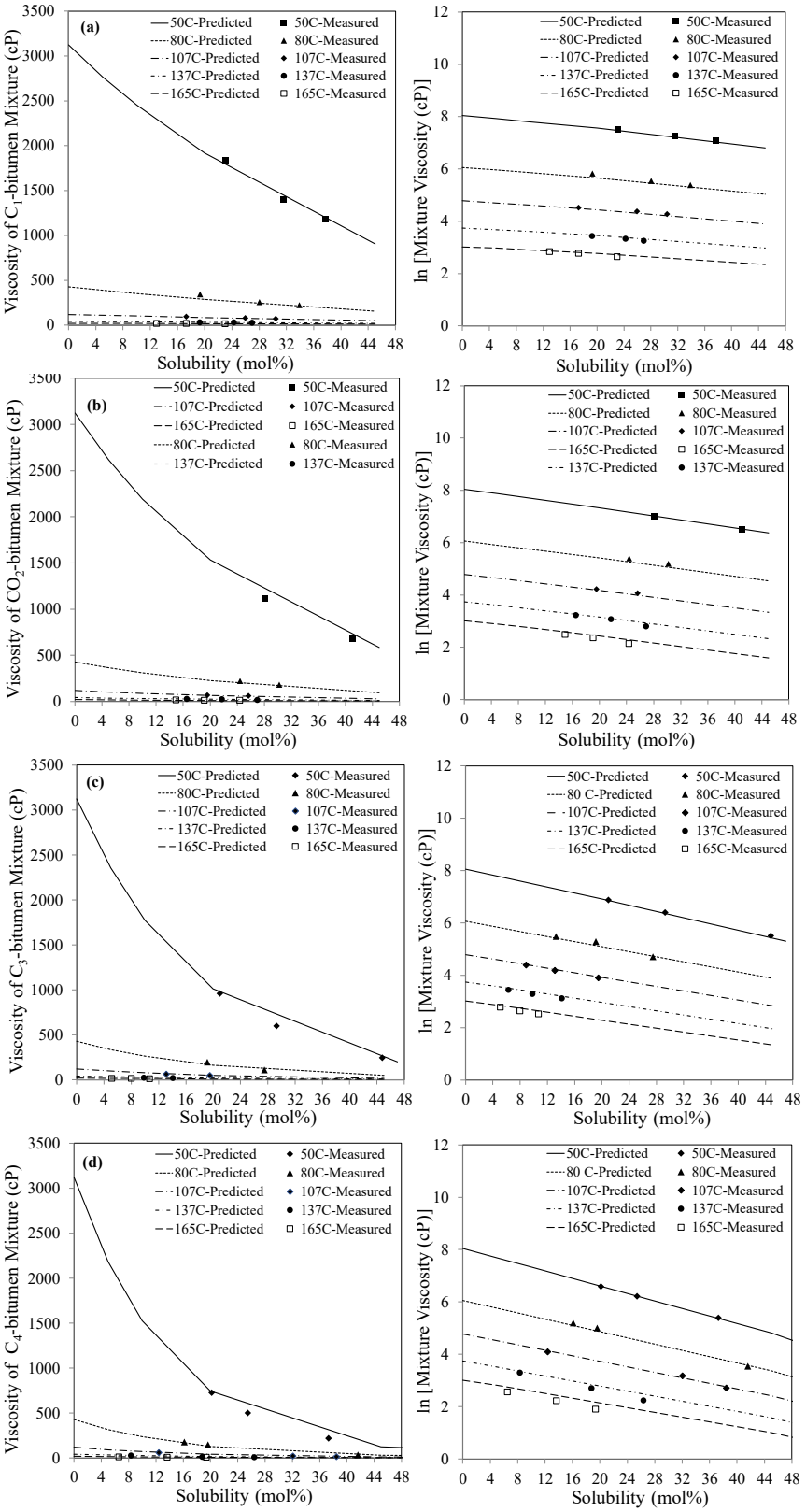

Figure 5-2: Measured and predicted viscosity of the equilibrated liquid phase formed from interactions of bitumen with a) C_1 b) CO_2 c) C_3 and d) C_4. Viscosities are predicted using the modified logarithmic mixing model

Table 5-3: Viscosity of saturated bitumen with CO_2

T (°C)	P (kPa)	μ(cP)	x_s	T (°C)	P (kPa)	μ(cP)	x_s
50	0	3124	0.00	117	3253	48	0.19
50	2812	1109	0.28	117	4432	41	0.24
50	4473	676	0.41	127	0	59	0.00
60	0	1481	0.00	127	3253	35	0.17
60	2812	648	0.25	127	4432	30	0.23
60	4473	457	0.38	137	0	42	0.00
73	0	639	0.00	137	3253	25	0.17
73	800	320	0.22	137	4432	22	0.22
73	4473	209	0.35	137	5804	16	0.27
80	0	428	0.00	147	0	33	0.00
80	3309	240	0.24	147	3253	19	0.16
80	4473	200	0.30	147	4432	16	0.21
88	0	281	0.00	147	5804	12	0.26
88	3481	159	0.23	155	0	26	0.00
88	4432	140	0.29	155	3253	16	0.15
98	0	176	0.00	155	4432	13	0.20
98	3481	99	0.21	155	5804	10	0.25
98	4432	88	0.27	165	0	20	0.00
107	0	119	0.00	165	3253	12	0.15
107	3253	68	0.20	165	4384	10	0.19
107	4432	59	0.26	165	5804	8	0.24
117	0	82	0.00	-	-	-	-

Table 5-4: Viscosity of saturated bitumen with C_1

T (°C)	P (kPa)	μ(cP)	x_s	T (°C)	P (kPa)	μ(cP)	x_s
50	5480	1835	0.23	117	8030	60	0.25
50	8110	1400	0.32	117	10340	50	0.31
50	10310	1180	0.38	127	4550	48	0.15
60	8160	780	0.30	127	8000	40	0.25
60	5780	900	0.23	137	6120	31	0.19
73	5520	420	0.21	137	8000	28	0.24
73	8160	370	0.29	137	9050	26	0.27
80	5140	340	0.19	147	4740	24	0.15
80	8070	255	0.28	147	7680	20	0.23
80	10270	220	0.34	147	9050	18	0.26
98	10950	105	0.34	155	4050	20	0.13
98	8020	125	0.26	155	7760	16	0.23
107	4970	92	0.17	166	7890	14	0.23
107	8070	80	0.26	166	4110	17	0.13
107	9660	72	0.30	166	5680	16	0.17

Table 5-5: Viscosity of saturated bitumen with C_3

T (°C)	P (kPa)	μ(cP)	x_s	T (°C)	P (kPa)	μ(cP)	x_s
50	358	960	0.21	107	793	49	0.20
50	510	600	0.29	117	352	56	0.08
50	806	245	0.45	117	545	45	0.12

60	358	577	0.17	117	793	34	0.17
60	806	210	0.38	127	352	43	0.07
73	358	290	0.14	127	558	36	0.11
73	806	130	0.30	127	786	29	0.15
80	358	240	0.13	137	352	31	0.06
80	545	198	0.19	137	545	27	0.10
80	793	110	0.27	137	786	23	0.14
88	358	180	0.12	147	558	22	0.09
88	545	150	0.17	147	786	18	0.12
88	793	90	0.25	155	345	20	0.05
98	358	113	0.10	155	558	18	0.08
98	545	94	0.15	155	786	16	0.12
98	793	70	0.21	165	345	16	0.05
107	352	80	0.09	165	545	14	0.08
107	545	65	0.13	165	786	12	0.11

Table 5-6: Viscosity of saturated bitumen with C_4

T (°C)	P (kPa)	μ(cP)	x_s	T (°C)	P (kPa)	μ(cP)	x_s
50	138	727	0.20	117	793	12	0.33
50	172	503	0.25	127	248	35	0.09
50	248	220	0.37	127	255	34	0.10
60	248	210	0.29	127	655	16	0.24
80	207	180	0.16	127	827	9	0.30
80	248	150	0.20	137	248	27	0.08
80	524	35	0.42	137	572	15	0.19
88	248	116	0.17	137	827	9	0.26
88	793	11	0.54	147	248	22	0.07
98	248	80	0.14	147	255	21	0.08
98	255	78	0.15	147	572	12	0.17
98	655	22	0.37	147	827	5	0.24
98	793	14	0.45	155	255	16	0.07
107	248	60	0.12	155	572	10	0.15
107	655	24	0.32	155	827	4	0.21
107	793	15	0.38	166	269	13	0.07
117	255	47	0.11	166	572	9	0.14
117	269	46	0.12	166	827	7	0.19
117	655	20	0.28	-	-	-	-

Figure 5-3 presents profiles of pressure vs. solubility for the solvents at 80 ºC and 147 ºC obtained from the calibrated EOS in Chapter 4. We observe that for a specific increase in solvent solubility, more incremental pressure is required at higher temperatures compared to that at lower temperatures. At higher temperature, as the solvent solubility increases, more incremental pressure is required. More incremental pressure leads to more increase in liquid viscosities. Adversely, increasing solvent

solubility reduces mixture viscosity. Therefore, mixture viscosity reduces more slowly by increasing solvent solubility at higher temperatures.

Also, at each temperature, slope of pressure-solubility curve is lower for C_4 compared with the ones for C_3 and CO_2. Therefore, compared with C_3 and CO_2, less incremental pressure is required for increasing solubility of C_4 at each temperature. This leads to less increase in liquid viscosity. Therefore, C_4 reduces mixture viscosity more intensely by increasing solvent solubility compared with C_3 and CO_2.

We observe that C_4 has much higher solubility at 80°C than C_3 and CO_2. C_4 has high solubility at low temperature and pressure (e.g., 89% mol at 80 °C and 951 kPa). Also, as discussed earlier, solvents have more effective viscosity reduction at lower temperatures. Compared to C_4, C_3 has a similar solubility as C_4 in bitumen at higher pressures. For instance, at 80°C, C_3 and C_4 have solubility of 89% in Clearwater bitumen at 2963 kPa and 951 kPa, respectively. Therefore, C_4 has the potential to be used in hot solvent recovery methods in shallow and deep oil sand reservoirs. C_3 may be a more effective solvent in deeper reservoirs during hot solvent and solvent aided processes.

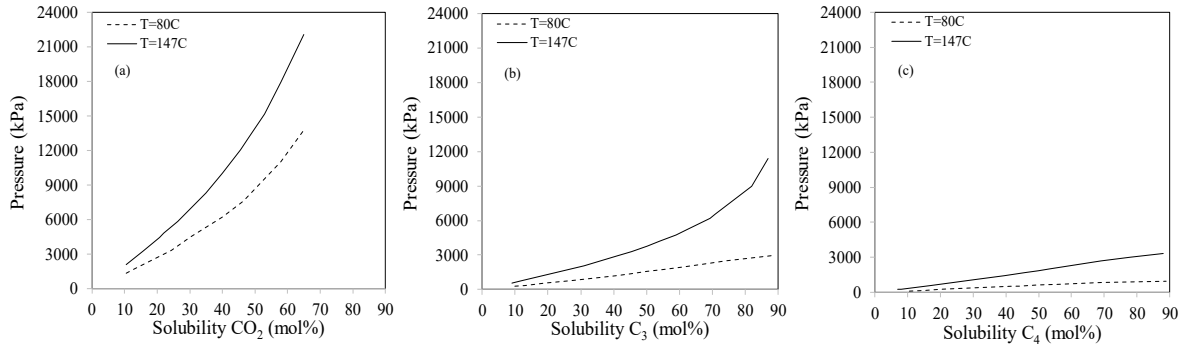

Figure 5-3: Profiles of pressure versus solubility of a) CO_2 b) C_3 and c) C_4 in Clearwater bitumen at 80 °C and 147 °C obtained from the calibrated EOS in Chapter 4

It is worthy to mention that asphaltene precipitation was not observed in the mixtures of solvent and bitumen we used for viscosity measurements. Most of our viscosity measurements have been conducted at C_4 solubility of less than 40% mol and C_3 solubility of less than 30% mol. These values are far less than the threshold solubilities for asphaltene precipitation from our filtration tests as presented in Chapter 4, subsection 4.3.6. According to the filtration test results at 140 °C, asphaltene precipitation is observed at C_4 solubility of 59% mol, and C_3 solubility of 32% mol. Also, there is a high chance of asphaltene precipitation at C_3 solubility of 80% mol.

During sampling from the liquid phase in reactor, pressure is reduced to make the liquid flow through the viscometer (about 10 psi pressure reduction). This may cause the dissolved gas to come out of the liquid and error in estimation of solvent solubility (i.e., up to 20% error in solubility estimation).

5.3.2 Modified Viscosity Model

The coefficients of α_1 and α_2 in Eq. 5-4 were optimized by applying the model for the measured viscosity data for CO_2-, C_1, C_3-, and C_4-bitumen systems. Table 5-7 presents the optimized coefficients for the four systems. α_1 decreases and α_2 increases monotonically with increasing carbon number of the hydrocarbon solvent. Verification of the modified viscosity model is shown in Figure 5-4. The viscosity model predicts the measured viscosity of CO_2-, C_1-, C_3-, and C_4-bitumen systems with an AARD of 8.9%, 6.8%, 6.5% and 16.7%, respectively. We perform a linear regression for the optimized α_1 and α_2 versus carbon number of the hydrocarbon solvents and interpolate the model parameters for C_2-bitumen mixtures. α_1 and α_2 are correlated versus carbon numbers of C_1 to C_4 with coefficient of determination (R^2) of 0.99 and 0.95, respectively:

$$\alpha_1 = -0.1656\text{CN} + 0.9586 \tag{5-10}$$

$$\alpha_2 = 1.9224\text{CN} + 1.9861 \tag{5-11}$$

Where, CN is carbon number of the hydrocarbon solvent. We obtain α_1 and α_1 for the viscosity model of C_2-bitumen system as 0.6274 and 5.8309, respectively. This model predicts the measured viscosities of C_2-Jacos bitumen and C_2-MacKay River bitumen systems (Nourozieh, 2013) with AARD of 38% in temperature range of 50 ^oC to 190 ^oC.

Table 5-7: Optimized coefficients for the key component in the viscosity model with bitumen as the key component

System	α_1	α_2	AARD (%)
CO_2-bitumen	0.6962	4.8333	8.9
C_1-bitumen	0.7903	4.1691	6.8
C_3-bitumen	0.4702	6.9718	6.5
C_4-bitumen	0.2909	10.1969	16.7

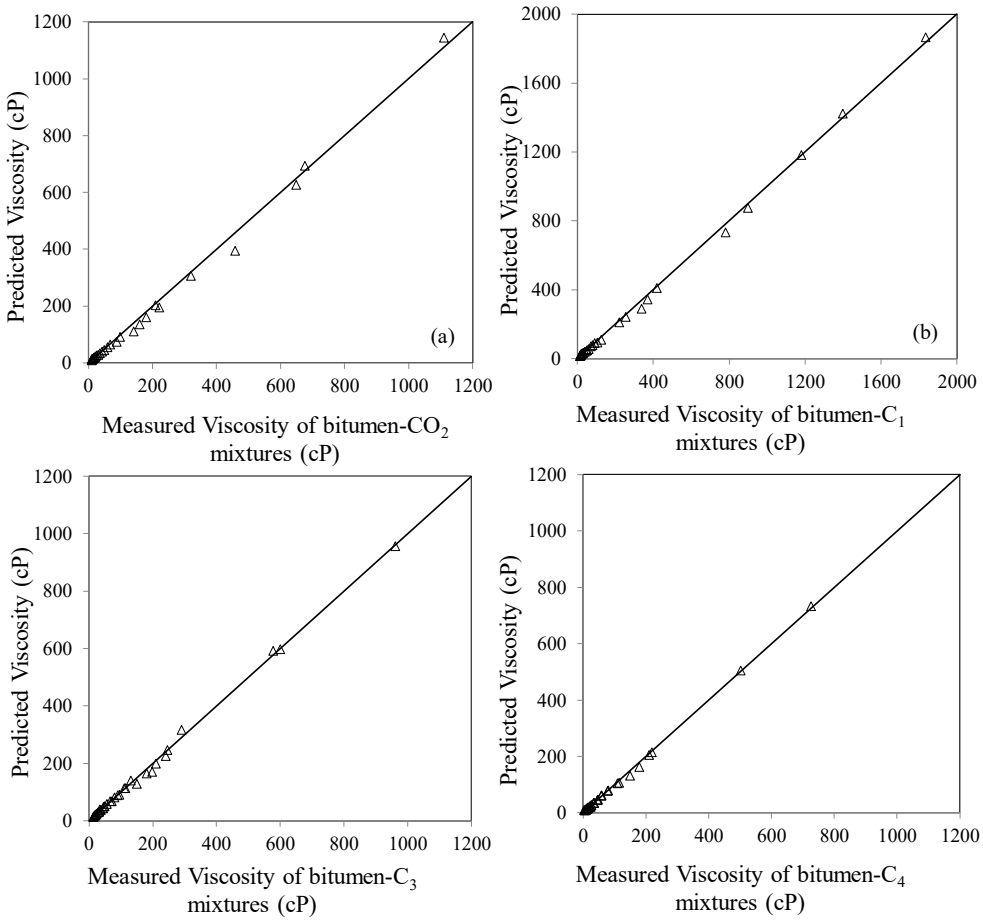

Figure 5-4: Comparison of the predicted and measured viscosities for systems of a) C_1-bitumen b) CO_2-bitumen c) C_3-bitumen and d) C_4-bitumen

As explained in Methodology, Section 5.2.3 viscosity of the pure solvents in liquid state for $T>T_{c,solvent}$ is estimated by extrapolating saturated liquid viscosity of the solvents at each temperature. This extrapolated viscosity may be different from the actual solvent viscosity in liquid state for $T>T_{c,solvent}$.

Regressing the modified viscosity model with solvent as the key component leads to new α_1 and α_2 as presented in Table 5-8. The viscosity model matches against the measured viscosity of CO_2-, C_3- and C_4-bitumen systems with an AARD of 14.9%, 9.5% and 17.5%, respectively.

Table 5-8: Optimized coefficients for the key component in the viscosity model with solvent as the key component

System	α_1	α_2
CO_2-bitumen	-23.4739	0.03604
C_3-bitumen	-20.9984	0.02641
C_4-bitumen	-13.1632	0.0255

It is worthy to mention that when the modified model is applied for predicting bitumen-solvent viscosity, the modified viscosity model performs similarly while using solvent or bitumen as the key component. This model can be applied for predicting viscosity of a system with more components other than solvent and bitumen. If the additional components have insignificant effect on the mixture viscosity, solvent should be selected as the key component in regression.

Figure 5-5 compares the C_3 liquid viscosity at temperatures less than $Tc_{,C3}$ and the modified C_3 viscosity which can match the viscosity data using the logarithmic viscosity model. Results show that the adjusted viscosities are about two orders of magnitude higher than the actual C_3 viscosity which are not representative of liquid C_3 properties. This large difference may cause erroneous simulation results.

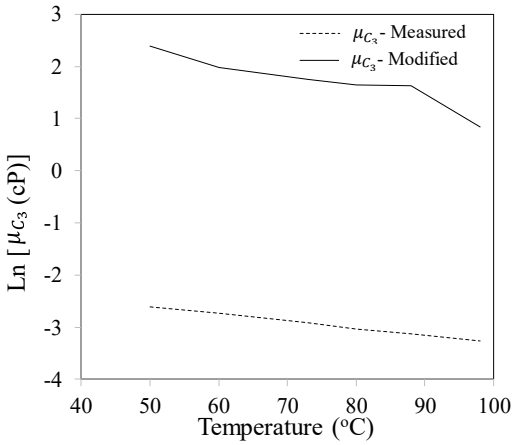

Figure 5-5: Comparison of the measured C_3 liquid viscosity and modified C_3 viscosity to match the measured mixture viscosity data using logarithmic viscosity model, μ_{C_3} is pure C_3 viscosity

We compared the performance of the modified viscosity model with Lobe (1974) and Shu (1984) correlations as shown in Table 5-9. The reason is that these correlations have predicted measured viscosities of CO_2-bitumen and hydrocarbon-bitumen systems with acceptable accuracy (Yarranton et al. 2008; Badamchi-Zadeh et al. 2009; Shu, 1984; Li, 2013).

Results show that the modified model predicts viscosity of CO_2-, C_3- and C_4-bitumen systems with more accuracy respect to Lobe and Shu correlations.

Table 5-9: Performance comparison of the modified viscosity model with Lobe (1973) and Shu (1984) correlations

System	Temperature range (°C)	Number of data	Reference	AARD of modified model	AARD of Lobe Correlation	AARD of Shu Correlation
CO_2-Cold Lake bitumen	50-98	12	Mehrotra and Svrcek,1988	16.6%	28%	32.5%
C_3-Surmont bitumen	100-190	15	Nourozieh, 2013	35.7%	37%	61%
C_4-Surmont bitumen	100-188	14	Kariznovi, 2013	22.3%	28.9%	22.5%

The modified correlation can predict viscosity of light solvents-bitumen mixtures in a wide range of temperature (i.e., 50°C to 165°C). This correlation showed better performance respect to Lobe and Shu correlations and logarithmic mixing rule. Also, it is superior to previous correlations as it requires minimum number of data (i.e., solubility and temperature) as the input and is applicable for thermal reservoir simulators.

5.3.3 Threshold Solvent Concentration

According to Eq. 5-8, TSC is defined as the concentration above which there is less than 0.3% normalized viscosity reduction per mol percent of solvent. This value is selected as the limiting criteria since bitumen viscosity does not change significantly by increasing solvent concentration beyond TSC. At this point, saturated bitumen viscosity is less than 5 cP which is low enough for bitumen recovery from SAGD and solvent-SAGD processes (Gates, 2007).

Figure 5-6a presents pseudo-ternary diagram of CO_2-bitumen system at 140 °C and 4000 kPa. The ternary diagrams are scaled based on mol%. As explained in Chapter 4, in the L_1 phase region, CO_2 solubility increases by CO_2 concentration. A similar behavior is also observed at higher temperatures. Figures 5-6b and 5-6c show calculated CO_2 solubility, L_1 phase viscosity and L_1 phase mol fraction as functions of solvent concentration using multiphase equilibrium and viscosity calculations along the mixing line. The plots indicate that at 140 °C and 4000 kPa, increasing CO_2 concentration beyond 2.2 wt.% has a negligible effect on CO_2 solubility and L_1 phase viscosity. For w_{CO2}>2.2 wt.% in the C_3-bitumen system, the vapor phase comes into equilibrium with the L_1 phase, additional solvent remains in the vapor phase and the L_1 phase mol fraction decreases. Figure 5-6 shows TSC of 2.2 wt.% for CO_2-bitumen system at 140 °C and 4000 kPa as additional CO_2 remains in the vapor phase and does not further reduce L_1 phase viscosity. At this concentration of CO_2, the bitumen

viscosity is reduced from 39.3 cP to 21.6 cP (~ 1.8X reduction). We performed similar calculations at 4000 kPa and 120°C, 160°C and 180°C to estimate TSC at different temperatures (see Figure 5-9). TSC for CO_2 decreases as temperature increases from 120°C to 180°C.

The C_3-bitumen system shows similar phase behavior at 120 ºC <T<180 ºC . Liquid-vapor equilibrium is also observed in C_3-bitumen system similar to CO_2-bitumen system for the whole temperature range at 4000 kPa. Figure 5-7 shows TSC of 10.3 wt.% for C_3-bitumen system at 140 ºC and 4000 kPa as additional C_3 remains in the vapor phase and does not further reduce L_1 phase viscosity. At this concentration of C_3, the bitumen viscosity is reduced from 39.3 cP to 4.3 cP (~ 9.1X reduction).

Figure 5-8a shows the co-existence of equilibrated L_1 and L_2 phases in C_4-bitumen system at 140 ºC and 4000 kPa. As explained in Chapter 4, the C_4-bitumen system exhibits L_1-L_2 phase equilibrium for T<148 ºC, which is not observed for the C_3 and CO_2 systems when 120 ºC <T<180 ºC. Figure 5-8b shows that for w_{C4} >59.6 wt.% C_4 condenses into the L_2 phase, and thus, L_1 phase fraction decreases. Although L_2 phase appears at w_{C4}>59.6 wt.%, L_1 phase viscosity is not significantly reduced for w_{C4}>13.8 wt.%. Therefore, 13.8 wt.% is selected as TSC at 140 ºC and 4000 kPa which satisfies Eq. 5-8. At this concentration of C_4, the bitumen viscosity is reduced from 39.3 cP to 2.5 cP (~ 15.5X reduction).

According to the calculated L_1 phase viscosity, TSC for C_4 is 12.5 wt.%, 13.8 wt.%, 15 wt.% and 16 wt.% at 120°C, 140°C, 160°C and 180°C, respectively. It should be noted that TSC for the C_4-bitumen system is below the C_4 solubility limit at each temperature. The existence of additional solvent above these concentrations has limited effect on viscosity reduction.

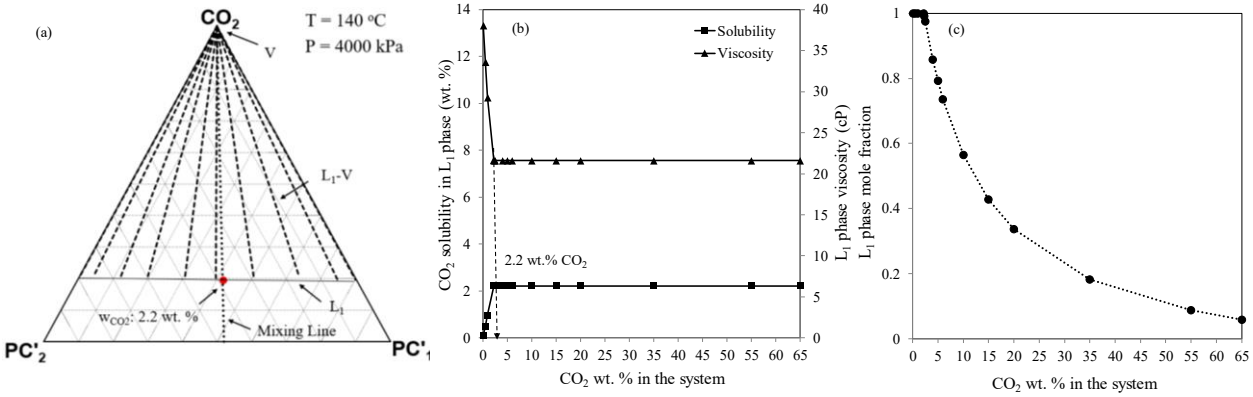

Figure 5-6: a) Pseudo-ternary diagram for CO_2-bitumen system at 4000 kPa and 140°C and effect of CO_2 concentration on b) solubility and liquid phase viscosity and c) liquid phase mole fraction at 140°C and 4000 kPa from EOS predictions (Eghbali and Dehghanpour, 2018)

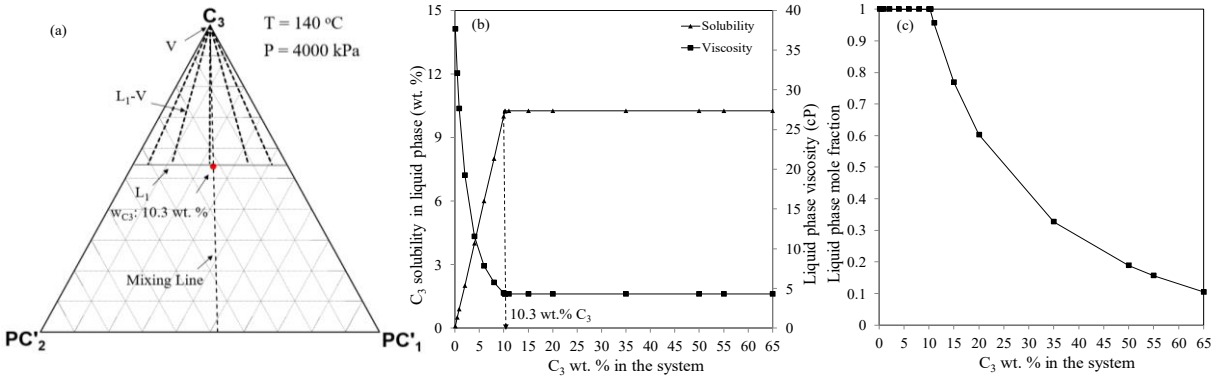

Figure 5-7: a) Pseudo-ternary diagram for C_3-bitumen system at 4000 kPa and 140°C and effect of C_3 concentration on b) solubility and liquid phase viscosity and c) liquid phase mole fraction at 140°C and 4000 kPa from EOS predictions

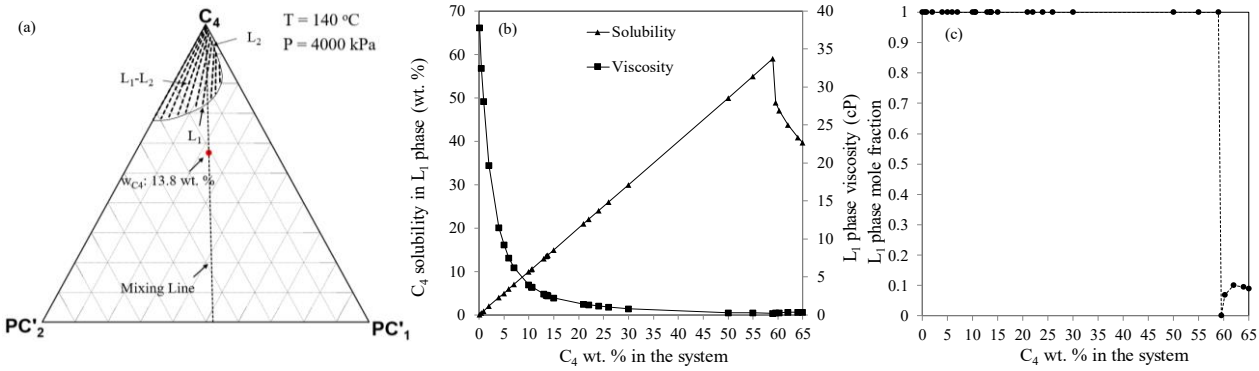

Figure 5-8: a) Pseudo-ternary diagram for C_4-bitumen system at 4000 kPa and 140°C and effect of C_4 concentration on b) solubility and liquid phase viscosity and c) liquid phase mole fraction at 140°C and 4000 kPa from EOS predictions (Eghbali and Dehghanpour, 2018)

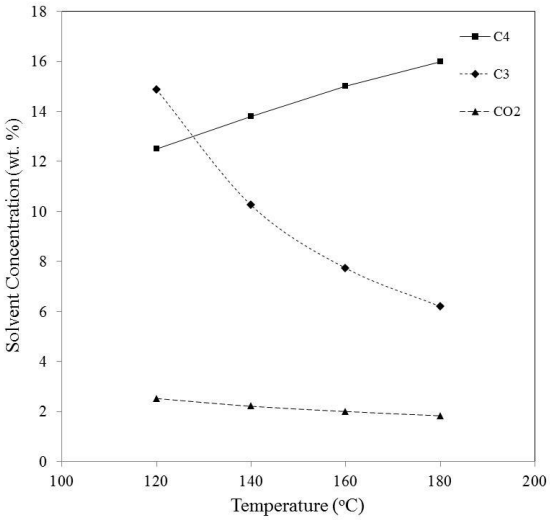

Figure 5-9: Threshold solvent concentrations in bitumen-solvent system at 4000 kPa and different temperatures

Figure 5-10 shows the profiles of the viscosity of L_1 phase equilibrated from mixing solvents at TSC values with bitumen compared with bitumen viscosity for the temperature range of 120°C<T<180°C. Table 5-10 summarizes the maximum solubility of the solvents, minimum TSC values and the liquid phase viscosity for CO_2-, C_3-, and C_4-bitumen systems at the minimum TSC over the temperature range studied. Table 5-11 presents a qualitative comparison of the solvents solubilities and their effect on bitumen viscosity.

As shown in Table 5-10, the minimum TSC for CO_2, C_3 and C_4 is 1.8 wt.%, 6.2 wt.% and 12.5 wt.%, which results in reducing the bitumen viscosity by up to 1.7, 5.6, and 15.2 times, respectively, when 120°C< T <180°C.

Table 5-10: Maximum solvent solubility, minimum TSC and liquid phase viscosity for CO_2-, C_3-, and C_4-bitumen systems at 4000 kPa

System	Maximum solubility (wt.%) bitumen at 4000 kPa	Minimum TSC (wt.%)	Viscosity at 120°C (cP)	Viscosity at 180°C (cP)
Clearwater Bitumen	-	N/A	73.8	15.4
CO_2-bitumen	2.5	1.8	44.3 (1.7x reduction)	9.1 (1.7x reduction)
C_3-bitumen	14.9	6.1	13.1 (5.6x reduction)	3.3 (4.7x reduction)
C_4-bitumen	60	12.5	4.9 (15.2x reduction)	1.4 (10.8x reduction)

Table 5-11: Summary of the CO_2, C_3 and C_4 solubilities and their effect on bitumen viscosity

System	Equilibrium phases in solvent-bitumen mixture	Maximum solvent Solubility in bitumen	Viscosity reduction effect
CO_2-bitumen	L-V	Low	Low
C_3-bitumen	L-V	Medium	Medium
C_4-bitumen	L-L-V	High	High

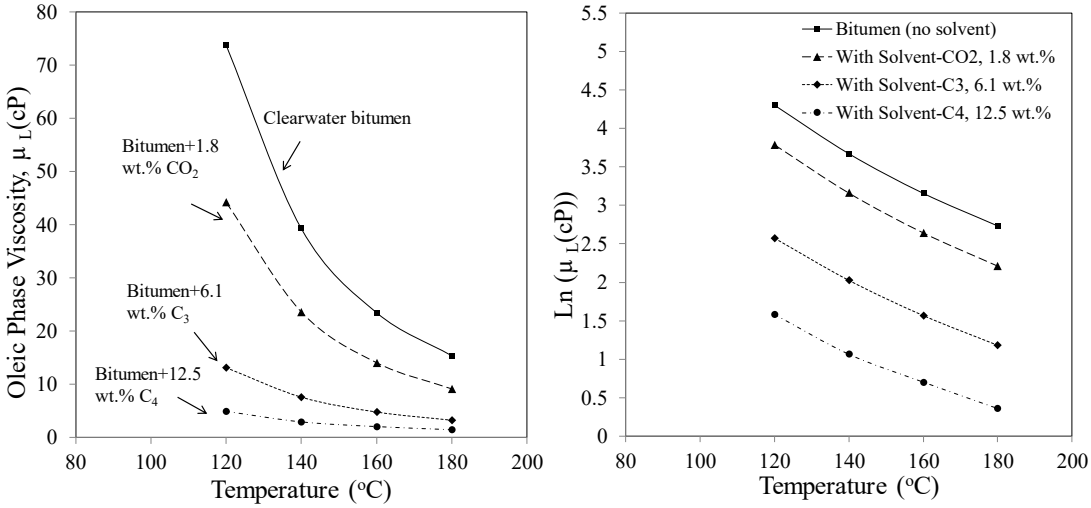

Figure 5-10: Effect of solvents on the reduction of oleic (L_1) phase viscosity at the threshold solvent concentration at 4000 kPa and in the temperature range of 120°C to 180°C

5.4 SUMMARY

A HPHT set up was customized to measure viscosity of the saturated Clearwater bitumen with CO_2, C_1, C_3 and C_4. A modified viscosity model was regressed against the viscosity data. The calibrated viscosity model predicted viscosity of light solvents-bitumen mixtures as a function of solvent solubility and temperature. Threshold solvent concentration was estimated for each solvent at reservoir pressure and elevated temperatures. The effects of solvents dissolution on bitumen viscosity were investigated. Summary of the key results in this study is as follows:

1. Viscosity measurements show that C_3 and C_4 dissolution in bitumen results in greater viscosity reduction than CO_2 and C_1 dissolution for 50°C<T<165 °C. This difference is more pronounced at lower temperatures. For each solvent studied, the viscosity reduction effect by solvent dissolution is more pronounced at lower temperatures. The reason is that at high temperatures, the effect of solvent dissolution is masked by the significant effect of increasing temperature on reducing the dead oil viscosity. Also, higher pressure is required to increase solvent solubility by a specific amount at higher temperature. Higher pressure lead to more increase in liquid viscosity. Therefore, viscosity reduces more slowly by increasing solubility at higher temperatures.

2. C_4 has more viscosity reduction effect compared with C_3 and CO_2. This is because at each temperature, slope of pressure-solubility curve is lower for C_4 compared with the ones for C_3 and CO_2. Therefore, compared with C_3 and CO_2, less incremental pressure is required for increasing solubility of C_4 at each temperature.

Less incremental pressure leads to less increase in mixture viscosity. Therefore, C_4 reduces mixture viscosity more intensely by increasing solvent solubility with respect to C_3 and CO_2.

3. The minimum threshold concentration for CO_2, C_3 and C_4 is 1.8 wt.%, 6.1 wt.% and 12.5 wt.%, respectively, for 120°C<T<180°C. At these concentrations, bitumen viscosity can be reduced by 1.7, 5.6 and 15.2 times by CO_2, C_3 and C_4, respectively at 120°C.

4. The significant C_4 solubility in bitumen and more viscosity reduction potential of C_4 compared with CO_2 and C_3 suggest thatC_4 may be a better solvent than C_3 and CO_2 for solvent-based and solvent aided processes.

5. C_4 has the potential to be used in hot solvent injection methods in shallow and deep oil sand reservoirs. C_3 may be a more effective solvent in deeper reservoirs during hot solvent injection and solvent aided processes. The reason is that C_4 has high solubility at low temperature and pressure. Also, solvents have more effective viscosity reduction at lower temperatures. Compared to C_4, C_3 has a similar solubility as C_4 in bitumen at higher pressures and a specific temperature.

6. The modified viscosity model can predict viscosity of light solvents-bitumen mixtures in a wide range of temperature (i.e., 50°C to 165°C). This correlation is superior to the existing correlations for predicting viscosity of liquid mixtures as it requires minimum number of data (i.e., solubility and temperature) as the input and is simpler to be applied in thermal reservoir simulators. The modified viscosity model showed better performance than the existing correlations in predicting CO_2-, C_3-, C_4-bitumen viscosity data from literature.

7. The experimental solubility and viscosity data from this study can be used to optimize the recovery from solvent-based and solvent aided processes.

5.5 NOMENCLATURE

AARD	Average absolute relative deviation
BIP	Binary interaction parameter
CN	Carbon number
EOS	Equation of State
MW	Molecular weight
HPHT	High pressure-high temperature
PC	Pseudo component
PR-EOS	Peng-Robinson equation of state
P-V	Pressure-volume

TSC	Threshold solvent concentration (weight fraction)
V	Vapor phase

Greek symbols

α	Regression parameter of the modified viscosity model
ω	Acentric factor
Φ	Volume fraction
ν	Kinematic viscosity (m^2/s)
μ	Dynamic viscosity (cP)
ρ	Density (kg/m^3)

Roman symbols

L_1	Oleic phase rich in bitumen
L_2	Oleic phase rich in solvent
N_i	Weighting factor of ith component in the modified viscosity model
N_{data}	Number of data
P_{sat}	Saturation pressure (kPa)
P_c	Critical pressure (kPa)
P_r	Reduced pressure
T_b	Boiling point temperature (°C)
T_c	Critical temperature (°C)
T_r	Reduced temperature
V_c	Critical volume ($cm^3/gmol$)
V_s	Solvent molar fraction
V_o	Oil molar fraction
w	Weight fraction
x	Mole fraction
z	Overall mole fraction

Chapter 6: Optimization of Solvent Aided Process

6.1 INTRODUCTION

Co-injection of a wide range of solvents including pure hydrocarbons from C_3 to C_8 and diluents with steam have been studied (Nasr et al., 2003; Gates, 2007; Ivory et al., 2008; Orr, 2009; Li and Mamora, 2010; Li et al., 2011; Yazdani et al., 2011). However, there are a few studies on co-injection of C_3 and C_4 with steam (Li et al., 2011; Ardali et al.; 2010). Ardali et al. (2010) concluded that C_4 is an optimal solvent for recovery of Cold Lake bitumen using SAP. However, Li et al. (2011) found that co-injection of C_3 with steam decreases performance production of SAP compared with SAGD. In these studies, the effect of steam-solvent (i.e., C_3/C_4)-bitumen phase behavior on bitumen viscosity at steam-bitumen interface is not well understood. Also, the effects of injection strategy on the efficiency of C_3- and C_4-steam co-injections are not investigated.

Simulation, experimental (i.e., lab scale) and pilot scale studies showed improved oil production rates and lower steam-oil ratios in solvent-steam co-injection compared to SAGD (Nasr et al., 2003; Ivory et al., 2008; Gates, 2007; Gupta et al., 2005; Gupta and Gittins, 2006; Li et al., 2011b; Yazdani et al., 2011; Li and Mamora, 2010; Ardali et al., 2012; Mohammadzadeh et al., 2012). Pilot scale C_4-steam co-injection was conducted by EnCana in Christina Lake oil-sand reservoir using SAP. The results showed 57% increase in oil rate and 38% reduction in CSOR (Gupta et al., 2005). Besides all promising results of solvent-steam co-injection, there are also evidences that co-injection of some solvents with steam has resulted in no improvement or even a worse performance compared to steam-only injection (Jiang et al., 1998; Canbolat et al., 2002; Li and Mamora, 2011; Li et al., 2011; Shu and Hartman 1988). For instance, in Nexen's SAP test in Long Lake in 2006 where a diluent containing hydrocarbons from C_7 to C_{12} was co-injected with steam, oil rate increased by 6% and CSOR reduced by 7% (Orr, 2009). The results were less encouraging than the pilot tests by EnCana (Orr, 2009; Orr et al., 2010). Steam-solvent co-injection project of Suncor in the Firebag area where naphtha was co-injected with steam,

exhibited no improvement in the oil production rate (Orr, 2009). Low volatility of the co-injected solvent/diluent has been considered to be responsible for this result. Solvent concentration, solvent type and-injection strategy were varied during pilot scale and field scale co-injection studies. Also, field applications are mostly limited to pilot scales due to unfavorable economics (Ardali et al., 2012; Gupta and Gittins, 2005; Leaute, 2002; Leaute and Carey, 2005).

Therefore, understanding the effects of key parameters controlling steam-solvent-bitumen phase behavior and SAP's efficiency is critical to its optimization in field scale.

6.1.1 Optimization of Solvent-Steam Co-injection Processes

Recovery processes that involve solvents are usually expensive. Therefore, it is important to find an optimum solvent-steam co-injection strategy (i.e., amount and type of solvent to be co-injected with steam versus time) to maximize hydrocarbon recovery and minimize energy consumption. There are several feasible combinations of steam and solvent for SAP. However, investigating optimal options using field scale pilots is difficult and costly. Therefore, it is useful to apply simulation to optimize a solvent-steam co-injection process in terms of solvent type, solvent concentration and co-injection strategy.

Simulation and experimental studies have been performed to investigate different factors affecting performance of hybrid solvent-steam processes. These factors include solvent type, solvent concentration and injection strategy. Govind et al. (2008) examined co-injection scenarios of steam with C_4, C_5, a mixture of C_6-C_8 and C_7 at 4000 kPa. They concluded that co-injection of C_4 with steam leads to the highest recovery. Experimental studies of Ardali et al. (2012) showed that co-injection of C_6 with steam leads to 20% increase in recovery factor. Nasr et al. (2002) concluded that C_6 and diluents with carbon numbers higher than 6 are the most preferred solvents in Expanding Solvent-SAGD process. Ardali et al. (2010) concluded that solvents heavier than C_4 are suitable for solvent-steam co-injection in an Athabasca bitumen reservoir at 2100 kPa and C_4 is suitable for solvent-steam co-injection in a Cold Lake reservoir at 3400 kPa. Li et al. (2011) found that heavy solvents such as C_7 and C_{12} are suitable when they are co-injected with steam at optimal concentrations of 5-7% mol. Several simulation studies for SAP optimization show conflicting results. This is due to the complexity of heat and mass transfer and uncertainties in input simulation

parameters such as phase behavior of the solvent-bitumen system, geological and petrophysical properties, etc. Moreover, the effect of steam-light solvents (i.e., C_3 and C_4)-bitumen phase behavior on bitumen viscosity at steam-bitumen interface is not well understood.

Previous studies have been performed to optimize injection strategy in solvent assisted SAGD process. They suggested co-injecting lighter solvents after heavier solvents during solvent-steam co-injection to vaporize and recover the condensed heavier solvents (Gates and Gutek, 2008; Gupta and Gittins, 2007b; Edmunds et al., 2010). However, optimizing the injection strategy has not been performed for light solvents in terms of solvent concentration and by considering economic evaluations in SAP.

This Chapter presents simulation results of C_3- and C_4-steam co-injection during SAP for four years. We investigate the phase behavior of steam-solvent-bitumen and its effect on bitumen viscosity at steam-bitumen interface. Also, we investigate the parameters affecting the efficiency of SAP. The optimum co-injection strategy is designed by considering economic evaluations.

6.2 METHODOLOGY

In the following subsections we explain the methodology for investigating the parameters controlling SAP's performance and optimizing this process. The methodology of this study is summarized in Figure 6-1.

6.2.1 Reservoir Simulation

We simulate solvent-steam co-injection into a developed steam chamber. It involves three key stages: preheating for 3 months, steam injection for 6 months and solvent-steam co-injection for 3 years. C_4 and C_3 are used as solvents. The injection strategy of the base case simulation model is presented in Table C-1. Preheating process is simulated by in-situ heating of the injector and producer wells. The producer well is opened to flow during this period to simulate the actual preheating process. The actual process is performed by circulating steam between the injection and production wells in the field to establish communication between the wells. After 3 months preheating, steam is injected for 6 months and the steam chamber forms during this period. Steam chamber reaches the top of the reservoir after 9 months (i.e., preheating

and steam-only injection period). Then we start co-injecting solvent with steam into the developed steam chamber.

6.2.1.1. Dimensions and Discretization

The reservoir model is homogenous with initial reservoir temperature and pressure of 12°C and 2500 kPa, respectively. Its dimensions are 50 m*800 m*12 m in x, y and z directions, respectively (Cenovus Energy, 2018). Figure 6-2 shows a half reservoir with production and injection wells in one side. This assumes that the steam chamber is symmetric with identical processes on both sides. Steam chamber is the volume of the reservoir in which rock temperature rises to the point where steam and vaporized solvent can be sustained at reservoir pressure conditions. The production and injection wells are located in one side of the reservoir as half of the steam chamber is simulated due to the symmetry.

To perform 2D simulations, the model is discretized to 1 m*800 m*1 m grid blocks in x, y and z directions, respectively. After discretization, the model is refined to 0.2 m*0.2 m grid sizes in x and z directions within 36 m of the wells in x-direction and across the reservoir width (Figure 6-2b). This is found to be the optimum size based on the sensitivity analysis on grid size (see Appendix C). It is worthy to mention that the results of 3D simulation with two grids in the y direction ($\Delta y = 400$ m) were the same as the results of 2D simulation with one grid in y direction ($\Delta y = 800$ m). Therefore, to reduce the simulation time, we conduct 2D simulation in this study.

6.2.1.2. Rock and Fluid Properties

The initial water saturation in the reservoir is 0.45 and the rest of the pore space is filled with "live" Clearwater bitumen (Cenovus Energy, 2018). Live bitumen is a mixture of 11.2% mol C_1 and 88.8% mol dead bitumen, corresponding to a GOR of 6.5 sm^3/sm^3. Gas-liquid K values are generated using winprop module of CMG and a calibrated PR-EOS for system of bitumen C_1 and C_4/C_3 solvents. Bitumen components are lumped into a single component before the calibration. PR-EOS is caliberated against PVT data presented by Eghbali and Dehghnapour (2018). The thermophysical properties of the components and binary interaction parameters between the components in the fluid model used for generating K values are presented in Tables B-2 and B-3, respectively. We used the modified viscosity model for systems of C_3- and C_4-Clearwater bitumen presented by Eghbali and Dehghanpour (2018) to predict viscosity of the oil phase.

The measured residual saturation of oil after steam flooding is 0.15 from coreflood experiments of Cold Lake oil-sand samples (Cenovus Energy, 2018). The relative permeability model used is independent of temperature. We considered overburden and underburden heat losses in the simulation using reservoir thermal properties. The thermal conductivities are weighted using nonlinear mixing through the correlation of Anand et al. (1973). A semi-analytical model is used for heat transfer to or from an adjacent formation of infinite extent (Vinsome and Westerveld, 1980).

The effects of dispersion, capillarity and asphaltene precipitation are not considered in the simulation. Also, the simulation model is a synthetic homogenous model in terms of rock and fluid properties. The production well is located 1 m above the base of the model and 5 m below the injector well. The temperature of the injected steam is the saturation temperature of water at the injection pressure (i.e., P_{inj}=3500 kPa). The quality of the steam is 90%. The production well is subject to the maximum liquid flow rate constraint of 200 m^3/day at surface conditions and a maximum steam flow rate of 5 m^3/day and minimum bottom hole pressure constraint of 3400 kPa. The parameters of the model are listed in Table B-4. It is worthy to mention that reservoir porosity, permeability, depth, pressure and rock end points are from (Cenovus Energy, 2018) and the rest of properties in Table B-4 are assumed from literature.

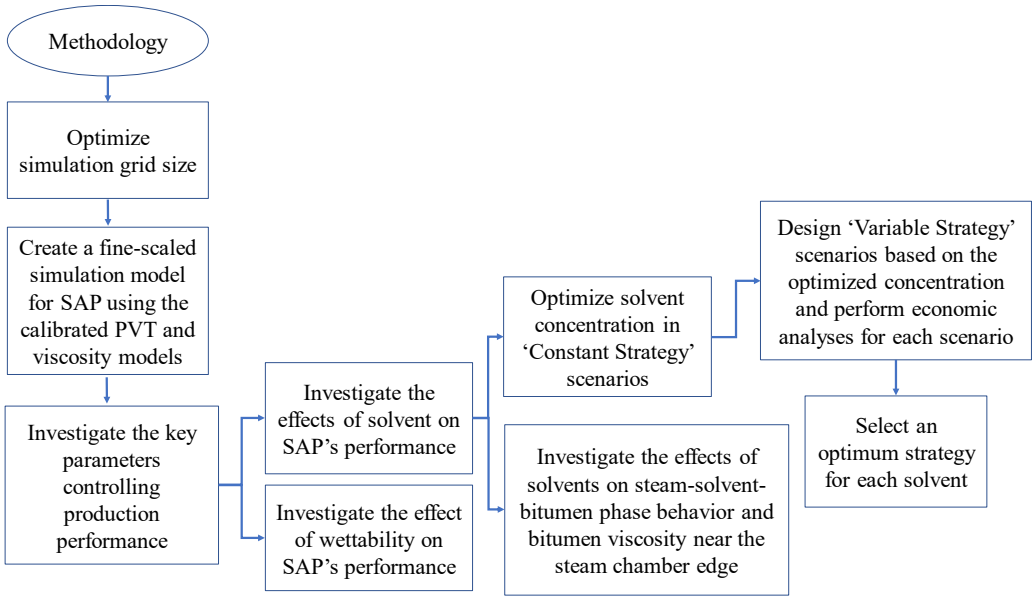

Figure 6-1: Flow-chart diagram of the methodology used for optimization of SAP

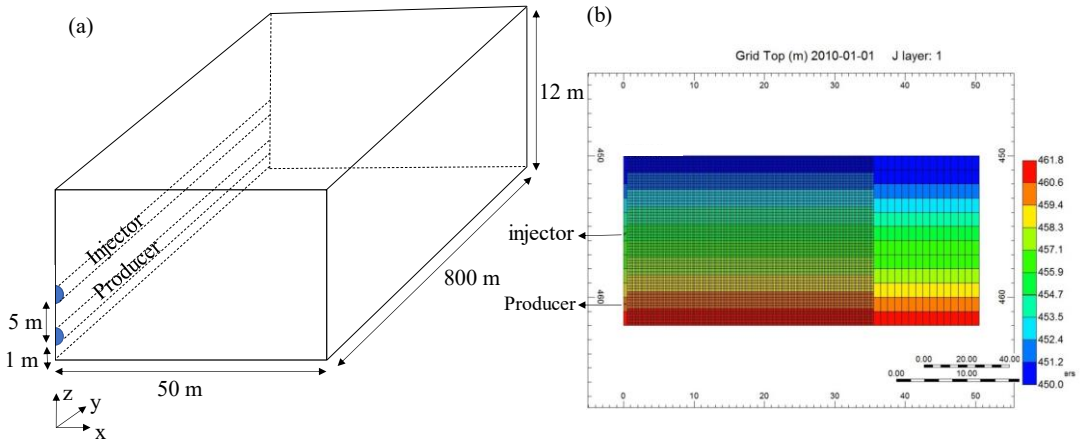

Figure 6-2: Half simulation model in cartesian coordinate in a) 3D view and b) 2D view of x-z plane

6.2.2 Effects of Key Parameters on SAP Performance

We investigated the effects of key parameters controlling efficiency of SAP to optimize field performance. These parameters include reservoir wettability, solvent type, solvent concentration and solvent co-injection strategy (i.e., co-injected solvent concentration versus time).

6.2.2.1. Effects of Wettability

We changed water end point relative permeability ($K_r^o{}_{w(o)}$) at residual oil saturation from 0.02 up to 0.3 to investigate the effect of rock wettability on the performance of SAP. It is worthy to mention that this range of $K_r^o{}_{w(o)}$ covers the range of $K_r^o{}_{w(o)}$ obtained from measurements and/or history matching in oil-sand reservoirs (Adegbesan, 1991; Beattie et al., 1991; Kisman and Yeung, 1995; Kisman, and Acteson, 1988;).

6.2.2.2. Effects of Solvent

We investigated the effects of 1) solvent type 2) solvent concentration and 3) co-injection strategy on SAP's performance. First, we investigated the main stages of oil recovery during SAP and the effect of solvent type on SAP's performance. To understand the effect of solvent type, we investigated phase behavior of steam-solvent-bitumen and its effect on bitumen viscosity at steam-bitumen interface. Second, we performed sensitivity analysis on solvent concentration within a constant injection strategy. This means that solvent concentration is constant for each period of solvent-steam co-injection (see Table B-1). It is worthy to mention that we divided the solvent-steam co-injection period into three one-year periods as shown in Table B-1 to customize the solvent concentration within each period. The reason is that we observed

distinguished effect of C_4-steam co-injection during the first year of co-injection as will be explained in Section 6.3.1. We designed scenarios with constant-concentration strategy in which the solvent concentration in the co-injection stream increases from 0% mol (i.e., SAGD) to 14% mol. Then we compared the ultimate bitumen recovery and Cumulative Steam Oil Ratio (CSOR) to obtain the optimum solvent concentration at 3500 kPa. Third, we designed scenarios with variable-concentration strategy in which solvent concentration changes periodically. Then, we performed economic analyses for all variable-concentration strategies to find the optimum co-injection scenario. For this purpose, we changed the solvent concentration in each stage of solvent-steam co-injection with a descending trend. The average of the three solvent concentrations equals the optimum concentration in the constant-concentration strategy. Optimum cocnentration in constant-concentration strategy was obtained in the previous step for each solvent. For instance, possible combinations of the concentrations with descendening concentration trend satisfying the average of 2% mol include: (3-2-1)%, (3-3-0)%, (4-2-0)%, (4-1-1)%, (5-1-0)% and (6-0-0)%. We calculated Net Present Value (NPV) of each scenario using Eq. F-1 to optimize the co-injection scenario. In this formulation, we considered the cash back from bitumen recovery and solvent recovery and the expenses regarding solvent injection, steam generation and water injection. Assumptions of this calculation are listed in Table F-1. It is worthy to mention that the designed scenarios are run in a full field model instead of the half model for NPV calculations. Also, the same steam quality and injection temperature are used in both SAGD and SAP models.

6.3 RESULTS AND DISCUSSION

In this section, we present the simulation results to explain the effects of key parameters controlling efficiency of SAP. These parameters include reservoir wettability, solvent type, solvent concentration, and co-injection strategy. Also, we present optimized scenarios for C_3- and C_4-steam co-injections. It is worthy to mention that sensitivity analysis on wettability, solvent type and solvent concentration are performed under constant-concentration strategy.

6.3.1 Production Performance of SAGD Process and SAP

Figure 6-3 compares the bitumen production rate between SAGD process and SAP at 3500 kPa. It shows that bitumen rate starts declining after 3 months of production

under SAGD. This is because the steam chamber approaches top of the reservoir and SAGD efficiency reduces by overburden heat losses. C_4-steam co-injection during SAP generally increases oil rate compared with steam injection during SAGD. This increase in oil rate eventually declines after about one year co-injection and stabilizes to a value close to that from SAGD. Appendix D compares the trend of bitumen production rate in SAGD the one from SAGD field data operated in Burnt Lake oil-sands as presented in Appendix D. The results show similar trend of oil production rate versus time from simulation with the one from field data.

Figure 6-3a shows that the reservoir oil is produced in three main stages during SAP. These three stages last for about 4, 6 and 30 months, respectively, during the total 4 years of simulation. Oil rate increases significantly and peaks in the first stage. It then declines and peaks again in the second stage. Oil rate stabilizes in the third stage at a value close to that from SAGD. Most of the total recovered oil (~65%) is produced during the first two stages. Most of the total recovered oil (~65%) is produced from the first two stages. We explain the recovery stages in the section 6.3.1.1.

As mentioned in the methodology section, the modified viscosity model is applied in the simulation model. It is worthy to mention the logarithmic viscosity model is the default model in the commercial simulator. Applying the logarithmic viscosity model in simulation causes 2% overestimation of the ultimate bitumen recovery of C_4-steam co-injection process.

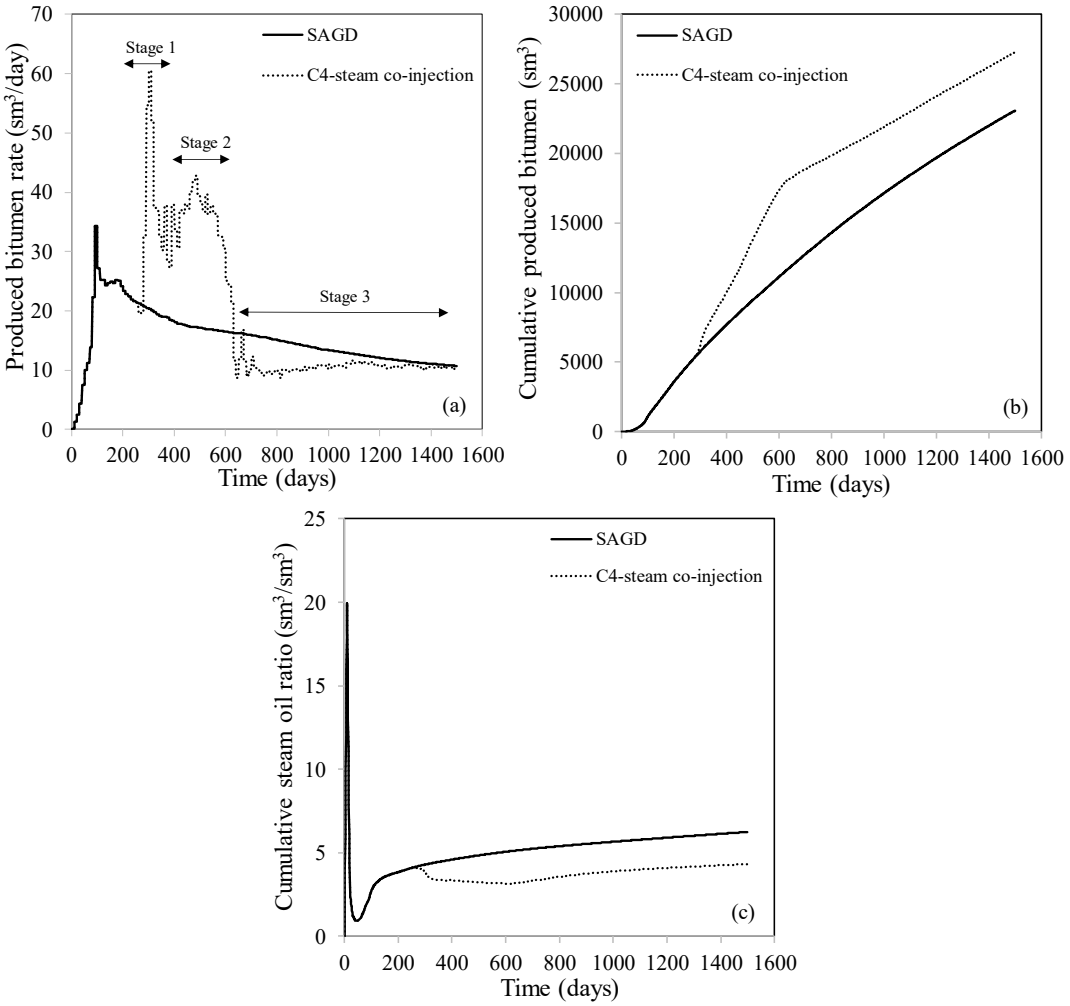

Figure 6-3: Comparison of a) produced bitumen rate b) cumulative produced bitumen and c) cumulative steam oil ratio between SAGD and C_4-steam co-injection processes at 3% mol C_4 and 3500 kPa

6.3.1.1. Main Stages of Oil Recovery during SAP

Here, we investigate the main stages of oil recovery during in SAP. Figures 5-4 to 5-12 show the profiles of oil, gas, water saturations and C_4 mol fraction in the oil phase (i.e., xC_4) at different simulation times.

6.3.1.1.1. First Stage

There is the first peak in the oil production profile during the first stage of recovery. Figures 6-5 to 6-7 show the profiles of phase saturations and C_4 mol fraction in the oil phase (xC_4) during this stage. As Figures 6-5a and 6-5d show, right before solvent co-injection, steam chamber has arrived the top of the reservoir. At this stage, steam-only injection could not efficiently displace the oil in the chamber as oil saturation in the chamber is above the residual oil saturation in presence of water (i.e., S_{orw}=0.15). As Figure 6-5b shows, when C_4-steam co-injection starts, vaporized solvent moves to the upper parts of the steam chamber. Subsequently, vaporized C_4

condenses near the upper parts of the steam chamber edge. Steam chamber edge is where liquid-vapor-aqueous (L+V+W) phases transition to liquid-aqueous (L+W) phases (i.e., the gas saturation reaches zero). This transition can be observed in the gas saturation profiles where gas saturation reduces from high values to zero (Figure 6-5d). Figure 6-6b shows that condensed C_4 accumulates almost uniformly at all parts of the chamber edge in the oil phase. Comparison of Figures 6-6 and 6-5 shows the first lateral growth of the chamber. The condensed C_4 dilutes the heated bitumen and further reduces viscosity of the heated bitumen. The mobilized bitumen drains with the condensed C_4 and water toward the production well. This leads to the first lateral growth of the chamber and consequently the first peak in the oil rate profile. Comparison of Figures 6-6 and 6-7 shows that condensed C_4 and water saturation increase near the bottom of the steam chamber. This is due to the gradual oil drainage with condensed C_4 and water toward the production well.

6.3.1.1.2. Second Stage

Oil rate reaches the second peak in its profile during the second stage of recovery. Figures 6-8 to 6-10 show the profiles of phase saturations and C_4 mol fraction in the oil phase (xC_4) during this stage. As Figure 6-8a shows, at the start of the second stage, oil saturation is reduced near to the residual oil saturation at the top of the steam chamber, near the chamber edge. Also, there is local oil displacement inside the chamber as we observe tracks of small oil saturation (below the S_{orw}) near the top of the steam chamber (Figures 6-9a to 6-12a). The reason is that at the beginning of the second stage, C_4 mol fraction (xC_4) increases in the oil phase at the upper parts of the chamber and near the edge (i.e., $xC_4>0.8$). When steam chamber reaches a grid block with high xC_4, temperature of the diluted oil phase increases and the solvent portion of the oil phase evaporates partially. If the block oil saturation is near the residual oil saturation (S_{orw}), as a result of this solvent vaporization oil saturation reduces below the residual saturation (S_{orw}) (Keshavarz et al., 2014a).

Figures 6-9 and 6-10 show chamber edge grows more in lateral direction and simultaneously water saturation increases at the bottom parts of the chamber edge. Over time, condensed C_4 mixes with the heated bitumen and the diluted and heated oil drains with water toward the production well.

6.3.1.1.3. Third stage

Oil rate declines and stabilizes in the third stage of recovery. Figures 6-11 to 6-12 show the profiles of phase saturations and C_4 mol fraction in the oil phase (xC_4) during this stage. Figure 6-11 shows initialization of the conical shape of the steam chamber during the third stage. Conical shape in this paper explains shape of the steam chamber when upper parts become much wider than the bottom parts. As it was shown in Figure 6-3a, oil rate reduces to a stabilized value after about one-year solvent-steam co-injection. Figures 6-11b to 6-12b show accumulation of the condensed C_4 in a limited area near the middle parts of the chamber edge during the stabilized stage. Also Figures 6-11c to 6-12 c show increase in water saturation at the bottom of the steam chamber respect to previous stages. As water saturation increases at the bottom parts, condensed C_4 accumulates above the accumulated water due to the gravity segregation. During the stabilized period, conical shape becomes more pronounced by increasing water saturation at the bottom parts of the steam chamber. This reduces available space for the injected solvent. Therefore, vaporized solvent moves toward the top parts of the chamber and condenses mainly at the middle parts of the edge in a limited area. The accumulated solvent in this region has limited contact area with the heated bitumen. Besides, the accumulated solvent in a limited area reduces the chamber edge temperature. Also, rate of heat transfer between the steam and the bitumen reduces. Therefore, after one year, oil rate reduces and stabilizes at a constant value.

Wettability of the reservoir is one of the parameters that can control water production. Water production affects the accumulation of water at the bottom of the steam chamber. Therefore, wettability controls the adverse effect of gravity segregation and water blockage in the third stage of recovery. Also, it was observed that additional solvent co-injection during the third stage cannot improve oil recovery during the third stage. Therefore, total amount of injected solvent and the strategy of the steam-solvent co-injection may affect the performance of this process. We investigate the effect of wettability and solvent (i.e., solvent type, solvent concentration and solvent-steam co-injection strategy) on the SAP's performance as will be presented in Sections 6.3.2 to 6.3.5.

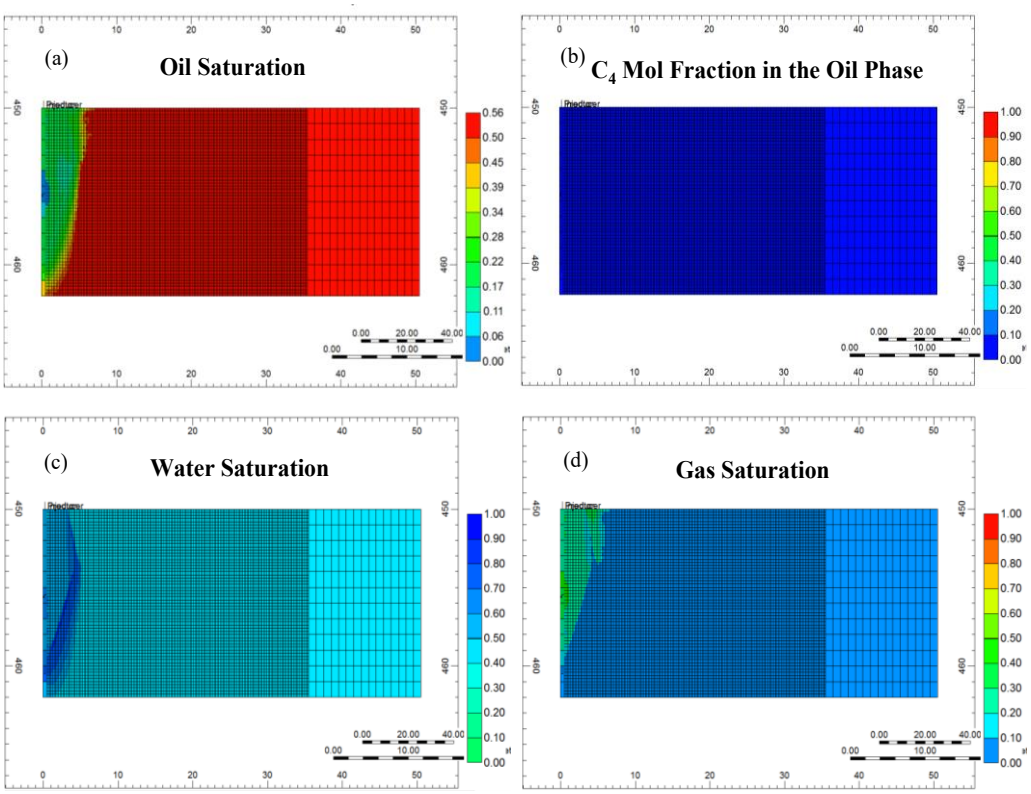

Figure 6-4: Profiles of a) oil saturation b) oil mol fraction in the oil phase c) water saturation and d) gas saturation right before co-injection of C_4 steam (i.e., at 270 days) at 3500 kPa and C_4 concentration of 3% mol in the co-injection stream

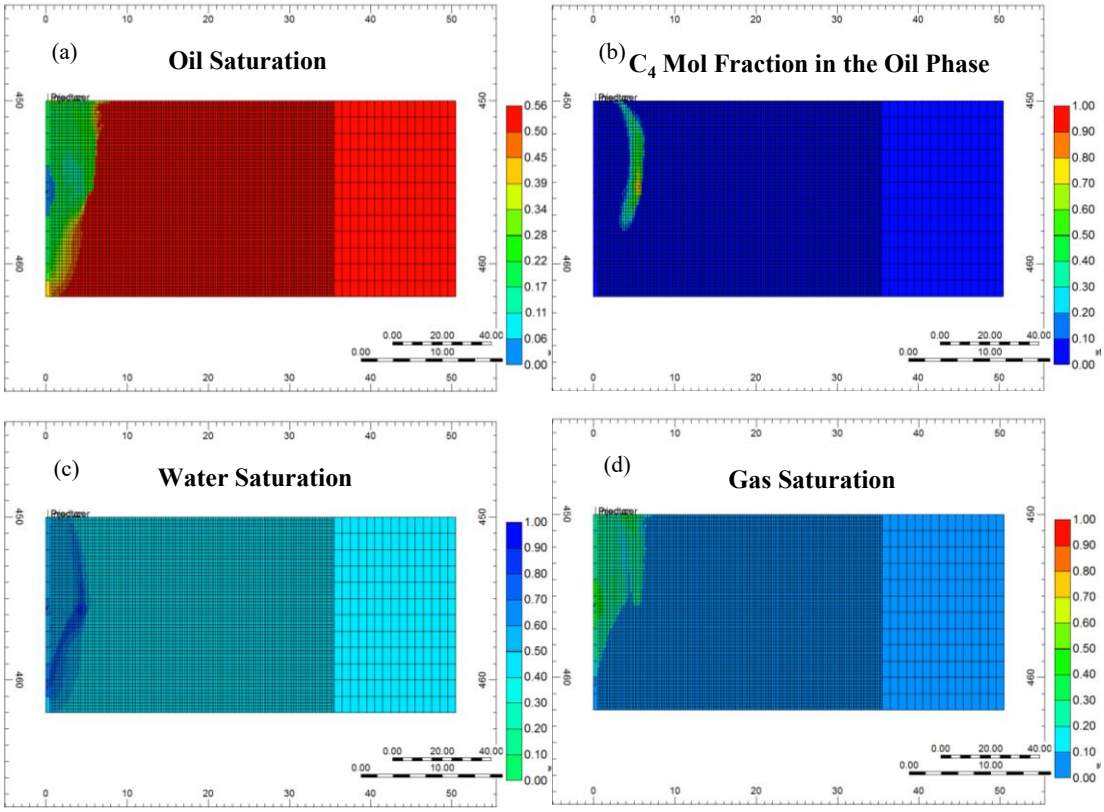

Figure 6-5: Profiles of a) oil saturation b) oil mol fraction in the oil phase c) water saturation and d) gas saturation at the beginning of the first stage period (i.e., at 280 days) at 3500 kPa and C_4 concentration of 3% mol in the co-injection stream

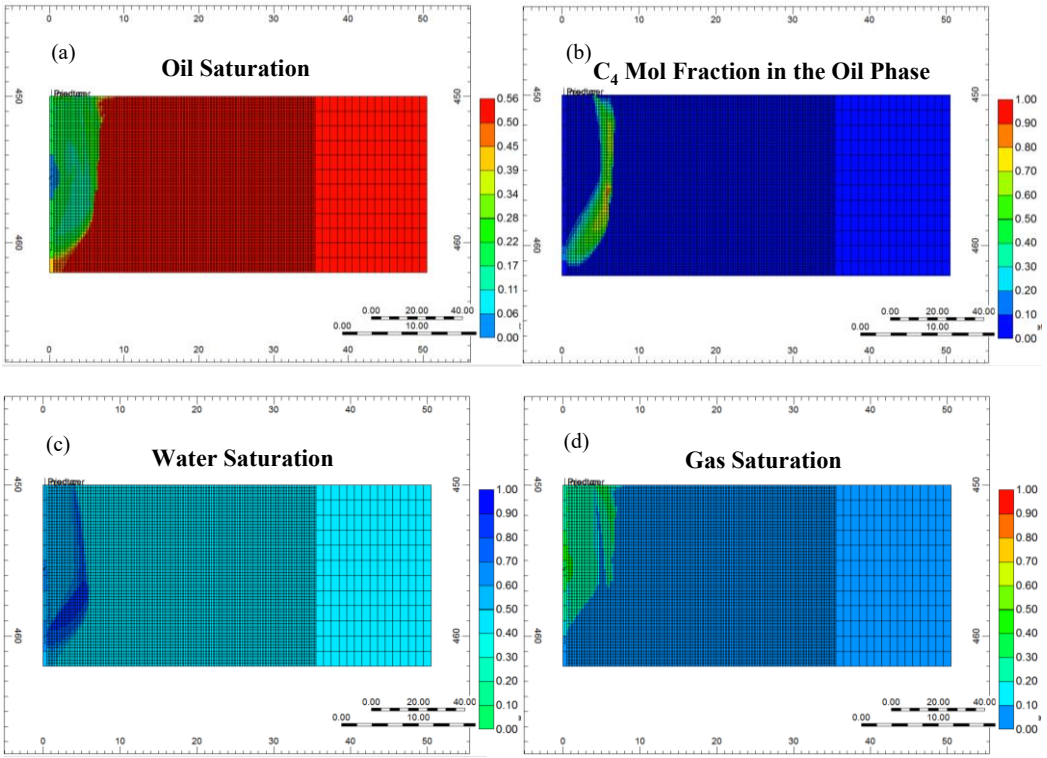

Figure 6-6: Profiles of a) oil saturation b) oil mol fraction in the oil phase c) water saturation and d) gas saturation during the first stage period (i.e., at 300 days) at 3500 kPa and C_4 concentration of 3% mol in the co-injection stream

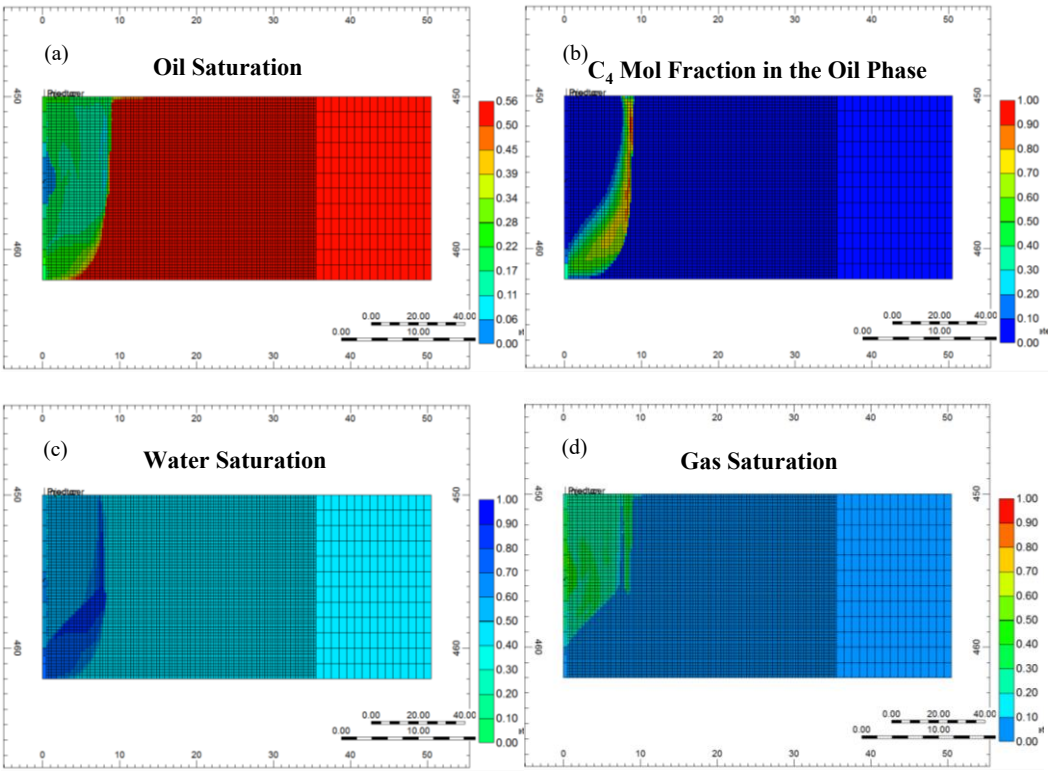

Figure 6-7: Profiles of a) oil saturation b) oil mol fraction in the oil phase c) water saturation and d) gas saturation at the end of the first stage (i.e., at 390 days) at 3500 kPa and C_4 concentration of 3% mol in the co-injection stream

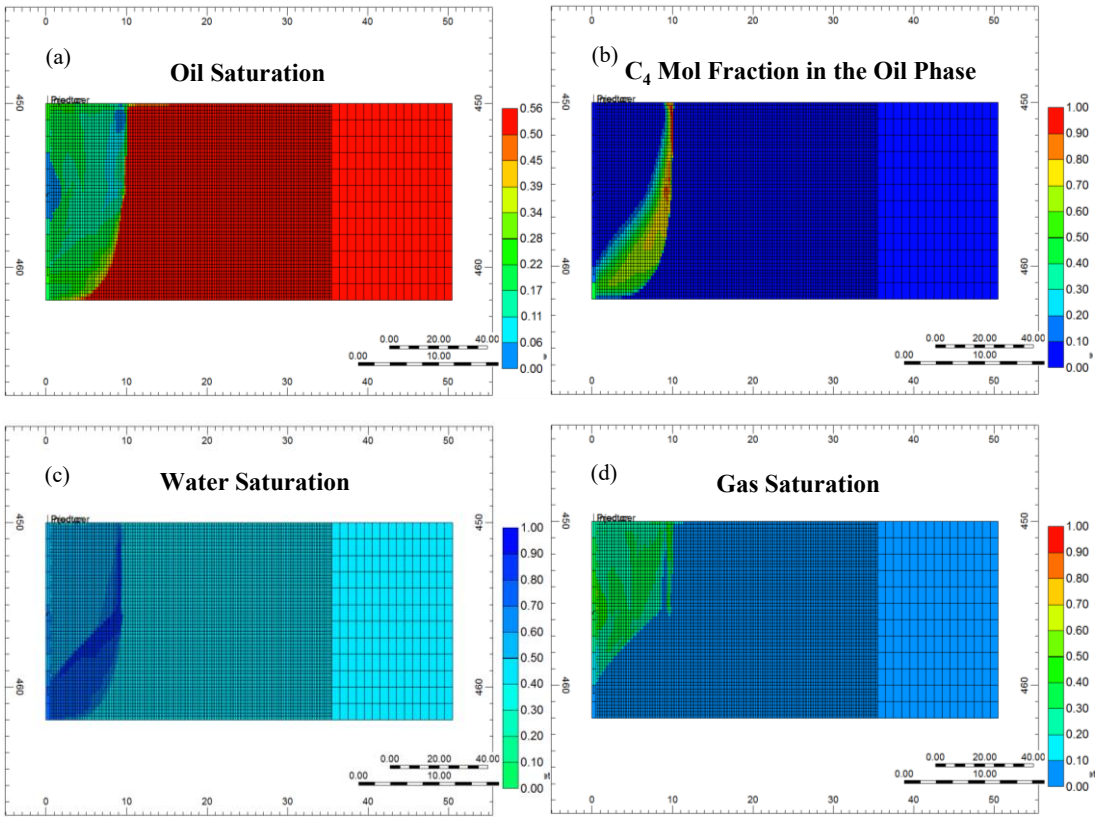

Figure 6-8: Profiles of a) oil saturation b) oil mol fraction in the oil phase c) water saturation and d) gas saturation at the beginning of the second stage (i.e., at 430 days) at 3500 kPa and C_4 concentration of 3% mol in the co-injection stream

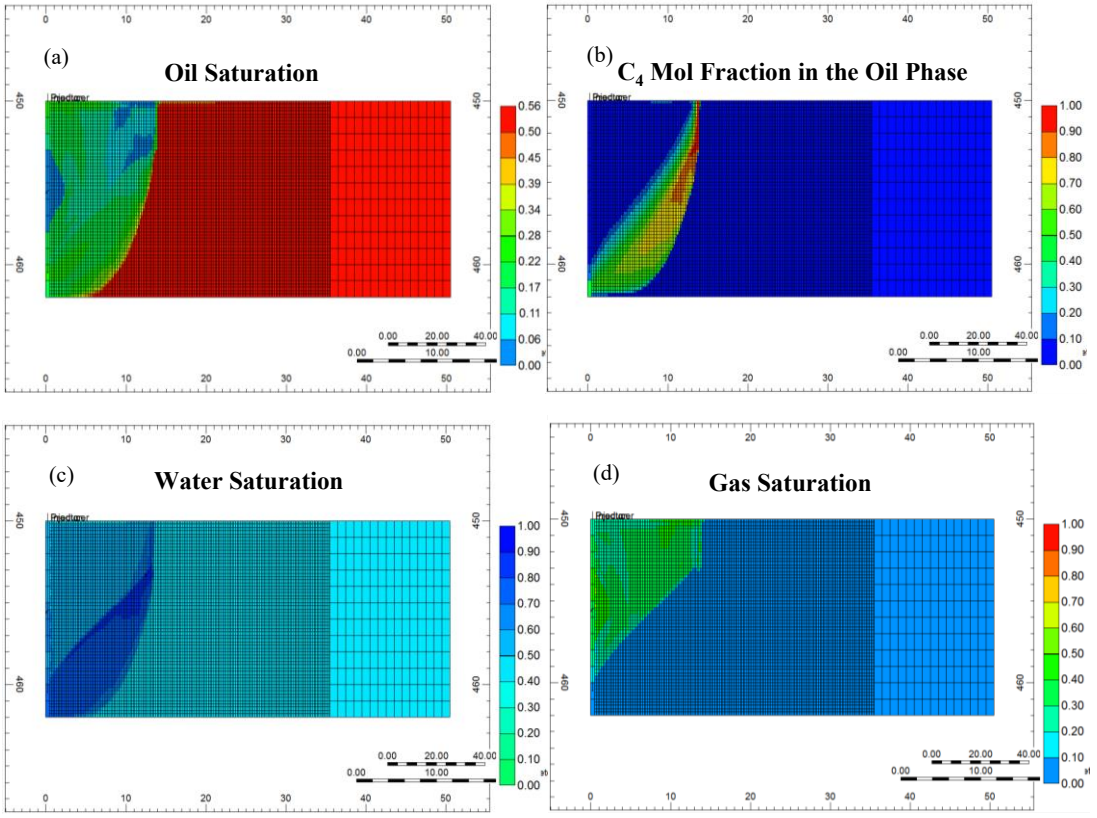

Figure 6-9: Profiles of a) oil saturation b) oil mol fraction in the oil phase c) water saturation and d) gas saturation during the second stage (i.e., at 520 days) at 3500 kPa and C_4 concentration of 3% mol in the co-injection stream

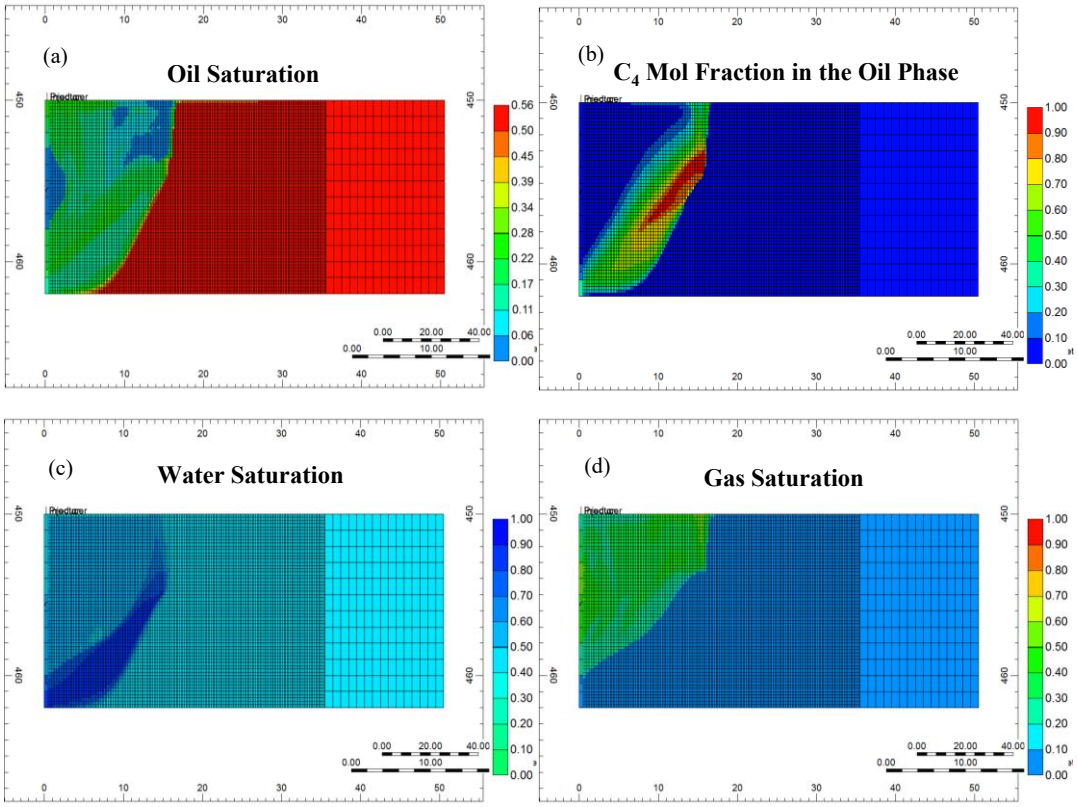

Figure 6-10: Profiles of a) oil saturation b) oil mol fraction in the oil phase c) water saturation and d) gas saturation at the end of the second stage (i.e., at 600 days) at 3500 kPa and C_4 concentration of 3% mol in the co-injection stream

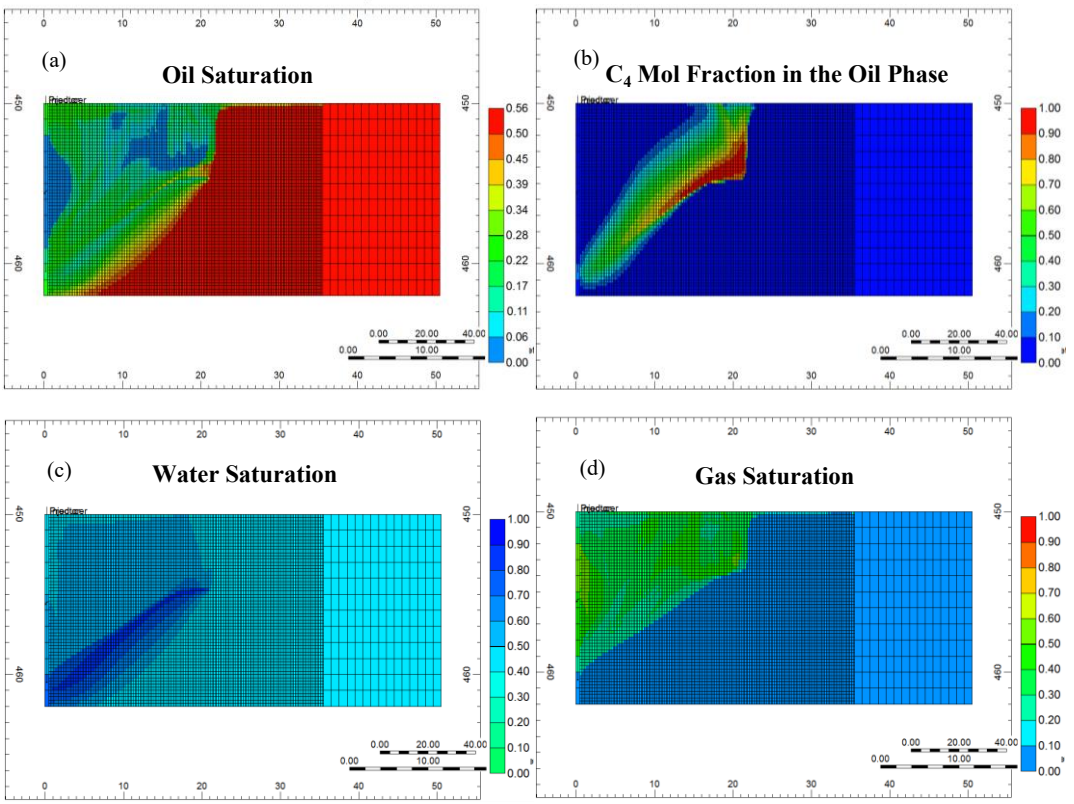

Figure 6-11: Profiles of a) oil saturation b) oil mol fraction in the oil phase c) water saturation and d) gas saturation during the stabilized rate period (i.e., at 1020 days) at 35kPa and C_4 concentration of 3% mol in the co-injection stream

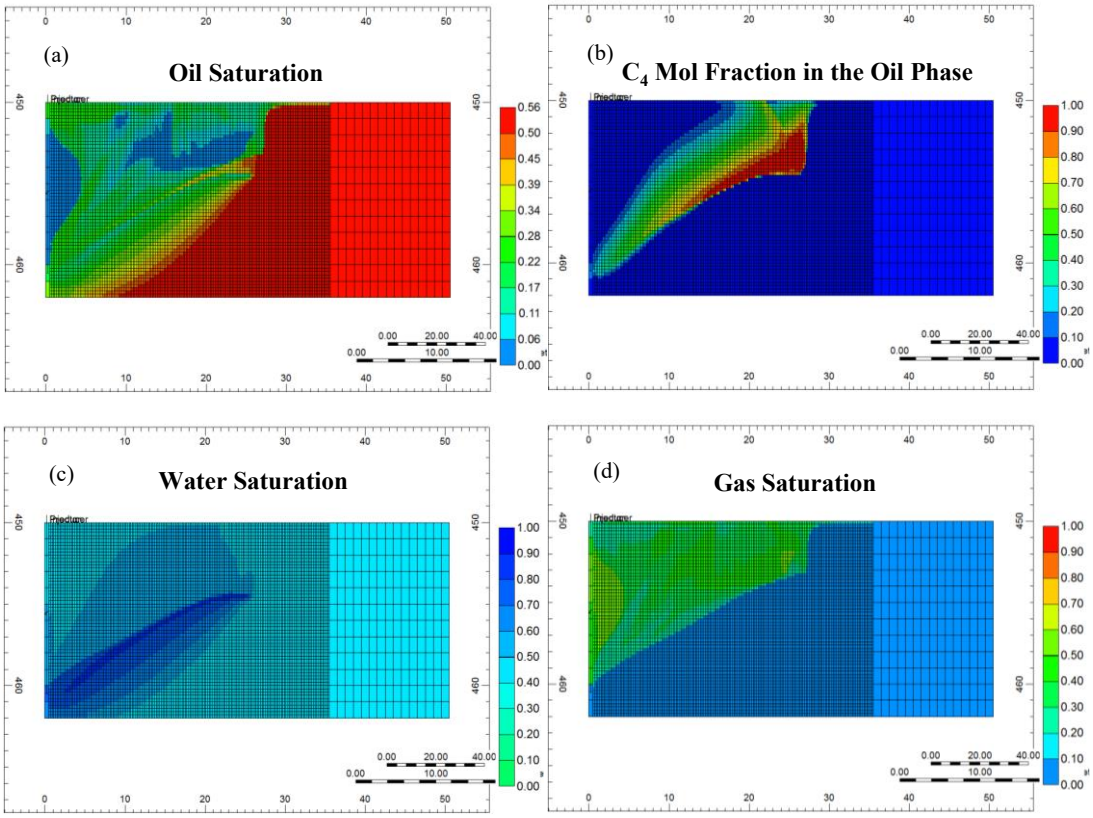

Figure 6-12: Profiles of a) oil saturation b) oil mol fraction in the oil phase c) water saturation and d) gas saturation at the end of the simulation (i.e., at 1500 days) at 3500 kPa and C_4 concentration of 3% mol in the co-injection stream

6.3.2 Effects of Wettability on SAP's Performance

Here, we perform sensitivity analysis on end-point of water relative permeability ($K_r^o{}_{w(o)}$) by varying it from 0.02 to 0.3. We compare production performance, phase saturations and temperature of SAP with different $K_r^o{}_{w(o)}$ values. End-point of oil relative permeability ($K^o_{ro(w)}$) is not changed in these sensitivity analyses.

Figure 6-13 shows that increasing $K_r^o{}_{w(o)}$ leads to an increase in bitumen production rate and ultimate cumulative bitumen recovery with respect to the base case (i.e., $K_r^o{}_{w(o)}$=0.02). Figure 6-13b shows that at $K_r^o{}_{w(o)}$=0.3, second stage of the oil rate profile lasts longer respect to the base case. Also, with increasing $K_r^o{}_{w(o)}$, decline of bitumen production rate from the second peak to the stabilized value is smoother and later. Figures 6-14 and 6-15 show profiles of xC_4, oil saturation, water saturation and temperature for simulation models with $K_r^o{}_{w(o)}$ values of 0.02 and 0.3.

These profiles show that with increasing $K_r^o{}_{w(o)}$, less water accumulates at the bottom of the steam chamber. Therefore, the steam chamber is able to propagate more unfirmly across the width of the reservoir at higher $K_r^o{}_{w(o)}$ values. At $K_r^o{}_{w(o)}$ of 0.3, there is much less area occupied by water at the bottom of the chamber edge compared

with the case with $K_r^o{}_{w(o)}$ of 0.02. Therefore, steam chamber can propagate more in vertical direction. Also, the gasous solvent has more space for condensation at the edge of the chamber instead of accumulating behind the chamber edge in a limited area. Therefore, there is more effective contact area between the condensed solvent and the heated bitumen.

The effect of water accumulation and development of a more conical shape steam chamber by gravity segregation becomes more pronounced during solvent co-injection compared with steam-only injection. This happens mainly during the second and third (i.e. , stabilized region) stages. As mentioned earlier, oil rate reduces at the end of the second stage due to the adverse effect of gravity segregation and water phase accumulation at the bottom of the chamber. Increasing $K_r^o{}_{w(o)}$, leads to the reduction of this effect, later reduction and smoother reduction trend of oil rate from the second region to the stabilized region (Figure 6-13b).

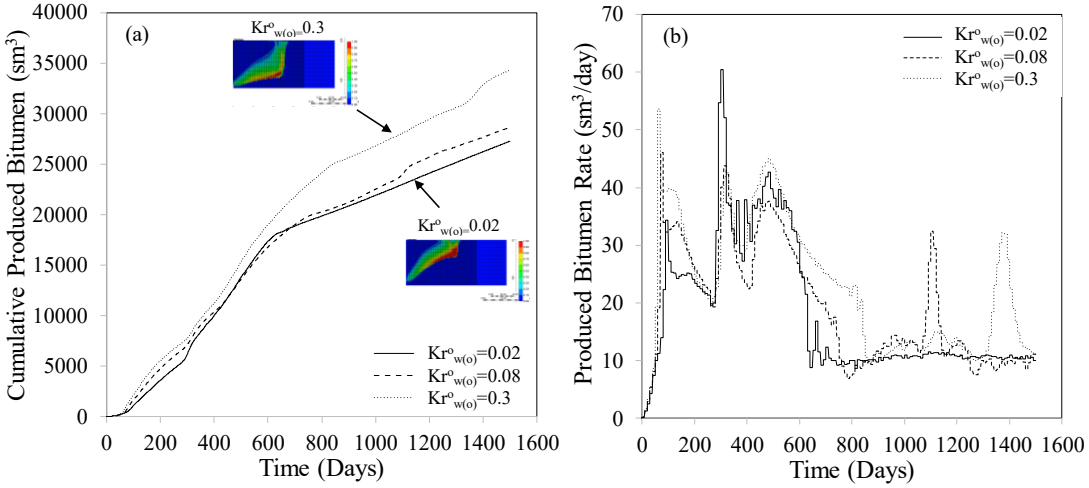

Figure 6-13: Effect of reservoir wettability on a) cumulative produced bitumen and b) produced bitumen rate during SAP

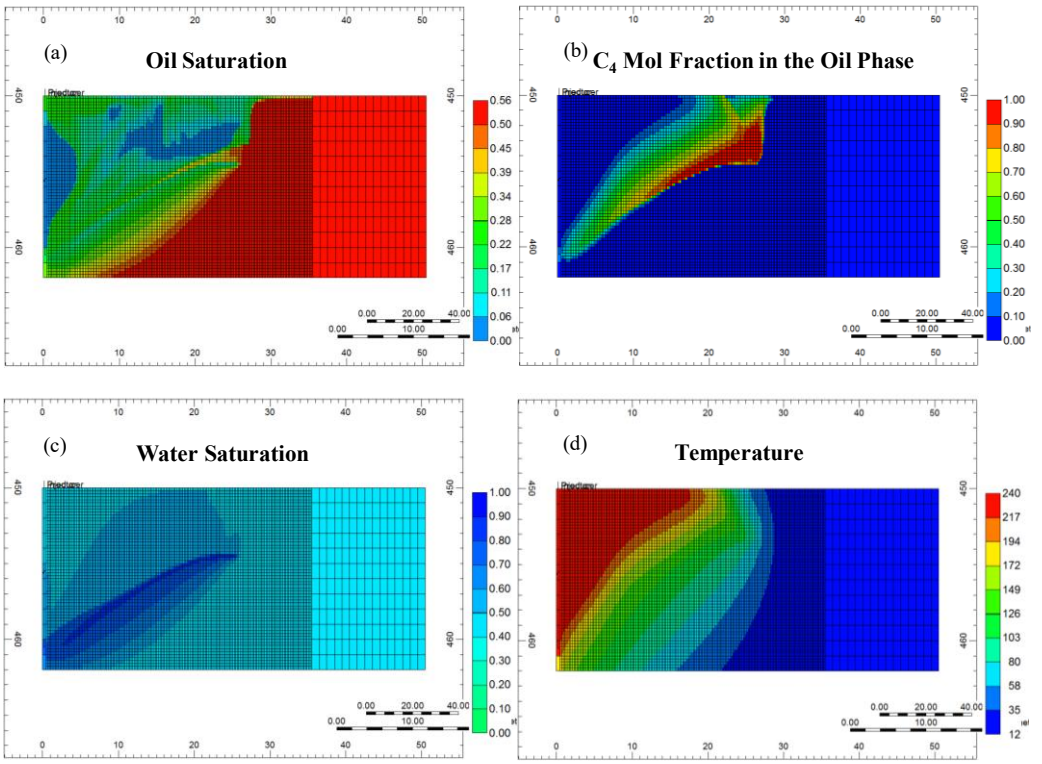

Figure 6-14: Profiles of a) oil saturation b) C_4 mol fraction in the oil phase c) water saturation and d) temperature at the end of simulation for $K_r^o{}_{w(o)} = 0.02$ during SAP

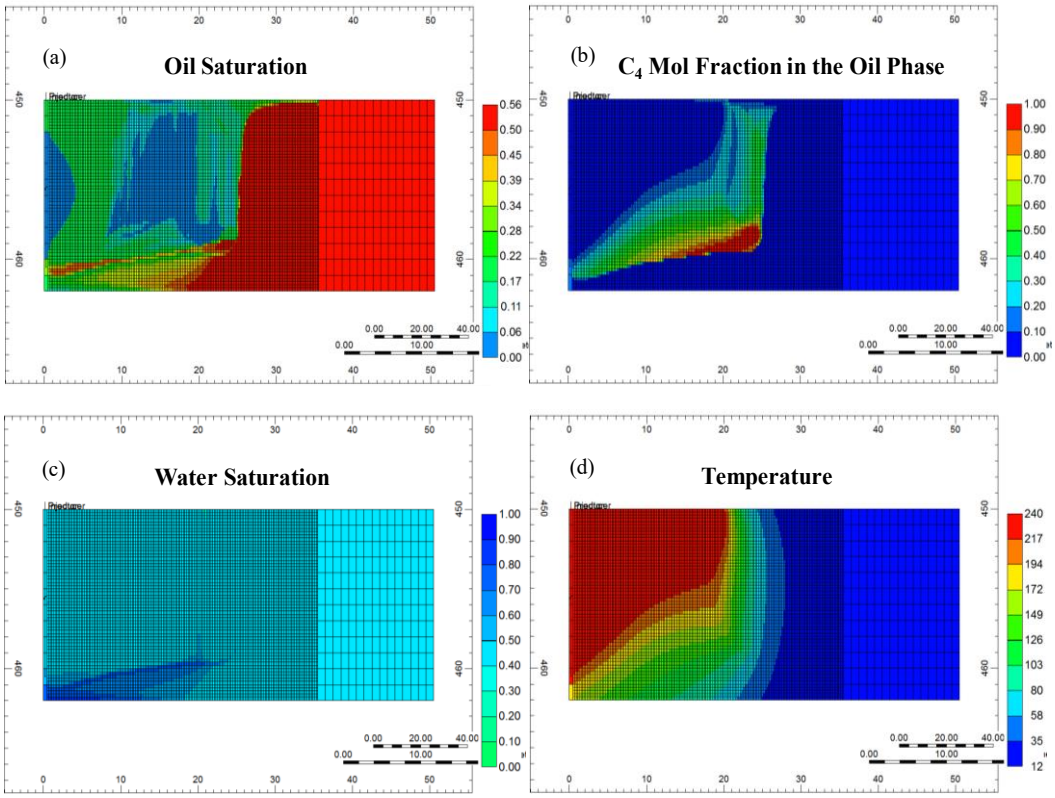

Figure 6-15: Profiles of a) oil saturation b) C_4 mol fraction in the oil phase c) water saturation and d) temperature at the end of simulation for $K_r^o{}_{w(o)}=0.3$ during SAP

6.3.3 Effects of Solvent Type on SAP's Performance

In this section, we investigate the effect of solvent type (i.e., C_4 and C_3) on the performance of SAP. First we compare the production performance of SAP in C_3- and

C_4-steam co-injections with SAGD's. Then we investigate the effect of each solvent on the phase behavior of the system near the edge of the steam chamber.

Solvent cocnentration in the injection stream is 3% mol and 2% mol for C_4 and C_3, respectively. These values will be shown further to be the optimum concentrations at 3500 kPa in constant-concentration strategy. Co-injecting these solvents at the mentioned optimum concentrations result in maximum bitumen recovery among the scenarios with constant-concentration strategy. Figure 6-16 shows profiles of oil production rate, cumulative bitumen production and CSOR for C_3- and C_4-steam co-injection during SAP in comparison with the one during SAGD. Both solvent-steram co-injection processes lead to higher bitumen recovery and lower CSOR compared with those from SAGD process. C_3- and C_4-steam co-injection lead to 1.5% and 5% increase in ultimate recovery factor (URF) at 3500 kPa, respectively. Also, C_3- and C_4-steam co-injection processes reduce CSOR from 6.2 in SAGD to 4.7 and 4.3 sm^3/sm^3, respectively (~30% CSOR reduction).

Production rate in C_3-steam co-injection process is less than the production rate in C_4-steam co-injection process during the three stages of production. We observe that in C_3-steam co-injection process, oil production profile decreases to the stabilized stage later and with smoother trend than in C_4-steam co-injection process. The is because oil rate is less in C_3-steam co-injection process which leads to slower water accumulation and creation of conical steam chamber. Slower water accumulation leads to later beginning of the adverse effect of gravity segregation and delayed start of the stabilized stage. To understand the effect of solvent type on SAP's performance, we explain and compare the effects of C_3 and C_4 on the phase behaviour of the system near the chamber edge.

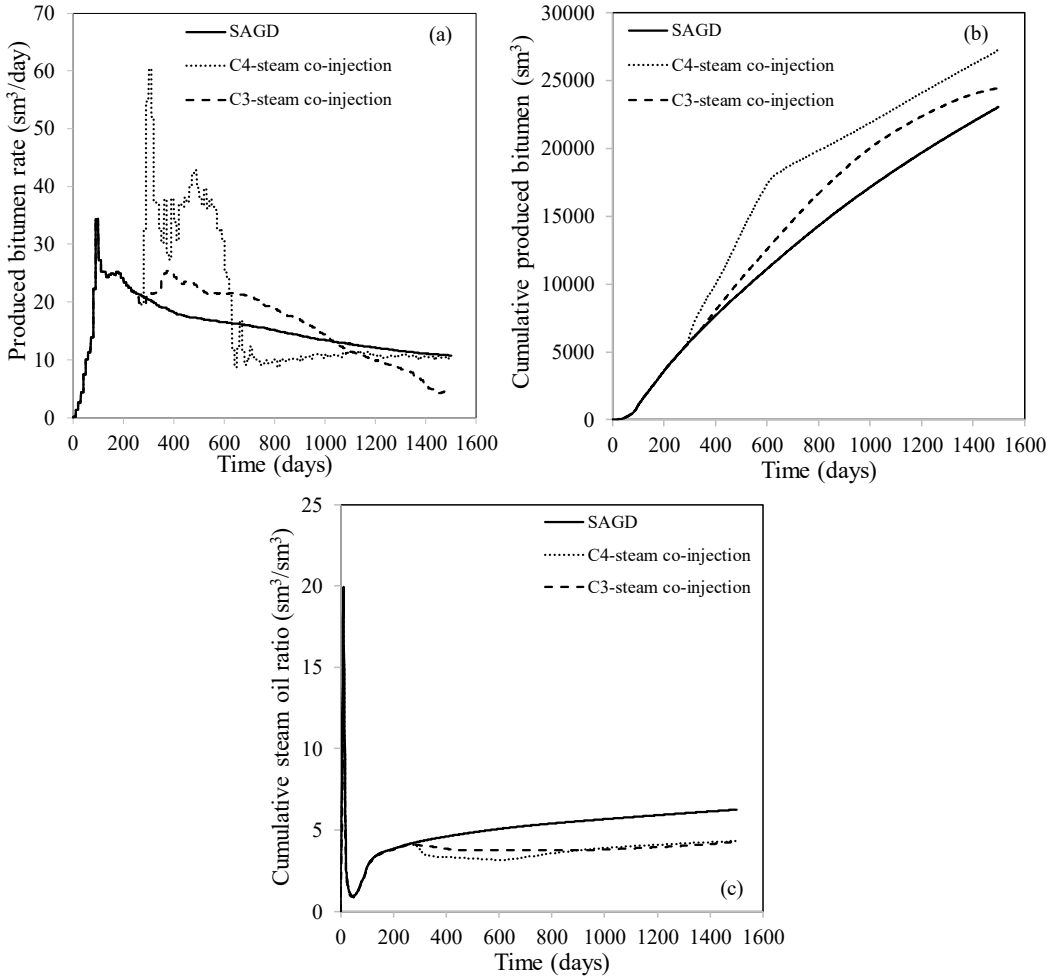

Figure 6-16: Comparison of a) produced bitumen rate b) Cumulative produced bitumen and c) cumulative steam oil ratio between SAGD, C_3-steam co-injection at 2% mol solvent and C_4-steam co-injection processes at 3% mol solvent and 3500 kPa

We also simulated co-injection of CO_2-steam co-injection at 3% mol solvent and 3500 kPa to compare its efficiency with C_3-, and C_4-steam co-injections (see Figure G-1). The results showed that URF in CO_2-steam co-injection reduces by 10.4% respect to the SAGD process. Therefore, we will only investigate the effect of C_3 and C_4 on the efficiceny of SAP.

6.3.3.1 Effects of C_3 and C_4 on Phase Behavior Near the Chamber Edge

we present phase saturations, compositions of C_4 and water in both oil and gas phases and temperature profiles of C_4-steam co-injection process at 3500 kPa and 3% mol C_4 under constant-concentration strategy to understand the effect of C_4 on phase behaviour of steam-C_4-bitumen near the chamber edge.

Figure 6-17 shows the profiles of phase saturations, temperature and components mol fraction in the equilibrated phases vs. horizontal distance from the injection well at 5 m depth below the top of the reservoir for C_4-steam co-injection process. These

profiles include phase saturations, C_4 mol fraction in the oil phase (xC_4), water mol fraction in the gas phase (y_w), C_4 mol fraction in the gas phase (yC_4) for two simulation times of 520 and 890 days. Edge of the steam chamber is shown Figures 6-17a to 6-17f which corresponds to the first block with zero gas saturation away from the steam chamber at a specified depth. The edge of the steam chamber is the interface between L+V+W and L+W regions.

We observe that as water saturation (S_w) increases over the horizontal distance, yw reduces in steam chamber, yC_4 increases and vapor phase gets richer from C_4. Simultaneously, temperature begins to decrease from the injection temperature by increasing yC_4 in the chamber. Near the chamber edge, C_4 condenses as the temperature decreases and xC_4 increases and accumulates in the oil phase. Oil saturation reduces near the edge where both C_4 and water are condensed. Over time (i.e., 890 days), we observe a region rich in C_4 (solvent zone) and a region rich in water (water zone) in front of the chamber edge where gas saturation is zero.

Co-injection of solvent with steam reduces saturation temperature of the vapor phase including vaporized solvent and steam mixture. Steam condenses at the steam-bitumen interface and delivers heat of condensation to the bitumen and reduces bitumen viscosity. As more water condenses at the interface, yw reduces and yC_4 increases. Increase in solvent mol fraction in the gas phase causes more reduction in the saturation temperature of the vapor phase as solvent saturation temperature is much less than water saturation temperature. Gaseous C_4 which travels within the steam chamber reaches the steam-bitumen interface and condenses. Condensed C_4 in the oil phase further reduces oil phase viscosity. Subsequently, mobilized oil phase produces with water along the chamber edge. As temperature is reduced over the horizontal distance, gas phase disappears, C_4 condenses and xC_4 increases in the oil phase. Gradually more C_4 accumulates in the oil phase within the solvent zone in L+W region near the chamber edge. Also, water saturation increases ahead of the solvent zone in L+W region due to water condensation and gravity segregation over time. L+W region is the mixing zone where heated bitumen is diluted with condensed C_4. Oil saturation reduces in this region due to oil production after mixing with condensed water and solvent. Phase behavior of different regions and its effect on the oil displacement during SAGD and SAP is also visualized using ternary diagrams in Appendix E.

Inside the steam chamber and near the edge, we observe a region where C_4 mol fraction in the oil and gas phases (i.e., xC_4 and yC_4) are high. We explain this phenomenon as follows.

Figure 6-18a shows T-xy diagram of solvent-hexane at 2500 kPa with minimum boiling temperature azeotropes of 182 ºC at x=y=0.64. for C_6 concentration less than 0.64 in the vapor phase, water and vapor phases are in equilibrium. Gradually, vapor temperature reduces and C_6 concentration enhances in the vapor phase. This trend lasts until reaching to the azeotrope temperature and concentration where both steam and solvent co-condense (Khaledi et al., 2015). When the temperature of the steam-bitumen interface approaches the azeotrope temperature of solvent-steam mixture, three phases of oil-gas and water co-exist in equilibrium. At this condition, gaseous solvent condenses in the oil phase which leads to high solvent mol fraction in the oil phase (i.e., $xC_6>0.9$ for C_6-steam, Figure 6-18a). This co-condensation temperature of solvent and steam near the steam-bitumen interface increases as solvent volatility decreases. Profile of solvents azeotrope temperature versus solvent mol fraction in the gas phase is shown in Figure 6-18b. As hydrocarbon solvent becomes heavier, temperature increases and solvent mol fraction decreases in the gas phase. As Figure 6-18b shows, C_4 concentration in the gas phase at the azeotrope condition is high in C_4-steam mixture (i.e., $yC_4>0.9$). This may be the reason for observing grid blocks with high yC_4 and xC_4 inside the chamber and near the edge (Figure 6-17c and 6-17d).

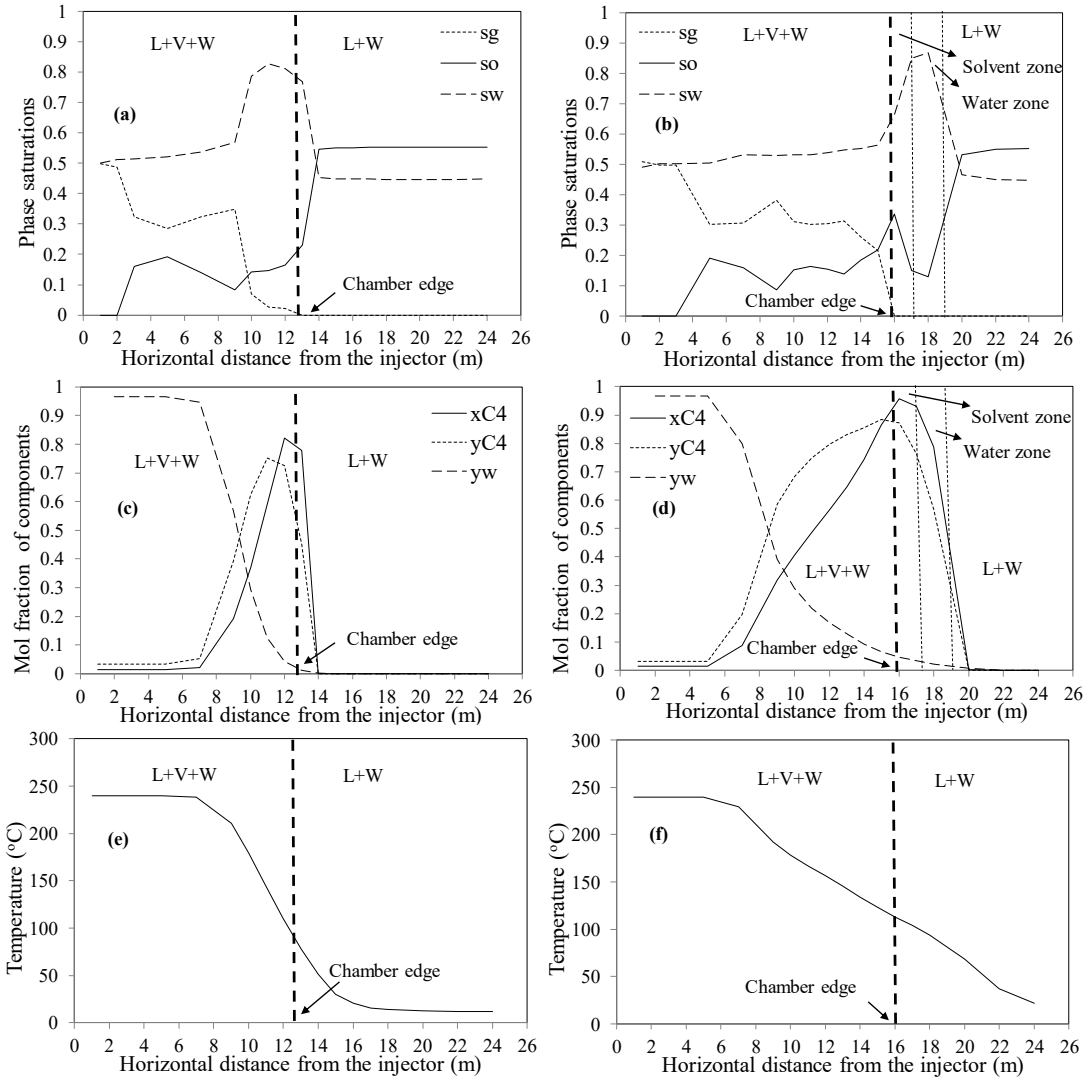

Figure 6-17: Profiles of phase saturations, mol fraction of water in gas phase, mol fraction of C_4 in liquid and gas phases and temperature vs. horizontal distance from the injector at 5 m depth below the reservoir top at 520 days (a, c, e) and 890 days (b, d, f) of simulation

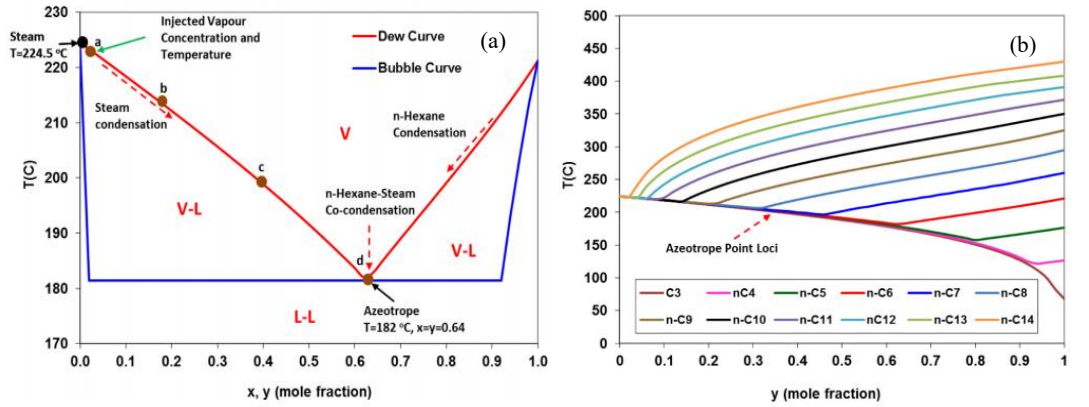

Figure 6-18: Profiles of a) Temperature vs. mol fraction of C_6 in equilibrium phases (T-xy diagram) for nC6-steam system, and b) minimum boiling temperature azotrope loci at 2500 kPa (Khaledi et al., 2015)

We run C_3-steam co-injection process at 3500 kPa and 3% mol C_3 in the co-injection stream to compare the phase saturations, C_3 and water compositions in oil

and gas phases and temperature profiles with C_4-steam co-injection process. Figure 6-19 presents the profiles of phase saturations, C_3 mol fraction in the oil and gas phases, water mol fraction in the gas phase and temperature in C_3-steam co-injection process at 520 and 890 days. As Figures 6-19c and 6-19d show, in front of the chamber edge, xC_3 decreases sharply to zero and mixing zone (i.e., L+W region near the chamber edge) is much thinner than the one in C_4-steam co-injection process. Gas saturation is higher in the chamber for C_3-steam co-injection process compared with C_4-steam co-injection process due to less C_3 solubility compared with C_4 in the oil phase. The maximum gas saturation near the chamber edge reaches 0.4 and 0.1 for C_3-steam and C_4-steam co-injection processes, respectively, at 520 days. Also, chamber edge temperature is 53 ºC and 78 ºC for C_3-steam and C_4-steam co-injection processes, respectively, at 520 days (i.e, 25 ºC temperature difference). Lower chamber edge temperature in C_3-steam co-injection process can be explained by more volatility of C_3 compared with C_4 which leads to lower chamber edge temperature (53 ºC respect to 78 ºC). Higher gas saturation near the chamber edge impedes heat transfer from steam to the oil zone. This also causes less chamber edge temperature in C_3-steam co-injection process compared with C_4-steam co-injection process. C_3 has less solubility than C_4 in bitumen at the same simulation time and solvent concentration in the co-injection stream (i.e., 3% mol). Maximum xC_3 (i.e., 0.75) is less than maximum xC_4 (i.e., 0.82) near the chamber edge at 520 days. C_3 and C_4 solubilities in bitumen at the chamber edge at 520 days are 0.78 and 0.16, respectively. Therefore, oil phase viscosity at the chamber edge is higher for C_3-steam co-injection process (425.4 cP at 520 days) compared with C_4-steam co-injection (0.6 cP at 520 days). This is because there is less solvent solubility in the oil phase and lower chamber temperature in the C_3-steam co-injection compared with C_4-steam co-injection process. All these factors cause slower C_3 diffusion into the oil phase compared with C_4 according to Wilke-Change equation (Chang and Wilke, 1955):

$$D = 7.4 \times 10^{-10} \frac{T(xMw)^{1/2}}{\eta V^{0.6}} \tag{6-1}$$

Here, D is the diffusion coefficient in cm^2/s, T is temperature in K, Mw is molecular weight of bitumen, η is the solution viscosity in poise, V is molar volume of the solvent (i.e., C_3 or C_4) in cc/gmol, x is an associated parameter for the solvent having the value of 1 for unassociated liquids and values of 2.6, 1.9 and 1.5 for water, methanol and ethanol, respectively. At the chamber edge, C_3 and C_4 have diffusion coefficients of

7.9×10^{-12} and 5.9×10^{-9} m^2/s in the oil phase, respectively at 520 days. This causes less C_3 mixing with bitumen and a sharper xC_3 profile near the chamber edge in C_3-steam co-injection process compared with to C_4-steam co-injection process. Lower oil rate near the chamber for C_3-steam co-injection process than C_4-steam co-injection process is another reason for having less convection and solvent-bitumen mixing near the edge.

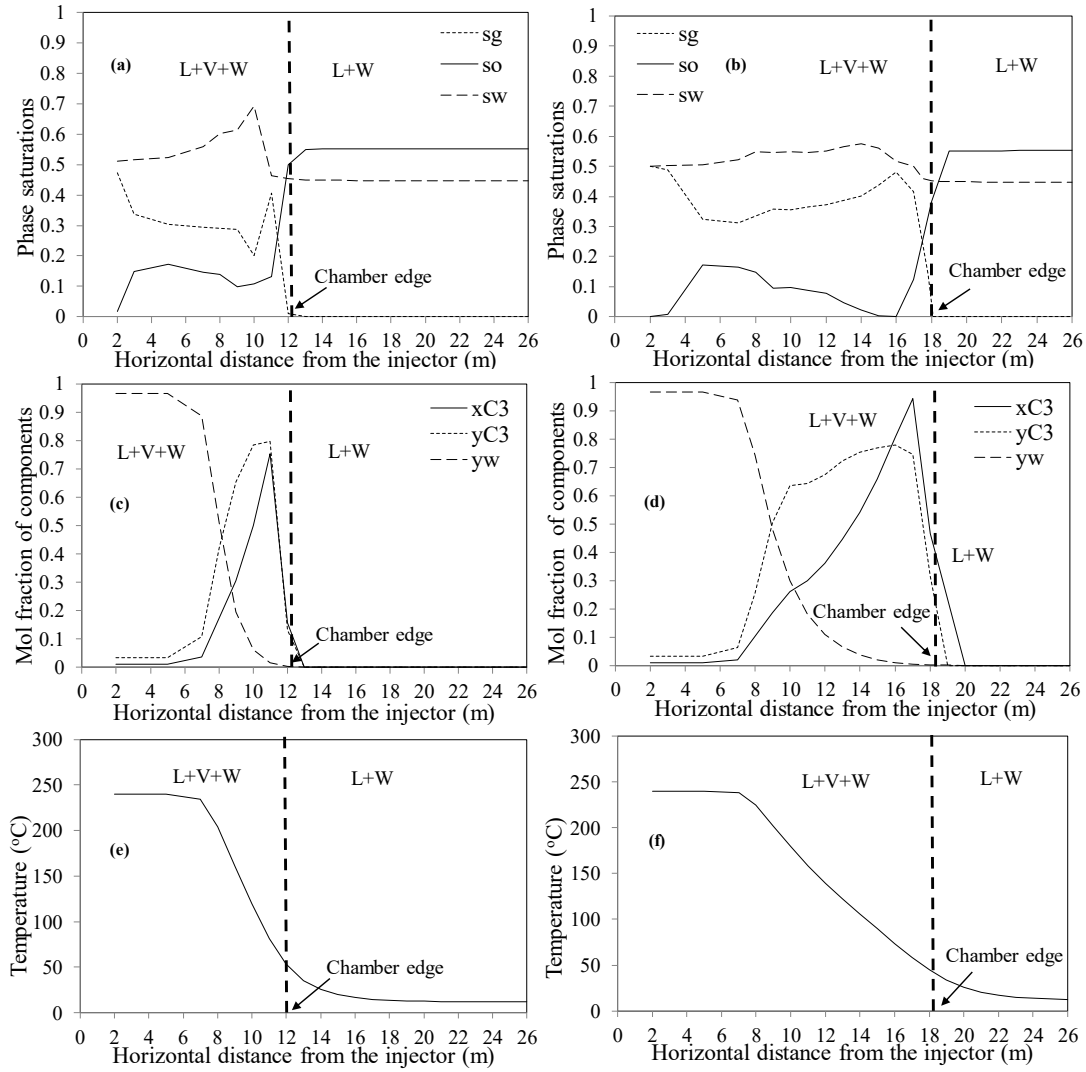

Figure 6-19: Profiles of phase saturations, mol fraction of water in the gas phase, mol fraction of C_3 in liquid and gas phases and temperature vs. horizontal distance from the injector at height of 5 m below the reservoir top at 520 days (a,c,e) and 890 days (b, d, f) simulation

According to Figures 6-19b and 6-19d, solvent and water zones are not observed infront of the chamber edge in C_3-steam process. C_3 condensation temperature is much lower than water condensation temperature compared with that of C_4. In the other words, the difference between C_3 and water condensation temperatures is more than the difference between C_4 and water condensation temperatures. Therfore, C_3 condenses at farther horizontal distance from the injector and from the water compared

with C_4. . Over time, gravity segregation leads to seperation of condesed water and condensed solvent in a way that water zone gets farther from the chamber edge as it was observed in the profiles of C_4-steam co-injection process at 890 days. However, phase behavior plays an stronger role than gravity segregation for C_3-steam co-injection process which leads to observing a thinner mixing zone infront of the chamber edge compared with C_4-steam co-injection process.

Figure 6-20 presents profiles of oil phase viscosity for C_3- and C_4-steam co-injection at 890 days. Table 6-1 summarizes the effects of C_3 and C_4 on the phase behaviour properties near the chamber edge during SAP. We observe that in C_4-steam co-injection, viscosity of the oil phase both inside the steam chamber and near the chamber edge is much lower compared to those in C_3-steam co-injection process. At the chamber edge oil phase viscosity is reduced to 139.6 cP and 0.1 cP for C_3- and C_4-steam co-injections, respectively at 890 days. Comparison of Figures 6-17b and 6-19b show that oil saturation approaches to the minimum values of 0.39 and 0.14 near the chamber edge, in the mixing zone (i.e., L+W region) for C_3- and C_4-steam co-injections, respectively at 890 days. The combined effects of the temperature distribution and solvent-bitumen mixing near the chamber edge lead to lower oil phase viscosity in C_4-steam compared with C_3-steam co-injection. Therfeore, oil displacement near the chamber edge is more efficient in C_4-steam co-injection compared with that in C_3-steam co-injection.

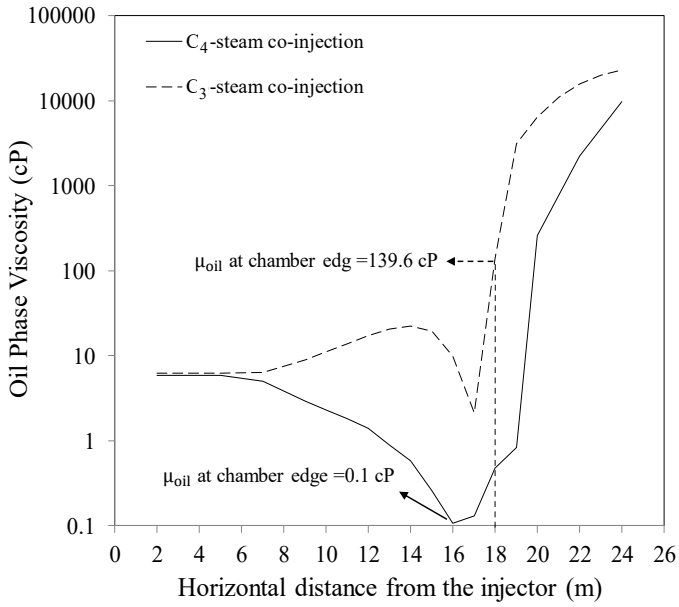

Figure 6-20: Profiles of oil phase viscosity at 890 days for C_3- and C_4-steam co-injection processes at height of 5 m below the reservoir top at 3400 kPa and 3% mol solvent concentration

Table 6-1: Comparison of the phase behaviour properties near the chamber edge between C_3-and C_4-steam co-injection processes

Co-injection Process	T_{sat} of solvent at 3500 kPa (°C)	Maximum Sg near the chamber edge (at 520 days)	Maximum x_s near the chamber edge at 520 days	x_s at the chamber edge at 520 days	T at the chamber edge at 520 days (°C)	μ_{oil} at the chamber edge at 520 days (cP)	Solvent D into the oil phase at 520 days (m^2/s)	μ_{oil} at the chamber edge at 890 days (cP)	Thickness of the mixing zone near the chamber edge	Minimum S_o in the mixing zone at 890 days
C_3-steam	86	0.4	0.74	0.16	53	425.4	7.9×10^{-12}	139.6	Thin	0.39
C_4-steam	147	0.1	0.82	0.78	78	0.6	5.9×10^{-9}	0.1	Thick	0.14

6.3.4 Effects of Solvent Concentration in a Constant-Concentration Strategy

To find the optimum solvent concentration in the co-injection stream, ultimate bitumen recovery factor (URF) and cumulative steam oil ratio (CSOR) are plotted for various solvent (i.e., C_3/C_4) concentration. Figure 6-21 shows URF and CSOR versus C_4 mol% in the co-injection stream at 3500 kPa. As Figure 6-21a shows, at 3500 kPa, URF reaches to the maximum value at 3% mol C_4. For C_4 concentrations above 3%, URF decreases and CSOR has no significant reduction. Therfore, 3% mol is the optimum C_4 concentration during SAP at 3500 kPa. Figure 6-21b shows that optimum C_3 mol% in the co-injection stream is 2% at 3500 kPa. The reason is that additional solvent more than the optimum concentration exceed the solvent solubility in the oil phase at the reservoir pressure and temperature near the chamber edge. Therefore, extra solvent goes to the gas phase which reduces steam chamber temperature and consequently the heating effect of the steam chamber. Below the optimum concentration solvent concentration is not enough to effectively dilute the bitumen. Therefore, bitumen recovery becomes maximum at optimum solvent concentration.

As the operating pressure of the process changes, the optimum solvent concentration changes. We estimated the optimum C_4 and C_3 concentrations at lower (3000 kPa) and higher (4000 kPa) opertaing pressure conditions as presented in Appendix G. Figures G-1 and G-2 show that optimum solvent concentration decreases by increasing operating pressure. At lower operating pressures, temperature of the steam chamber is lower. Therefore, more solvent is required to compensate for the lower rate of heat transfer between the steam and bitumen. The optimum values for C_3 are less than the ones for C_4 at each pressure. C_3 solubility is less than C_4 solubility in bitumen. Therefore, threshold C_3 concentration in the system of C_3-bitumen is less than threshold C_4 concentration for effective bitumen viscosity reduction. This leads to less optimum concentration for C_3 than C_4 at each pressure.

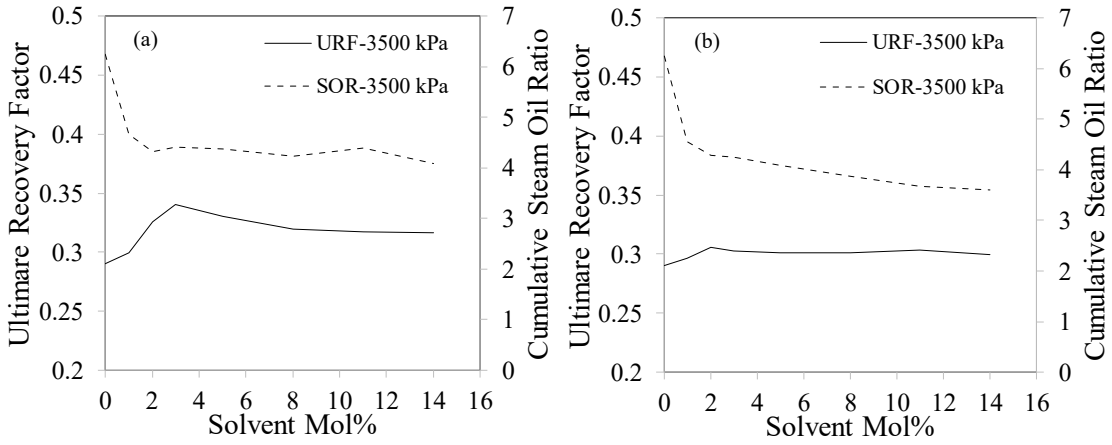

Figure 6-21: Ultimate bitumen recovery factor (URF) and cumulative steam oil ratio (CSOR) versus a) C_4 mol% and b) C_3 mol% in the constant-concentration strategy during SAP at 3500 kPa

6.3.5 Effects of Constant- and Variable-Concentration Strategies

Compared with the constant-concentration strategy, we design scenarios which inject a higher solvent concentration during early periods and then switching to lower concentrations during later periods. The reason for the descending trend is that we observed no improvement in oil production rate by more solvent-steam co-injection after about one year of co-injection.

6.3.5.1 C_4-Steam Co-injection during SAP

In this part, we designed scenarios with variable-concentration strategy in which the average C_4 concentration is 3% mol. We estimated NPV for each scenario including the constant-concentration strategy i.e., (3-3-3)% and the designed variable-concentration strategies to select an optimum co-injection scenario. It is worthy to mention that in our simulation model injection rate increases by increasing solvent concentration and this increases total volume of injected solvent and steam in variable-concentration strategies compared with those in constant-concentration strategy. The reason is that the injection well in the simulation model works based on the constraint of maximum bottom hole pressure. Therefore, by increasing solvent concentration, oil rate increases and steam chamber grows faster. This results in higher oil and gas production rates and more gas injection rate to meet the set bottom hole pressure. In the variable-concentration strategies, since the early-time solvent concentration increases, early-time injected steam and solvent increases. This results in increasing total injected solvent and steam volume compared with those in constant-concentration strategy. Before this, we explain how early-time (i.e., during the first year of colvent-steam co-injection) higher concentration and late-time lower concentration in variable-

concentration strategies affect bitumen and solvent recoveries.Early-time is the first year of solvent-steam co-injection and late-time is the third year of co-injection.

6.3.5.1.1 Effects of constant- and variable-concentration strategies on bitumen recovery

Figure 6-22 shows profiles of produced bitumen rate and cumulative produced bitumen for the constant-concentration strategy of C_4-steam co-injection (i.e., (3-3-3)%) and for (6-2-1)% representing the variable-concentration strategies. Figure 6-22b shows lower cumulative bitumen production in the variable-concentration strategy compared with the constant-concentration strategy in C_4-steam co-injection process. In the variable-concentration strategy by increasing early-time solvent concentration more than the average value (i.e., 3%), oil rate increases in this period. However, as early-time oil rate increases, water accumulates earlier at the bottom of the steam chamber and subsequently the unfavorite gravity segregation effect starts earlier compared with the case with constant-concentration strategy. Therfore, the stabilized stage reaches earlier and oil rate reduces earlier with sharper trend than the case with the constant-concentration strategy. This causes reduction in the cumulative produced bitumen.

Figure 6-23 presents cumulative produced bitumen, total recovered solvent, CSOR and NPV for the constant-concentration strategy and the variable-concentration strategies of C_4-steam co-injection process. We observe that CSOR of all scenarios with variable solvent concentration are higher than that for (3-3-3)% scenario. The reason is that bitumen recovery does not improve by increasing volume of injected steam. Solvent recovery for the variable-concentration strategies increases compared with the constant-concentration strategy one, however, bitumen recovery reduces. (3-3-3)% scenario maximizes bitumen recovery, minimizes CSOR and maximizes NPV. This scenario enhances bitumen recovery factor by 5% and reduces CSOR by 33% respect to SAGD process.

6.3.5.1.2. Effect of variable-concentration strategy on solvent recovery

Figure 6-23 shows that solvent recovery increases in variable-concentration strategies compared with that in constant-concentration strategy. In C_4-steam co-injection process, as the solvent concentration reduces over time, solvent recovery increases. The recovered solvent comes mainly from the gas phase. The produced oil phase carries bitumen and dissolved solvent. Therefore, higher the bitumen recovery

higher the solvent recovery from the oil phase. In C_4-steam co-injection, when oil recovery is decreased by decreasing solvent concentration, the recovered solvent from the oil phase decreases. However, the increased total solvent recovery is compensated by increasing solvent recovery from the gas phase. Also, as the oil phase production rate reduces, oil saturation reduces near the production well and this may lead to higher gas saturation and gas relative permeability. Therefore, by reducing oil production, additional solvent is recovered from the gaseous phase in the reservoir.

As the solvent concentration decreases during the second and thrid stage of solvent-steam co-injection, solvent recovery increases. During the second and third stages, water accumulations by gravity segregation causes adverse effect on oil and solvent recovery. As solvent co-injection reduces during these periods, adverse effect of gravity segregation decreases and more solvent is produced.

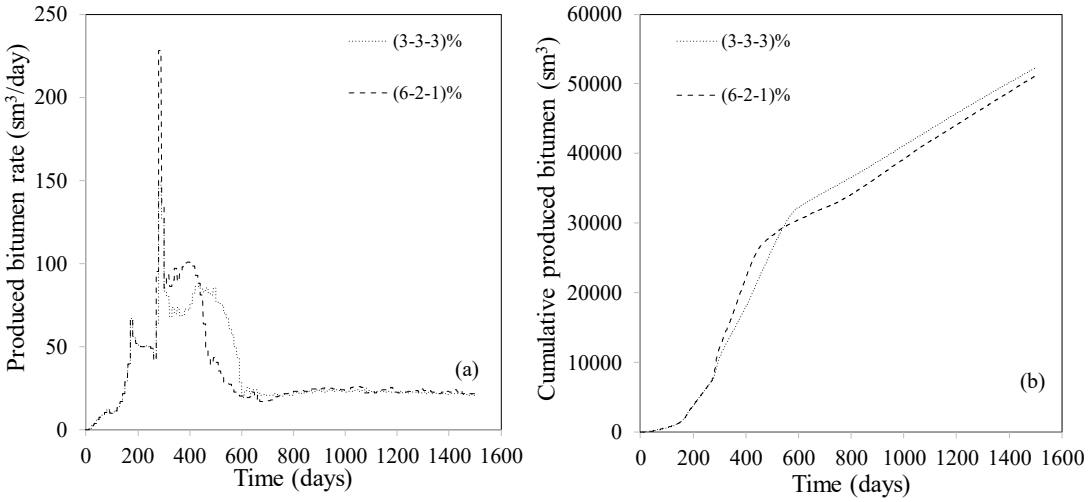

Figure 6-22: Comparison of the a) produced bitumen rate and b) cumulative produced bitumen vs. time between the optimum constant-concentration strategy (3-3-3)% and (6-2-1)% variable-concentration strategy for C_4-steam co-injection during SAP at 3500 kPa

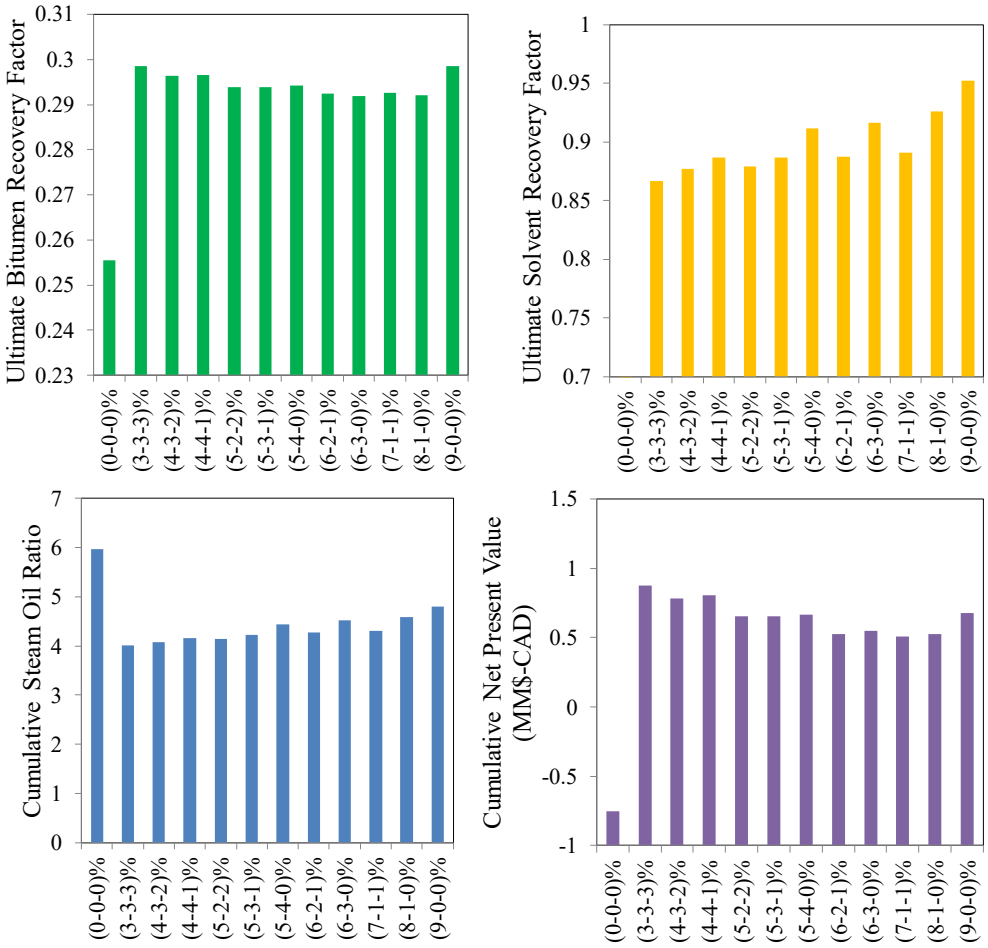

Figure 6-23: Comparison of the ultimate cumulative bitumen production and estimated Net Present Value (NPV) between different co-injection scenarios and variable C_4 concentration in the injection stream at 3500 kPa

6.3.5.2 C_3-Steam Co-injection during SAP

We designed scenarios with variable-concentration strategy where average C_3 concentration is 2% mol, the optimum concentration in constant-concentration strategies. We estimated NPV for each scenario including the constant-concentration strategy i.e., (2-2-2)% and the designed variable-concentration strategies to maximize performance of this process.

6.3.5.2.1. Effect of variable-concentraration strategy on bitumen recovery

Figure 6-24 shows profiles of produced bitumen rate and cumulative produced bitumen for the constant-concentration strategy of C_3-steam co-injection (i.e., (2-2-2)%) and for (4-1-1)% among the variable-concentration strategies. We observe higher cumulative bitumen production in the variable-concentration strategy compared with the constant-concentration strategy in C_3-steam co-injection process. Lower oil rate of C_3-steam co-injection process compared with C_4-steam co-injection process leads to slower water accumulation. This leads to slower impact of gravity segregation on oil

production rate than that in C_4-steam co-injection case. Therefore, higher solvent concentration during the early time has less impact on enhancing adverse effect of gravity segregation and reduction of bitumen recovery in C_3-steam process compared to C_4-steam proccess. Moreover, lower oil production rate causes slower propagation of steam chamber in C_3-steam co-injcetion process compared with C_4-steam co-injection process. Therefore, increasing early time solvent concentration may have positive effect on early time propagation of steam chamber and increase in early time oil production rate. As dicussed earlier, existance of C_3 in the reservoir causes more reduction in the temperature of chamber edge compared to C_4. Therefore, the scenarios with less late-time C_3 concentration in late time, have the chance of producing more bitumen (i.e., higher stabilized oil rate) compared with the constant-concentration strategy. As Figure 6-24b shows, increasing early time concentration compared with the constant-concentration strategy, causes a sharper reduction in the oil production rate to a stabilized rate. However, due to the increase in early time and late time (i.e., stabilized) rates, cumulative produced bitumen increases.

Figure 6-25 presents cumulative produced bitumen, total recovered solvent, CSOR and NPV for the constant-concentration strategy with optimum concentration and the designed variable-concentration strategies C_3-steam co-injection process. We observe that bitumen recovery increases in some of variable-concentration strategies compared with the constant-concentration strategy in C_3-steam co-injection process. (4-1-1)% scenario maximizes bitumen recovery, minimizes CSOR and maximizes NPV.

6.3.5.2.2. Effect of variable-cocentration strategy on solvent recovery

As Figure 6-25 shows, all variable-concentration strategies have higher solvent recovery compared with the constant-concentration strategy. This is because reducing solvent concentration over time leads to increasing solvent recovery. (4-1-1)% scenario still has higher solvent recovery compared with the constant-concentration strategy. Although other variable-concentration scenarios have more solvent recovery than (4-1-1)%, NPV is maximum for this scenario.. As a result of lower C_3 price respect to the oil price in NPV calculation, the effect of solvent recovery on NPV is less than the effect of bitumen recovery. (4-4-1)% scenario maximizes bitumen recovery, minimizes CSOR and maximizes NPV. This scenario enhances bitumen recovery factor by 2.6% and reduces CSOR by 34% respect to SAGD process.

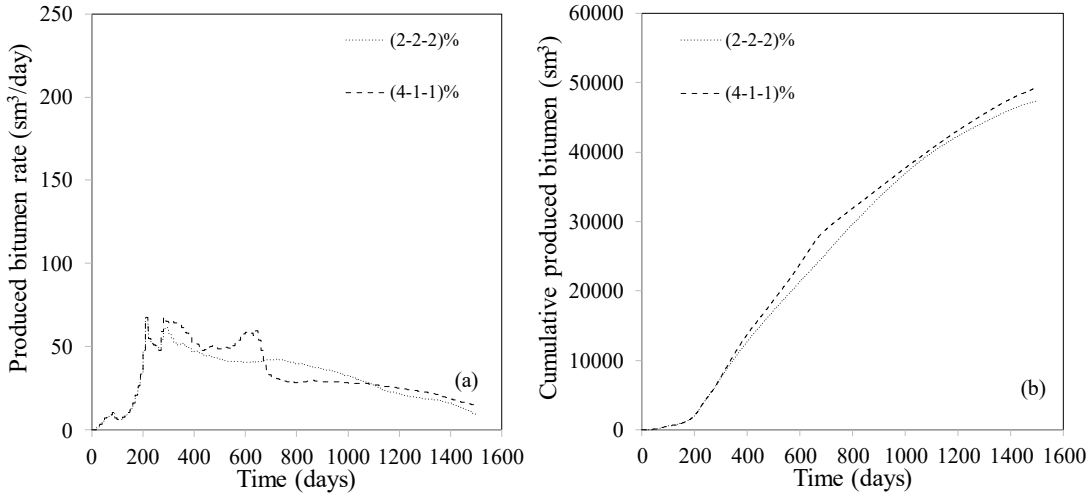

Figure 6-24: Comparison of the a) produced bitumen rate and b) cumulative produced bitumen vs. time between the optimum constant-concentration strategy (2-2-2)% and optimum variable-concentration strategy (4-1-1)% for C_3-steam co-injection during SAP at 3500 kPa

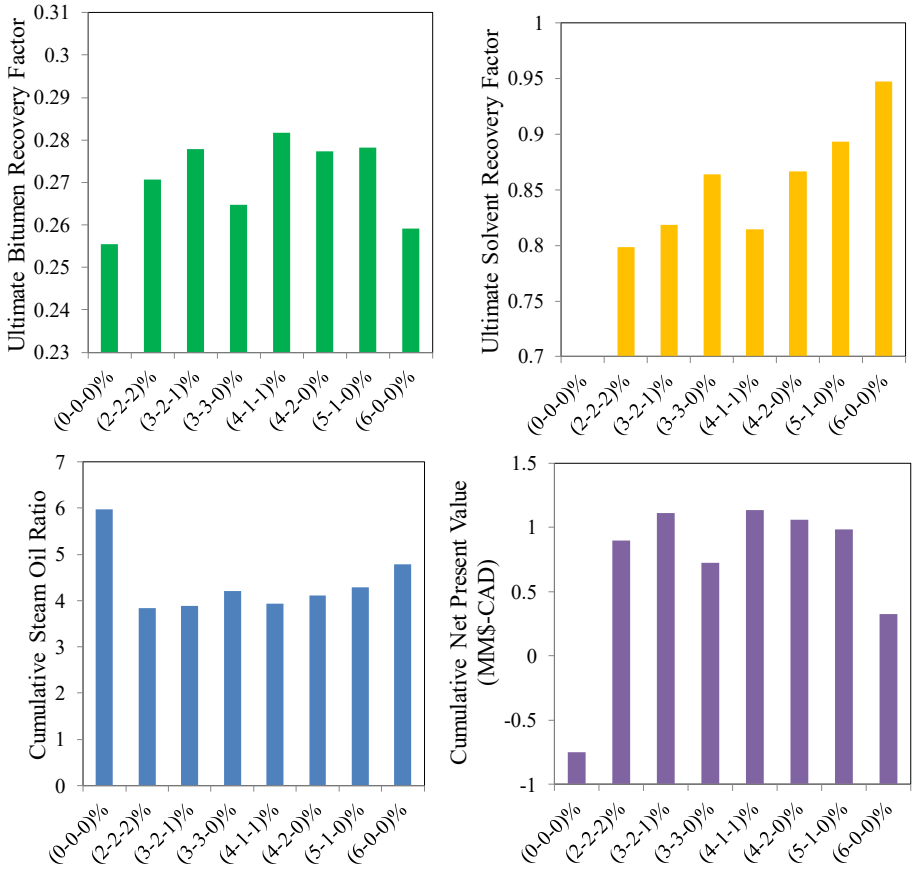

Figure 6-25: Comparison of the ultimate cumulative bitumen production and NPV between different scenarios with variable C_3 concentration in the injection stream at 3500 kPa

6.4 SUMMARY

In this Chapter, we investigated the effect of key parameters controlling efficiency of Solvent-Aided-Process (SAP). We also optimized co-injection of C_3- and C_4-steam during SAP in terms of solvent concentration and co-injection strategy. The main conclusions from this study are as follows:

1. Senitivity analysis on grid block size showed optimum grid size of 0.2 m. More refinement below 0.2 m increases simulation time significantly and has insignificant effect on numerical dispersion.

2. Fine-scale simulations showed three main stages of oil recovery during Solvent Aided Process (SAP). Oil production rate reaches to two peaks during the first and second stages then reduces to an stabilized value. During the first stage, oil production rate increases as a result of C_4 condensation near the chamber edge and dilution of the heated bitumen. During the second stage, chamber grows laterally, and local oil displacement improves in the chamber. However, as water accumulates at the bottom of the chamber, adverse effect of gravity segregation reduces the oil production rate to a stabilized rate in the third stage.

3. Increasing the end-point of water relative permeability ($K_r^o{}_{w(o)}$) has siginificant effect on bitumen recovery during SAP. Increasing $K_r^o{}_{w(o)}$ leads to an increase in bitumen recovery by reducing adverse effects of water accumulation and gravity segregation. As $K_r^o{}_{w(o)}$ increases, water blockage at the bottom of the steam chamber reduces. Therefore steam chamber volume and also the effective contact area between the condensed solvent and the heated bitumen increase.

4. Applying C_3- and C_4-steam co-injection with their optimized strategies during SAP lead to 2.6% and 5% increase in SAGD ultimate bitumen recovery factor at 3500 kPa, respectively. C_3- and C_4-steam co-injections reduce SAGD cummulative steam oil ratio (CSOR) by 34% and 33%, respectively.

5. Co-injection of solvent with steam reduces chamber edge temperature. As temperature reduces over horizontal distance from injector, gas phase approaches zero and condensed C_4 accumulates in the oil phase, mixes with heated bitumen and reduces bitumen viscosity within the mixing zone. In this zone, condensed water and diluted bitumen produce along the chamber edge. Over time, two regions rich in condensed solvent and rich in water appears in the mixing zone due to gravity segregation.

6. Compared with C_4-steam co-injection process, bitumen viscosity near the chamber edge is higher in C_3-steam co-injection process. This is because there is less solvent (i.e., C_3) solubility in the oil phase and lower chamber temperature in the C_3-steam co-injection process. Higher bitumen viscosity and lower chamber edge temperature decreases C_3 diffusion rate into bitumen compared with the C_4 case. The combined effects of the temperature distribution and solvent-bitumen mixing near the chamber edge lead to lower oil phase viscosity near the chamber edge in C_4-steam compared with C_3-steam co-injection. This results in more efficient oil displacement near the chamber edge in C_4-steam co-injection compared with that in C_3-steam co-injection.

7. Mixing zone near the chamber edge in C_3-steam co-injection process is much thinner than the one in C_4-steam co-injection process. This is because compared to C_4, C_3 has slower diffusion into bitumen. Also, oil production rate is less in C_3-steam co-injection process compared with C_4-stream co-injection.

8. Optimum strategy for C_4-steam co-injection process is co-injecting C_4 with steam at constant 3% mol concentration at 3500 kPa. The optimum strategy for C_3-steam co-injection process is co-injecting C_3 with steam at 4%, 1% and 1% mol concentrations in three stages of 410 days. The C_3-steam co-injection is performed after 3 months preheating and 6 months steam-only injection at 3500 kPa.

9. In strategies with variable solvent concentration, higher C_4 concentration than the average value at the early times, increases early time oil rate. However, higher early time oil rate accelerates the adverse effect of gravity segregation and causes earlier oil rate reduction to the stabilized rate. In variable-concentration strategies, as the solvent concentration reduces in later times, solvent recovery increases.

10. In contrast with C_4-steam co-injection process, variable-concentration strategies with higher C_3 concentration at early times and lower concentration at late time have the chance of increasing ultimate bitumen recovery. Less oil rate of C_3-steam co-injection process leads to slower water accumulation and less adverse effect of gravity segregation. Therefore, in C_3-steam co-injection process, higher early time solvent concentration has less impact on the adverse effect of gravity segregation compared to C_4-steam co-injection proccess. Moreover, increasing early time solvent concentration may accelerate early time propagation of steam chamber.Also, compared to C_4, existance of C_3 in the reservoir causes more reduction in the

temperature of chamber edge. Therefore, less C_3 concentration at the late times, have the chance of producing more bitumen (i.e., higher stabilized oil rate) compared with the constant-concentration strategy.

6.5 NOMENCLATURE

BIP	Binary interaction parameter
CSOR	Cumulative steam oil ratio
D	Diffusion coefficient (cm^2/s)
EOS	Equation of State
GOR	Gas oil ratio (sm^3/sm^3)
L	Oleic phase
MW	Molecular weight
NPV	Net Present Value
PC	Pseudo component
PR-EOS	Peng-Robinson equation of state
URF	Ultimate recovery factor
V	Vapor phase
W	Aqueous phase

Greek symbols

ω	Acentric factor
η	Solution viscosity in Eq (6-1) (poise)
μ	Dynamic viscosity (cP)
ρ	Density (kg/m^3)

Roman symbols

C_t	Net cash flow during period t in NPV Eq. (F-1)
C_o	Total investment cost
Krgl	Gas relative permeability at initial liquid saturation
Krow	Oil relative permeability at initial water saturation
Krwo	Water relative permeability at residual oil saturation
K_i	Equilibrium constant of ith component
N_p	Cumulative oil production (sm^3)
P_{sat}	Saturation pressure (kPa)
P_{inj}	Injection pressure (kPa)
Pc	Critical pressure (kPa)
r	Discount rate
$R_{royalty}$	Royalty rate in Eq. (F-2)
R_{tax}	Tax rate in Eq. (F-2)
Sorg	Residual oil saturation in presence of gas
Sorw	Residual oil saturation in presence of water (sorw)
Sw	Water saturation
T_b	Boiling point temperature (K)
T_c	Critical temperature (K)
V_c	Critical volume ($cm^3/gmol$)
w	Weight fraction
x	Mole fraction
xC_4	Mol fraction of C4 in oleic phase
yw	Water saturation in the gas phase
yC_4	Mol fraction of C4 in gas phase
z	Overall mole fraction

Chapter 7: Conclusions and Recommendations

In Chapter 3, we presented a new algorithm for global minimization of the Gibbs Free Energy for isothermal, isobaric flash. We showed that the advantage of the new algorithm in terms of robustness and efficiency is more pronounced for more complex phase behavior, in which multiple local minima of the Gibbs Free Energy are present. One example of this complex phase behavior is co-existence of two oleic phases. This is possible at the edge of the steam chamber during C_4-steam co-injection where C_4 accumulates near the edge. In Chapter 4, we characterized the multiphase behavior of CO_2-, C_3-, and C_4-bitumen systems by conducting CCE tests on Clearwater bitumen from the Cenovus Osprey Pilot. A PR-EOS model was regressed to data from the CCE tests to predict solvent solubility at reservoir pressure and different temperatures. We also experimentally investigated the effect of solvents on asphaltene precipitation at elevated temperatures. In Chapter 5, viscosity of the saturated bitumen with CO_2, C_3 and C_4 was measured and a viscosity model was adjusted to the measured data to predict viscosity of light solvents-bitumen mixtures as a function of solvent solubility and temperature. A threshold solvent concentration was estimated for each solvent at reservoir pressure and elevated temperatures. In Chapter 6, we investigated the effect of key parameters on efficiency of SAP using fine-scaled simulations. We also optimized C_3-, and C_4-steam co-injection during SAP. The main conclusions from this study are presented as follows:

1. In contrast to the sequential stability/flash approach, the number of equilibrium phases is part of the solution in the new algorithm developed for multiphase equilibria calculation. Therefore, false solutions are not necessary for multiphase flash with the new algorithm. The advantage of the new algorithm in terms of robustness and efficiency is more pronounced for more complex phase behavior, in which multiple local minima of the Gibbs Free Energy are present. One example of this complex phase behavior is co-existence of two oleic phases. This is possible at the edge of the steam chamber during C_4-steam co-injection where C_4 accumulates near the edge.

2. The new algorithm can be initialized with either a biased or unbiased scheme because it can handle an arbitrary number of sampling compositions. This also yields the flexibility that the algorithm offers in terms of robustness and efficiency. For example, one can initialize the algorithm with more sampling compositions for enhanced robustness by capturing more information regarding the Gibbs Free Energy during the iteration.

3. Experimental data of CO_2-, C_3- and C_4-bitumen systems and multiphase-equilibrium calculations indicate that C_4 has much higher solubility in bitumen than C_3 and CO_2 at reservoir pressure and elevated temperatures. At 120°C<T<180°C and 4000 kPa, maximum C_4 solubility in bitumen (i.e., 60 wt.%) is higher than the maximum solubility of C_3 (14.9 wt.%) and CO_2 (2.5 wt.%) in bitumen.

4. The C_4-bitumen CCE tests show the development of a secondary oleic phase (L_2) at 84.6 wt.% C_4. Three phases exist in equilibrium: a C_4-lean oleic phase (L_1) containing the highest amount of heavy-hydrocarbon components, a light (C_4-rich) oleic phase (L_2), and a vapor (V) phase that is almost pure C_4. CCE test observations indicate the extraction of heavier components by the L_2 phase at higher pressures. The L_2 phase becomes darker by extracting heavier hydrocarbon components from the L1 phase.

5. Compositional analysis and asphaltene-content measurement of the samples from the L1 and L2 phases indicate that C_4 can upgrade bitumen by extracting light-hydrocarbon components into the L_2 phase.

6. According to the experimental results, the C_4-bitumen system exhibits liquid/liquid separation at T<140 ºC. In contrast with CO_2-bitumen and C_3-bitumen systems, the EOS model indicates two types of two-phase regions for the C_4-bitumen system (L_1/L_2 in 120ºC<T<148ºC and L_1/V in 148 ºC<T<180ºC). C_4 solubility increases significantly by increasing the concentration up to the value where the V/L_2 phase forms. However, by the appearance of the L_2 phase, a reduction in C_4 solubility occurs. Also, when the vapor phase forms, C_4 solubility cannot be increased further.

7. Simulated distillation results show that the L_1 phase from the C_4-bitumen CCE test is heavier than the L_1 phase from the C_3-bitumen CCE test and both are heavier than the original bitumen. Although C_3 may cause formation of asphaltene in the L_1 phase, C_4 can extract lighter hydrocarbon components into a C_4-rich liquid phase (L_2),

resulting in a heavier liquid phase (L_1). The extracting-condensing mechanism and asphaltene precipitation result in a lighter L_1 phase in C_3-bitumen system than that in C_4-bitumen system.

8. C_3 and C_4 cause more asphaltene precipitation than CO_2. One reason can be an increase in the ratio of saturate to asphaltene of solvent-bitumen system by introducing C_3 and C_4 compared with CO_2. Another reason can be the higher solubility of C_3 and C_4 than CO_2 in bitumen. Mixing a high amount of C_3 with bitumen (i.e., 78.3 wt.% C_3) causes significant asphaltene precipitation in the L_1 phase. C_3 has more potential for asphaltene precipitation than C_4, and asphaltene precipitation by C_3 increases significantly by increasing C_3 dissolution. Application of C_3 and C_4 at high concentrations may cause asphaltene precipitation in solvent-based and solvent-aided thermal methods.

9. Viscosity measurements show that C_3 and C_4 dissolution in bitumen results in greater viscosity reduction than CO_2 and C_1 dissolution for $50°C<T<165$ °C. This difference is more pronounced at lower temperatures. For each solvent studied, the viscosity reduction effect by solvent dissolution is more pronounced at lower temperatures. The reason is that at high temperatures, the effect of solvent dissolution is masked by the significant effect of increasing temperature on reducing the dead oil viscosity. Also, higher pressure is required to increase solvent solubility by a specific amount at higher temperature. Higher pressure lead to more increase in liquid viscosity. Therefore, viscosity reduces more slowly by increasing solubility at higher temperatures.

10. The modified viscosity model can predict viscosity of light solvents-bitumen mixtures in a wide range of temperature (i.e., 50°C to 165°C). This correlation is superior to the existing correlations for predicting viscosity of liquid mixtures as it requires minimum number of data (i.e., solubility and temperature) as the input and is simpler to be applied in thermal reservoir simulators. The modified viscosity model showed better performance than the existing correlations in predicting CO_2-, C_3-, C_4-bitumen viscosity data from literature.

11. The experimental solubility and viscosity data from this study can be used to optimize the recovery from solvent-based and solvent aided processes.

12. C_4 has the potential to be used in hot solvent injection methods in shallow and deep oil sand reservoirs. C_3 may be a more effective solvent in deeper reservoirs during hot solvent injection and solvent aided processes. The reason is that C_4 has high solubility at low temperature and pressure. Also, solvents have more effective viscosity reduction at lower temperatures. Compared to C_4, C_3 has a similar solubility as C_4 in bitumen at higher pressures and a specific temperature.

13. Additional solvent above solvent threshold concentration, has insignificant effect on solvent solubility and reducing bitumen viscosity. The minimum threshold concentration for CO_2, C_3 and C_4 is 1.8 wt.%, 6.2 wt.% and 12.5 wt.%, respectively, for $120°C<T<180°C$. At these concentrations, bitumen viscosity can be reduced by 1.7, 5.6 and 15.2 times by CO_2, C_3 and C_4, respectively at 120°C.

14. Co-injection of C_4-steam leads the dilution of the heated bitumen, lateral growth of the steam chamber and improvement in local oil displacement. All these lead to an increase in oil production rate. However, oil production rate reduces by additional solvent-steam co-injection after a while. This is because water accumulates at the bottom of the chamber. This reduces steam chamber volume and the effective contact area between the condensed solvent and the heated bitumen.

15. Reservoir wettability has siginificant effect on performance of SAP. As the reservoir gets less water wet, bitumen recovery increases due to reducing water blockage at the bottom of the steam chamber.

16. Co-injection of solvent with steam reduces chamber edge temperature. As temperature reduces over distance, gas phase disappears and condensed C_4 accumulates in the oil phase, mixes with heated bitumen and reduces bitumen viscosity (i.e., mixing zone).

17. Compared with C_4-steam co-injection process, bitumen viscosity near the chamber edge is higher in C_3-steam co-injection process. This is because there is less solvent solubility in the oil phase and lower chamber temperature in the C_3-steam co-injection process. Higher bitumen viscosity and lower chamber edge temperature decreases C_3 diffusion rate into bitumen compared with C_4 case. Mixing zone near the chamber edge in C_3-steam co-injection process is much thinner than the one in C_4-steam co-injection process. The combined effects of the temperature distribution and solvent-bitumen mixing near the chamber edge lead to lower oil phase viscosity near

the chamber edge in C_4-steam compared with C_3-steam co-injection. This results in more efficient oil displacement near the chamber edge in C_4-steam co-injection compared with that in C_3-steam co-injection.

18. In scenarios with variable solvent cocnentration, higher C_4 concentration than the average value at the early times, increases early time oil rate. However, this causes to decrease ultimate recovery because higher early time oil rate accelerates the adverse effect of gravity segregation. In contrast with C_4-steam co-injection process, higher C_3 concentration at early times and lower concentration at late time during variable-concentration scenarios may increase ultimate bitumen recovery. The reason is that less oil rate of C_3-steam co-injection process leads to less adverse effect of gravity segregation. Moreover, increasing early time solvent concentration may accelerate early time propagation of steam chamber. Also, compared to C_4, existance of C_3 in the reservoir causes more reduction in the temperature of chamber edge. Therefore, less C_3 concentration at the late times, have the chance of producing more bitumen (i.e., higher stabilized oil rate) compared with the scenario with constant concentration. In variable-concentration scenarios, as the solvent concentration reduces in later times, solvent recovery increases.

19. Optimum solvent concentration for C_3-steam and C_4-steam co-injection processes during SAP is 2% mol and 3% mol, respectively at 3500 kPa. Optimum scenario for C_4-steam co-injection process is co-injecting C_4 with steam at constant 3% mol concentration at 3500 kPa. The optimum scenario for C_3-steam co-injection process is co-injecting C_3 with steam at 4%, 1% and 1% mol concentrations in three stages of 410 days after 3 months preheating and 6 months steam-only injection at 3500 kPa. Applying C_3- and C_4-steam co-injection with their optimized strategies during SAP lead to 2.6% and 5% increase in SAGD ultimate bitumen recovery factor at 3500 kPa, respectively. They reduce SAGD cummulative steam oil ratio (CSOR) by 33%.

20. The significant C_4 solubility in bitumen suggests stronger condensing effects during the interaction of bitumen with C_4 compared with C_3 and CO_2. C_4 has more viscosity reduction potential than CO_2 and C_3. Compared with C_3, C_4 has less potential for causing asphaltene precipitations. Therefore, C_4 may be a better solvent than C_3 and CO_2 for solvent-based and solvent-aided thermal methods. According to the results

of this study, both C_3 and C_4 are applicable for solvent-aided process which has the potential to increase efficiency of SAGD process.

7.1 SUGGESTED FUTURE WORK

To address the limitations of this study the following points are recommended as possible directions for further studies.

1. The phase behaviour and viscosity experiments are performed on a dead bitumen sample which is heavier than the in-situ bitumen. This can affect the phase behaviour and viscosity predictions.

2. In the viscosity measurement set-up, by applying a gasometer at the outlet of the reactor during the viscosity measurements, solvent solubility can be measured accurately at the test temperature and outlet pressure. This improves accuracy of the results.

3. Considering reservoir heterogeneity during simulations leads to a more realistic design of optimum Solvent Aided Process

4. Running in-house compositional simulation in which, the developed algorithm multiphase equilibria can be applied for predicting composition and amount of equilibrium phases including L_2 phase. This helps to accurately predict distribution of solvent in all potential liquid phases near the chamber edge. Also, solubility of water in the oil phase can be considered using the Equation of State and the developed algorithm. Extension of this study with a phase behavior model that can properly handle the mutual solubility of water and hydrocarbon components can improve the reliability of the results. Furthermore, applying the developed algorithm in stand-alone compositional simulation verifies its robustness in a wide range of composition, temperature and pressure.

5. Measuring onset of asphaltene precipitation in solvent-bitumen mixtures to be able to tune an Equation of State against the onset experimental data and predict asphaltene precipitation. Also, considering asphaltene precipitation during the simulation leads to a more realistic comparison of the efficiency of solvents during SAP.

6. Simulating co-injection of a mixture of gases (i.e., CO_2 and C_4) with steam during SAP. Simulating CO_2-based wind down processes after SAGD to reduce energy

intensity and green-house gas emissions. Also, simulating pressure blow down processes after SAP to enhance solvent recovery.

7. Due to the complexity of phase behavior, the reservoir oil in this study is considered to be two-component including C_1 and a lumped hydrocarbon component. Furthermore, the available solvent for co-injection may be multi-component. Extension of the current work to a system of multicomponent oil and solvent can improve the practical significance of the research.

References

Abdel-Ghani, R.M. 1995. EOS Mixing Rules for Multi-Phase Behavior. M. S. Thesis, the University of Calgary, Calgary (January 1995).

Adegbesan KO.: "A Successful History Match of a Thermal Horizontal Well Pilot", paper SPE 21539 presented at the International Thermal Operations Symposium, Bakersfield, California, February, 1991

AEUB, 2002, Statistical series 2000-18: Alberta's Reserves 1999, Volume 1. An Alberta Energy and Utility Board (AEUB) publication.

Ahmedzhanov, T. K., Nuranbaeva, B. M., Zhappasbaev, B. Z., Julomanov, T. D., & Bolathanov, B. B. (2013). DEVELOPMENT INNOVATIVE METHODS FOR INCREASING OIL RECOVERY DURING THE PRODUCTION OF HIGH-VISCOSITY AND PARAFFIN OIL. International Journal of Applied and Fundamental Research, (2), 345-345.

Akbarzadeh, K., Hammami, A., Kharrat, A., Zhang, D., Allenson, S., Creek, J., Kabir, S., Jamaluddin, A., Marshall, A.G., Rodgers, R.P. and Mullins, O.C., 2007. Asphaltenes—problematic but rich in potential. Oilfield Review.

Alsaifi, N.M. and Englezos, P. 2011. Prediction of Multiphase Equilibrium Using the PC-SAFT Equation of State and Simultaneous Testing of Phase Stability. *Fluid Phase Equilibria* **302** (1): 169-178.

Ammar, M.N. and Renon, H. 1987. The Isothermal Flash Problem: New Methods for Phase Split Calculations. *AIChE* J. **33**(6): 926-939.

Alberta Royalty Review, Wikipedia, The Free Encyclopedia, 11, Sep., 2018.

Anand, J., Somerton, W.H., and Gomaa, E., "Predicting Thermal Conductivities of formations from Other Known Properties," SPEJ, Vol. 13, No. 5, October 1973, pp. 267-273.

Ardali, M., Mamora, D.D., and Barrufet, M. 2010. A Comparative Simulation Study of Addition of Solvents to Steam in SAGD Process. CSUG/SPE Paper 138170 presented at Canadian Unconventional Resources and International Petroleum Conference, Calgary, Alberta, Canada, October 19-21.

Ardali, M., Barrufet, M., and Mamora, D.D. 2012a. Laboratory Testing of Addition of Solvents to Steam to Improve SAGD Process. Paper SPE 146993 presented at SPE Heavy Oil Conference Canada, Calgary, Alberta, Canada, June 12-14.

Ardali, M., Barrufet, M.A., Mamora, D.D., Qiu, F., 2012b. A Critical Review of Hybrid Steam/Solvent Processes for the Recovery of Heavy Oil and Bitumen. Paper SPE 159257 presented at SPE Annual Technical Conference and Exhibition, San Antonio, Texas, USA, October 8-10.

Arrhenius, S., 1887. The viscosity of aqueous mixture. Z. Phys. Chem, 1, pp.285-298. Ashrafi, M., et al. Experimental and Numerical Investigation of Steam Flooding

in Heterogeneous Porous Media Containing Heavy Oil. Society of Petroleum Engineers. 2011.

Asomaning, S., Watkinson, A. P. (2000).Heat Transfer Engineering.

Baker, L.E., Pierce, A.C., and Luks, K.D. 1982. Gibbs Energy Analysis of Phase Equilibria. SPE J. 22 (5): 731-742. SPE-9806-PA.

Bazyleva A, Akeredolu B, and Liberatore MW. Viscosity of Alaska Heavy Oil Saturated with Methane. Energy Fuels. 2013.

Badamchi-Zadeh, et al. Phase Behavior and Physical Property Measurements for VAPEX Solvents: Part I. Propane and Athabasca Bitumen. Petroleum Society of Canada. 2009.

Beattie, C.I., Boberg, T.C., and McNab G.S. 1991. Reservoir Simulation of Cyclic Steam Stimulation in the Cold Lake Oil Sands, SPE Reservoir Engineering.

Behzadfar, E., 2014. The flow properties of bitumen in the presence of carbon dioxide, Doctoral dissertation, University of British Columbia.

Bingham, E.C. The Variable Pressure Method for the Measurement of Viscosity. Proceeding of American Society for Testing Materials 18 (Part II). 1918.

BP Statistical Review of World Energy (BP, 2011); available at http://www.bp.com.login.ezproxy.library.ualberta.ca/statisticalreview.

Butler, R.M. and Mokrys, I.J. Recovery of Heavy Oils using Vaporized Hydrocarbon Solvents: Further Development of the VAPEX Process. J. Can. Pet. Technol. 1993.

Canadian energy research institute (CERI). 2013.Canadian oil sands supply costs and development projects (2012-2046).

Canbolat, S., Akin, S., and Kovscek A.R. 2002. A Study of Steam-Assisted Gravity Drainage Performance in the Presence of Noncondensable Gases. Paper SPE 75130 presented at Improved Oil Recovery Symposium, Tulsa, Oklahoma, USA, April 13-17.

Chaikunchuensakun S., Stiel, L.I. and Baker, E.L. 2002. A Combined Algorithm for Stability and Phase Equilibrium by Gibbs Free Energy Minimization, Ind. Eng. Chem. Res. 41 (16): 4132–4140.

Cenovus Energy, 2018, Author's Private Communication with Cenovus Energy, Reservoir Properties of Clearwater Formation in Cold Lake Region, Alberta, Canada.

CMG, Computer Modelling Group, Ltd. STARS, User manual. 2013.

Chung, F.T.H., Jones, R.A., and Nguyen, H.T. Measurements and Correlations of the Physical Properties of CO2/Heavy-Crude-Oil Mixtures. SPE Reservoir Eng., 1988.

Chang, P. and Wilke, C.R., 1955. Some Measurements of Diffusion in Liquids. The Journal of Physical Chemistry, 59(7), pp.592-596.

Cragoe, C.S. Changes in the Viscosity of Liquids with Temperature, Pressure and Composition. Proc World Pet Cong London. 1933.

Das, S.K. and Butler, R.M., 1995, January. Extraction of heavy oil and bitumen using solvents at reservoir pressure. In Technical meeting/petroleum conference of the South Saskatchewan section. Petroleum Society of Canada.

Deng, X., Huang, H., Zhao, L., Law, D. H.-S., and Nasr, T. N. Simulating the ES-SAGD Process with Solvent Mixture in Athabasca Reservoirs. J. Can. Pet. Technol. 2010.

Deo, M. D., Wang, C. J., and Hanson, F. V. (1991). Solubility of carbon dioxide in tar sand bitumen: experimental determination and modeling. Industrial & Engineering Chemistry Research, 30(3), 532-536.

Edmunds, N., Moini, B., & Peterson, J. (2010, September 1). Advanced Solvent-Additive Processes by Genetic Optimization. Society of Petroleum Engineers. doi:10.2118/140659-PA

Edmonds, B., Moorwood, R., Szczepanski, R., et al. 1999. Measurement and Prediction of Asphaltene Precipitation from Live Oils. Third International Symposium On Colloid Chemistry in Oil Production, 14-17.

Edmunds, N., Moini, B., and Peterson, J. (2010, September 1). Advanced Solvent-Additive Processes by Genetic Optimization. Society of Petroleum Engineers. doi:10.2118/140659-PA.

Eghbali, S., and Okuno, R. Successive Substitution Augmented for Global Minimization of the Gibbs Free Energy. SPE Annual Technical Conference and Exhibition. SPE 175060-MS. 2015.

Eghbali, S., Dehghanpour, H., Dragani, J., and Zhang, X., 2018. Phase Behavior and Viscosity of Bitumen-CO2/Light Hydrocarbon Mixtures at Elevated Temperatures: A Cold Lake Case Study. SPE Canada Heavy Oil Technical Conference. Society of Petroleum Engineers.

Eghbali, S., and Dehghanpour, H. 2018. An Experimental and Modelling Study of Solvent-Bitumen Phase Behavior at Elevated Temperatures using Cold Lake Bitumen. SPE Journal.

Firoozabadi, A. 1999. Thermodynamics of Hydrocarbon Reservoirs, first edition: McGraw-Hill Education.

Guan, J., 2013. Physical Properties of Athabasca Bitumen and Liquid Solvent Mixtures, Doctoral dissertation, University of Calgary.

Han, G. and Rangaiah, G.P. 1998. A Method for Multiphase Equilibrium Calculations, Comput. and Chem. Eng. 22 (7-8): 897-911.

Frauenfeld, T. W., Kissel, G. A., and Shibing Zhou, W. PVT and Viscosity Measurements for Lloydminster-Aberfeldy and Cold Lake blended Oil Systems. Canadian International Petroleum Conference. Petroleum Society of Canada. 2002.

Freitag, N. P., Sayegh, S. G., and Exelby, R. A New Semi-Automatic PVT Apparatus for Characterizing Vapex Systems. Society of Petroleum Engineers. 2005.

Gao, J., Okuno, R. and Li, H.A., 2016. June. An Experimental Study of Multiphase Behavior for n-Butane/Bitumen/Water Mixtures. In SPE Canada Heavy Oil Technical Conference. Society of Petroleum Engineers.

Gates, I.D. 2007. Oil phase Viscosity Behavior in Expanding-Solvent Steam-Assisted Gravity Drainage. Journal of Petroleum Science and Engineering.

Gates, I. D., and Gutek, A. M. H. 2008. U.S. Patent No. 7,464,756. Washington, DC: U.S. Patent and Trademark Office.

Gautam, R. and Seider, W.D. 1979. Computation of Phase and Chemical Equilibrium. AIChE Journal 25(6): 991-1007.

Gonzales, E. and Galeana, C., 2004, Asphaltene Precipitation in Crude Oils: Theory and Experiments. American Institute of Chemical Engineers.

Govind, P.A., Das, S.K., Srinivasan, S., and Wheeler, T.J. 2008. Expanding Solvent SAGD in Heavy Oil Reservoirs. Paper SPE/PS/CHOA presented at the 2008 SPE International Thermal Operations and Heavy Oil Symposium, Calgary, Alberta, Canada, October 20-23.

Gupta, A.K., 1990. Steady State Simulation of Chemical Process. PhD dissertation, University of Calgary, Calgary (November 1990).

Gupta, A.K., Bishnoi, P.R., and Kalogerakis, N. 1991. A Method for the Simultaneous Phase Equilibria and Stability Calculations for Multiphase Reacting and Non-Reacting Systems. Fluid Phase Equilib. 63(1): 65-89.

Gupta, S., Gittins, S., and Picherack, P. Insights Into Key Issues with Solvent Aided Process. Canadian International Petroleum Conference. Calgary. 2001.

Gupta, S., Gittins, S., and Picherack, P. 2005. Field Implementation of Solvent Aided Process. Journal of Canadian Petroleum Technology 44 (11): 8-13.

Gupta, S. C., and Gittins, S. D. 2006. Christina Lake solvent aided process pilot. Journal of Canadian Petroleum Technology, 45(09).

Gupta, S. C., and Gittins, S. D. 2007. Effect of solvent sequencing and other enhancements on Solvent Aided Process. Journal of Canadian Petroleum Technology, 46(09).

GLJ petroleum consultants, Natural gas and sulphur price forecast, Jan, 2017, https://www.gljpc.com/historical-forecast.

Haddadnia, A., Zirrahi, M., Hassanzadeh, H., & Abedi, J. (2017). Solubility and thermo-physical properties measurement of CO2-and N2-Athabasca bitumen systems. Journal of Petroleum Science and Engineering, 154, 277-283.

Haghighat, P. and Maini, B., 2008, Role of Asphaltene Precipitation in Vapex Process. Paper PETSOC 2008-087 presented at the Canadian International Petroleum Conference/SPE Gas Technology Symposium Joint Conference, Calgary, Alberta, Canada, 17-19 June.

Han, B., Peng, D.Y., Fu, C.T., and Vilcsak, G. 1992. An apparatus for phase equilibrium studies of carbon dioxide + heavy hydrocarbon systems. Canadian Journal of Chemical Engineering 70 (6): 1164-1171.

Han, B., Yang, G., Ke, J., Mao, C., and Yan, H., 1998, Phase Equilibria of Supercritical Propane Fengcheng Bitumen System and the Density and Viscosity of the Liquid Phase. Fluid Phase Equilibria.

Heidemann, R.A. 1983. Computation of High Pressure Phase Equilibria. Fluid Phase Equilibria 14: 55-78.

Hildebrand, J.H., 1936, Solubility of Non-Electrolytes. American Chemical Society Monograph Series, Reinhold Publishing Corporation, New York.

Huang, S.H. and Radosz, M. 1990. Phase behavior of reservoir fluids II: Supercritical carbon dioxide and bitumen fractions. Fluid Phase Equilibria 60 (1): 81-98.

Ito, Y. and Chen, J., 2009, January. Numerical history match of the Burnt Lake SAGD process. In Canadian International Petroleum Conference. Petroleum Society of Canada.

Ivory, J. J., Zheng, R., Nasr, T. N., Deng, X., Beaulieu, G., and Heck, G. 2008, January. Investigation of low-pressure ES-SAGD. In International Thermal Operations and Heavy Oil Symposium. Society of Petroleum Engineers.

Jha, K.N. 1986. A laboratory study of heavy oil recovery with carbon dioxide. Journal of Canadian Petroleum Technology 25 (2): 54–63.

Jiang, Q., Butler, R., and Yee, C.T. 1998. The Steam and Gas Push (SAGP)-2: Mechanism Analysis and Physical Model Testing. Petroleum Society's 49th Annual Technical Meeting, Calgary, Alberta, Canada, June 8-10.

Kariznovi, M. Phase Behavior Study and Physical Properties Measurement for Athabasca Bitumen/Solvent Systems Applicable for Thermal and Hybrid Solvent Recovery Processes. PhD thesis. University of Calgary. 2013.

Kariznovi, M., Nourozieh, H., and Abedi, J. Measurement and Correlation of Viscosity and Density for Compressed Athabasca Bitumen at Temperatures Up to 200ºC. Journal of Canadian Petroleum Technology. 2014.

Kaul, P.K. 1992. A New and Efficient Approach for Two Phase Equilibrium Prediction Using Cubic Equations of State. MS Thesis, Mississippi State University, Mississippi State, Mississippi (December 1992).

Kendall, J. and Monroe, K. The Viscosity of Liquids II. The Viscosity-Composition Curve for Ideal Liquid Mixtures. Journal of American Chemical Society. 1917.

Keshavarz, M., Okuno, R. and Babadagli, T., 2014. Efficient oil displacement near the chamber edge in ES-SAGD. Journal of Petroleum Science and Engineering, 118, pp.99-113.

Khaledi, R., Boone, T. J., Motahhari, H. R., and Subramanian, G. (2015, June 9). Optimized Solvent for Solvent Assisted-Steam Assisted Gravity Drainage (SA-SAGD) Recovery Process. Society of Petroleum Engineers. doi:10.2118/174429-MS

Kisman, KE., and Acteson, W.H.: "Application of Basal Water Sands to Enhance Thermal Recovery", Proceedings of the Fourth UNITAR Conference on Heavy Crude and Tar Sands, Edmonton, August, 1988, Volume 4,

Kisman, K.E. and Yeung, K.C., 1995, January. Numerical study of the SAGD process in the Burnt Lake oil sands lease. In SPE international heavy oil symposium. Society of Petroleum Engineers.

Kokal, S. L., Najman, J., Sayegh, s. G. and George, A. E., 1992, Measurement and Correlation of Asphaltene Precipitation from Heavy Oils by Gas Injection, J. of Can. Petrol. Technol.

Kokal, S., Al-Ghamdi, A. and Krinis, D. 2003. Asphaltene Precipitation in High Gas-Oil Ratio Wells. Paper SPE 81567 presented at SPE Middle East Oil Show, Bahrain, 9-12 June.

La, H., and Guigard, S. E. 2015. Extraction of hydrocarbons from Athabasca oil sand slurry using supercritical carbon dioxide. The Journal of Supercritical Fluids, 100, 146-154.

Leaute, R.P. 2002. Liquid Addition to Steam for Enhancing Recovery of Bitumen with CSS: Evolution of Technology from Research Concept to a Field Pilot at Cold Lake. SPE/Petroleum Society of CIM/CHOA Paper Number 79011, Calgary, Alberta, Canada, November 4-7.

Leaute, R.P., and Carey, B.S. 2005. Liquid Addition to Steam for Enhancing Recovery (LASER) of Bitumen with CSS: Results from the First Pilot Cycle. Paper Number 2005-161 presented at the 56th Canadian International Petroleum Conference, Calgary, Alberta, Canada, June 7-9.

Li, W. and Mamora, D.D. Phase Behavior of Steam with Solvent Co-injection under Steam Assisted Gravity Drainage (SAGD) Process. SPE EUROPEC/EAGE Annual Conference and Exhibition. SPE 130807. Barcelona. Spain. 2010.

Li, W., Mamora, D.D., Li, Y., 2011a. Light-and Heavy-Solvent Impacts on Solvent-Aided-SAGD Process: A Low-Pressure Experimental Study. Journal of Canadian Petroleum Technology 50(4): 19-30.

Li, W., Mamora, D.D., and Li, Y. 2011b. Solvent-Type and -Ratio Impacts on Solvent-Aided SAGD Process. SPE Reservoir Evaluation and Engineering 14 (3): 320-331.

Li, Z. and Firoozabadi, A. 2012. General Strategy for Stability Testing and Phase-Split Calculation in Two and Three Phases. SPE J. 17(4): 1096-1107. SPE-129844-PA.

Lederer, E.L. Viscosity of Diluted Mixtures. Paper 200, proceedings of the 14th World Petroleum Congress, London, 1933.

Linstrom, P.J., and Mallard, Eds., W.G., 2017, NIST Chemistry WebBook, NIST Standard Reference Database Number 69, National Institute of Standards and Technology. retrieved August 9, 2018. Gaithersburg MD, 20899, doi:10.18434/T4D303.

Lobe, V.M. University of Rochester, Rochester, New York, USA. MSc. Thesis. 1973.

Lohrenz, J., Bray, B.G., Clark, C.R. Calculating Viscosity of Reservoir Fluids from their Composition. J. Pet. Technol. 1964.

Luo, P., Yang, C., and Gu, Y. 2007a. Enhanced solvent dissolution into in-situ upgraded heavy oil under different pressures. Fluid Phase Equilibria 252 (1-2): 143-151.

Luo, P., Yang, C., Tharanivasan, A.K., and Gu, Y. 2007b. In situ upgrading of heavy oil in a solvent-based heavy oil recovery process. Journal of Canadian Petroleum Technology 46 (9): 37-43.

Luo, P. 2009. Asphaltene precipitation and its effects on a solvent-based heavy oil recovery process (Doctoral dissertation, University of Regina).

Mattar, L., Brar, G.S., and Aziz, K. Compressibility of Natural Gases. J. Can. Pet. Technol. 1975.

McRory, R.E., 1982. Energy heritage: oil sands and heavy oils of Alberta. Alberta Energy and Natural Resources.

Mehra, R. K., Heidemann, R. A., and Aziz, K. 1983. An Accelerated Successive Substitution Algorithm, Can. J. of Chem Eng. 61 (4), 590-596.

Mehrotra, A.K., and Svrcek, W.Y.. Measurement and Correlation of Viscosity, Density and Gas Solubility for Marguerite Lake Bitumen Saturated with Carbon Dioxide. AOSTRA J. Res. 1984.

Mehrotra, A.K., and Svrcek, W.Y. Viscosity, Density and Gas Solubility Data for Oil sand Bitumens. Part I: Athabasca Bitumen Saturated with CO and C_2H_6, AOSTRA J. Res. 1985.

Mehrotra, A.K. and Svrcek, W.Y. Viscosity, Density and Gas Solubility Data for Oil sand Bitumens. part II: Peace River Bitumen Saturated with N_2, CO, CH_4, CO_2 and C_2H_6. AOSTRA J. Res. 1985b.

Mehrotra, A.K. and Svrcek, W.Y. Viscosity, Density and Gas Solubility Data for Oil sand Bitumens. part III: Wabasca Bitumen Saturated with N_2, CO, CH_4, CO_2 and C_2H_6. AOSTRA J. Res. 1985c.

Mehrotra, A.K., and Svrcek W.Y. Correlations for Properties of Bitumen Saturated with CO_2, CH_4 and N_2, and Experiments with Combustion Gas Mixtures. J. Can. Pet. Technol. 1982.

Mehrotra, A.K., and Svrcek, W.Y. Properties of Cold lake Bitumen Saturated with Pure gases, the Canadian Journal of Chemical Engineering, 1988.

Mehrotra, A.K., Eastick, R.R., and Svrcek, W.Y. Viscosity of Cold lake Bitumen and its Fractions. Canadian Journal of Chemical Engineering. 1989a.

Mehrotra, A.K. A Mixing Rule Approach for Predicting the Viscosity of CO_2-Saturated Cold Lake Bitumen and Bitumen Fractions. Journal of Petroleum Science and Engineering. 1992.

Metz, B., Davidson, O., de Coninck, H., Loos, M., and Meyer, L. 2005. IPCC special report on carbon dioxide capture and storage. Intergovernmental Panel on Climate Change, Geneva (Switzerland). Working Group III.

Michelsen, M.L. 1982a. The Isothermal Flash Problem. Part I. Stability. *Fluid Phase Equilib.* **9**(1): 1-19.

Michelsen, M.L. 1982b. The Isothermal Flash Problem. Part II. Phase-Split Calculation. *Fluid Phase Equilib.* **9**(1): 21-40.

Miadonye, A., Doyle, N.L., Britten, A., Latour, N. and Puttagunta, V.R., 2001. Modelling viscosity and mass fraction of bitumen-diluent mixtures. Journal of Canadian Petroleum Technology, 40(07).

Miadonye, A., Singh, B., and Puttagunta, V.R. Viscosity Estimation for Bitumen-Diluent Mixtures. Fuel Science and Technology International. 1995.

Monnery, W. D., Svrcek, W. Y., Mehrotra, A. K. Viscosity: A critical review of practical predictive and correlative methods. Can. J. Chem. Eng. 1995.

Mohammadzadeh, O., Rezaei, N., and Chatzis, I. (2012, January). More Insight into the pore-level physics of the solvent-aided SAGD (SA-SAGD) process for heavy oil and bitumen recovery. In SPE Heavy Oil Conference Canada. Society of Petroleum Engineers.

Moreno LS, Babadagli T., 2013, Quantitative and visual characterization of asphaltenic components of heavy-oil and bitumen samples after solvent interaction at different temperatures and pressures. In: Paper SPE 164123 presented at the international symposium on oilfield chemistry 2013 joint conference, The Woodlands, Texas, USA, 8–10 April.

Mohammed-Singh, L. and Singhal, A.K. Lessons Learned from Trinidad's CO2 Immiscible Projects. SPE Reservoir Eval. Eng. 2005.

Motahhari, H.R. et al. Prediction of the Viscosity of Solvent Diluted Live Bitumen at Temperatures up to 175 oC. Canadian Unconventional Resources Conference. SPE 149405-MS. Calgary. 2011.

Motahhari, H. et al. Extension of the Expanded Fluid Viscosity Model to Characterized Oils, Energy and Fuels. 2013.

Nasr, T.N., Beaulieu, G., Golbeck, H., and Heck, G. 2003. Novel Expanding Solvent-SAGD Process "ES-SAGD". Journal of Canadian Petroleum Technology 42 (1): 13-16.

Nasr, T.N. and Ayodele, O.R., 2005, January. Thermal techniques for the recovery of heavy oil and bitumen. In SPE International Improved Oil Recovery Conference in Asia Pacific. Society of Petroleum Engineers.

Nghiem, L.X. and Li, Y.K. 1984. Computation of Multiphase Equilibrium Phenomena with an Equation of State. *Fluid Phase Equilib.* **17**(1): 77-95.

Nielsen, B., W. Svrcek, W., Mehrotra, A., Ing. Eng. Chem. Res. 33 (1994) 1324-1330.

Nourozieh, H. Phase Partitioning and Thermo-Physical Properties of Athabasca Bitumen/Solvent Mixtures, PhD thesis. University of Calgary. 2013.

Nourozieh, H., Kariznovi, M., and Abedi, J. Phase Behavior Study of Butane/Athabasca Bitumen Mixtures Applicable for Thermal and Hybrid Solvent Recovery Processes. Society of Petroleum Engineers. 2014.

Nourozieh, H., Kariznovi, M., and Abedi, J. Measurement and Correlation of Solubility and Physical Properties for Gas-Saturated Athabasca Bitumen. Society of Petroleum Engineers. 2016.

Nourozieh, H., Kariznovi, M., and Abedi, J. Measurement and Modelling of Solubility and Saturated-Liquid Density and Viscosity for Methane/Athabasca-Bitumen Mixtures. Society of Petroleum Engineers. 2016.

Okuno, R. 2009. Modeling of multiphase behavior for gas flooding simulation. PhD Dissertation, University of Texas at Austin.

Okuno, R., Johns, R.T., and Sepehrnoori, K. 2010. A New Algorithm for Rachford-Rice for Multiphase Compositional Simulation, *SPE J.* **15**(2): 313-325. SPE-117752-PA.

Orr, F.M. 2004. Greenhouse Gas Storage Keynote Presentation, SPE Annual Technical Conference and Exhibition, Houston, Texas, USA.

Orr, B. 2009. ES-SAGD; Past, Present and Future. Paper SPE-129518-STU presented at the 2009 SPE International Student Paper Contest at the SPE Annual Technical Conference and Exhibition, New Orleans, Louisiana, USA, October 4-7.

Orr, B.W., Srivastava, P., Sadetsky, V., and Stefan, B.J. 2010. Reducing Steam Oil Ratio in Steam-Assisted Gravity Drainage. CSUG/SPE Paper 136851 presented at the Canadian Unconventional Resources and International Petroleum Conference, Calgary, Alberta, Canada, October 19-21.

Pedersen, K. S., and Fredenslund, A. An Improved Corresponding States Model for the Prediction of Oil and Gas Viscosities and Thermal Conductivities. Chemical Engineering Science. 1987.

Peng, D.-Y. and Robinson, D.B. 1976a. A New Two-Constant Equation of State. *Ind. Eng. Chem. Fundam*. **15**(1): 59-64.

Peng, D.-Y. and Robinson, D.B. 1976b. Two and Three Phase Equilibrium Calculations for Systems Containing Water. *The Can. J. of Chem. Eng.* **54**(6): 595-599.

Perschke, D.R. 1988. Equation of State Phase Behavior Modelling for Compositional Simulation. PhD dissertation, the University of Texas at Austin, Austin, Texas (December 1988).

Ranger, M. J., and Gingras, M., 2010. Geology of the Athabasca oil sands: Field Guide & Overview. Canadian Society of Petroleum Geologists.

Redford, D.A. and McKay, A.S. 1980. Hydrocarbon-Steam Processes for Recovery of Bitumen from Oil Sands. Paper SPE 8823 presented at SPE/DOE Enhanced Oil Recovery Symposium, Tulsa, Oklahoma, USA, April 20-23.

Robinson, D.B. and Sim, S.K. 1981. The behavior of bitumen mixture during in-situ recovery; A Progress Report on Agreement 184, University of Alberta, Edmonton, AB.

Robinson, D.B., Kalra, H., and Sim, S.K. 1980. Behavior of bitumen-water-gas systems; Final Report on AOSTRA Research Agreement 43, University of Alberta, Edmonton, AB.

Saber, N., & Shaw, J. M. 2011. On the phase behaviour of Athabasca vacuum residue+ n-decane. Fluid Phase Equilibria, 302(1-2), 254-259.

Sandler, S. I. 2017. Chemical, biochemical, and engineering thermodynamics. John Wiley & Sons.

Saner, W.B. and Patton, J.T. CO_2 Recovery of Heavy Oil: Wilmington Field Test. J. Pet. Technol. 1986.

Sahin, S., Kalfa, U., and Celebioglu, D. Bati Raman Field Immiscible CO2 Application-Status Quo and Future Plans. SPE Reservoir Eval. Eng. 2008.

Shu, W.R. A Viscosity Correlation for Mixtures of Heavy Oil, Bitumen, and Petroleum Fractions. SPE Journal. 1984.

Shu, W.R. and Hartman, K.J. 1988. Effect of Solvent on Steam Recovery of Heavy Oil. SPE Reservoir Engineering 3 (2): 457-465.

Speight, J.G., 1978. Thermal cracking of Athabasca bitumen (pp. 123-154). Elsevier: Amsterdam.

Sayegh, S.G., Rao, D.N., Kokal, S., and Najman, J. 1990. Phase behaviour and physical properties of Lindbergh heavy oil/CO2 mixtures. Journal of Canadian Petroleum Technology 29 (6): 31–39.

Takamura, K., 1982. Microscopic structure of Athabasca oil sand. The Canadian Journal of Chemical Engineering, 60(4), 538-545.

Talbi, K. and Maini, B. Evaluation of CO2 Based VAPEX Process for the Recovery of Bitumen from tar sand reservoirs. SPE International Improved Oil Recovery Conference in Asia Pacific. SPE 64868. Kuala Lumpur. 2003.

Tedeschi, M.N., 1991, January. [13] reserves and production of heavy crude oil and natural bitumen. In 13th World Petroleum Congress. World Petroleum Congress.

Venkatramani, A. V., and Okuno, R. Compositional Mechanisms in Steam-Assisted Gravity Drainage and Expanding-Solvent Steam-Assisted Gravity Drainage with Consideration of Water Solubility in Oil. Society of Petroleum Engineers. 180737-PA. 2017.

Venkatramani, A. V. and Okuno, R. 2014. Modelling of Multiphase Behavior for Water/n-Alkane Mixtures by Use of the Peng-Robinson EOS. Presented at the SPE Heavy Oil Conference-Canada, Calgary, 10–12 June. SPE-170100-MS. https://doi.org/10.2118/170100-MS.

Vinsome, P.K.W., and Westerveld, J., "A Simple Method for Predicting Cap and Base Rock Heat Losses in Thermal Reservoir Simulators," JCPT, July-September 1980, pp. 87-90.

Wang, J. and Buckley. J., 2003, Energy and Fuel, 17(6).

Whitson, C. H. Michelsen, M. H. 1989. The Negative Flash. *Fluid Phase Equilib*. **53**: 51-71.

Wiehe, I.A., Yarranton, H.W., Akbarzadeh, K., Rahimi, P.M., Teclemariam, A., 2005, The paradox of asphaltene precipitation with normal paraffins. Energy Fuels 19, 1261–1267.

Wilson, G. 1969. A Modified Redlich-Kwong Equation of State, Application to General Physical Data Calculations. Paper presented at AIChE 65th National Meeting, Cleveland, Ohio, 4-7 May.

Yaws, C.L. 1999. Chemical Properties Handbook. McGraw-Hill, New York.

Yazdani, A. et al. A Parametric Simulation Study for Solvent Co-injection Process in Bitumen Deposits. Canadian Unconventional Resources Conference. SPE 148804. Calgary. 2011.

Yazdani, A. and Maini, B.B. Measurements and Modelling of Phase Behavior and Viscosity of a Heavy Oil/Butane System. J. Can. Pet. Technol. 2010.

Zhu, D. and Okuno, R. 2015a. Robust Isenthalpic Flash for Multiphase Water/Hydrocarbon Mixtures. SPE J. SPE-170092-PA. Preprint.

Zhu, D. and Okuno, R. 2015b. Analysis of Narrow-Boiling Behavior for Thermal Compositional Simulation, Paper presented at SPE Reservoir Simulation Symposium, Houston, Texas, USA, 23-25 February, SPE-173234-MS.

Appendices

Appendix A.

A.1 Correlations used for estimating pseudo-components properties

Specific gravity of pseudo-components:

$$SG_i = 1.07 - exp\big(3.56073 - 2.93886 Mw_i^{0.1}\big) \quad \text{A-1}$$

Specific gravity of plus fraction (Alboudwarej et al. (2003)):

$$SG_{C+} = 670 Mw_{C+}^{0.0629} \quad \text{A-2}$$

Boiling temperature of pseudo-components (Riazi (2005):

$$T_{bi}(K) = 1090 - exp(6.9955 - 0.11193 \times CN_i^{\frac{2}{3}}) \quad \text{A-3}$$

Boiling temperature of the plus fraction (Pedersen et al. (1985))

$$T_{b,C+}(K) = 97.58 \times Mw_{C+}^{0.3323} \times SG_{C+}^{0.04609} \quad \text{A-4}$$

Critical temperature (Lee and Kesler (1975))

$$T_{c,i} = 341.7 + 811 SG_i + (0.4244 + 0.1174 SG_i) T_{b,i} + \frac{(0.4669 - 3.2623\, SG_i) \times 10^5}{T_{b,i}} \quad \text{A-5}$$

Critical pressure (Lee and Kesler (1975)):

$$P_{c,i} = exp[8.3634 - \frac{0.0566}{SG_i} - \left(0.24244 + \frac{2.2898}{SG_i} + \frac{0.11857}{SG_i^2}\right) \times 10^{-3} \times T_{b,i} + \left(1.4685 + \frac{3.648}{SG_i} + \frac{0.47227}{SG_i^2}\right) \times 10^{-7} \times {T_{b,i}}^2 - (0.42019 + \frac{1.6977}{SG_i^2}) \times 10^{-10} \times T_{b,i}^3] \quad \text{A-6}$$

Acentric factor (Lee and Kesler (1975))

$$\omega_i = \frac{ln\big(P_{br,i}\big) - 5.92714 + \frac{6.09648}{T_{br,i}} + 1.28862\, ln\big(T_{br,i}\big) - 0.169347 \times T_{br,i}^6}{15.2518 - \frac{15.6875}{T_{br,i}} - 13.4721\, ln\big(T_{br,i}\big) + 0.4357 \times T_{br,i}^6} \quad \text{A-7}$$

$for\ T_{br,i} \le 0.8$

$$\omega_i = -7.904 + 0.1352 K_{w,i} - 0.007465 K_{w,i}^2 + 8.359 T_{br,i} + \frac{\big(1.408 - 0.01063 \times K_{w,i}\big)}{T_{br,i}} \quad for\ T_{br,i} > 0.8 \quad \text{A-8}$$

$P_{br,i} = \frac{P_{b,i}}{P_{c,i}}$ and $T_{br,i} = \frac{T_{b,i}}{T_{c,i}}$ where P_b is the pressure at which T_b is measured e.g., the normal boiling point at 14.7 psia. Pressure and temperature are in psia and R, respectively. $K_{w,i}$ is Watson characterization factor:

$$K_w = \frac{(1.8 T_b)^{1/3}}{SG} \quad \text{A-9}$$

T_b is in K in this equation.

Critical volume (Twu (1983))

$$V_c = [1 - (0.419869 - 0.505839\psi_i - 1.56436\psi_i^3 - 9481.70\,\psi_i^{14})]^{-8} \quad \text{A-10}$$

$$\psi_i = 1 - \frac{T_{b,i}}{T_{c,i}} \quad \text{A-11}$$

V_c is in ft^3/lbmol.

Mixing rule for estimating pseudo-components critical properties:

$$T_{c,k} = \frac{\sum_{i=m}^{i=n} z_i Mw_i T_{c,i}}{\sum_{i=m}^{i=n} z_i Mw_i} \quad \text{A-12}$$

$$P_{c,k} = \frac{\sum_{i=m}^{i=n} z_i Mw_i P_{c,i}}{\sum_{i=m}^{i=n} z_i Mw_i} \quad \text{A-13}$$

$$\omega_{c,k} = \frac{\sum_{i=m}^{i=n} z_i Mw_i \omega_i}{\sum_{i=m}^{i=n} z_i Mw_i} \quad \text{A-14}$$

Equation of State

Peng-Robinson (1978) equation of state is one of the most widely used EOSs in the petroleum industry. It uses two parameters as given below:

$$P = \frac{RT}{v-b} - \frac{a}{v^2 + 2bv - b^2} \quad \text{A-15}$$

$$a = a_c \alpha(T) \quad \text{A-16}$$

Where $a_c = 0.457235529\ \frac{(R\,T_c)^2}{P_c}$

$$\sqrt{\alpha(T)} = \left[1 + m\left(1 - \left(\frac{T}{T_c}\right)^{0.5}\right)\right] \quad \text{A-17}$$

$$m = 0.37464 + 1.54226\,\omega - 0.26992\,\omega^2 \ \ for\ \omega < 0.49 \quad \text{A-18}$$

$$m = 0.37464 + 1.48503\,\omega - 0.164423\,\omega^2 + 0.016666\,\omega^3\ for\ \omega \geq 0.49 \quad \text{A-19}$$

$$b = 0.077796\frac{(RT_c)}{P_c} \quad \text{A-20}$$

To extend a cubic EOS to mixtures of Nc components, the following van der Waals mixing rules are used:

$$a_m = \sum_{i=1}^{Nc} \sum_{j=1}^{Nc} x_i x_j\, a_{ij} \quad \text{A-21}$$

$$b_m = \sum_{i=1}^{Nc} x_i\, b_i \quad \text{A-22}$$

Parameters a_m and b_m are used in the same EOS as a pure fluid. the combining rule for a_{ij} is

$$a_{ij} = \sqrt{a_i a_j}(1 - k_{ij}) \quad \text{A-23}$$

where k_{ij} is the binary interaction parameter (BIP) between components *i* and *j*.

A.2 Re-calibrated EOS model for plotting pseudo ternary diagrams

Table A-1: Properties of the pseudo components in the re-calibrated EOS used for plotting pseudo-ternary diagrams

Component	Mw_i	T_c (K)	P_c (kPa)	ω	V_c (m^3/kgmol)
PC_1'	297.41	688.25	1931.4	0.83	0.78
PC_2'	1158.47	937.56	728.0	1.36	1.26

Table A-2: Optimized BIP values after EOS re-calibration used for plotting pseudo-ternary diagrams

	CO_2	C_3	C_4	PC_1'	PC_2'
CO_2	0.0000	0.1350	0.1300	0.0737	0.1037
C_3	0.1350	0.0000	0.00087	0.0360	0.0390
C_4	0.1300	0.00087	0.0000	0.0690	0.0888
PC_1'	0.0737	0.0360	0.0690	0.0000	0.0000
PC_2'	0.1037	0.0390	0.0888	0.0000	0.0000

Appendix B. Properties of the reservoir simulation model

Table B-1: The injection strategy of the base-case simulation model for solvent-steam co-injection process during SAP

Time (days)	Stage	Composition of the Co-injection Stream (mol%)	
		Solvent	Water
0-90	Preheating	0	1
90-270	SAGD	0	1
270-680	Solvent-Steam Co-injection	3	97
680-1090	Solvent-Steam Co-injection	3	97
1090-1500	Solvent-Steam Co-injection	3	97

Table B-2: Properties of the pseudo components in the calibrated fluid model used for generating gas-liquid K-values

Component	Mw_i	T_c (K)	P_c (kPa)	ω	V_c (m^3/kgmol)
C_1	16.04	190.6	4600.2	0.008	0.099
C_3	44.10	369.8	4245.5	0.152	0.203
n-C_4	58.12	425.2	3799.7	0.193	0.255
Bitumen	475	839.05	886.6	1.32	1.480

Table B-3: Optimized binary interaction parameters in the calibrated fluid model generating gas-liquid K-values

	C_1	C_3	n-C_4	Bitumen
C_1	0.0000	0.0000	0.0000	0.0000
C_3	0.0000	0.000	0.0000	0.0317
n-C_4	0.0000	0.0000	0.0000	0.058
Bitumen	0.0000	0.0317	0.058	0.0000

Table B-4: Properties of the simulation model used for reservoir simulation of Clearwater Formation

Property	Value
Porosity	0.33
Horizontal permeability	1200 md
Vertical permeability	960 md
Initial reservoir pressure at the depth of 456 m	2500 kPa
Initial reservoir temperature	12 °C
Initial oil saturation	0.51
Initial water saturation	0.45
Residual oil saturation in presence of water (sorw)	0.15
Residual oil saturation in presence of gas (sorg)	0.16
Water relative permeability at residual oil saturation ($K_r^o{}_{w(o)}$)	0.02
Oil relative permeability at initial water saturation (Krow)	1
Gas relative permeability at initial liquid saturation (Krgl)	0.8
Minimum producer bottom hole pressure	3400 kPa
Maximum producer steam rate	5 m^3/day
Steam quality	0.9
Three phase relative permeability (CMG, 2013)	Stone's model II
Formation compressibility	5e-6 1/kpa
Rock heat capacity	2.3e6 J/m^3°C
Over/underburden heat capacity	2.3e6 J/m^3°C
Over/underburden thermal conductivity	1.5e5 J/m^3day°C
Bitumen thermal conductivity	1.2e4 J/m^3day°C
Gas thermal conductivity	4000 J/m^3day°C

Appendix C. Sensitivity analysis on the simulation grid size

We performed a sensitivity analysis on the grid size in x and z directions to investigate the effect of grid size on the simulation results. Subsequently we obtained an optimum size based on the simulation run time and numerical dispersion criteria. We changed grid size in x and z directions from 1m to 0.08 m and compared the cumulative bitumen recovery and material balance error. Figure C-1 presents profiles of cumulative bitumen recovery at different grid sizes from 1 m down to 0.08 m. As Figure C-1 shows, bitumen recovery increases significantly by increasing grid size above 0.2 m. Simulation results for the models with 0.08 m and 0.2 m grid sizes are almost similar however the simulation run time is significanlty higher for the model with 8 cm grid size. Numercial dispersion for the model with 0.2 m grid size is almost similar to the one with 8 cm grid size as the material balance error is less than 0.005 for both 0.2 m and 0.08 m models. Therefore, we select the model with 0.2 m grid size as the base case for our simulations.

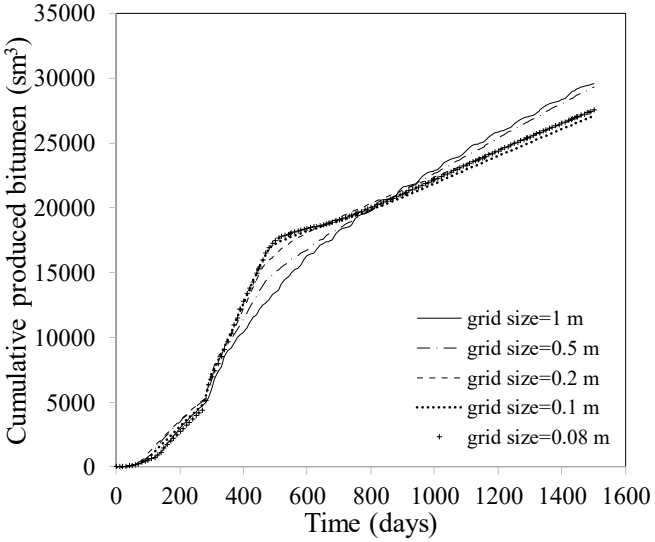

Figure C-1: Effect of grid size in x and z directions on bitumen recovery during SAP

Appendix D. Comparison of the bitumen production rate trend from SAGD simulation with literature

Figure D-1a shows the field produced oil rate from well pair 1 of SAGD process vs time in Burnt Lake oil-sand located in Clearwater Formation. Three pairs of SAGD wells began production in April of 1997 after three months of circulation (Ito and Chen, 2009).

To compare the oil rate trend versus time, we prepared a normalized plot as shown in Figure D-1b. In this plot, the oil rate values are divided by the maximum oil rate. Time values of the field data are re-scaled based on the maximum time of the simulation (i.e., 4.1 years). Therefore, field time values are divided by 4.1 years. Figure D-1b shows that produced oil rate has a reduction after a peak period in both simulation and field data. As it was explained in section 6.3.1, this reduction in the oil rate happens when the steam chamber reaches to the top of the reservoir and overburden heat loss increases. Beginning of this reduction is a function of the reservoir and fluid properties such as reservoir thickness, shale layers, etc. Thickness of the reservoir is 33 m in Burnt Lake oil-sand and 12 m in the simulated Clearwater formation in this study. Therefore, steam chamber in the Burnt Lake reservoir reaches to the top of the reservoir later than that in Clearwater Formation at the same CSOR. As a result, there is a more elongated peak time period in the Burnt Lake compared with Clearwater Formation.

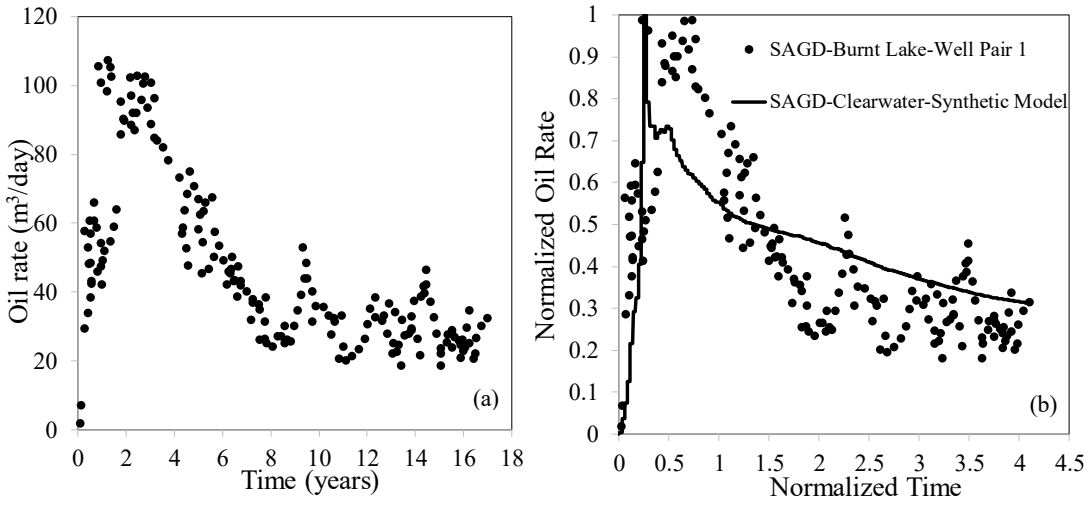

Figure D-1: a) Produced oil rate vs time from SAGD operation in Burnt Lake (Ito and Chen, 2009) b) comparison of the normalized produced oil rate from Burnt Lake SAGD operation with the one from SAGD simulation of this study

Appendix E. Ternary diagram

In this section we generate ternary diagram at a specific cell at different simulation times to visualize and compare the mechanism of oil displacement during SAGD and SAP. For this purpose, we perform material balance calculations using the K value tables for hydrocarbon and water components to calculate the phase composition and phase mol fractions at a specified composition, pressure and temperature. Here are the equations for calculating 7 unknown parameters of bitumen mol fraction in the oil phase (x_b), C_4 mol fraction in the oil phase (xC_4), bitumen mol fraction in the gas phase (y_b), C_4 mol fraction in the gas phase (yC_4), C_1 mol fraction in the gas phase (yC_1), oil phase mol fraction (n_L) and gas mol fraction (n_V).

$$z_b = x_b * n_L + y_b * n_V \quad \text{(E-1)}$$

$$z_{C4} = x_{C4} * n_L + y_{C4} * n_V \quad \text{(E-2)}$$

$$z_{C1} = (1 - x_{C1} - x_{C4}) * n_L + y_{C1} * n_V \quad \text{(E-3)}$$

$$K_{C1} = \frac{y_{C1}}{(1-x_{C1}-x_{C4})} \quad \text{(E-4)}$$

$$K_{C4} = \frac{y_{C4}}{x_{C4}} \quad \text{(E-5)}$$

$$K_b = \frac{y_b}{x_b} \quad \text{(E-6)}$$

$$K_W = 1 - y_{C1} - y_{C4} - y_b \quad \text{(E-7)}$$

Where z_i and K_i are overall mol fraction and equilibrium constant of ith component, respectively. Ternary diagram of the C_4-C_1-bitumen-water system is generated for a specific cell at different simulation times.

Ternary diagram of the C_4-C_1-bitumen-water system is generated for a specific cell (i.e., 17,1,5) at different simulation times. The cell is located in the fifth row below the top of the reservoir and steam chamber reaches to this cell until the end of simulation. Composition of C_1 and C_4 are summed up and assigned to one apex in ternary diagrams (see Figures E-1a to E-1d).

At 740 days and 87 ^oC, oil and water phases co-exist in equilibrium. C_4 is reached to the cell and C_4 mol fraction in the oil phase is 82%. The cell is located in the water zone at this time. Over time (at 1010 days), C_4 accumulates in the oil phase. C_4 overall composition and C_4 mol fraction in the oil phase increase to 5.8% and 95%, respectively. At 1010 days, two phases of oil and water co-exist in equilibrium at 109 ^oC. At this time, the cell is in the solvent zone and by more C_4 condensation, oil phase mol fraction is increased. At 1295 days, cell enters the steam chamber at 118 ^oC where

three phases of oil, water and gas co-exist at equilibrium. At this time, cell is near the chamber edge and C_4 fraction is increased in the gas phase (i.e., 94%) due to water condensation from the vapor phase into the water phase. At this time, cell is located at the co-condensation temperature of C_4-water mixture. C_4 mol fraction in the oil phase is 93%. At the end of the simulation (i.e., 1500 days), cell temperature is increased to 125 ºC and still three phases of oil, water and gas co-exist. C_4 mol fraction is reduced to 84% as the temperature is increased.

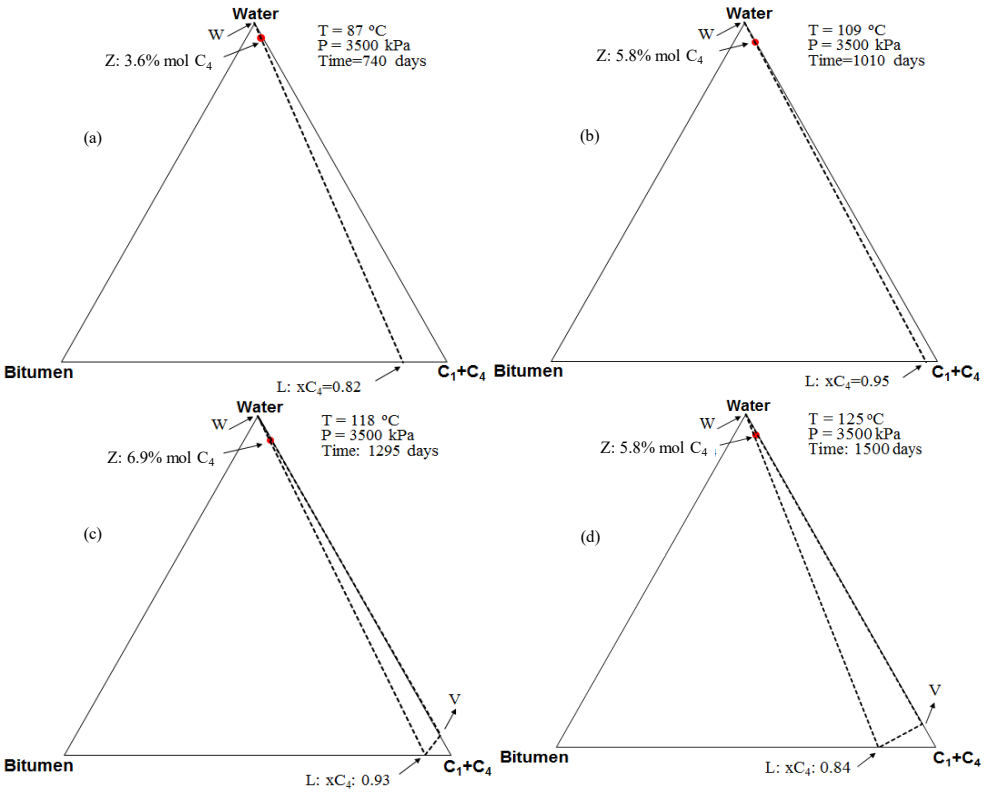

Figure E-1: Ternary diagrams of water-C1-bitumen-C4 system at cell 17,1,5 at a) 740 days b) 1010 days c) 1295 days and d) 1500 days during SAP at 3500 kPa

Ternary diagrams of water-C_1-bitumen system is also presented in cell 17,1,5 and different simulation times in Figures E-2a to E-2d. As Figures show, this cell is located in the water zone at 740, 1010 and 1295 days. In this zone, as more water condenses and more oil is produced, overal mol fraction of bitumen and oil phase mol fraction reduces in the cell (i.e., overall composition gets closer to the water apex). As temperature increases to 240 ºC, vapor phase appears in the system and at this time cell is in the steam chamber. At this high temperature, C_1 is vaporized and the oil phase gets rich in bitumen. As there is no dissolved C_4 in the oil phase, the only mechanism for oil production is mobilization of bitumen by water condensation and transfer of the steam latent heat to the cold bitumen. However, in SAP, accumulation of C_4 in the oil phase near the chamber edge (up to xC_4=0.95) leads to further reduction in heated

bitumen viscosity respect to SAGD. At 1010 and 1295 days, oil phase viscosity is 0.14 cp and 0.16 cP in SAP, respectively. However, at these times, oil phase viscosity is 30 cP and 7.6 cP in SAGD process, respectively.

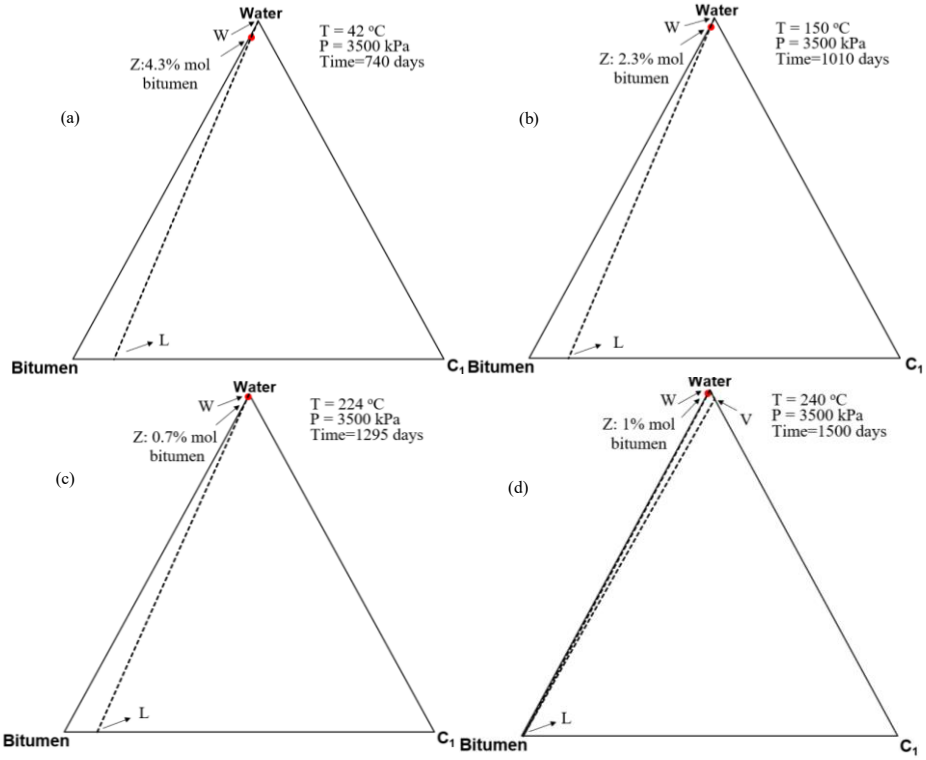

Figure E-2: Ternary diagrams of water-bitumen-C1 system at cell 17,1,5 at a) 740 days b) 1010 days c) 1295 days and d)1500 days during SAGD process at 3500 kPa

Appendix F. Net Present Value

Net Present Value is calculated from the following Eq.

$$NPV = \sum_{t=1}^{T} \frac{C_t}{(1+r)^T} - C_o \quad \text{(F-1)}$$

Where and T is number of time periods, C_t is net cash inflow during the period t, C_o is total initial investment costs and r is discount rate. We calculated C_t using Eq. F-2.

$$C_t = \begin{bmatrix} C_{bitumen} \times (1 - R_{royalty}) \\ + \\ C_{solvent} - C_{inj,solvent} - C_{inj,steam,elct} - C_{inj,steam,fuel} - C_{inj,steam,opt} \end{bmatrix} \times (1 - R_{tax}) \quad \text{(F-2)}$$

Where $C_{bitumen}$, $C_{solvent}$, $C_{inj,solvent}$, $C_{inj,steam,elct}$, $C_{inj,steam,fuel}$ and $C_{inj,steam,opt}$ are bitumen revenue, solvent revenue, solvent injection cost, steam injection cost (electricity), steam injection cost (fuel) and steam injection cost (operation), respectively. $R_{royalty}$ and R_{tax} are royalty rate and tax rate, respectively.

As capital cost is given in $/bbl, we use ultimate SAGD cumulative bitumen production to estimate capital cost for all processes (i.e., $\text{Capital cost} = \text{Ultimate } N_{p,SAGD}(\text{bbl}) \times 19.25 = 5.42$ MM$).

Table F-1: Inputs for NPV calculation, prices are in CAD

Item	Value
Capital cost ($/bbl of oil) (CERI, 2013)	19.25
Steam generation (electrical)/Water volume (bbl) (CERI, 2013)	2.69
Steam generation (Fuel)/Water volume (bbl) (CERI, 2013)	2.09
Operational and maintenance cost ($/bbl of oil) (CERI, 2013)	0.4
Solvent Cost ($/bbl of C_4) (GLJ, 2017)	54.2
Solvent Cost ($/bbl of C_3) (GLJ, 2017)	26.7
Oil price ($/bbl) (GLJ, 2017)	56.8
Discount rate	0.15
Tax rate	0.2
Royalty rate (Alberta Royalty, 2018)	0.0346

Appendix G

G.1 Production Performance of CO_2-steam Co-injection Process

Figure G-1 presents profiles of cumulative produced bitumen and CSOR for SAGD, CO_2-, C_3- and C_4- co-injections. Co-injection of C_3-steam and C_4-steam leads to 1.2% and 5% increase in URF with respect to the SAGD process at 3500 kPa and 3% mol solvent concentration in the solvent-steam stream. However, co-injection of 3% mol CO_2 with steam causes 10.4% reduction in URF respect to the SAGD case. The reason should be much less solubility of CO_2 respect to C_3 and C_4 in bitumen. Solubility of CO_2, C_3 and C_4 in bitumen at 140 ^oC and 3500 kPa is 17% mol, 50% mol and 88% mol, respectively. CO_2's solubility may not compensate for the adverse effect of reduction in steam chamber temperature. Therefore, bitumen recovery in CO_2-steam co-injection reduces respect to the SAGD process.

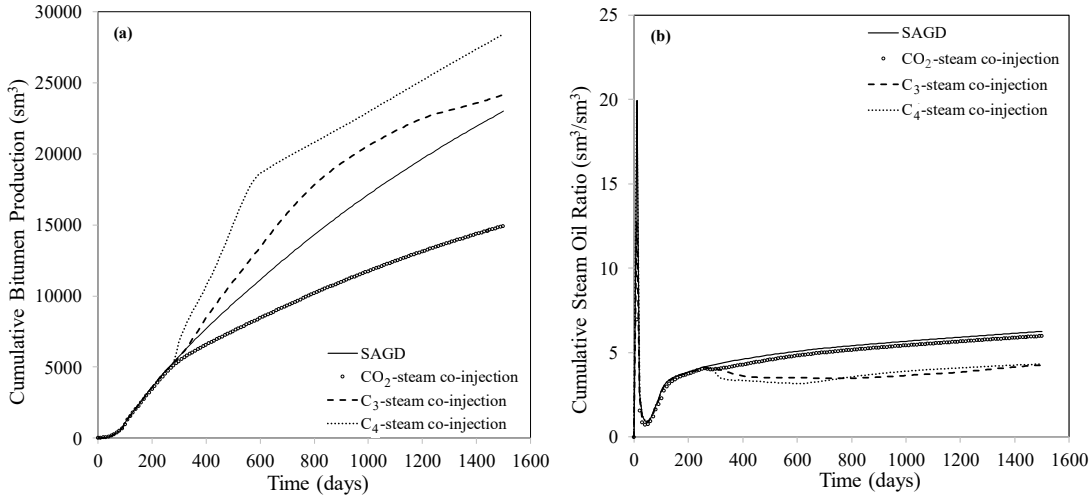

Figure G-1: Comparison of the a) cumulative produced bitumen and b) cumulative steam oil ratio between SAGD, CO_2-, C_3- and C_4-steam co-injection processes at 3% mol solvent concentration and 3500 kPa

G.2 Effect of Pressure on Optimum Solvent Concentration

Figure G-2a shows that maximum URF occurs at 1.5% mol C_4 at 4000 kPa. Above this concentration, CSOR reduces. However, this reduction is due to less steam consumption by adding more solvent to the co-injection stream. As this additional solvent does not lead to improvement in bitumen recovery, reduction of CSOR for concentrations above 1.5% may not lead to more efficient and economic process. Optimum C_4 mol% in the co-injection stream during SAP is 9%, 3% and 1.5% at 3000, 3500 and 4000 kPa, respectively. Figure G-3 presents URF and CSOR shows that optimum C_3 mol% in the co-injection stream is 5%, 2% and 0.5% at 3000, 3500 and 4000 kPa, respectively.

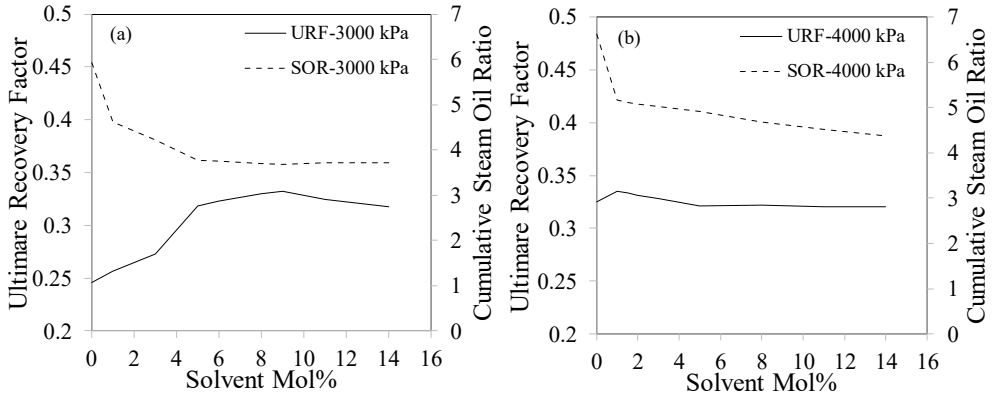

Figure G-2: Ultimate bitumen recovery factor (URF) and cumulative steam oil ratio (CSOR) versus C_4 mol% in the constant co-injection strategy during SAP at a) 3000 kPa and b) 4000 kPa

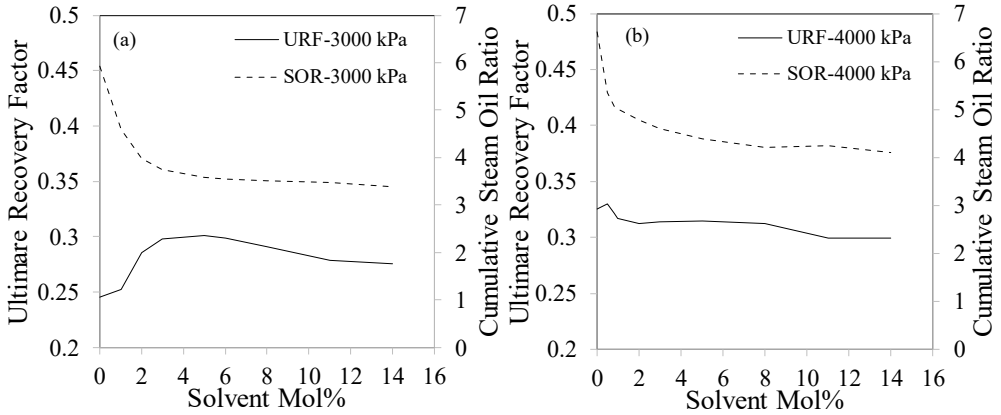

Figure G-3: Ultimate bitumen recovery factor (URF) and cumulative steam oil ratio (CSOR) versus C_3 mol% in the constant co-injection strategy during SAP at a) 3000 and b) 4000 kPa